A study to delineate arsenic safe and unsafe aquifers by hydrogeological, microbiological and numerical methods

Thesis submitted

In partial fulfillment of the requirement for the degree of

Doctor of Philosophy

by

Mr. Sandip Sampatrao Sathe

Under the guidance of

Prof. Chandan Mahanta

Department of Civil Engineering

Indian Institute of Technology, Guwahati

Guwahati- 781039, Assam, India

Department of Civil Engineering

Indian Institute of Technology, Guwahati

Declaration

I declare that the work embodied in this thesis is the result of investigations carried out by me in the Department of Civil Engineering, Indian Institute of Technology Guwahati, India. I hereby declare that the work presented in this thesis is to the best of my knowledge, original, except as acknowledged in the text. Other assistance received has been acknowledged. This material has not been submitted, either in whole or in part, for a degree or at any university.

Mr. Sandip Sampatrao Sathe

Research Scholar

Registration number: 126104022

Department of Civil Engineering

Indian Institute of Technology, Guwahati

Date:

Place:

Department of Civil Engineering

Indian Institute of Technology, Guwahati

Certificate

This is to certify that **Mr. Sandip Sampatrao Sathe** has been working under my supervision since July 2012 as a Ph. D. scholar. His thesis entitled "**A study to delineate arsenic safe and unsafe aquifers by hydrogeological, microbiological and numerical methods"** is an authentic record of the results obtained from the research work carried under my supervision in the Department of Civil Engineering, Indian Institute of Technology Guwahati, Assam, India.

I certify that he has fulfilled all the requirements according to the rules of this institute regarding the investigations embodied in his thesis work have not been submitted elsewhere for a degree.

Dr. Chandan Mahanta

(Thesis Supervisor)

Professor

Department of Civil Engineering

Indian Institute of Technology Guwahati

781039, Guwahati

Assam, India

Date:

Place:

Acknowledgment

I am indebted to many people who helped me over the year in this research work. It is my privilege to acknowledge these persons who have helped in various ways for the completion of my research work.

First and foremost, I would like to thank my supervisor, **Prof. Chandan Mahanta**, for the confidence he placed on me for carrying out this research work. His continuous guidance, motivation, and support have made this thesis seeing the light of the day. One of the most important qualities about him is that he provides liberty in work, which helped me to explore and learn the new technical methods. He was always calm and understood the student's point of view which helped at various stages of my thesis work completion. I really admire him because of his great passion for research work and above all he is a great human being. He will always be my inspiration because of this friendly and supportive nature. I feel lucky to have him as a mentor for my thesis.

I take the utmost pleasure to thank the Chairman of my doctoral committee, **Prof. P. K. Ghosh** and other members **Prof. K. Pakshirajan** and **Dr. S. Kartha** for their valuable suggestion and inputs throughout the work.

I want to thank **Prof. Gautam Barua** (former Director) and **Prof. Gautam Biswas,** Director of IITG for creating a wonderful campus and hospital facility, especially for the married scholar and their family members. I owe sincere thanks to the ministry of Human Resource Development, Government of India, for providing fellowship in the duration of my Ph.D. I am equally thankful to the Public Health Engineering Department (PHED), Bongaigaon and Darrang district of Assam, for all assistance and sharing data during for completing this thesis work. Also,

to the Assam Water Research and Management Institute, Society (AWRMIS) and Regional Meteorological Department (RMD) Guwahati, India, Ministry of Earth Sciences, India for sharing valuable meteorological data for completing the thesis work.

I want to express my gratitude to **Prof. A. K. Sarma**, (former HOD), **Prof. Subhashish Datta** (former HOD) and **Prof. Chandan Mahanta** (Head of the Civil Engineering Department), also Environmental Engineering laboratory in-charge **Dr. A. Kalamdad, Prof. P. K. Ghosh, Dr. H. Kota** and scientific officers & lab assistant **Ms.Jonali Saikia, Mr. Chitta R. Medhi, Mr. P. Pathak, Dr. K. K. Senapati, Mr. M. Borah, Mr. Kaustubh Acharyya** and **Mr.Aniruddha Gogoi** for the help and facilities provided for completion of this research work. I want to extend my sincere gratitude to **Er. Khanidra Das, Mr. L. Rahaman, Mr. Bodhiram Deka** and fieldwork peoples of Bongaigaon and Darrang district PHE department of Assam for taking care during work and help.

I gratefully acknowledge to the Department of Chemical Engineering, Department of Physics, Department of Chemistry, Centre for Environment, Centre for Nanotechnology and Central Instruments Facility for providing instrumental laboratory facilities for completion of this research work.

I feel deep gratitude for my friends who have made my research and sport experience at IIT Guwahati unforgettable: Mr. Sachin Pawar, Dr. Digvijay Pawar, Mr. Abhishek Bhosle, Mr. Shivanand Mali, Dr. Ratan Sarma, Mr. Devraj, Mr. Ganesh Sarma, Rajesh Atthanere, Sachin Tomar, Dr. Sushant Padhi, Dr. Arvind Shakya, Dr. Dhamodharan, Satish, Manoj Kr. Yadav, Uttam, Akshay, Yudhaveer, Atul, Akhil, Ravi Shukla, Sumit, Tarun, Avinash, Sandeep Markam, Manish, Anirudha Mahagaokar, Swagatam, Dr. Lalit Goswami, Narendra, Somnath, Bhanu,

Girish, Leichombam Menan, Laxmi, Sourabh Ahuja, Abhishek Joshi, with them I shared my pains, sorrows, fun and laughter. It was impossible to imagine a life in the campus without them.

Most of all, I want to thank my family: my mother **(Mrs. Suvarna),** Father **(Mr. Sampatrao)**, my spouse (**Mrs. Dipali**) and daughter (**Miss. Gautami)** who has been a constant source for encouragement, support, patience, and unconditional love. Your sacrification can't be repaid ever.

by

Mr. Sandip S. Sathe

Abstract

Arsenic contaminated groundwater aquifers (viz. < 70 m) in the alluvial floodplain of Brahmaputra have recently been reported as serious health concern since last one decade. Deposition of suspended sediments carried by numerous tributaries over a flat terrain of BFP and Ganga- Meghana flood plain (i.e., West Bengal, India, and Bangladesh) have the manifest equal potential of the source. Geogenic source of arsenic and the cause for mobilization in shallow aquifers of Brahmaputra flood plain (BFP) is less understood. The causes for the heterogeneous distribution of arsenic such as high (H*As*CR) and low (L*As*CR) contaminated region over parts of the BFP has more concern for the hydro-geologist. Understand the process and predominant mechanism prevailing in this region. Two study sites viz. Bongaigaon, H*As*CR and Darrang, L*As*CR district of Assam, India selected. Delineate the safe arsenic region and predict the arsenic concentration variation over the study area aquifers is a prerequisite to mitigate the problem. It's hypothesized that the cause for H*As*CR and L*As*CR region has controlled by an integrated factor such as arsenic bearing minerals dissolution and reduction mediated by indigenous microbes in the shallow aquifer. Moreover, an effect of metrology, topography, and stratigraphy has major control of arsenic mobilization in H*As*CR and L*As*CR region's aquifers.

Two sets of groundwater samples were collected and analyzed for 20 water quality parameters as per the American Public Health Association (APHA, 1998) standard method. The hydro-geochemistry of both the study area revealed a high concentration of dissolved Fe, Mn, HCO_3^{-}, and PO_4^{-2}. The heterogeneous high concentration of Cl^{-}, SO_4^{-2}, NO_3^{-}, NO_2^{-}, and PO_4^{-2} concentration was measured in second set groundwater samples of the H*As*CR study area. In the first set groundwater sample, topographically, distinctly varying arsenic concentration measured in L*As*CR region, namely in Pub Mangaldai (85 µg µg L^{-1}), Paschim Mangaldai (67 µg L^{-1}) and

Sipajhar (22 μg L^{-1}) were measured. Similarly, in H*As*CR groundwater samples, Tapatari (352 μg L^{-1}), Boitamari (66 μg L^{-1}) and Srijangram (171 μg L^{-1}) were measured. In second sets of groundwater sampling in both the study areas, comparatively low maximum *As* concentration was measured viz. maximum 37 μg $L^{-1}$and 56 μg L^{-1} in H*As*CR and L*As*CR respectively, groundwater samples. Predominate Ca^{+2}– Na^{+}– HCO_3^{-} facie was common in all the sets of groundwater samples. Comparing ionic concentration of Ca^{+2}, Na^{+}, HCO_3^{-}, and Mg^{+2} with meteoric global water, line signifies that dissolution of carbonate and silicate mineral was the common cause for high HCO_3^{-} concentration in both the study areas. The saturation index values estimated for each set of study areas depicted that precipitation (i.e. positive values) of iron and manganese bearing minerals act as a sink for low arsenic concentration in the region in H*As*CR and L*As*CR study area. Negative saturation index values for arsenic bearing minerals suggested the aquifer conditions favoring for the dissolution.

The physical characteristics of sediments such as color and texture showed a predominantly gray color observed in the high arsenic concentration region near Manas and Brahmaputra River in H*As*CR whereas comparatively low arsenic concentration region was observed in brown color sediments. The particle size distribution curves help to decipher the predominant aquifer and aquiclude, which validates the on-field prepared lithology for each bore wells. The pH of sediment depicts strongly acidic (i.e. gray color) to alkaline (i.e. brown color) condition. The results of sediment pH are well corroborated with the groundwater pH, and it was measured for the respective sediment color region. The selective aquifer sediment characterization showed that aquifers are enriched with total organic carbon and nitrogen, the presence of detrital and authigenic minerals. The maximum TOC content measured in both the study areas was 9% however, distinctly less TOC content was measured in brown color sediments. Highest 73 cmol kg^{-1} of CEC

was measured in L*As*CR region sediments samples, whereas the highest 60 cmol kg^{-1} of CEC was measured in brown color sediment samples of H*As*CR. High nitrogen content, i.e. 43.5 mg $g^{-1}$was measured in the yellow-gray color coarse sand with granules of H*As*CR study area, whereas, comparatively low (19.4 mg g^{-1}) content was measured in the deep gray medium sand samples of L*As*CR study area.

Elemental analysis of sediment samples was carried in XRF, FESEM-EDS, and ASTM soil digestion method. Potential arsenic concentration was measured in both the study areas sediments. Indigested sediment samples, maximum *As* the concentration of 107 µg g^{-1} and 63.2 µg g^{-1} was measured in H*As*CR and L*As*CR region sediment samples, respectively. In XRF analysis, considerably high *As* concentration, i.e. 50 mg kg^{-1} and 61 mg kg^{-1} was measured in H*As*CR and L*As*CR region sediment samples, respectively. In results of sequential extraction method, almost similar *As* concentration of 77 mg kg^{-1} and 53 mg kg^{-1} was measured in H*As*CR and L*As*CR sediment samples, respectively. In this analysis distinctly high *As* affinity was observed with poorly crystalline or amorphous oxide of Fe, Al and Mn phase minerals for H*As*CR study area sediment samples. Arsenic affinity was also observed with other elements (viz. Ca, Mg and K) in L*As*CR sediment samples. The elemental ratio of O/*As* in FESEM-EDS analysis supports the finding of above methodology, which suggests that *As* was co-precipitated with ferric oxide and get adsorbed on sediment surface. The morphological analysis of sediment samples showed presence of detrital and authigenic minerals in H*As*CR study area aquifers samples whereas, considerably more distorted crystalline shapes of different mineral were observed in the L*As*CR aquifer samples. The minerals characteristic peaks observed in XRD and FTIR analysis further supports the presence of arsenic, iron, manganese, chromium, aluminum and detrital clay minerals in H*As*CR and L*As*CR samples. The highest arsenic adsorption capacity was observed at pH 7 for

As^{+5} than As^{+3} whereas, Pseudo-second order kinetic reaction model was best fitted to the selective depth sediment samples. In Langmuir and Freundlich isotherm arsenic adsorption study, comparatively Freundlich isotherm showed the best fit. The adsorption coefficient value 'K_d' 14.3 L kg^{-1} and 11 L kg^{-1} was measured for As^{+3} and As^{+5}, respectively for H*As*CR sediment samples. Similarly, the equal adsorption coefficient values, i.e. 13 L kg^{-1} was measured for L*As*CR sediment samples.

In a preliminary microbiological study, predominantly *Pseudomonas aeruginosa* bacterium of As^{+5} reducing characteristic was isolated from groundwater samples of H*As*CR study area. Similarly, in the second sets of the groundwater sampling, two bacteria namely *Lysinibacillus sphaericus and Acinetobacter nosocomialis* were isolated and identified by 16 Sr RNA analysis from the H*As*CR study area, which showed As^{+5} reducing characteristic. Similarly, from L*As*CR study area, predominately As^{+5} reducing bacterium, namely *Pseudomonas aeruginosa and Bacillus licheniformis* were isolated and identified in the 16Sr RNA analysis. The maximum arsenic tolerance limit for *Lysinibacillus sphaericus* and *Acinetobacter nosocomial* was 1000 mg L^{-1} and 1500 mg L^{-1} respectively from H*As*CR and *Pseudomonas aeruginosa*, and *Bacillus licheniformis* bacterium arsenic tolerance limit was 1250 mg L^{-1} and 1500 mg L^{-1} respectively, was found through optimum density curve method.

To manage and mitigate the arsenic-contaminated groundwater problem at the regional scale, a numerical groundwater modeling software (viz. GMS 10.2) was used. A 3D transient state predictive groundwater flow (viz. MODFLOW) and contaminant transport (viz. MT3DMS) conceptual model for two distinctly different arsenic-contaminated (i.e., H*As*CR and L*As*CR) regions were developed. The model was built by using the hydro-geological data, empirical values, and formulas. The model calibration, sensitivity analyses, and validation were done by varying

boundary conditions. The MODFLOW results suggested that groundwater contours in both the study areas were directly controlled by the complex hydrostratigraphy, surface water bodies and indirectly controlled by the change in meteorological conditions. The observed residual head difference in intransient state MODFLOW model results observed between the computed head (-0.5 m, 0.7 m, -5.6 m, -0.8 m for H*As*CR and -3.2 m and -6.7 m for L*As*CR district study area) and observed head credential data's of CGWB well for each region. It matched reasonably with the computed head and observed head within the permissible limit of 5% difference. The MT3DMS model, for arsenic contaminant transport model was used for the assessment of shallow and deeper aquifers vulnerability, showed that the downward movement of *As* has made the deeper aquifer unsafe for drinking water and irrigation purposes.

Thus, the transient state predictive groundwater flow and contaminant transport modeling study has inferred that aquifers with high flushing capability, negligible vertical hydraulic conductivity can be delineated as *As* safe groundwater source irrespective of sediment color. The detailed data about water quality, stratigraphy, and metrological information replicates the actual groundwater flow and contaminant distribution in different aquifer depth would help for future groundwater policy and management.

The combined results of shallow aquifer groundwater hydrogeochemistry have suggested that the rate of weathering (e.g., silicate), dissolution (e.g. carbonate, Fe, Mn) and precipitation of solid phase minerals (viz. *As*, Fe, Ca, Cu and Pb) are the primary processes responsible for *As* mobilization in both the study areas. Secondary effect mainly by competing ions (e.g. HCO_3^- and PO_4^{3-}) on adsorption sites of Fe and Mn bearing minerals have been identified and which are more vulnerable to groundwater table fluctuation in both the study area. These findings suggest that microbial metabolic activities were equally responsible for iron-oxy/hydroxide reductive

dissolution, which control *As* mobilization in the dynamic fluvial floodplains of BFP. Therefore, use of experimental data in both the numerical modeling simulation has inferred that estimation, delineation, and mitigation of *As* contaminanted groundwater is a technically viable tool for a complex hydro-stratigraphy and it can be used as an effective decision-making tool.

Content

List of the Tables

List of the Figures

Abbreviations and acronyms

AAS	Atomic absorption spectroscopy
As(III)	Trivalent Arsenic, Arsenite
As(V)	Pentavalent Arsenic, Arsenate
ASTM	American Society for Testing and Materials
Avg.	Average
AWRMI	Assam Water Research and Management Institute
BDL	Below Detection Limit
C	Carbon
CEC	Cation exchange capacity
CGWB	Central Ground Water Board
DEM	Digital Elevation Model
DO	Dissolved Oxygen
EC	distribution coefficients
EDS	Electric Conductivity
F	Fluoride
Fe	Iron
FESEM	Energy Dispersive Spectroscopy
FTIR	Field Emission Scanning Electron Microscope
GBM	Fourier-transform infrared spectroscopy
GPS	Global Positioning System
HAsCR	Ganga-Megana-Brahmaputra
HTW	hand-pump tube wells
k	Number of Contaminants Species
K_d	High arsenic contaminant region
K_x & K_y	Horizontal Hydraulic Conductivity
Kz	Vertical Hydraulic Conductivity
L*As*CR	Low arsenic contaminant region
Max.	Maximum
Min.	Minimum
MODFLOW	Modular Finite-Difference Flow Model
MT3DMS	Modular Transport 3-Dimensional Multi-Species model
OH	Hydroxyl
ORP	Oxidation Reduction Potential
P_e	Peclet Number
PHED	Public Health Engineering Department

PWSS	Public Water Supply Scheme
RASA	Regional Aquifer System Analysis
S.D.	Standard Deviation
SRTM	Shuttle Radar Topography Mission
Ss	Specific Storage
SSE	Selective Sequential Extraction
Sy	Specific Yield
T%	Transmittance
TDS	Total Dissolved Solid
TEM	Transmission electron microscopy
UNICEF	United Nations International Children's Emergency Fund
UTM	Universal Transverse Mercator
WGS	World Geodetic System
WHO	World Health Organization
XRD	X-ray fluorescence
XRF	X-ray powder diffraction
ρ	Pearson correlation coefficient

Chapter 1

1 Introduction

1.1 Background

Arsenic (*As*) is a notorious poison, threatening the lives of millions of people over the world. Long term consumption of low *As* concentrated groundwater and *As* containing food cycle produces a broad array of effect on human health such as a skin ailment to painful skin lesions, which is also known as keratosis. Chronic fatigue diseases to humans such as liver, bladder and kidney cancer, also cardiovascular and peripheral vascular diseases, neurological effect, diabetes, acute lung cancer and consequently thereby death have also been reported (Bhattacharya et al., 2002; Fendorf et al., 2010; McArthur et al., 2004a; van Geen et al., 2008; Wenzel et al., 2001a). The geogenic source of *As* in the alluvial aquifer of Brahmaputra floodplain (BFP) has threatened the lives of several millions of people (Chakraborti et al., 2002; Goswami, 1985; Sailo and Mahanta, 2016a, 2013; Sathe et al.,2018; Verma et al., 2015a). The occurrence of objectionably high concentration of *As* in groundwater has long been detected in shallow (<70m) aquifer groundwater of Bongaigaon and Darrang district and other parts of Brahmaputra basin, Assam, India (Das et al., 2016; Kumar et al., 2016; R T Nickson et al., 2000; Sailo and Mahanta, 2013; Sathe et al., 2018; A. K. Singh, 2004). The study conducted by Singh (2004) over parts of BFP has reported that 20 out of 30 districts [viz. Jorhat (194 - 657 µg L^{-1}), Dhemaji (100 - 200 µg L^{-1}), Golaghat (100-200 µg L^{-1}), Karimganj and Dhemaij (>300 µg/l), and Lakhimpur (50-550 µg L^{-1})] groundwater well samples of Assam has measured dissolved *As* concentration above 50 µg L^{-1} whereas, in Karimganj and Dhemaji district 19% of the groundwater samples have recorded *As* concentration more than 50 µg

L^{-1} and in 2% groundwater samples *As* concentration was measured above 300 µg L^{-1}. Furthermore, in the year 2005, a joint study carried by Public Health Engineering Department (PHED) of Assam had analyzed in total 5,729 groundwater samples from 30 districts of Assam state. Their results have shown that 18 districts groundwater samples, containing *As* concentration above 50 µg L^{-1} in the shallow aquifer. Recent studies by Mahanta et al., (2015) and (Verma et al., 2015) have reported that highest *As* concentration in groundwater samples was measured as 606 µg L^{-1} and 130 µg L^{-1} in Bongaigaon and Darrang districts, respectively. Other toxic elements such as Cd (< 0.89 µg L^{-1}, Cr (<0.48 µg L^{-1}), Zn (19 to 400 µg L^{-1}) and Cu (<0.34 µg L^{-1}), Fe (55 to 43161µg L^{-1}), Mn (170 to 6000µg L^{-1}), Na (6193.95 to 67292.3 µg L^{-1}) and Mg (3114.79 to 16435.7µg L^{-1}) was also reported in the analyzed samples (Mahanta et al., 2015; Nordborg, 2007; A. Singh, 2004).

The Brahmaputra Flood Plain (BFP) is also known as one of the largest alluvial flood plains in the world. It has complex hydro-geologically strata and dynamic fluvial plain. It is comprised of numerous perennial tributaries and small streams, which are originated from the eastern Himalayans ranges (Verma et al., 2015). The geology of BFP has been characterized as a Holocene age alluvial formations (Mahanta et al., 2015). The average groundwater table occurs in this region at a depth of ~10 m below ground level (bgl) (Mahanta et al., 2015). It is a more economical and easily available water source in remote places of BFP. It has made most of the population to rely on groundwater source in this region. Daily usage of this *As* contaminated groundwater by the habitations leads to chronic *As* poising and health hazard risk to the peoples living shortly. Therefore, these regions had constantly demanded a sustainable *As* safe groundwater management plans and efficient source of groundwater in BFP. Understand the cause of *As* source, management

plans for a safe *As* groundwater source in shallow aquifer of BFP has been carried out to avoid the risk of major health hazard for these people.

1.2 Thesis objectives and hypothesis

The present study aims to identify the source of *As* in the shallow aquifer sediments of BFP and the mechanism involved for the heterogeneous distribution of *As*, also predict the future *As* concentration with numerical contaminant transport modeling and delineate the *As* safe aquifer region for the study areas. The following objectives were set to complete the research work:

1. Evaluate the shallow aquifer hydro-geochemistry; identify a predominant hydrogeochemical facies and minerals saturation indices, along with identity possible weathering mechanism responsible for *As*-mobilization in groundwater of high arsenic contaminated region (H*As*CR) and low arsenic contaminated region (L*As*CR).
2. Find the mineralogical genesis, morphology and elemental characterization of aquifer sediments from H*As*CR and L*As*CR region, and understand the role of sediment color for delineation of *As* safe aquifer.
3. Isolate, identification and characterization of indigenous microbes from H*As*CR and L*As*CR study area and find their maximum tolerance limit in *As*-contaminated synthetic water at lab scale.
4. Delineate *As* safe aquifer in the contaminated region using a numerical software by developing a groundwater flow (i.e. MODFLOW) model and a predictive groundwater contaminant (i.e. MT3DMS) transport model.

Its been hypothesized that the geogenic source of *As* is mainly present in the shallow aquifers of the BFP, which is probably controlled or mobilized by complex hydrostratigraphy and redox

condition simultaneously. This study further probed to understand the adsorption capacity of sandy aquifer material (i.e., brownish, reddish and grayish color) by fitting the adsorption model. Their physical characterization was further used to construct a numerical contaminant model. The biotic factors such as indigenous microbes prevailing at the high *As* contaminated region and its characteristics (viz. Reduction or oxidation) have to study at lab scale. It has also been hypothesized that high dissolved *As* can also be controlled by the indigenous bacterium in the H*As*CR and L*As*CR study areas. Mitigate the *As* contamination problem at a regional scale, and a predicative contaminant transport model have to be built using experimental and meteorological data.

1.3 Significance of the research work

Since last two decades, numerous studies have reported high *As* contaminated groundwater regions from various parts of the world and established broad consciences about *As* mobilization mechanism based on various experimental results. The BFP (formed by numerous transboundary tributaries of Brahmaputra River) has a potential source of *As* in weathered sediment which has barely been studied and characterized since last two decades. The suspended sediment load carried by the Brahmaputra River contributes a major volume of sediment to form a flat alluvial floodplain in Bangladesh, which is also known for the highest *As* contaminated groundwater country in the world.

Results of this study expected to contribute towards a broad understanding of a hydro-geochemical process, minerals weathering, dissolution, and precipitation in shallow aquifer. Isolation, characterization, and effect of indigenous microbes on *As* mobilization will decipher the cause of high and low *As* contaminated regions which will help to understand the role of biotic factor in the study areas. Utilization of all experimental data to replicate the natural groundwater

table scenario using numerical groundwater modeling software to mitigate and decide the best groundwater policies for *As* contamination problem at the regional scale.

1.4 Thesis organization

A thesis is compiled in five chapters: Chapter 1 is an introductory chapter which concisely explains the present status of *As* in BFP. This chapter includes the set of objective and hypothesis of this work, which also explains the necessity of this research work. Chapter 2 presents the relevant literature survey according to the set objective, which includes the general hydro-geochemistry in parts of the alluvial aquifers in the world. The various methods for sediment characterization and their significance in *As*-contaminated aquifers at a basin or regional scale study.

Furthermore, a literature survey explains the role of the indigenous bacterium and its characteristics impart certain aquifer condition and causes for the heterogeneous distribution of *As* in parts of basin or region. The application of numerical groundwater flow and contaminate transport model provides an effective scientific tool for assessing the regional scale *As* contaminated aquifer and can provide immediate mitigation solution considering meteorological effects over the study area. Chapter 3 introduces the importance of the H*As*CR and L*As*CR study area. It further explains in details the materials and methodologies followed for the analysis of groundwater, sediment characterization, indigenous bacterium isolations and input parameters, data, and boundary conditions used for the numerical modeling.

In Chapter 4, presents the precise results obtained from the above methodologies with the discussion. Subsection 4.1 presents the hydro-geochemistry of both the study areas and shown major hydrogeochemical facies, minerals saturation indexes also weathering, dissolution, and evapotranspiration compared with the global meteoric water line. Furthermore, a statistical analysis

(i.e., Person correlation) explains the possible affinity of each element with other elements by numerical values and provides proof to a certain hypothesis. Subsection 4.2 provides insight into sediments physical, chemical, and biological characterization subsequently. Subsection 4.3 explains in details about the presence of indigenous bacteria present in H*As*CR and L*As*CR study area along with morphology, the maximum limit of *As* tolerances and characteristics. Subsection 4.4 showed the application of numerical modeling software for mitigating *As* contaminated groundwater problem at a regional scale.

Chapter 5, concisely presents the summary and conclusion of the obtained results. It also provides a further research scope for this research work. References and bibliography were enlisted by following the reference style of 'Journal of Contaminant Hydrology' journal, Elsevier in alphabetical order. The 'Appendix A' includes results of statistical correlation, minerals equilibrium state in liquid phases. Similarly, 'Appendix B' includes figures of CEC with depth wise variation in sediments, total sediment digestion results showing elemental variation with depth, morphological and elemental composition of authigenic and detrital minerals, characteristic peaks of minerals identified in XRD analysis, presence of functional groups, isotherm data and results of numerical groundwater and contaminant transport modeling.

Chapter 2

2 Literature review

Arsenic is a widely distributed toxic metalloid in the natural environment, which is well known for carcinogenic effects on humans and cause for deformities & mutations in the human body. Arsenic and its compounds accumulate in animals and plants body, which can be spread via food chains, harming the ecological environment and humanity (Cullen and Reimer, 1989). There are two ways of *As* groundwater pollution, i.e., the natural release of arsenic from high-arsenic underground water (Smedley and Kinniburgh, 2002) and anthropogenic activities (viz. Industrial emission) (Bhattacharya et al., 2002). Therefore, causes for high dissolved *As* concentration in Holocene age alluvial aquifers have an enormous concern in the world.

South Asian countries (viz. India, Bangladesh, Nepal, Bhutan, Pakistan, and Sri Lanka), which are well known for high *As* contaminated groundwater (McCarty et al., 2011). Since the last three decades, heterogeneous distribution of dissolved *As* over the region have been reported from these countries. Following sub-sections have explained in brief about the present status of *As* in these countries, esp. general hydro-geochemistry, solid-phase *As* concentration and presence of other affinities with toxic elements, the role of microbiology on *As* mobilization and application of numerical contaminant transport modeling for mitigation and policies making for the *As*-contaminated regions.

2.1 Present status of Arsenic in parts of the world

Knowledge and theories on groundwater and sediment *As* contamination has built enormously since past two to three decades. Naturally occurring *As* in groundwater used for drinking and cooking is a catastrophe to the global population. The worst affected Ganga-Meghana-Brahmaputra flood plain is commonly described as the largest poising of a population in history. Long-term exposures to the lowest level of *As* consumption (via. Food or drink water or air) had scientifically understood to produce a broad array of adverse effects on human health. Table 2.1 enlisted the severely *As* affected countries, source and causes for *As* mobilization in the world.

In India, the first time 16 arsenicosis patient was reported from West Bengal in 1983 (Chakraborti et al., 2002). Plant et al., (2003) reported that more than 60 % of the tube wells in southern Bangladesh and West Bengal, India are containing *As* concentration > 10 µg L^{-1}. Biswas et al., (2014) have reported that shallow aquifer (i.e., < 50 m) containing dissolved *As*, Fe and Mn concentration in 106 groundwater samples out of 413 samples. They contain *As* concentration below 10 µg L^{-1}. Therefore, studies over Ganga and Meghna flood plain have suggested that Pleistocene age (~ 70 ka) aquifer sediments are less *As* contaminated than the Holocene age (< 9.51 ka) aquifer sediments (Biswas et al. 2014a). The recent investigations in BFP about *As* vulnerability in groundwater sources by geogenic abundance has put the growing population on the edge of chronic *As* diseases (Kumar et al., 2016; Mahanta et al., 2015; Nordborg, 2007). The need for a long term secure and efficient source of groundwater in BFP has initiated prolonged water demand targeting economic and low *As* contaminated groundwater

Table 2. 1 Established hypothesis reported from different parts of the world

Hypothesis for geochemical processes	Affected areas/ aquifers	Arsenic concentration			Key finding	References
		Region/ Country	Maximum concentration of *As* in Groundwater (µg L^{-1})	Maximum concentration of *As* in Sediments (mg kg^{-1})		
Reductive dissolution of Fe oxy/hydroxides minerals	Brahmaputra floodplain,	Assam, India	657	43	**Source:** Holocene age aquifer sediments, **Release:** the Reductive dissolution of Fe-oxy/hydroxides	Sailo and Mahanta (2014); Singh (2004)
	Bengal Delta Plain (BDP),	West Bengal, India	4622	18	**Source:** Holocene age aquifer sediments rich in humic like substance **Release:** the Reductive dissolution of Fe-oxy/hydroxides	Kulkarni et al. (2017)
	South-East of China	China	676	1000	**Source:** Holocene age aquifer sediments rich in humic like substance **Release:** the Reductive dissolution of Fe-oxy/hydroxides	Zhang et al. (2017)

Oxidation of Arsenic ore	Padma-Meghna-Brahmaputra plain	West Bengal, India	298	3,200	**Source:** As-bearing pyrite, Holocene age aquifer sediments (Geogenic), grey color sediments, Fe oxy/hydroxides, organic matter, **Release:** High reducing aquifer condition, leaching from ore minerals (pyrite and Arsenopyrite) excessive abstraction of **Groundwater type:** Ca-HCO_3^-, high HCO_3^-	Mallick and Rajagopal, (1996); Biswas et al. (2011); Das et al. (1995); Matschullat et al. (2000)
Competitive ions desorption	Brahmaputra floodplain, Bengal Delta Plain,	Assam, West Bengal, India , Bangladesh, Nam Du, Vietnam	NR	43	**Source:** Holocene age aquifer sediments **Release:** Desorption of As (III)/(V) through competitive sorption reactions by PO_4^{-3}; HCO_3^- and $Si(OH)_4$ **Distribution:**Alluvium plains of BDP	Mahanta et al. (2015); Bauer and Blodau (2006); Appelo et al. (2002);Sailo and Mahanta (2014);Nath et al. (2008a); Nath et al. (2008b); Radu et al., (2005);
Vertical infiltration	Bengal Delta Plain,		50 to 32000	8 to 18	**Source:** Indigenous microbial colonies, Geogenic **Release:** Dissolved natural organic matter (NOM) enhance redox reactions	Chatterjee et al. (2005); Gault et al. (2005); Nath et al. (2008b); Deng et al., (2018);

					Distribution: Shallow aquifer of alluviums of BDP	Chatterjee et al., (2005)
Biogeochemical	Brahmaputra flood plain	India	657	17.2	**Source:** Sediment, *Pseudomonas aeruginosa* **Release:** the microbiologically reductive dissolution of amorphous iron oxides **Distribution:** Shallow aquifers	Sathe et al.,(2018)
	Babagorgor Spring	Iran	614	NR	**Source:**Groundwater, prokaryotic bacteria **Release:** biotransformation of arsenite to arsenate **Distribution:** Shallow aquifers	Jebelli et al., (2017)
	Hubei Province, China, Yangtze and Jianghan	China	186 to 1200	19 to 82	**Source: S**ediments and exogenous organic carbon, *Pseudomonas, Clostridium and Geobacter* **Release:** the microbiologically reductive dissolution of amorphous iron oxides **Distribution:** Shallow aquifers (26 m and 36 m)	Deng et al., (2018); Wang et al., (2017)
River morphology	Red River and Mekong delta	Vietnam	1400	50	**Source:** Holocene aquifers,reduction of reactive, poorly crystalline iron oxides control arsenic release.	Stahl et al. (2016)

					Release: microbiologically reduction or oxidation of Arsenic **Distribution:** Shallow aquifers	

Note: Not reported is abbreviated as NR

(Enmark and Nordborg 2007, Sailo and Mahanta 2013, Verma et al. 2015) in this region. The study area chosen for thesis work is located between the Bhutan Himalayas on its Northside and Brahmaputra river flood plains on its Southside (Verma et al. 2015). In China, 70% of the region has been recognized for high *As* contamination (Wei and Zhou, 1992). Furthermore, out of which 95% of the extracted arsenic of China are found in Guangxi, Hunan, and Yunnan, southwest China (Zhang et al., 2017). The recent study conducted by Schaefer et al. (2017) in Jianghan Plain of China, observed that shallow aquifer (i.e., ~ 18m to 20 m) sediment contains *As* >100 mg kg^{-1} in the solid phase. The overall understanding from the Table 2.1 was, the buried sedimentary samples showed coupling with anaerobic microbial respiration with subsurface organic carbon-containing aquifers which suggest the primary mobilization mechanism for rapid release and seasonal variation of *As* into groundwater aquifers.

2.2 Topography and geomorphology

In Holocene age, fluvial floodplain distributions of *As* concentration was observed to be controlled by river geomorphology (Stahl et al. 2016, Van Geen et al. 2013). High *As* concentration (viz. >10 µg L^{-1}) in groundwater aquifers was found near the rivers where the suspended sediment load has deposited on nearby regions of this river bank (Stahl et al., 2016). In some studies, low *As* concentration groundwater regions were found in the Pleistocene age aquifers (Biswas et al., 2014a; van Geen et al., 2003). Arsenic contaminated aquifers in the South and South-East Asia other affinities in the main part of the numerous river and tributaries network. The general topographical and geomorphologic conditions affect the surface water and groundwater interaction which is mainly observed on the adjacent shallow aquifers of the region. In some aquifer condition, the reverse groundwater flow was observed; whereas heavy pumping from the deeper groundwater aquifer could further replenished by the surface water bodies (Viz. Rivers and its tributaries).

Studies over the have BFP suggested that the geological age of the alluvial sediments is from Proterozoic age to Holocen age (Mahanta et al. 2015). Therefore, it can be well understood that the sediments carried by the tributaries draining from Bhutan Himalayas could be the main repositories of the arsenic-bearing minerals in BFP. Possible change in aquifer condition i.e. oxidizing to reducing environment, can releases solid pahse *As* into the groundwater aquifer. Ahmed et al., (2004) and McArthur et al., (2004) have done studies related to release of *As* from iron oxy/hydroxides by the reductive dissolution mechanism in the shallow aquifer, based on the hypothesis that the presence of organic matter in the subsurface aquifer which is mainly observed at the meandering rivers esp. Hugli and Sunti River morphology. Similarly, Postma et al., (2007) and Postma et al., (2012) studies have found an effect of topography and geomorphology of the Red river deposits in Vietnam which contain high *As* concentration.

2.3 Effects of geographical features

High *As* enriched groundwater aquifers in India are identified in Holocene age alluvial sediment basin found near to a young mountainous range of Himalaya (Mukherjee et al., 2014a; Ravenscroft et al., 2009). Various authors have made the connection between the spatial variability in arsenic concentrations and the geomorphologic setting of the shallow aquifers with high and low *As* contaminated region. Hoque et al., (2014) study on spatial variability of arsenic in groundwater have concluded that palaeosols act as shields and prevent arsenic from moving into shallow palaeo-inter fluvial aquifers in the Ganges River floodplain of the Bengal Basin. Chakrabarti et al., (2013) and Sahu and Saha, (2015) have correlated the variability in *As* concentrations with the geomorphologic setting (i.e., meandering river) with the floodplain of Ganges River. Nath et al., (2005); Mukhopadhyay et al., (2006); and Desbarats and Koenig, (2014) have concluded that the high arsenic concentrations were found in the abandoned meander bends (oxbow lakes).

The oxbow lake water and the fine-grained sediment which are filled-in oxbow lakes (clay plugs), were reported as the two main sources for reactive organic matter (Harvey et al., 2002; Mailloux et al., 2013; McArthur et al., 2004). Desbarats and Koenig, (2014) proposed that the organic matter in the clay plugs triggers the reactive dissolution of iron oxy/hydroxides and releases of the adsorbed arsenic. Ghosh et al., (2015) documented TOC values of 0.7% in the Jalangi River floodplain observed in the shallow Holocene age clay sediments. Desbarats and Koenig, (2014) produced a simplified reactive solute transport model for the migration of *As* in the clay plug sediments as a consequence of heavy groundwater pumping for irrigation purposes. They concluded that leakage of groundwater through clay-plug sediments (channel-fill sediments in the terminology of Desbarats et al. (2014)) is the principal effect of heavy irrigation pumping.

The mobilization mechanism of *As* in the aquifer is commonly attributed to the reduction of Fe (III)-oxy/hydroxides, e.g., Bhattacharya et al., (1997); von Brömssen et al., (2008, 2007) and McArthur et al. (2004) have observed that elevated (>10 µg L^{-1}) levels of *As* in groundwater of Holocene age aquifer mainly containing grey color sands; whereas low concentrations of *As* (<10 µg L^{-1}) mainly observed in the Pleistocene age aquifer which contains brown color sands. This observation is attributed to the redox characteristics, including adsorption properties of the aquifer materials and the presence of Fe-oxides (Stollenwerk et al., 2007). In Bangladesh, Radloff et al., (2011) have shown that the migration of *As* from shallow to deeper aquifers can be significantly influenced by adsorption on aquifer sediments. Therefore, measurement of distribution coefficients (K_d) of *As* on sediments will potentially provide information about the mobility of *As* in contaminated aquifers. The K_d values for As^{+3} and $As^{+5}$for Pleistocene and reduced Holocene aquifer sediments of West Bengal, India, and Bangladesh are available in the literature (Jessen et al., 2008; Nath et al., 2009; Stollenwerk et al., 2007).

All studies indicate the intricate relationship between the geomorphology, fluvial depositional setting, groundwater migration, and intensity of the arsenic pollution. The results of these studies are spot observations that account for local sources and variations in *As* concentrations in the studied sites but did not explain the enormous scale and basin-wide extent of arsenic pollution. It implies a ubiquitous source of microbial respiration to cause the release of arsenic from it's solid-state (Acharyya and Shah, 2007).

2.4 Lesser understood *As* mobilization process

Elevated *As* levels in the aqueous environment have resulted from both natural processes and anthropogenic activities. Most *As* problems are the result of mobilization under natural conditions, including weathering reactions, biological activities and volcanic emissions (Mukherjee et al., 2008b; Mukherjee and Fryar, 2008; Pal et al., 2002). However, few studies have focused on the delineation of safe aquifer according to sediment oxidation and reduction condition and its role in *As* mobilization. Such conditions (anoxic to oxic and vice versa) may have a pronounced effect on the mobility of *As* in the groundwater. Recently, Parsons et al., (2013) shown that repetitive redox cycling can decrease *As* mobility during reducing conditions.

On the other hand, aeration of the reduced aquifer sediments from irrigation and agricultural activities or groundwater drawdown during dry season may cause subsurface redox conditions to change from predominantly reducing to oxidizing condition, which affects on *As* (III) and could get adsorbed onto aquifer sediments through partial oxidation of *As* (V) (Parsons et al., 2013). The present study, therefore, aims to evaluate *As* (III) adsorption behavior on Holocene age (reduced) shallow aquifer sediments under oxidation condition.

2.5 Hydrogeology of Alluvium flood plain highlight

2.5.1 High *As* groundwater in arid-semiarid inland basins

Growing knowledge on *As* in semi-arid to arid regions are predominantly laid on a Holocene age alluvial floodplain (Guo et al., 2014; Mandal and Suzuki, 2002; Mukherjee et al., 2014b). In India, *As* contamination are found within an average range of 10 to 30 µg L^{-1} in sub-tropical humid climate states (viz. Assam, West Bengal, Uttar Pradesh, Bihar, Rajasthan, Chhattisgarh) (Eiche et al., 2017; Meng et al., 2017a; Sathe et al., 2018). Studies over these states have identified that acidic to alkaline groundwater pH conditions are responsible for the high and low *As* contaminated groundwater regions in GBM basins in India. Thus, it finally inferred that solid-phase *As* bearing iron mineral dissolution was the predominant source for high *As* concentration in GBM.

2.5.2 Major Ions

Major ions concentrations were considerably higher in the shallow groundwater wells compared to the deeper groundwater wells, which suggests that the presence of vertical stratification within the groundwater aquifer is possible. The co-existing competitive anions such as HCO_3^-, SO_4^{2-}, PO_4^{3-}, Cl^-, F^-, $H_2PO_4^-$ and SiO_3^{2-} were found to compete with the adsorbed *As* on different mineral surfaces and cause for increase the *As* content in groundwater (Kong et al. 2014; Smedley et al., 2005; Smith et al., 2003). Amongst these anions Cl^-, $H_2PO_4^-$ and oxides of SiO_3^{2-} have observed as a strong inhibiting effect on the solid phase Fe- oxy/hydroxides minerals for arsenite [*As* (III)] (Livesey and Huang, 1981). Moreover, a significant effect of competent anions HCO_3^-, Cl^-, F^- and SO_4^{2-} for arsenate [*As* (V)] adsorption on sediment sites were observed (Goh and Lim, 2005). Similarly, competitive cations such as Ca^{+2}, $Mg^{+2,}$ and Na^+ provides additional scope to *As* [*As* (III) and *As* (V)] for adsorption due to direct electrostatic force with arsenic cations (Smith et al., 2002). Smedley et al., (2003) study in Huhhot Basin, Inner Mongolia,

showed that Fe, Mn, NH_4^+, HCO_3^- and PO_4^{-3} common ions are responsible for high *As* concentration in the reduced groundwater condition. Also, high *As* concentration with low SO_4^{-2} concentration was observed in strongly reducing aquifer condition (Smedley et al., 2003).

2.5.3 Role of competitive ions and facies

Groundwater pH controls the adsorption and desorption behavior on sediment or minerals surfaces. Mainly *As* (V) sorption was decreasing as pH of the groundwater increases whereas, maximum *As* (III) adsorption was observed between groundwater pH 4 to 9 (Giles et al., 2011). Compared to *As* (III) with *As* (V), *As* (III) require less contact time to attain equilibrium state in the natural environment. Effective adsorption of *As* (V) was observed at acidic to alkaline pH than adsorption of *As* (III) on different mineral surfaces (Leupin and Hug, 2005).

Bicarbonate (i.e. HCO_3^-) is typically the most abundant anion (approximately 465 mg L^{-1}) in most of the groundwater. In all the basins, groundwater evolved mainly from Ca^{+2} dominant to Na^+ dominant and sometimes Cl^- rich when evaporation plays an important role in the low lying parts of the basins. Yinchuan plain has the least chemically evolved water as it still contains significant Ca^{+2} and high *As* concentration in the groundwater (Han et al., 2013). The concentration of different ions showed a distinct relationship with high and low *As* concentration groundwater region, in parts of the world (Mahanta et al., 2015; Neidhardt et al., 2014; Sharma et al., 2014; van Geen et al., 2008). The predominantly hydrogeochemical facies such as Ca^{+2}–HCO_3^-, Na^+–Ca^{+2}–HCO_3^- and Na^+–HCO_3^- type found in most of the shallow aquifer high *As* contaminated regions (Mukherjee et al., 2009; Mukherjee and Fryar, 2008). Thus, the presence of these facies into groundwater suggests that shallow aquifers of these regions are replenished by the fresh surface water or rainfall (Cao et al., 2018; Mahanta et al., 2015; Verma et al., 2015a).

At the sub-basin scale, Verma et al. (2015) studied groundwater samples according to four geomorphologic settings classification, they have found different hydrogeochemical facies such as Ca^{2+}–HCO_3^-; Na^+–Ca^{2+}–HCO_3^- and Ca^{2+}–Na^+– HCO_3^-. In channel sediments of Brahmaputra river, the younger alluvial recent floodplain of Brahmaputra as Ca^{2+}–Na^+– HCO_3^-, the older flood plain of the Brahmaputra and its tributaries as Na^+–Ca^{2+}–HCO_3^- and Na^+–Ca^{2+}–HCO_3^- observed in piedmont deposits. These results suggested that the carbonate dissolution and silicate weathering were the predominant mechanisms cause for major facies in the study area groundwater samples. Similarly, Mahanta et al. (2015) analyzed groundwater from near tributary (i.e. Manas river) region of Brahmaputra river, found Na^+–HCO_3^- and Ca^{2+}–HCO_3^- facies. In the western region of West Bengal has also reported predominate Ca^{2+}–HCO_3^- facie in reducing and post anoxic aquifer condition (Mukherjee et al., 2008). In deep artesian groundwater, Na^+–HCO_3^- or mixed-ion (with an equal proportion of Ca^{2+}, Na^+ and K^+) type facies were observed in Huhhot Basin of China (Wen et al., 2013).

Thus, these studies in different parts of the alluvial flood plains suggested that the abundance of carbonate and silicate minerals, dissolution or weathering in the aquifer sediment controls the major ionic concentration in high and low *As* contaminated groundwater aquifer. Moreover, elevated concentration of Ca^{+2}, Mg^{+2} and HCO_3^- were results of carbonate mineral dissolution, while the weathering of silicate minerals and cation exchange process are responsible for Na^+ and K^+, which was understood by comparing the concentration with local meteoric water line (LMWL) and global meteoric water line (GMWL) (Mukherjee et al., 2008).

The positive correlation of dissolved *As* concentration was observed with HCO_3^-. It suggested that competitive anion sorption such as HCO_3^- has a significant effect of *As* in solid phase of iron oxide (Meng et al., 2017). High bicarbonate concentration in groundwater is often

caused by the oxidation of organic carbon mediated by indigenous microbes due to the reductive dissolution of Fe-oxyhydroxides minerals. It increases the alkalinity of groundwater and desorbs the adsorbed *As* from minerals surfaces (Nickson et al., 2000). Similarly, a positive correlation of dissolved iron and manganese concentration with *As* deciphers, significant affinity and favorable sorption capacity (Dixit and Hering, 2003; Giles et al., 2011) with such minerals surfaces. Maximum *As* adsorption was observed on amorphous iron hydroxide minerals (viz. goethite, ferrihydrite, magnetite, hematite, rhodochrosite, lepidocrocite, etc.) for dissolved arsenate and arsenite (Giles et al., 2011). Moreover, sulfate, phosphate, and hydrogen carbonate were observed less competent for *As* (III) adsorption (Arienzo et al., 2002; Burton et al., 2009).

2.5.4 Sediment characteristics and role in *As* mobilization

In subsurface aquifer condition, usually, sediments or aquifers regarded as a buffer zone for groundwater pollutants but, sediment-water interface, complex hydro-geochemistry (viz. adsorption, desorption, and precipitation), aquifer oxic or anoxic aquifer condition, indigenous microbes control the hydro-geochemistry of groundwater (Sun et al., 2016). Conversely, sediments accumulate toxic pollutants and become the source for certain pollutant (Deng et al., 2018). Therefore, the role of *As* cycle in the aquifer sediments and groundwater significantly controlled by Fe-oxy/hydroxide solid phase concentration, which easily be agglomerated and dissolute in aquifer cycle (Anawar et al., 2004). Lab-based experimental studies on adsorption or desorption process of sediment-water interface showed close correlation: when *As* is released from sediments to water, which possibly pollutes subsequent depth aquifers as well as surface water. The oxide forms of different minerals (viz. iron, aluminum, and manganese) and organic matter adsorb the *As* through complex surface reactions, which usually precipitates and susceptible for further dissolution (Livesey and Huang, 1981).

Organic matter contains various functional groups such as carboxyl, phenolic hydroxyl, alcoholic extract hydroxyl, ether, and amides. They coordinate well with *As* and increase adsorption site on sediments (Wang and Mulligan, 2006). Research studies have observed that organic acid (e.g., citrate and humic acids) could decrease phosphate (PO_4^{3-}) adsorption on the specific surface area of iron-bearing minerals (e.g., goethite and hematite). Sailo and Mahanta, 2014 study has suggested that Fe oxy/hydroxide reductive dissolution mechanism via respiration of organic matter (i.e. decompose organic matter under consumption of oxygen) releases associated adsorbed or co-precipitated *As* into study areas aquifer. Studies over different *As* concentration and varying sediment color have proven that the concentration of organic matter in sediments is directly proportional to the adsorption capacity of dissolved *As* (Zhang et al., 2017). He et al., (2009) noted that *As* in contaminated region of the Hetao Plain, China, is rich in organic matter, reducing environment and high groundwater pH which facilitates to mobilization, enrichment, and transformation of arsenic in the study area region.

2.6 Role of microbiological species on arsenic mobilization

Besides the abiotic factors, several *As* (III) oxidizing and *As* (V) reducing bacteria are also known for controlling *As* mobilization via dissimilatory reduction or detoxification mechanisms. While some of the prokaryotes are enabled to sustain life by reduction and oxidation of arsenic forms (Rhine et al., 2005). Bacteria viz., *Clostridium, Pseudomonas, Brevundimonas, Rhodococcus, Agrobacterium, Staphylococcus, Enterobacter, Rhizobium, Bacillus, Geobacter, Desulfitobacterium, Exiguobacterium, Desulfocapsa* etc. are well known for their redox capability for *As* mobilization, worldwide (J Akai et al., 2008; Cai et al., 2016a; Chen et al., 2017; Jebelli et al., 2017b; Sathe et al., 2018; Zhang et al., 2016). Table 2.2 enlists the list of few bacteria isolated from *As* contaminated sites. Moreover, to the best of our knowledge, there are scarce reports on the

studies over isolation and identification of microbes for *As* mobilization into groundwater over BFP.

2.6.1 Aerobic *As*(III) oxidizers

Many micro-organisms that interact and transform inorganic arsenic species have been identified. Oxidation of *As* (III) by indigenous bacteria was first reported in 1918, whereas, Turner, 1949 has reported 15 heterotrophic *As* (III)-oxidizing bacterial strains. Heterotrophic bacteria for *As* (III) oxidation mechanism were generally considered as an electron acceptor whereas, chemolithoautotrophic bacteria considered as an electron donor with CO_2 fixation and oxygen reducer. The isolated arsenite-oxidizing bacteria's from different parts of the *As* contaminated regions of the world were classified as α-, β-, γ- *Proteobacteria, Bacteroidetes, Actinobacteria, Firmicutes, Aquificae, Deinococcus-Thermus, Chlorobi, Chloroflexi, Nitrospira, Crenarchaeota, Achromobacter, Agrobacterium, Alcaligenes, Hydrogenophaga, Pseudomonas* and *Thermus,* etc.(Oremland and Stolz, 2005; Salmassi et al., 2002; Santini et al., 2000). Figure 2.1 shows a typical bacterial *As* (III) oxidation process, and such an oxidation process is considered as a detoxification metabolism because *As* (V) is much less toxic than *As* (III). Furthermore, *As* (V) is negatively charged and easy to be absorbed, thus arsenite-oxidizing bacteria have been used for cleaning a high *As* contaminated water and in the different filtration unit (Lièvremont et al., 2003). Figure 2.1 shows a schematic diagram for the oxidation process of arsenite in a microbial cell. Aerobic arsenite-oxidizing bacteria's belongs to *Alpha* and *Beta*-proteobacteria mainly.

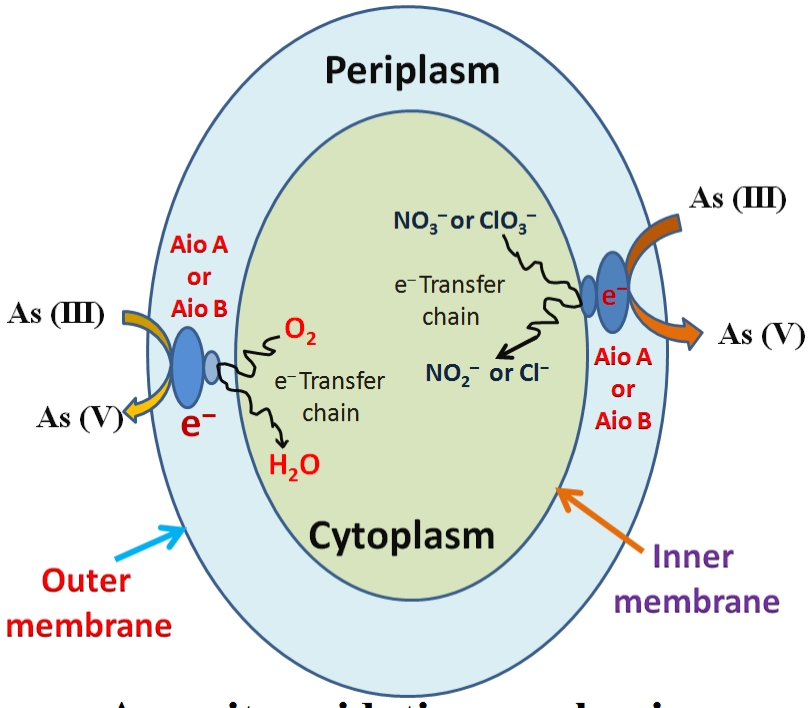

Arsenite oxidation mechanism

Figure 2. 1 Schematic diagram shows the arsenite oxidation mechanism commonly found in the bacteria.

They all are mesophiles (i.e. they can grow in moderate temperature) and includes chemolithoautotrophs (obtain carbon from the fixation of carbon dioxide and energy from the oxidation of inorganic compounds) and heterotrophs (cannot fix carbon dioxide and instead use organic carbon for making cell material). Therefore, such an organism obtains energy by coupling growth with arsenite to the reduction of oxygen, nitrate or chlorate (Osborne and Santini, 2012). Two different enzymes (Aio and Arx) are responsible for the oxidation of arsenite to arsenate, depending on whether the organisms use oxygen or nitrate as electron acceptors (Osborne and Santini, 2012). The arsenite which enters the periplasm is oxidized to arsenate by the Aio, and then the electrons are transferred to other proteins involved in the electron transport chain which results in the production of ATP and cause for the depletion of oxygen in groundwater.

2.6.2 Aerobic *As*(V) reducer

Studies over reducing aquifer groundwater conditions have well documents that geochemical mechanism for *As* (V) reduction mostly the cause for high *As* concentration in the groundwater aquifers. However, authors have also concluded that the dissolution of *As* is also significantly controlled by certain microbial metabolisms process, such as *Bacillus, Clostridium, Citrobacter, Desulfomicrobium, Sulfurospirillum,* and *Wolinella,* etc. (Fan et al., 2008; Silver and Phung, 2005). These bacteria's are well known as *As* (V) resistant microbes which can convert *As* (V) via detoxification systems (Oremland and Stolz, 2003; Rosen, 2002). The phosphate transporters (viz. Pit or Pst) known as the main carrier for *As* (V) transporter to enter the bacterial cells. After entering the *As* (V) into a bacterial cell, it further reduced by a cytoplasmic *As* (V) reductase (ArsC) with the aid of glutathione or ferredoxin as the reducing power. Then, it finally excreted out *As* (III) through the cell (via a membrane efflux pump) (e.g. ArsB or Acr3) (Rosen,1999). In some bacteria, an ATPase of Ars A is bound to ArsB which facilitate to efflux *As* (III), confirming that an organism was exposed to high level of toxic form of arsenic. Similarly, in ArsC bacteria, *As* (III) also extrude by the same mechanism.

Arsenate respirators use *As* (V) as a terminal acceptor in anoxic groundwater condition. They couples growth by oxidizing inorganic (e.g. sulfide) and organic (e.g. acetate) compounds and generally considered as an electron donor (Stolz, 2012). If *As* (V) enters the cells (most probably through the phosphate transport system) it is reduced to *As* (III) inside the cell (*i.e.*, in the cytoplasm) and the efflux pump *As* (III) out of the cell through ArsB coupled to ArsA-mediated ATP (adenosine triphosphate) hydrolysis (Figure 2.2). The respiratory arsenate reductase (Arr), which is located in the periplasm or is attached to the cytoplasmic membrane is the terminal reductase in an electron transport chain and receives the electrons for arsenate reduction from

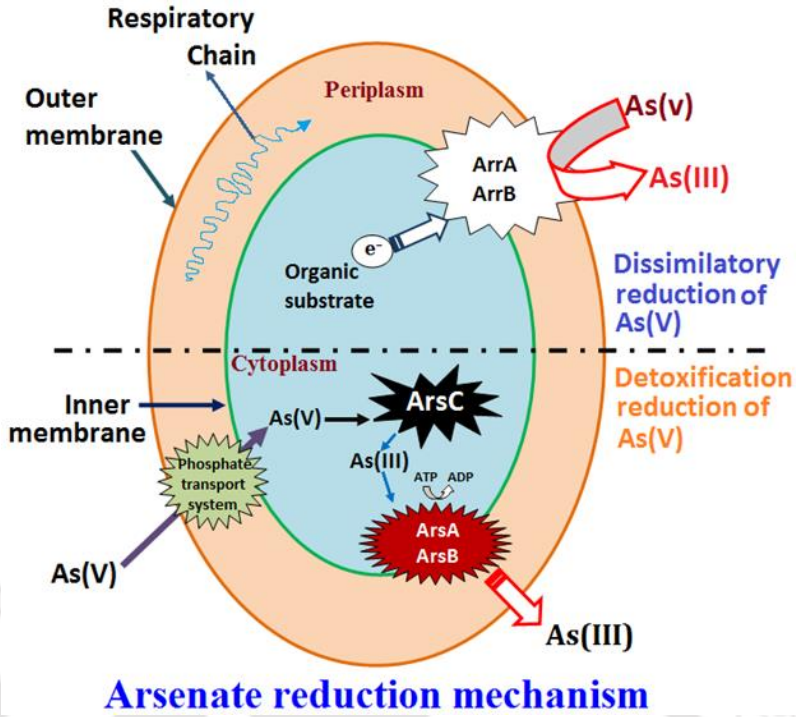

Figure 2. 2 Schematic diagram shows the arsenate reduction mechanism commonly found in bacteria.

various electron donors which are oxidized in the cytoplasm.

2.6.3 Fe-reducing bacteria

The molecular analysis of isolated microbes indicates the amorphous nature of iron oxides reduction leads for high *As* mobilization. The known iron-reducing bacterias are *Pseudomonas*, *Geobacter*, and *Clostridium*, were usually found in sediments from other *As*-contaminated aquifers in Cambodia, West Bengal of India, China Plain in Taiwan and Utah Basin in USA (Héry et al., 2010; Liao et al., 2011; Mirza et al., 2014; Rowland et al., 2007). However, Sulfate-reducing bacteria, in contrast, immobilizes *As* by Fe (II) sulfide minerals (Deng et al., 2018). Previous studies indicated that the seasonal decrease of *As* in shallow groundwater was mainly caused by the incursion of surface water containing O_2 and NO_3^- during groundwater recharge

Table 2. 2: Summary of a literature review of the isolated bacteria from high and low arsenic-contaminated regions

S. No.	Study area	Microorganism	*As* the concentration of the isolation area	Reference
1.	Samta Village, Bangladesh	*Clostridium acetobutyrlicum, Clostridium beijerinckii, Clostridium butyricum, Clostridium scatologenes*	12.8 mg kg^{-1}	J. Akai et al., (2008)
2.	Hunan, China	*Pseudomonas stutzeri*	284 mg kg^{-1}	Zhang et al., (2016)
3.	Chifeng, Mongolia, China	*Bacillus sp., Desulfitobacterium sp., Exiguobacterium sp.*	300 mg kg^{-1}	Cai et al., (2016)
4.	Jianghan plain, Central China	*Aeromonas sp.*	14.61 mg kg^{-1}	Chen et al., (2017)
5.	Boseong, Korea	*Sulfate-reducing microbe*	71.2 mg kg^{-1}	Ko et al., (2017)
6.	Mono Lake, California, USA	*Bacillus arsenicoselenatis*	200 to 300 µM	Blum, Switzer, et al., (1998)
7.	Bendigo, Australia	*Bacillus macyae*	2.5 mg L^{-1}	Santini et al., (2004)
8.	Cache Valley Basin, USA	*Desulfocapsa, Geobacter, Shewanella*	3.24 , 7.7 and 3.75 mg kg^{-1}	(Mirza et al., 2014)
9.	Japan	*Geobacter sp.*	40 mg kg^{-1}	Ohtsuka et al., (2013)
10.	Japan	*Anaeromyxobacter sp.*	13,000 mol kg^{-1}	Kudo et al., (2013)
11.	Babagorgor Spring, Iran	*Pseudomonas xanthomo, Bacillus licheniformis, Aeromonas salmonicida, Brevundimonas diminuta, Acinetobacter calcoaceticus, Bacillus oceanisediminis, Rhizobium halotolerans, Prolinoborus fasciculus, Pseudomonas chengduensis, Bacillus flexus, Pseudomonas stutzeri*	0.614 mg L^{-1}	Jebelli et al., (2017)
12.	Burdwan, India	*Bacillus sp, Aneurinibacillus aneurinilyticus*	0.119 mg L^{-1}	Dey et al., (2016)
13.	West Bengal, India	*Pseudomonas sp., Rhizobium sp., Brevundimonas sp., Rhodococcus sp., Herbaspirillum sp.,*	0.015 to 1.4 mg L^{-1}	Paul et al., (2015)

		Rheinheimera sp., Phyllobacterium sp.		
14.	Lakhimpur and Jorhat, India	*Brevundimonas, Pseudomonas, Acidovorax, Staphylococcus, Caulobacter Enterobacter*	2 to 161 mg L^{-1}	Ghosh and Sar, (2013)
15.	West Bengal, India	*Agrobacterium, Rhizobium, Ochrobactrum, Achromobacter*	---	Sarkar et al., (2013))
16.	Shanyin, Northwestern China	*Achromobacter, Acidovorax, Sinorhizobium, Agrobacterium tumefaciens, Pseudomonas sp.*	0.2 to 1.09 mg L^{-1}	(H. Fan et al., 2008)
17.	HAsCR, India	*Pseudomonas aeruginosa*	0.02 to 17 mg kg^{-1}	(S. Sathe et al., 2018)

(Schaefer et al., 2016, 2017). Table 2.2 showed summery of microbiology literature review. Deng et al. 2018 results showed that the microbial sulfate reduction could also affect the temporal variation of *As* in the groundwater of Jianghan Plain, China.

2.7 Predictive contaminant groundwater model using numerical analysis software

An analytical solution for the groundwater flow evolution was first time applied by Toth, (1963) for on hypothetical small drainage basins (viz. local, intermediate and regional). His research analysis suggested that a flow line of large unconfined groundwater flow system does not cross the topographical features (i.e., man-made and natural), whereas the geological and meteorological features, control the gravity-driven groundwater flow.

In the numerical method approach, the model developed by Freeze and Witherspoon, (1966) used numerical finite-difference method for representing three dimensional (3D) (nonhomogeneous, anisotropic basin) steady-state regional groundwater flow model. The research study concluded that the application of the numerical method could be used to solve any geological and water-table configurations problems. It has the advantage of data storage and computer-oriented methods; it also saves time and is simpler than the analytical method. Later on (Freeze, 1971) developed a 3D transient state model; a saturated-unsaturated numerical model for non-homogenous anisotropic geologic basins. The developed model provides quantitative hydrographs

of surface infiltration, stream base flow, groundwater recharge and contour for small basins. This model allows the user to apply for any generalized region shape and time variant changing boundary condition and also, handles both saturated and unsaturated aquifers.

Applications of computer-based numerical groundwater flow models were started in the Regional Aquifer-System Analysis (RASA) program of U.S. Geological Survey in 1978, where a group of researcher intensively studied 25 regional aquifer systems for 18 years. In this program, a computer-based numerical groundwater flow models were applied for groundwater simulation considering the future effect of groundwater development and change in land use pattern at the regional scale. Finally, the reports were compiled and published in national groundwater atlas and RASA program bibliography, which was published including 1105 reports of various publications (Sun, 1997). Similarly, Netherland and China have developed groundwater flow regional-scale models and published reports on case studies in the past few decades (Engelen and Kloosterman, 2012; Hao et al., 2009).

2.8 Mitigation of arsenic problem

Mitigation or safe aquifer delineation strategies were documented in the last few years, considering technical feasibility and socioeconomics limitations for *As* contaminated flood plain (Biswas et al., 2011). Based on the current knowledge and joint-filed work carried along with PHED Assam, has concluded that the central and state governments implementing various mitigation strategies plan across the state. Some of them have installed deeper aquifer tube wells for community water supply schemes, providing treated surface water, groundwater filter unit sponsored by WHO and UNICEF organization, conducting water safety awareness programs at school, colleges, and community level.

2.9 Delineation of *As* safe aquifers and regions

Literature reviews from the Bengal delta, Brahmaputra-Ganga floodplain, and the Mekong deltas insinuate that *As*-rich water occurs mainly in the shallow groundwater, whereas groundwater from the deeper aquifer was found less contaminated and yielding less than 10 µg L^{-1} of *As* from the groundwater (Biswas et al., 2011; Mukherjee and Fryar, 2008; Radloff, 2010; von Brömssen et al., 2007). In the Bengal delta, generally water extraction below 150 to 200 m depth is considered as a deeper aquifer, but in many cases, this can be below 200 m (Biswas et al., 2011). In the Red River and the Mekong deltas, *As* concentration was low at depths of>50 m and >70 m (Winkel et al., 2011). Verma et al. (2015) study over Brahmaputra floodplain, suggested that aquifer in piedmont deposits yields less *As* contaminated groundwater. Biswas et al., (2014a) study for Nadia District, West Bengal India, suggested that bore well which is taped into a brown sand aquifer can be used as *As* safe groundwater aquifer. Hossain et al. (2014) have developed a sediment color tool for delineating *As* safe aquifer. Their results concluded that compared to black color sediment the red color sediments from the shallow aquifers could provide *As* safe groundwater for the region.

In contrast, Mukherjee et al., (2011) results of numerical modeling suggested that groundwater abstraction from the deeper aquifer by irrigational pumping wells can contaminate the deeper aquifer. Biswas et al. (2011) suggested that the reductive dissolution mechanism of Fe and Mn oxy/hydroxide minerals is the predominant cause for mobilization of high *As* in deeper screened wells in Ganga flood plain.

Chapter 3

3 Materials and Method

3.1 Groundwater sampling

Groundwater sampling sites were decided based on a study conducted by Mahanta et al. (2015), Sailo and Mahanta (2013) and PHED in Bongaigaon (high *As* contaminated region; H*As*CR) and Darrang (low *As* contaminated region; L*As*CR) districts groundwater results, obtained on field using arsenator field testing kit during sampling. Groundwater samples were collected after the post-monsoon session in the year of 2013 and 2017. Samples were collected from shallow aquifer groundwater sources (viz. private and government installed wells), where the distinct concentration difference was observed in a field testing kit. Obligatory information's (includes screening interval and length, water table, well depth, date of installation, the total number of people dependent on the source, etc.) were collected from the records preserved by PHED department and well owners during sampling. Before the transport of samples, cation and anion analyzing water sampling bottles and lab wares were thoroughly cleaned. Before groundwater sampling, hand pumps were purged for 7-10 minutes, to ensure that only groundwater from the main aquifer was sampled and all stagnant water was expelled out.

Field portable instruments and YSI multiprobe kit (YSI Inc. 550A, Sondes) were used to determine the temperature and time-dependent groundwater parameters in the field. The instrument was calibrated, and measurements were recorded after EC, pH and temperature readings

were stabilized. Shallow aquifer groundwater and core drilled sediment samples were collected from three adjoining district blocks closer to Brahmaputra River. Groundwater samples were collected from PHED installed bore wells (depth 100 ft. to 160 ft.) and private well (depth 80 ft to 100 ft.) sources and the surrounding region of drilling wells. The samples were filtered through 0.45 µm cellulose nitrate filters (Sartorius AG, Germany) and preserved. Samples for cation analysis were acidified on site with 0.5 ml of 6N HNO_3 (Suprapur quality, Merck, Germany) immediately after collection and unacidified samples for anion analysis were collected in separate bottles. Sediment samples were collected in zipping lock airtight bags and stored in the dark at -4°C until further analysis.

3.2 Groundwater analysis

3.2.1 Analytical method

Obligatory time and temperature sensitive parameters were analyzed using multi-parameter water testing kit in-situ. The YSI multiprobe testing kit (YSI Inc. 550A, Sondes) was used to determine pH, ORP (µS/cm), DO (mg L^{-1}), EC (mV), TDS (mg L^{-1}) and temperature (°C) at the site. Cation and anion concentration was precisely quantified according to water testing methods specified in the American Public Health Association (APHA) (Clesceri et al., 1996), while heavy metal quantification viz. Fe, Mn, Mg, Al, Cr, Pb, and Cu were done using Atomic Absorption Spectroscopy (AAS) (Varian, SpectrAA-55, HG-AAS,) and the flame atomizer mode was used for quantification of metals. Vapor Generation Assembly (VGA) with minimum 1 µg l^{-1} detection limit was used for *As* quantification. The instrument was calibrated using an arsenic AAS standard solution (Loba chemicals: product code A 300N) and was found to be within ± 0.2%

as per certified value. Precision was evaluated by verifying the standard deviation values for three individual runs of the same sample and was found typically better than 5% (1σ) in each sample analysis (Nath et al. 2008). Cation mainly Ca^{+2}, Na^{+}, and K^{+} were measured on Flame photometer (Make: Systronics, Model: 128) and anion such as NO_3^-, PO_4^{3-}, Cl^- and HCO_3^- measured on UV-Visible spectrophotometer (Make: Agilent Technologies, Singapore, Model: Cary 100) and Ion chromatography (IC) (Make: Metrohm, Switzerl and Model: Basic IC 792) methods.

3.2.2 Speciation modeling

Saturation indices were calculated using the following relationship as follows, SI=log (IAP/ KT), where IAP is the ion activity product, and KT is the equilibrium solubility constant of a mineral phase at ambient temperature were calculated for selected groundwater samples using Visual MINTEQ 3.1. The saturation index values for the aqueous species were calculated based on the inbuilt main thermodynamic database (thermo.vdb). From the total twenty analyzed groundwater parameters, parameters thirteen were used in the calculations.

3.3 Sediment sampling and analysis

Sediment sampling sites have shown in Figure 3.1 for H*As*CR and L*As*CR study area. Core sediment samples were collected from every ~1.5 m depth using reverse rotary drilling method after a post-monsoon season in the year of 2011 and 2013 for L*As*CR (i.e. Darrang district) and H*As*CR (i.e. Bongaigaon district) study area of Assam (Biswas et al., 2014a, 2012; H Fan et al., 2008b; Tauhid-Ur-Rahman et al., 2011).

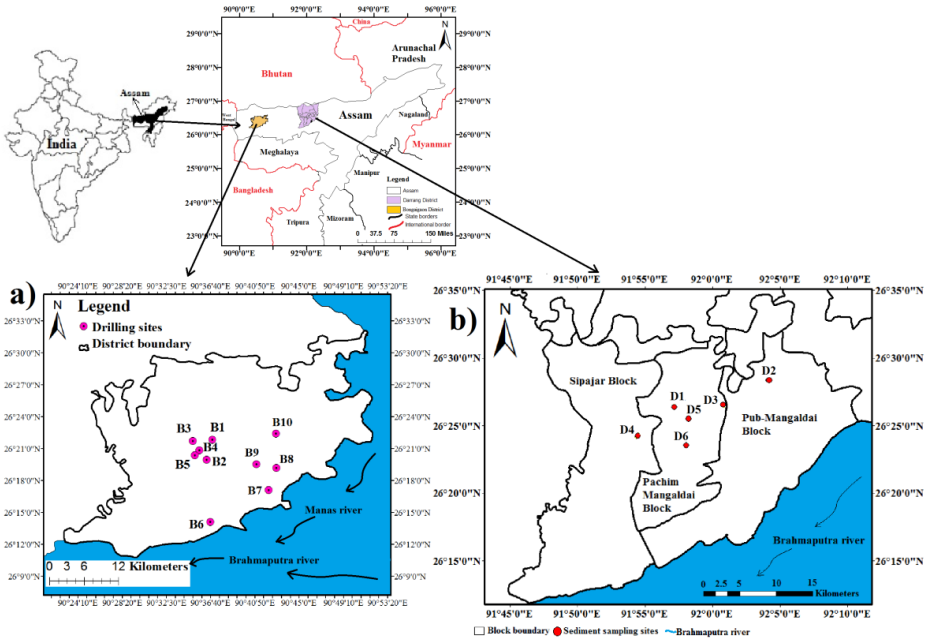

Figure 3. 1 Location map of Bongaigaon and Darrang district with respect to India, where a) and b) showed the location of drilling wells from where sediment samples collected.

The collected sediments were texturally classified into five classes (viz. clay, fine sand, medium sand, coarse sand, and granule), whereas according to Munsell sediment color classification, they were further classified into 32 and 41 hues for H*As*CR and L*As*CR study area sediment samples (Biswas et al. 2014a, Mahanta et al. 2015).

3.3.1 Physical characteristics

3.3.1.1 Color classification and coloration causes

At present, the gap between the redox cycle, which measures the *As* exposure and mitigation in terms of sediment coloration was being inadequately understood. Therefore, experiments have been carried out to understand the causes of different sediment color mainly gray, brown, yellow and white sediment present in the study area. It is believed that the black sand grains were covered by Fe sulfides. To test this theory, color change experiments from brown to black were carried out.

The following white, brown, gray, dark-gray sand samples of Bongaigaon district was used. The sand sample was placed in a beaker and exposed to the H_2S gas for 10 min. Hydrogen sulfide gas was produced by adding HCl and Na_2S in a separate beaker, which can be understood via following chemical reaction:

$$Na_2S + 2\,HCl \rightarrow H_2S + 2\,NaCl$$

Then, the samples were exposed to the H_2S gas for 10 minutes.

3.3.1.2 Grain size distribution

For a precise grain size classification for the selective depth sediment samples, laser particle size analyzer (LPSA) was used (Master Seizer 2000 Ver. 5.22 Serial Number: MAL100332; Malvern Instruments Ltd. Malvern, UK) by following a wet dispersion method. For this test, ~ 0.5 gram of the sediment samples were dried overnight and used further for the analysis. To ensure proper dispersion of sediment sample a fan speed of 180 r. p. m was set and double distilled water used for each sediment analysis. The data were recorded from 0.00001μm to 2000 μm size range (Song et al., 2006).

3.3.2 Chemical characteristics

3.3.2.1 Sediment pH study

The experimental procedure mentioned in American Society for Testing and Materials (ASTM) code D4972 − 13 was used for a pH sediment determination. For sediment pH determination, approximately 10 g of air-dried, sieved sediment (i.e., 2 mm size) was used. The respective sediment samples were added into a 150 ml beaker and approximately 10 mL of the

$CaCl_2$ (0.01 M) solution was added. Then, this mixture was further shaken thoroughly, and the pH value of individual samples was measured using a pH-sensitive electrode (Make: Thermo Fisher Scientific, Model: Orion A111).

3.3.2.2 Cation exchange capacity (CEC)

The cation exchange capacity is a measure of the negative surface charge on the mineral surface. The ASTM code D7503 – 10 was followed for measuring the soluble and bound cation exchange capacity (CEC) of fine-grained sediment samples. This test method is applicable for measuring the soluble and bound cations as well as the CEC of fine-grained inorganic soils. Usually, clay minerals in fine-grained soils carry a negative surface charge that is balanced by bound cations near the mineral surface. These bound cations can be exchanged by other cations in the pore water, which are referred to as soluble cations. The CEC generally is satisfied by calcium (Ca^{2+}), sodium (Na^{+}), magnesium (Mg^{2+}), and potassium (K^{+}), although other cations may be present on the surface of sediment but, it depends on the environment in which the soil exists. In soils with appreciable gypsum or calcite, dissolution of these minerals will release Ca^{+} in a solution that may affect the measurement.

In this test, soluble salt from the sediment surfaces was washed off with de-ionized water first, and then the concentration of soluble salts within the extract was measured. The bound cations on the clay were measured by using a solution containing an index ion that forces the existing cations present on the surface of sediment. The total concentrations of bound and soluble cations in this solution were measured on a flame photometer instrument. The CEC is measured by

displacing the index ion with another salt solution and measured the amount of the displaced index ion.

3.3.2.3 Determinations of Bound cations

This test method describes the procedures for measuring the soluble and bound cations as well as the CEC for fine-grained inorganic soils. Clay mineral in fine-grained soils carries a negative surface charge that is balanced by bound cations near the mineral surface. These bound cations can be exchanged by other cations in the pore water, which are referred to as soluble cations. The cation exchange capacity is a measure of the negative surface charge on the mineral surface. The CEC generally is satisfied by calcium (Ca^{2+}), sodium (Na^{+}), magnesium (Mg^{2+}), and potassium (K^{+}), although other cations may be present depending on the environment in which the soil exists. The cation exchange capacity (CEC) of a soil is a measure of the quantity of negatively charged sites on soil surfaces that can retain positively charged ions (cations) such as calcium (Ca^{2+}), magnesium (Mg^{2+}), and potassium (K^{+}), by electrostatic forces. Cations retained electrostatically are easily exchangeable with cations in the soil solution. A soil with a higher CEC has a greater capacity to maintain adequate quantities of Ca^{2+}, Mg^{2+}, and K^{+} than a soil with a low CEC. A soil with a higher CEC may not necessarily be more fertile because a soil CEC can also be occupied by acid cations such as hydrogen (H^{+}) and aluminum (Al^{3+}).

Cation exchange capacity was determined by ammonium acetate extraction buffered at pH 7 following ASTM method D7503–10 (Tesfahunegn et al., 2013). In this test method, the soluble salts from the mineral surface are washed off with de-ionized water, and then the concentration of soluble salts within the extract was measured. The bound cations of the clay were measured by

using a solution containing an index ion that forces the existing cations in the bound layer into solution. The total concentration of bound and soluble cations in this solution was measured. The CEC was measured by displacing the index ion with another salt solution and measuring the amount of the displaced index ion.

3.3.2.4 Determinations of soluble cations

Determination of soluble cations we used only air-dry soil that passes the No. 10 US Standard Sieve (i.e. 2 mm size). The test was carried by adding a mass of 2g air-dried soil sample each in 100 mL of distilled water covered container and fitted tightly into the vertical shaker. Place the containers on the end-over shaker and shake for 1 h at 30 r.p.m. Using a vacuum filter unit the sample was filtered in a separate container using 2.5 μm filter paper. The extract was transferred to a 100 mL acid washed volumetric flask, and volume was diluted up to the volumetric flask mark. The extracts of the different cation (in mg L^{-1}) were measured by Flame Photometer.

3.3.2.5 Total organic matter (TOC)

For determining the carbon content in selective depth sediment samples, loss on ignition (LOI) technique was utilized as the test procedure suggested by Dean, 1974 and quantified using flowing formula:

$$LOI_{550} = \frac{DW_{105} - DW_{550}}{DW_{105}} \times 100 \ldots (1)$$

where LOI_{550}: loss (%) in the sediment weight after ignition at 550°C; DW_{105}: the dry weight of the sediment sample before combustion; and DW_{550}: dry weight (in grams) of the sample after

combustion at 550°C. All weights were corrected for moisture or water content prior to organic matter content calculation.

3.3.2.6 Determination of total nitrogen (TKN)

To determine total nitrogen in different depth sediments, Total Kjeldahl Nitrogen (TKN) (U.S.A.: Thomas scientific) method was adopted (Standardization, 1995). Air dried 0.5 g to 1g sediment sample was used for this analysis, even to detect less nitrogen content in the sample. Then, to enhance the chemical reaction, one catalyst tablet (Potassium sulfate + Copper sulfate in 5:1) and 10 ml concentrated sulphuric acid (H_2SO_4) was added along with sediment sample in the digestion tubes. Along with the sediment sample, total nitrogen content in the blank (i.e., Distilled water) sample was also determined.

The digestion unit was first heated until the temperature reaches to 250˚C. Then, the water inlet was switched on. After reaching to the desired temperature, the digestion tubes were placed side by side in the digestion unit, and distillation caps were fitted over each digestion tube. The time was set at 120 minutes, and the instrumentation unit was allowed to run. After completion of the digestion process, these tubes were allowed to cool at room temperature. Distilled water was added and mixed properly to make the mixture reach 100 mL mark. Prior to distillation, 35% of NaOH and distilled water was added in the distillation unit arrangement. The timer was set for 4 minutes at the distillation unit. A 25 mL boric acid solution was added to the sample mixture and transferred into a conical flask. Then, the distillation process started for each sample. Simultaneously, a distilled solution of deep greenish color was collected into the conical flask, which comes out during the distillation process. Finally, the extracted solutions were titrated with 0.02 N sulphuric acids till the

end point (i.e. the color of solution turn into light purple), and the burette reading was recorded for the determination of total nitrogen content in a sediment sample.

Calculations;

$$W_n = \frac{(V_1 - V_0) \times C(H^*) \times u}{m \times m_t} \times 100 \ldots (2)$$

Where:

'W_n' is total nitrogen content in percentage

'V_1' is the volume in ml of sulphuric acid used in the titration of the sample,

'V_o' is the ml of sulphuric acid used in the titration of a blank sample,

C (H*) is the concentration of H* in the H_2SO_4 in mole per liter is used (0.02 mol L^{-1}),

'u' is the molar mass of nitrogen (g mol^{-1} = 14),

'm' is the mass of the test sample,

'm_t' is the dry residue, expressed as g/100g based on oven dried soil material,

3.3.2.7 ASTM sediment digestion method

Total concentrations of *As* in sediment samples was determined by ASTM (D 3974-81) method, and this practice is applicable for the subsequent determination of volatile, semi-volatile, and non-volatile metals present in the sediment sample. Standardized practices for digesting sediments for subsequent chemical analysis will facilitate inter and intra-areal comparisons as well as a comparison of data generated by different groups. Samples collected in the field were screened to remove foreign objects prior to homogenization for chemical examination and analysis. Large objects were mechanically removed, and small ones were eliminated by sieving the sample through

a 10-mesh (2 mm openings) sieve. The screening provided based on discrimination for sediment and foreign objects or materials. The purpose of homogenization was to minimize errors due to poor mixing and the inclusion of extraneous materials. Standardized procedures for drying sediment samples provide a means for reporting analytical values to a common dry weight basis. Due to limited sample availability, we used ≈4 g samples and weighed with accuracy ± 0.1 mg for the moisture determination. Moisture was determined by keeping the weighted sample in an oven for 2h at 105 ± 2 °C.

The use of total digestions also eliminates the ambiguities and interpretational difficulties associated with partial digestions and the operational definitions that accompany them. Digestion practice "A" was followed for total sediment digestion. A 4 g dried samples were taken in a 250 mL beaker and mixed into 100 mL deionized water. Then the blank solution was prepared by adding 1 mL of concentrated HNO_3 and 10 ml of concentrated HCl. This mixture was kept on a hot plate at 95ºC till the solution remains approximately 10 to 15 mL. Then each sample was filtered and transferred to a 50 ml volumetric flask and diluted till the mark.

Calculations;

Following equation was used for metal quantification in the sample:

$$B = \frac{M}{N} \times 100 \ldots (3)$$

Where:

B = percentage solids of the samples

M = dry weight of the sample

N = wet weight of the sample

The concentration of each element by the following the calculation

$$C = \frac{(Q-S)\times V}{U} \ldots (4)$$

Where:

Q = concentration of the elements in the digested solution in µg mL^{-1},

S = concentration of the trace elements found in the reagents/glassware blank in µg L^{-1}

V = volume of extraction used in mL,

U = weight of the sample corrected to a dried sample at 105° C in g,

C = trace element per gram of dry sample in µg.

The concentration of the metal in a wet sample

$$A = C \times \left(\frac{B}{100}\right) \ldots (5)$$

3.3.2.8 X-ray fluorescence (XRF)

The total elemental composition obtained for different sediments were determined by using an X-ray Fluorescence (XRF) (PANalytical, model: Epsilon 3) method (operated at 20 kV volt and current 0.1mA). The estimated accuracy was ±1 µg g^{-1}. The air-dried and pulverized sediment samples (approximately 1.5 to 2 g) were well mixed to form a required size of pellet for each sample. The total elemental concentrations in sediment samples were determined by using a powder press method, and the instrument was calibrated using the Geological Survey of Japan (JSD-2) soil and sediment standard material before analysis.

3.3.2.9 Selective Sequential extraction

Modified sequential extraction method (SSE) was applied to characterize *As* distribution in sediments. Before the analysis sample was air-dried as described by (Wenzel et al., 2001). Modified procedure was followed to examine the *As* concentrations associated with five "operationally

defined phases" within the sediment, including non-specifically bound (outer sphere surface complexes), specifically bound (inner sphere surface complexes), amorphous hydrous Fe (Mn, Al) oxides (e.g., ferrihydrite), crystalline (hydrous) Fe (Mn, Al) oxides (e.g., goethite, hematite and magnetite), and residual (e.g., aluminosilicates; framework silicates, such as quartz) (Haque et al., 2008; Wenzel et al., 2001).

Before extraction analysis, selective aquifer sediment samples were air-dried at room temperature (35°C) overnight. Then dried sediments were homogenized using mortar-pestle and passed through a 2-mm sieve. All the reagents were obtained from Sigma-Aldrich and prepared strictly using Milli-Q ultra-pure water (18.2 Ω cm). In brief, the five-step extraction procedure (Wenzel et al., 2001) followed for *As* extraction, could be described as Fraction 1: A 1.0 gm (dry weight) of sediment sample along with 25 mL of 0.05 M $(NH_4)_2SO_4$ reagent was placed into a 50 mL centrifugation tube (Fisher Scientific). Then, the mixture was agitated for 4 hours at 20°C in an orbital shaker (LabTech, India) and subsequently centrifuged (Remi, India) for 15 minutes at 6000 r.p.m. The resultant supernates were filtered (0.45µm filter paper), acidified with ultra-pure HNO_3 (HiMedia, India), and stored in 100 mL specimen tube (Tarson, India) at 4°C before analysis.

The residual soil was used for subsequent extraction step Fraction 2: The residue from the fraction 1 was embedded with 25 mL of 0.05 M $NH_4H_2PO_4$ solution in a 50 mL centrifuge tube and subsequently agitated for 16 hours at 20°C on the orbital shaker as described above. Subsequently, the mixture was centrifuged, filtered, and acidified as a step, as mentioned earlier. Fraction 3: The obtained residue from fraction 2 was embedded with 25 mL of 0.2 M NH_4-oxalate buffer solution in a 50 mL centrifuge tube, and pH 3.3 was adjusted using oxalic acid. Then the mixture was

agitated for 4 hours at 20°C in a dark place, and then centrifuged, filtered, and acidified as described above. To account for the potential carryover, the procedure described by (Haque et al., 2008) was followed, to recover re-adsorbed *As* onto the amorphous metal oxides. Fraction 4: The residual from fraction 3 was subsequently embedded in a solution of 0.2 M NH_4-oxalate buffer in a 50 mL centrifuge tube, and then the mixture pH 3.3 was adjusted using 0.1 M ascorbic acid. Then, the mixture containing the centrifuge tube was placed in a heated water bath (96 ± 3 °C) shaker and agitated for 30 minutes. After cooling, the mixture containing centrifuge tube was centrifuged, filtered, and acidified as described above.

The potential carryover procedure described above was employed to recover *As* re-adsorbed onto crystalline Fe and Al oxide minerals. Furthermore, the mixture containing centrifuge tube was centrifuged, filtered, and acidified as described above. Fraction 5: The residue from the above fraction was digested by following ASTM acid digestion method D3974 − 09 (ASTM 2015), after cooling, the solution mixture was centrifuged, filtered and acidified as described above.

3.3.2.10 Morphological and Elemental analysis

Elemental compositions and morphological study were studied using field emission scanning electron microscopy and energy-dispersive X-ray spectrometer (FESEM-EDS) (Zeiss, Sigma, Germany), respectively. Field emission scanning electron microscope (FESEM) and energy dispersive spectroscopy (EDS) (FESEM, Hitachi S-640) equipped with a JEOL-JSM 5800 LV microscope. For FESEM and EDS analysis, sediment samples (~1 g) were dispersed in acetone, drop caste onto the stub, dried at the ambient room temperature for 2 h and gold coated using a sputter coater (EMS 7620 'Mini' Sputter Coater). Morphological analyse was carried by varying EHT (Extra High Tension) from 1.5 kV to 3 kV and magnification from 2 KX to 65 KX.

Semi-quantitative analysis was carried by following EDS analysis which was carried out at a fixed 20 kV accelerating voltage (EHT). Addition to EDS analysis, electron probe micro analyzer (EPMA) methodology (i.e. elemental mapping) was used to detect an *As* and other metal concentration on an agglomerated particles over the selected scanned area for analysis.

3.3.2.11 X-ray diffraction (XRD)

Mineralogical compositions were determined by using powder X-Ray diffraction (XRD) (Bruker, Model-D8- Advance) method. Prior to XRD analysis, the air-dried sediment samples were gently pulverized using mortar and pestle (Sailo and Mahanta 2014). Then, the sample was mounted on the "quartz plate" and data was collected at 2θ from ~5° to 70°, degree with a step size of 0.02° for 4s, using copper (Cu Kα radiation = 1.5418Å) as a target material for single-crystal diffraction. The obtained characteristic X-ray spectra were interpreted using X'Pert high score plus software.

3.3.2.12 Sediment Characterization by Infrared (IR) spectroscopy

In Fourier Transform Infrared (FTIR) Spectroscopy is a surface-sensitive technique that uses to interrogate adsorbent-solution interface interactions that occurred at a molecular scale. The IR spectra were determined using on PerkinElmer Spectrum Version 10.4.3 spectroscopy. The air-dried aquifer sediment samples of ~ 5 mg were used for FTIR analysis. The beam current was 300 mA and the synchrotron was run in top-up mode. Spectra were collected in the mid-IR spectral range (4000 cm^{-1} – 400 cm^{-1}) at 4 cm^{-1} resolution, with the co-addition of 128 scans, the aperture of 10 µm ×10 µm.

3.3.2.13 Kinetic and isotherm models

Adsorption study was conducted by following a batch technique. Prior to beginning the experiment, all sediment samples were air-dried overnight and stored at 4°C. In this adsorption study, we used both *As* (III) and *As* (V) fraction to understand the adsorption or removable capacity of the sediment. For this analysis, representative water-bearing aquifer sediments were used from different *As* concentration groundwater regions of the study areas. The selective sediments (viz. fine sand and medium sand) mainly consist of oxidized (dark brown), partly oxidized (brown-yellowish) and reduced (dark grey).

To study an effect of solutions pH [*As* (III) and *As* (V)] on sediment sample, a stock solutions of *As* (III) and *As* (V) were prepared by dissolving reagent-grade sodium arsenate (Na_2-$HAsO_4$–$7H_2O$; Loba Chemie) into de-mineralized distilled water (ddH_2O) (Mill-Q Water, M/S Millipore S.A.S., Molsheim, France). The stock solutions were stored at 4°C. The effects of pH on the *As* adsorption were tested for 6.5, 7 and 7.5 pH, which was close to the measured groundwater and sediment pH (Avg.7) samples. The pH of the ddH_2O water was alkaline (7.1±0.2); the pH of the solution was adjusted using concentrated 6N of HNO_3 and 1M of NaOH. Two grams of selective aquifer sediment was added into 20 mL of 300µg L^{-1} of *As*(V) and *As* (III). The samples were kept for 24 hours continuous in the end-over rotary shaker, and solutions were centrifuged, and the supernatant was analyzed for remaining *As* concentration.

In past decades, several mathematical models (viz. Elovich kinetic, Intra-particle diffusion model, Pseudo first and second order kinetic, etc.) have been proposed to describe adsorption reaction model data. Among these models, the most commonly used pseudo-first and second order

kinetic reaction model was used to estimate the adsorption capacity of *As* (III) & *As* (V) on the different aquifer sediments.

The following expression used to estimate the *As* uptake by the adsorbent as follows:

$$q_t = \frac{V}{m}\left(C_m - C_t\right) \ldots (6)$$

Where q_t is the amount of metal ion adsorbed on adsorbent (µg g^{-1}) at time '*t*', V is the volume of solution in liters (L), 'm' is the mass of adsorbent in grams (g), C_O is the initial concentration of the adsorbate (µg g^{-1}), at t = 0 and C_t is the concentration of the adsorbate (µg g^{-1}) at time '*t*'.

A pseudo first-order kinetic model mathematical expression can be written as follows:

$$q_t = q_e\left(1 - e^{-k_1 t}\right) \ldots (7)$$

It's liberalized form is:

$$\log\left(q_e - q_t\right) = \log q_e - \frac{k_1 \times t}{2.303} \ldots (8)$$

Where, q_e and q_t are the amount of the metal ions adsorbed on adsorbent (µg g^{-1}) at equilibrium and at a time 't' respectively while k_1 is the pseudo first order rate constant (minute $^{-1}$). The values of k_1 and q_e can are determined by using the experimental values of variables q_t obtained at a different time '*t*' by applying the method of least square to Equation (8).

The following Pseudo second order kinetic model expression used to estimate the *As* uptake by the adsorbent as follows:

$$\frac{dq_t}{dt} = k_2\left(q_e - q_t\right)^2 \ldots (9)$$

Where q_e is uptake at equilibrium a time (μg g^{-1}), q_t is uptake at a time't' and k_2 is pseudo second order rate constant $[g/(\mu g.min)]$. For the initial conditions at t = 0, $q_t = 0$ and at final t= t, $q_t = q_t$, Integrating the above equation to obtain a linear form can be represented as:

$$\frac{t}{q_t} = \frac{1}{k_2 q_e^2} + \frac{t}{q_e} \quad \ldots (10)$$

A plot of 't/q_t' vs. 't' was used to determine the parameters of pseudo second order kinetic model. The published literature over the study area measured average groundwater pH at around ~7±0.2 (Mahanta et al. 2015, Sailo and Mahanta 2014, 2013, 2016, Verma et al. 2015). For these reaction models, results obtained from pH studied (i.e. 7) was chosen for the solvent and studied the effect of *As* (III) & *As* (V) on sediment adsorption. Two different concentration (300 μg L^{-1} and 500 μg L^{-1}) *As* (III) & *As* (V) stock solutions were used for this study. In a 50 mL centrifuge tube (Tarson, India), 1:20 (1g of sediment sample and 20 ml solution), the ratio of adsorbent and adsorbate [*As*(III) & *As* (V) separately] was maintained for each sample analysis test. These tubes were then placed in an end-over mechanical shaker at 200 rpm; for a specified time interval (0.15, 0.30, 1, 2, 4, 6, 8, 12, 16, 24 hours), then the samples were taken out followed by centrifugation at 5000 r.p.m. Then, each aliquot was filtered through a 0.45 μm filter paper, and each filtrate was stored at ~ 4°C after acidification (adding 6N of HNO_3) until they were analyzed in the Atomic Absorption Spectroscopy (AAS). Along with sediment samples, a blanks sample (viz. ddH_2O water) was also analyzed to ensure that no chemical reaction enhances the *As* concentration or to be adsorbed on the walls of the centrifuge tube or magnetic needle from the aliquot obtained. The adsorbed *As* was calculated from the difference between the concentration before and after equilibrium with the sediment particles. The test was conducted under an atmospheric condition at

~35±2°C room temperature. The pH of the suspensions was measured immediately after completion of experiments, and it was almost constant throughout the experiments.

Similarly, batch isotherm study was conducted to understand the maximum adsorption capacity of the sediments. Batch adsorption isotherm technique was conducted for *As* (III) and *As* (V) on the selective depth sediment samples. Experimental methods explained by Sailo and Mahanta (2016), was followed for the isotherm study. Here, different initial arsenic concentrations of *As*(III) and *As* (V) (viz. 50 µg L^{-1}, 100 µg L^{-1}, 200 µg L^{-1}, 300 µg L^{-1}, 400 µg L^{-1}, 500 µg L^{-1}, 600 µg L^{-1}, 700 µg L^{-1} and 800 µg L^{-1}) was used separately for isotherm study. For each sample, a control sample was also set and used to verify the dissolution of total *As* from the sediment sample. The liquid to solid ratio of 20:1 was maintained for each time interval samples. The test was performed at neutral pH (i.e. 7) and was adjusted by adding HNO_3 (0.02 N) and NaOH (1M). The samples were kept for 24 hours continuous in end-over rotary shaker and solutions were further centrifuged and the supernatant was analyzed for the remaining *As* concentration. The samples for the isotherm study were placed in an end-over mechanical shaker at 200 r.p.m. For specified time interval (i.e. 0.15, 0.30, 1, 2, 4, 6, 8, 12, 16, 24 hours), tubes were centrifuged at 5000 rpm. Then the experimental procedure mentioned above for kinetic study was followed till sampling storage. The pH of the suspensions was measured immediately after completion of experiments and it was recorded almost constant (± 0.1) throughout the experiment. The samples were further analyzed in hydride generation atomic absorption spectrophotometer. The obtained results were checked by using the following linear Freundlich and Langmuir adsorption isotherms equation respectively, as follows:

$$\log q_e = \log k_f + \frac{1}{n}\log C_e \ldots (11)$$

$$\frac{C_e}{q_e} = \frac{1}{q_{\max} C_e} + \frac{1}{K_L q_{\max}} \ldots (12)$$

where, In Freundlich adsorption isotherm equation 11, a plot of $\log q_e$ (i.e. equilibrium adsorption concentration) versus $\log C_e$ (concentration at equilibrium) has an intercept K_f and slope 1/n, whereas in Langmuir adsorption isotherm equation 12, q_e is the equilibrium adsorption concentration (μg g^{-1}), C_e is the concentration at equilibrium (μg L^{-1}), n and K_f are the adsorption intensity and adsorption capacity, respectively for the sediment samples.

3.4 Microbiological study

3.4.1 Isolation and characterization of *As* resistant bacteria

For isolation of microbes from the sediment samples, the sediments collected (May 2013) using a reverse circulatory drilling method were recovered without the drilling fluid to minimize the possibility of contamination with non-indigenous micro-organisms. The sample was transported and stored at 4°C until further analysis. For the isolation of aerobic *As*-resistant bacteria from groundwater samples (collected in June 2017), non-acidified samples were used from the H*As*CR and L*As*CR arsenic contaminated regions of Bongaigaon and Darrang district of the study areas.

3.4.2 Media composition

Initially, arsenic resistant bacteria were isolated from the H*As*CR study area sediment samples. For isolation, aerobic *As*-resistant bacteria, gray and brown color (medium sand) samples were used. A 100 g of aquifer's sediment sample in 1L double-distilled water (ddH_2O, 18M Ω) was amended individually with sodium arsenite (Na*As*O_2) and sodium arsenate (Na_3*As*O_4) to yield a

final concentration of 500 mg L^{-1} and kept in a BOD incubator at 27°C for 7 days for the enrichment (Fan et al. 2008). A 10g of above enriched sediment sample (triplicates) was added to 100 ml of 0.85% NaCl solution and were agitated for the isolation of aerobic *As* resistant bacteria (Fan et al. 2008). The supernatant was serially diluted up to 10^{-7}, and further 100 µL of the resultant was added to chemically defined medium (CDM) (pH 7) plates, supplemented with 100 mg L^{-1} of Na_3AsO_4 and $NaAsO_2$ (Weeger D., 1999). The plates were then incubated for 7 days at 27 °C.

Similarly, for isolation of microbes from groundwater samples, amendment (using 100 mL groundwater) procedure mentioned above was followed by adding 1 mL of *As*-contaminated water (triplicates) to 100 mL of 0.85% NaCl solution and shaken for 10 min. The extraction solution was serially diluted and plated onto Luria Bertani (LB) agar plates (Goswami et al. 2017), containing 100 mg L^{-1} of $NaAsO_2$. The plates were kept inside an incubator at 30°C for 7 days. Then, single colonies were re-streaked several times to obtain pure isolates.

3.4.3 Qualitative $KMnO_4$ screening method

The obtained arsenic resistant bacteria were further tested for their abilities to oxidize *As*(III) ($NaAsO_2$) or reduce *As*(V) (Na_3AsO_4), using a qualitative $KMnO_4$ screening test method, with some minor modifications (Salmassi et al., 2002). Each arsenic resistant bacterium was cultured to an optical density (O.D.) of 0.4 in LB liquid medium containing 100 mg L^{-1} of either $NaAsO_2$ or Na_3AsO_4. Then, 40 µL of 0.01 mol L^{-1} $KMnO_4$ was added to 2 mL of the culture. Pink color of the mixture indicated positive arsenite oxidation reaction [formation of *As*(V)], and a yellow color indicated a positive arsenate reduction reaction [formation of *As*(III)].

3.4.4 16S rDNA sequencing and PCR

Sediment samples (0.25 g) were pretreated with 2ml sodium oxalate solution (0.3 M) passed through a 0.25 mM filter and DNA was extracted using a Fast DNA spin kit (Ultra Clean, Soil DNA isolation kit, MO BIO Laboratories). A fragment of the 16S rRNA gene, approximately 520 bp, was amplified by PCR from samples using the broad-specificity primers 8f and 519r24, using an iCycler (BioRad). Purified DNA (5 ml) and 2.5 ml of 25 mM primer stocks were added to the reaction mix to a final volume of 50 ml. The purity of the amplified product was determined by electrophoresis of 10 ml samples in a 1.0% agarose Tris-borate-EDTA (TBE) gel. DNA was stained with ethidium bromide and viewed under short-wave UV light.

3.4.5 Bacterial growth and Arsenic tolerance limitation

Bacterial biomass growth and bio-degradation were observed at a different initial *As* concentration in the range of 100 to 1800 mg L^{-1}. The batch experiments were conducted using 250 mL Erlenmeyer flasks by adding each bacterium in 100 mL of liquid nutrient agar, with different concentration of *As* (III) and *As* (V). Bacterial cell density was determined by measuring its absorbance at 600 nm, using a UV–Vis spectrophotometer (Agilent Technologies, Cary 100 series, Singapore). The bacterial growth was determined based on a standard graph plotted between OD_{600} versus cell dry weight (CDW).

3.4.6 Morphological analysis

Changes in the bacterial surface morphology observed due to a simultaneous uptake of *As* was examined by Field Emission Scanning Electron Microscopy (FESEM) (Zeiss, Sigma, Germany). The bacterium grown in the presence of *As* was used for this analysis. 1 mL of the

bacterial culture was centrifuged (10,000 rpm, for 10 min.) and washed twice with sterile ddH_2O water. The pellets obtained were diluted 10 times with ddH_2O water. A unit drop of this sample was mounted on aluminum stubs over double-sided carbon tape and dried overnight at 30°C prior to the analysis. After drying, the sample, it was coated with a thin gold layer by sputter coater before FESEM observation. The spectra obtained were compared with the biomass grown in the absence of arsenic. For FESEM-EDX analysis, a biomass sample was vacuum dried and mounted on aluminum stubs over double-sided carbon tape followed by double coating with a thin gold layer by sputter coater.

3.4.7 Growth characteristics

Infrared spectroscopy of the biomass grown in the presence and absence of *As* was carried out by Fourier Transform Infrared Spectrometer under dry air at room temperature (PerkinElmer, Spectrum Two, Singapore). Sample aliquots were centrifuged (8000 rpm, for 10 min) followed by washing with distilled water, and the pellets obtained were vacuum dried prior to FTIR analysis. The samples were uniformly mixed with KBr in 100:1 ratio. The analysis was performed over the entire wavenumber range with 20 consecutive scans at a 4.0 cm^{-1} resolution. FTIR spectra were taken under the transmittance mode.

3.5 Numerical modeling

3.5.1 Modular Three-Dimensional Finite-Difference Groundwater Flow Model (MODFLOW)

MODFLOW module in GMS 10.2, developed by the U. S. Geology Survey (USGS), was used for simulating transient state groundwater 3D flow model (Michael G. McDonald and

Harbaugh, 1988). Groundwater simulation (i.e. MODFLOW) based on the finite-difference method; which has a numerical approximation that allows for describing a solution for a complex groundwater flow problems. A rectangular grid was superimposed over the study area for horizontal subdivision of a region of interest into a number of rectangular cells. The vertical layers were used to subdivide the aquifer vertically into units of common hydro-geological properties (Lachaal et al., 2012). Groundwater flow is formulated as a differential water balance for every model cell, and the hydraulic head is solved for at the center of every model cell. MODFLOW allows for the specification of flows associated with wells, areal groundwater recharge, rivers, drains, streams, flow barriers, and other groundwater sources/sinks parameters present over the study area. This module numerically solves the three-dimensional groundwater flow equation for a porous medium using a finite-difference method as written below (equation 14):

$$\frac{\partial}{\partial x}\left(K_{xx}\frac{\partial h}{\partial x}\right)+\frac{\partial}{\partial y}\left(K_{yy}\frac{\partial h}{\partial y}\right)+\frac{\partial}{\partial z}\left(K_{zz}\frac{\partial h}{\partial z}\right)+W=S_s\frac{\partial h}{\partial t} \quad \ldots (14)$$

where *Kxx, Kyy,* and *Kzz* are values of principal hydraulic conductivity along the *x, y,* and *z* coordinate axes (m d^{-1}), respectively; *h* is the potentiometric head (m); *W* is a volumetric flux per unit volume representing sources and/or sinks term for groundwater (m^3 d^{-1}); *Ss* is the specific storage of the porous material (d^{-1}); and *t* is the time (d).

3.5.2 Modular Transport Three Dimensional Model Simulator (MT3DMS)

Arsenic contaminant transport simulation model has prepared using MT3DMS module for both the study areas. This module has a comprehensive set of options and capabilities for simulating advection, dispersion, diffusion, and chemical reactions simulation packages for *As* in contaminant transport simulation model under general hydrogeology conditions. The following partial

differential equation describes the fate and transport of species (e.g. 'k') in 3-D, for a transient groundwater flow systems the equation can be written as follows:

$$\frac{\partial\left(\theta C^{k}\right)}{\partial t}=\frac{\partial}{\partial x_{i}}\left(\theta D_{ij}\frac{\partial C^{k}}{\partial x_{j}}\right)-\frac{\partial}{\partial x_{j}}\left(\theta V_{i}C^{k}\right)+q_{s}C_{s}^{k}+\sum R_{n}\ \ldots(15)$$

Where θ = porosity of the subsurface medium, dimensionless, C^k is dissolved concentration of species k (ML^{-3}), t is time, $X_{i,j}$ is the distance along the respective cartesian co-ordinate axis (L), D_{ij} is hydrodynamic dispersion coefficient tensor (L^2/T), V_i is seepage or linear pore water velocity (LT^{-1}); it is related to the specific discharge or Darcy flux through the relationship, $V_i = q_i/\theta$, where q_i is volumetric flow rate per unit volume of aquifer representing fluid sources (positive) and sinks (negative) (T^{-1}), C_s^k is a concentration of the source or sink flux for species 'k' (ML^{-3}), $\sum R_n$ is chemical reaction term, $ML^{-3}\,T^{-1}$,

The left-hand side of Equation 15 can be expanded into two terms, i.e.

$$\frac{\partial\left(\theta C^{k}\right)}{\partial t}=\theta\frac{\partial C^{k}}{\partial t}+C^{k}\frac{\partial\theta}{\partial t}=\theta\frac{\partial C^{k}}{\partial t}+q_{s}^{'}C^{k}\ \ldots(16)$$

The chemical reaction term in Equation 16, can be used to include the effect of general biochemical and geochemical reactions on contaminant fate and transport. Considering only two basic types of chemical reactions, i.e., aqueous-solid surface reaction (sorption) and first-order rate reaction, the chemical reaction term can be expressed as follows:

$$\sum R_{n}=-\rho_{b}\frac{\partial C^{-k}}{\partial t}-\lambda_{1}\theta C^{k}-\lambda_{2}\rho_{b}C^{-k}\ \ldots(17)$$

ρ_b = Bulk density of the subsurface medium (ML^{-1})

C^{-k} is a concentration of species 'k' sorbed on the subsurface solids (MM^{-1}), λ_1 is First-order reaction rate for the dissolved phase (T^{-1}), λ_2 First-order reaction rate for the adsorbed (solid) phase (T^{-1}). Substituting Equations 16 and 17 into Equation 15 and dropping the species index for simplicity of presentation; Equation 15 can be rearranged and rewritten as:

$$\theta \frac{\partial C}{\partial t} + \rho_b \frac{\partial \overline{C}}{\partial t} = \frac{\partial}{\partial x}\left(\theta D_{ij} \frac{\partial C}{\partial x_j} \right) - \frac{\partial}{\partial x_j}(\theta V_i C) + q_s C_s - q_s^{'} - \theta C - \rho_b \overline{C} \ldots (18)$$

Equation 18 is essentially a mass balance statement, i.e., the change in the mass storage (both dissolved and sorbed phases) at any given time is equal to the difference in the mass inflow and outflow due to dispersion, advection, sink/source, and chemical reactions. Note that in the transport-governing equations described above, only a single porosity has been assumed. This porosity has been commonly referred to as "effective" porosity, which is generally smaller than the total porosity of the porous medium, reflecting the fact that some pore spaces may contain immobile water with zero groundwater seepage velocity.

The advection term of the transport equation describes the transport of miscible contaminants at the same velocity as the groundwater. For many field-scale contaminant transport problems, the advection term dominates over other terms. To measure the degree of advection domination, a dimensionless peclet number (P_e) is usually used, which is defined as

$$P_e = |v| L \ldots (19)$$

Where |v|= magnitude of the seepage velocity vector (LT^{-1})

L = characteristic length, commonly taken as the grid cell width (L)

D = dispersion coefficient (L^2T^{-1})

Dispersion mechanism in porous media refers to the spreading of contaminants over a greater region than would be predicted solely from the average groundwater velocity vectors (Anderson et al., 1999). The treatment of mechanical dispersion as a fickian process (in effect, addictive to diffusion) represents a pragmatic approach through which realistic transport calculations can be made without fully describing the heterogeneous velocity field, which, of course, is impossible to do in practice. Moreover, the fluid sink/source term of the governing equation, $q_s C_s$, represents solute mass entering the model domain through sources or leaving the model domain through sinks. The term $q_s^{'}$C may be viewed as the "internal" sink or source term, which represents the change in solute mass storage caused by the change in transient groundwater storage. It does not cause the mass to leave or enter the model domain.

3.5.3 Hydraulic properties of sediments

To determine the coefficient of permeability (i.e. hydraulic conductivity '*K*') of representative aquifer sediment, falling head permeability test [IS: 2720 (Part17)-1986] was followed. The falling head permeability test involves the flow of water through a relatively short thickness soil sample connected to a standpipe, which provides the water head and also allows measuring of the volume of water passing through the sample. The diameter of standpipe as '2.5 cm' was chosen for this test, which depends on the permeability of the tested soil. The test was carried out in acrylic material permeability cell (viz. outer diameter 'D' = 6 cm, inner diameter 'd'= 5cm, the height of cell 'h'= 10cm), manufactured especially for these sediment analyses.

Falling head permeability test was followed for the representative aquifer sediment samples (viz. clay, silty-fine sand, medium sand, and coarse sand with gravel). Prior to the analysis, moisture

content for each sediment samples (~1g) was determined. The dry density for clay, silty-fine sand and coarse sand with gravel was assumed to be 1.65 and 2.65 g $(cm^3)^{-1}$, whereas, for medium sand samples, it was measured by following the (Sherwood 1900) compaction testing procedure to obtain an experimental optimum moisture content. Sediment samples were saturated before starting the experiment and recorded time an allowable variation of about ±10%. On the basis of the recorded readings, hydraulic conductivity of the sample was calculated as:

$$K = \frac{a \times L}{A \times \Delta t} In\left(\frac{h_1}{h_2}\right) \quad \ldots (20)$$

where;

K: hydraulic conductivity (cm/sec), L: the height of the soil sample (cm), A: the samples cross section (cm^2),

a: the cross-section of the standpipe (cm^2),

Δ t: the recorded time for the water column to flow through the sample (minutes),

h_1 and h_2: the upper and lower water level in the standpipe measured at a certain time interval (cm)

The vertical hydraulic conductivity (K_z) value for clay and silt was assumed to be equal to 1/10 of horizontal (K_x=K_y) (Mukherjee et al., 2007b), whereas for sandy aquifer it was assumed twice of horizontal (K_x) hydraulic conductivity. Todd and Larry, (2005) mentioned empirical values for various repacked soil, especially porosity (e) and specific yield (Sy) were used for MODFLOW simulation. The horizontal anisotropy was assumed to be equal to one but the vertical anisotropy was calculated, taking a ratio of horizontal hydraulic conductivity (i.e. K_x) to vertical hydraulic

Table 3. 1: Regional data and its sources used for the model simulation

Data	No. of stations/ locations for Bongaigaon and Darrang study area	Period (years)	Source/organization
Rainfall and Temperature	Guwahati Airport and Dhubri	1996 to 2015	Regional Meteorological Center (RMC, Guwahati)and
River head stage	At Manas N H Xing GDS Site Khalihai, Tarabari and Mangaldai	1996 to 2015	Assam Water Research and Management Institute (AWRMIS)
Groundwater level	4 and 2	1996 to 2015	India-WRIS, (http://www.india-wris.nrsc.gov.in/)
Number of pumping wells	295 and 62	2013 to 2017	Personally collected data from both study areas
Lithology of wells	10 and 6	2013 to 2017	Drilled purposely for this study and for M5 & M6 wells data collected from Central Ground Water Board, North Eastern Region (NER), Guwahati, Assam
Arsenic	325 and 159 of groundwater sampling data from HAsCR and LAsCR respectively	2013 to 2017	Personally collected data from both study areas

conductivity (i.e. K_z) for the respective sediment samples. Lohman (1972) empirical equation which was used for the determination of specific storage for the respective aquifer thickness (i.e. b) given below:

$$S_S = 3\times10^{-6}(b) \quad \ldots (21)$$

where '*b'* is saturated aquifer thickness (m). The values within the range of $0.00005 < Ss < 0.005$ for confined aquifers, indicates that large hydraulic pressure difference needed for the significant water yield for respective aquifers.

3.5.4 Hydro-geological conceptual model development

A conceptual hydrogeological model was created for both the study areas using feature objects (viz. nodes/points, arcs and polygons, grid frame) and converted for MODFLOW and MT3DMS simulation. This facilitates to synthesize and frame the observed calculated and empirical data pertaining to hydrogeology and meteorology data reasonably. The 3D finite difference model grids were generated according to lithology and stratigraphy model output, and its inputs were automatically transferred from the conceptual model. A transient state (stress period 2013 to 2056) conceptual model was used to predicate the contamination level in vast complexities and heterogeneous (e.g., variations of aquifer properties at local-scale, seasonal crops pattern, surface water bodies, etc.) hydro-stratigraphy in both study area. The sources of observed and measured input data used for this study was collected from the authentic government organization and are listed in Table 3.1. Figure 3.2 a and 3.2 b showed 3D finite difference cell centered grid distribution, topographical features and boundary conditions used for the two study areas (H*A*sCR~ 389.6 km^2 and Darrang ~ 184.3 km^2). The surface elevation for the study area was defined according to SRTM-DEM data and ground elevation data of Google Earth software, which was used for constructing a fence diagram and stratigraphy modeling. The total number of grids 3,37,500 of equal cells size [125.8 m (x)× 137.9 m (y)× 6.32 m (z)] were assigned for Bongaigaon district study area, whereas for Darrang district study area, total 3,82,500 number of grids of equal cells size [125.1 m (x)× 65.5 m (y)× 3.37 m (z)] were distributed. The vertical grids were discretized according to the stratigraphy modeling results for HAsCR and LAsCR district area into a total number of 15 (z = 94.84 m thick) layers and 17 (z = 57.34 m thick) layers respectively. The locations of the drilling well and pumping well sites were recorded on the field using a handheld GPS set

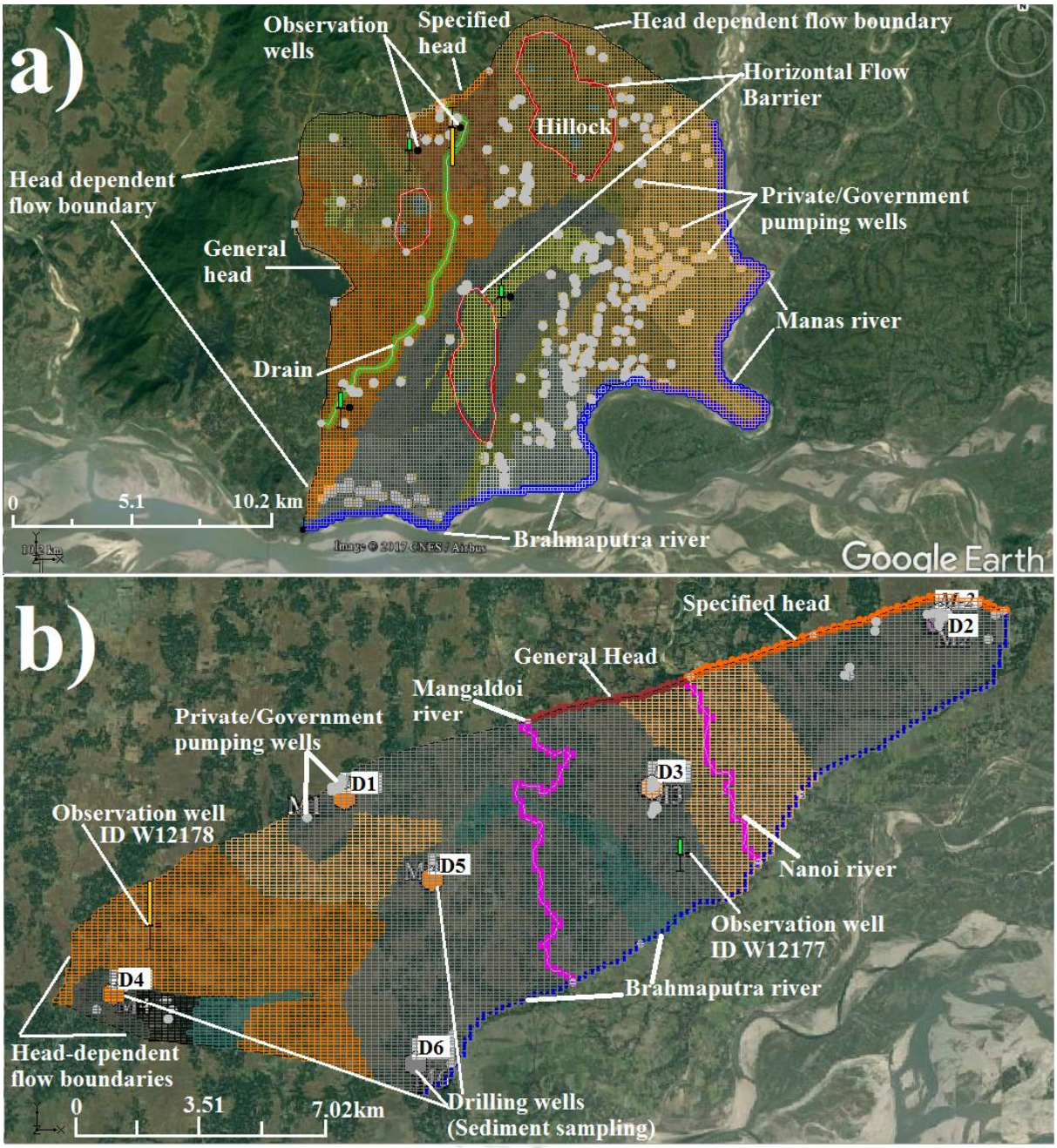

Figure 3. 2. Boundary conditions and finite difference grid for a) H*As*CR study area and b) L*As*CR study area, the grid color indicates the distribution of soil material over the study area.

(Garmin Montana 610) by a spherical coordinate system of longitude and latitude (datum WGS 84). These study areas were delineated using the Google Earth image, which was registered in software using GPS coordinates of known sites and was further projected to the Universal Transverse Mercator (UTM 1983), Zone 15 (96° W to 90°W Northern hemisphere) in the meter of length. It helps minimize the finite difference grid distortion and stratigraphic distribution over the two study areas. The origin coordinates of Bongaigaon district study area was covered between 257210.0 N and 2902390.0 W, whereas for Darrang district, the study areas were covered between 389904.0 N and 2918939.0 W.

3.5.4.1 Delineation of boundary conditions parameters

The aquifers and aquitard layers were assigned as convertible for each modeling simulation. Specified head boundary condition was assigned for the river Manas and Brahmaputra, whereas for the small seasonal rivers, i.e. Nanoi and Mangaldai tributaries of Brahmaputra River were assigned as Drains in MODFLOW simulation model. In H*As*CR study area (Figure 3.2a), Horizontal Flow Barrier (HFB package) boundary condition was assumed for natural outcrop, which would act as groundwater flow barrier, whereas along the north-western side of the study area head-dependent flow boundary condition was assigned. For H*As*CR and L*As*CR study areas, (Figure 3.2a, 3.2b) specified flux boundary conditions were assumed for the adjoining areas of the drains respectively, considering the topography of the study two areas.

3.5.4.2 Rivers conductance

The rivers were divided into appropriate reaches and attributes like channel width (W) and length (L). These values were measured approximately in meters from the "Google Earth Pro" 2017

software. River water depth (h) was assumed as average 6 m and coarse sand as bed material. River bed conductance (C) was calculated from the following empirical formula:

$$C = \frac{K \times W \times L}{h} \ldots (22)$$

where '*K*' is the vertical hydraulic conductivity of the bed material, 'W' is the width of the river channel, 'L' is the length of the river, 'h' is the depth of water in the river. Appendix Table 2.1 shows the calculated conductance results for respective river beds. For general head boundary condition, conductance value was assigned as 0.0082 [(m^2d^{-1}) m^{-1}] and 0.0069 [(m^2d^{-1}) m^{-1}] to H*As*CR and L*As*CR study areas respectively.

3.5.4.1 Surface water recharge and evapotranspiration

The potential recharge values for the study areas were attributed using the empirical equation by considering total precipitations, evapotranspiration, surface overflow, and meteoric water recharge into both study area aquifers. No detailed literature was available on total recharge and evapotranspiration for these study areas; hence they were considered as one of the least certain input parameters for the simulation model. The seasonal data of daily rainfall, temperature and humidity and wind speed for January to February (Post Monsoon, Rabi), March to July (Pre Monsoon), August to October (Monsoon) and November (Post Monsoon Kharif) were obtained from the Regional Meteorological Department (RMD), Guwahati, India, for the nearest stations of the study areas. The potential rainwater recharge was estimated using the following formula:

$$PR = R - ET = AR + SF \ldots (23)$$

whereas: 'R' is total precipitation, 'ET' is evapotranspiration and during dry seasons, during the dry season PR ≈ AR which is the meteoric water that actually recharges the aquifer when surface

overflow (SF) is negligible or almost zero. Accurate quantification of 'AR' and 'SF' data for the study area requires long-term hydraulic head and surface water stage measurements data from various locations in the study area.

The 'ET' was estimated for both the study area by using (Pike, 1964) equation as follows:

$$\mathrm{ET}\left(\mathrm{mm/month}\right)=\frac{\mathrm{P}}{\left(1+\left(\frac{\mathrm{P}}{\mathrm{PET}}\right)^{2}\right)^{1/2}}\ldots\ (24)$$

Where 'PET' is potential evapotranspiration (mm/month) and 'P' is average precipitation (mm/month). Potential evapotranspiration was estimated from Malmström, (1969) method as mentioned following:

$$\mathrm{PET}\left(\mathrm{mm/month}\right)=40.9\times e^{*}\left(\tau\right)\ldots\ (25)$$

Where $e^{*}=0.611\times\exp\left(\frac{17.3\times\tau}{\tau+237.3}\right)$ and τ is average monthly temperature (°C).

To avoid an error for the simulation, 'PR' for each study area was calculated from the available rainfall data from the RMC, Guwahati. The calculated recharge values were applied uniformly over the top layer of the model. The estimated input data for potential recharge and evapotranspiration are tabulated in Appendix Table 2.1 for the respective study areas.

3.5.4.2 Sink and Source parameters of As

In the study areas, two types of wells are typically used for extraction of groundwater: government or privately owned shallow depth (15 m to 60 m), hand-pump tube wells (HTW) or electric-motor driven and another was public water supply scheme (PWSS) deep tube well (80–120 m) high-yield capacity (45.5 m^3 d^{-1}). For MODFLOW simulations, a total number of 295 (constant

flow rate -1.3m^3 d^{-1}) and 62 (constant flow rate -1.6 m^3 d^{-1}) shallow depth HTWs of H*As*CR and L*As*CR study areas, respectively were used as sink parameters. The lateral conditions are generalized as per prescribed water head observed in the monitoring well. For the vertical boundaries, the upper part was defined as known-flux which was calculated using existing meteorological data (viz. rainfall recharge, evaporation), estimated parameters such as river leakage and assumed irrigation water recharge (~ 10 % of rainfall). The lower part is in contact with the impermeable bedrock of the confined aquifer so that they were set as impermeable (zero-flux) boundary.

To understand the concentration gradient for arsenite (As^{+3}) (highly mobile in reducing groundwater condition) in both the study areas, MT3DMS (modular three-dimensional transport model) module of GMS was used. For contaminate transport MT3DMS simulation model, it has been hypothesized that the source of As^{+3} is mainly geogenic in the shallow aquifers of the study areas and its concentration gradient is mainly controlled by the complex hydrostratigraphy and redox condition of the study area aquifers. The minimum As^{+3} concentration equal to 0.1 µg L^{-1} and 0.61 µg L^{-1} was assigned for H*As*CR and L*As*CR region. The maximum and average *As* concentration was assigned for the 5th and 4th layer as 352.7 µg L^{-1} and 40 µg L^{-1} for H*As*CR. Similarly, for L*As*CR, maximum As^{+3}concentration of 84.62 µg L^{-1} and average 29.87 µg L^{-1} was assigned for the 11th and 9th layer. For the As^{+3}sink parameters, –352.7µg $L^{-1}$and –84.62 µg L^{-1} value was assigned for all wells and rivers in all time steps stress periods simulation of Bongaigaon and Darrang district, respectively. The initial As^{+3} concentration along the boundaries (viz. for specified head and general head boundary conditions), was assigned as 352.7µg L^{-1} and 84.62 µg L^{-1} for Bongaigaon and Darrang district, respectively. Moreover, As^{+3}through top layer (i.e. from

agricultural land) was considered as 10 μg L^{-1}, which is 25% of the average measured concentration in groundwater samples.

For MT3DMS simulation, in advection package, standard finite difference method solution scheme was used with central in space weighting scheme. In chemical reaction package, results of the batch of As^{+3} adsorption isotherm study for the representative color sediment samples were used for MT3DMS simulation. Moreover, bulk density for clay, silt, and sand- gravel was assumed

Table 3. 2: Results of Freundlich isotherm adsorption coefficient values for selective aquifer sediment samples

Sample ID (depth in 'meter')	**Soil material and color**			As^{+3} **(m^3/mg)**
D1- 29	White coarse sand			8.20E-09
D2-50.3	Deep grey medium sand			9.44E-09
D3-24.4	Grey Coarse sand			1.17E-08
D4-22.9	Dark grey fine sand			1.31E-08
B1-7.6	Grey Fine sand			7.26E-09
B2-13.7	Grey Medium Sand			8.40E-09
B3-13.7	Grey Medium Sand			7.19E-09
B4-16.8	Yellow-orange Medium Sand			6.08E-09
B5-18.3	Yellow-orange Coarse Sand			2.89E-09
B6-16.8	Yellow-orange Coarse Sand			6.15E-09
B7-7.6	Yellow-orange Coarse Sand			1.26E-08
B8-25.9	Grey Medium Sand			1.43E-08
B9-27.4	Dark Coarse Sand			9.05E-09
B10-45.7	Yellow Gray Coarse sand			6.06E-09
B10-51.8	Yellow Gray Coarse sand			9.09E-09
Dispersion coefficients	**TRPT**	**TRVT**	**DMCOEF**	
As^{+3}	0.1	0.01	0.0000116	

Note As^{+3} is Arsenite, TRPT= ratio of Horizontal transverse dispersivity to longitudinal dispersivity, TRVT= ration of vertical transverse dispersivity to longitudinal dispersivity, DMCOEF = effective molecular diffusion coefficient package of MT3DMS simulation (Table 3.2).

(i.e. 11.6×10^{-6} cm^2 s^{-1}) value was used for arsenite in the dispersion as 1.1g/cm^3, 1.3g/cm^3, and 1.6 g/cm^3, respectively in chemical reaction package. For As^{+3} diffusivity constant, (Tanaka et al., 2013) experimental effective molecular diffusion coefficientEach model was run for steady condition initially then simulated for the transient condition. Gelhar et al., (1992) empirical relation for longitudinal dispersivity (α_L) was used empirically for a lateral distribution of soil greater than 3500 m length (L):

$$\alpha_L = 0.1 \times L \ldots (26)$$

Transverse dispersivity (α_T) was calculated using a statistical method developed by Xu and Eckstein, (1995) and was used for the respective aquifer sediment samples $\alpha_T = 0.83(\log L)^{2.414}$ … (27)

where L is the length of the flow path in 'meters.

3.5.5 Parameter estimation model calibration and sensitivity analysis

To understand the influence of various model parameters on groundwater contour distribution, a sensitivity analysis was performed for each study areas. In calibrating a flow model, it helps to go back to the basics of Darcy's law (here it is written in its 1D form along the x-axis):

$$q_x = -K_x \frac{\partial h}{\partial x} \ldots (28)$$

If the head gradients predicted by a model are too large, the relations in Darcy's law indicate that either the modeled fluxes are too large, or the modeled conductivities are too low, or both. Therefore, to estimate an actual hydraulic parameter for the aquifer sediments, the experimental values (hydraulic conductivity, porosity, specific storage, well or natural recharge/discharge rate)

and boundary conditions (head or Darcy flux along sections of the boundary) were adjusted several times to achieve a close fit with the observed head data (e.g., hydraulic head, flow rate).

In the MODFLOW, groundwater flow simulations for both the study areas were calibrated with the observation wellhead data. The measured and observed groundwater table by Mahanta et al. (2015) over both the study areas showed that on an average, a ground level generally lies within 10 m below ground level. Moreover, observation well data showed ~7±2 m groundwater fluctuation. For the MODFLOW calibration, maximum ± 5m and ± 10 m for H*As*CR and L*As*CR respectively, groundwater table fluctuation was allowed.

Chapter 4

4 Results and Discussion

4.1 Groundwater quality

Individual and seasonal groundwater sample results for both the study areas are presented in Appendix Table A 1.1, 1.2, 1.3, and 1.4. From H*As*CR a total of 215 groundwater samples (i.e. 2013 samples) were analyzed, out of which, 173 samples (i.e., 80%) showed dissolved *As* concentration >10 µg L^{-1}, whereas 42 samples (i.e., 20 %) were found within the WHO (World Health Organization) guideline limit (i.e. *As* <10µg L^{-1}) (WHO, 2015) (Table 4.1). Among all the three blocks of H*As*CR samples, Tapattari block showed the highest *As* contamination (i.e. 100%), whereas Boitamari block was found to be moderately contaminated (i.e., 56%) and Srijangram block was the least (i.e., 46 %) contaminated region (Appendix Table A 1.1).

Thegroundwater analysis showed that pH of groundwater was found in the range of 5.6 to 8.8 (mean 7.2 ± 0.7) with a low DO content (i.e. 0.6 mg L^{-1} to 2.4 mg L^{-1}) (mean 1.2 ± 1.7 V) in H*As*CR, and ORP values were in the range of –278.60 mV to –28.81 mV (mean -182.3 ±74.4 mV) which depicts a strong to moderate reducing aquifer condition. Groundwater temperature was almost uniform in all samples, ranging from 23.1 °C to 27.5°C (mean 25.4 ± 0.8 °C). Electrical conductivity (EC) was varied widely from 39.5µS $cm^{-1}$to 986µS cm^{-1} (mean

550 ± 259µScm^{-1}) at different depths. The Eh (Standard Hydrogen Electrode-SHE scale) values range from - 176.1 mV to 171.2mV (mean 36.3 ± 75 mV). The positive Eh_{SHE} values might be attributed to mixing of groundwater from several redox zones during pumping, which is mainly due to large screen intervals (between 30 feet and100 feet) provided in the tube wells. The positive Eh value showed the presence of moderate to strong reducing aquifers which was also evidenced by earlier studies in some other regions of the Brahmaputra basin (Mahanta et al., 2015).

The hydro-geochemical results of H*As*CR groundwater measured, HCO_3^- concentration was found in the range of 40 mg L^{-1} to 221 mgL^{-1} (mean 96.7 ±35.6) which was highest among other anion concentration whereas, highest cation concentration of Ca^{+2} was found in the range of 4.2 mg L^{-1}to 110.6mg L^{-1} (mean 46.8 ± 21.6 mg L^{-1}) in groundwater samples. Table 4.1 showed the predominance of cations concentration in the order of Ca^{+2}> K^+> Na^+> Mg^{+2} while the anions concentration followed the order of HCO_3^-> PO_4^{3-} > Cl^- > SO_4^{2-} in the high *As* concentration regions. The dissolved Fe concentration was measured in the range of 1.1 mg L^{-1} to 83.4 mg L^{-1} (mean 38 ± 20.3 mg L^{-1}) whereas; Mn concentration was measured in the range of bdl to 2.8 mg L^{-1}(mean 1 ± 0.7 mg L^{-1}). Highest *As* concentration was measured in the range of 0.1 to 352.7 µg L^{-1}(mean 55 ± 45µg L^{-1}) in this region as compared to L*As*CR which was measured in the range of 0.6 to 85 µgL^{-1} (mean 38 ± 24 µg L^{-1}).

In L*As*CR groundwater samples, 16 (i.e. 24%) well water samples were found within the WHO drinking water permissible limit (i.e., < 10 µg L^{-1}) whereas 52 (i.e. 76%) well water samples were found above the WHO drinking water permissible limit (Appendix Table A 1.2). In L*As*CR groundwater analysis, pH was found to be in the range 6.2 to 7.6 (mean 7.1 ±

0.1) whereas comparatively high DO concentration was measured in the range of 0.1mg L^{-1} to5 mg L^{-1} (mean 1.6 ± 1.7 mV). The ORP values were in the range of –388 mV to –50 mV (mean -210 ±84 mV) depicted strong to moderate reducing aquifer condition. The groundwater temperature was almost uniform in all samples, ranged from 24.6 °C to 28°C (mean 26 ± 0.5 °C). Electrical conductivity (EC) was varied widely from -108 to 348µS cm^{-1} (mean 188 ± 100 µS cm^{-1}) in different depths groundwater samples. The Eh (Standard Hydrogen Electrode-SHE scale) values ranged from - 188 to 150 (mean 21 ± 84 mV). In L*As*CR study area, the positive Eh_{SHE} values also depicting the mixing of groundwater from several redox zones during pumping.

The hydro-geochemical results of L*As*CR, HCO_3^-concentration was found to be in the range of 20 mg $L^{-1}$to 120 mg L^{-1} (mean 71 ± 23mg L^{-1}) which was highest among other anion concentration whereas, highest cation concentrations Ca^{+2} was found to be in the range 27 to 56 (mean 37 ± 12 mg L^{-1}) in the groundwater sample. The dissolved Fe concentration was measured in the range of 1.1 mg $L^{-1}$to 40 mg L^{-1} (mean 21 ± 9.3 mg L^{-1}) whereas Mn concentration was measured in the range of 0.1 mg L^{-1} to 2 mg L^{-1} (mean 0.7 ± 0.5 mg L^{-1}) (Table 4.2).

Additionally, other ions viz., Na^+ was in the range of 10 to 34 mg L^{-1}(mean 23 ± 6.4 mg L^{-1}),K^+ in the range of 0.1 to 23 mg L^{-1} (mean 8.1 ± 8.1 mg L^{-1}), Mg^{2+} in the range of 0.1 to 22 mg L^{-1}(mean 3.4 ± 6 mg L^{-1}), PO_4^{-3} in the range of 0.1 to 3.4 mg L^{-1}(mean 0.8 ± 1 mg L^{-1}),SO_4^{-2} in the range of 0.1 to 1.7 mg L^{-1}(mean 0.7 ± 0.5 mg L^{-1}),Cl^- in the range of 0.1 to 3.6 mg L^{-1} (mean 0.8 ± 0.8 mg L^{-1}) were detected in the groundwater samples (Table 4.2). The high concentration of PO_4^{3-} in dissolved groundwater may be due to prolonged application of

fertilizers for agricultural fields, untreated sewage or domestic solid wastes associated with large-scale human settlements and occupations. In both study area, agricultural practices and application of fertilizers are pronounced both in terms of rate and frequency and can substantially accumulate PO_4^{-3} in the soil (Mahanta et al., 2015).

The results of the combined study area viz. H*As*CR and L*As*CR groundwater samples for the year 2017 have shown in Table 4.3. In H*As*CR and L*As*CR groundwater analysis, pH was found to be in the range of 5; 5.8 to 7.3; 7 (mean 6.4 ± 0.6; 0.2). The pH values signify acidic to alkaline conditions, which were found due to the presence of alkali dolomite, birnessite, manganite with occasional jarosite and clayey minerals (Rowland et al., 2008). The ORP values were in the range of –169; –1007 mV to 143; 10 mV (mean -85; -87.2 ± 69; 104 mV) depict strong to moderate reducing conditions. The groundwater temperature was almost uniform in all samples, ranging from 22°C to 29.8; 26°C (mean 24.6 ; 23.2°C ± 2.7; 0.8°C) respectively. Electrical conductivity (EC) was found in wide range from – 64; 30 µS cm^{-1} to 1060; 953µS cm^{-1} (mean 461; 205µS cm^{-1} ± 290.6; 108.7 µS cm^{-1}) in different depths groundwater samples. The Eh (StandardHydrogen Electrode-SHE scale) values were ranged from - 31; 42.7 mV to 343; 210.4 mV(mean 116; 122.5 mV ± 69; 36.4 mV). Heavy metals such as Cr was in the range of bdl to 0.1 mg L^{-1}(mean 0.1 and bdl ± bdl mg L^{-1}) in HAsCR

Table 4. 1 Hydro-geochemical parameter of H*As*CR groundwater samples (*n=215*) unit is mg L^{-1}.

	Tapatari (*n=126*)					Boitamari (*n=61*)					Srijangram(*n=28*)				
	Min	**Max**	**Mean**	**Median**	**SD**	**Min**	**Max**	**Mean**	**Median**	**SD**	**Min**	**Max**	**Mean**	**Median**	**SD**
pH	6.4	8.8	7.2	7.1	0.4	5.6	8.7	6.8	6.8	0.7	6.1	7.8	7	7	0.5
Temperature (°C)	24.2	26.1	25.2	25.2	0.2	23.1	27.5	25.4	25.3	0.8	24.2	26	25.2	25.2	0.6
EC (µS cm^{-1})	104	986	528.3	546	215	39.5	963	550	604	258.5	137	860	439.8	367	210.6
DO (mg L^{-1})	0.6	2.4	1	1	0.3	0.6	1.8	1	1.2	0.2	0.6	2.1	1.2	1.2	0.2
ORP (mV)	-366.7	-28.8	-182.3	-190.5	71.6	-376.1	-70	-174.1	-164.8	59.5	-289.4	-60.5	-163.7	-156.1	74.4
Eh (mV)	-166.7	171.2	17.7	9.5	72	-176.1	130	26	35.2	59.5	-89.4	139.5	36.3	44	75
***As*[a]**	8.1	352.7	55.1	38	45.4	0.3	66.2	18.7	10.7	16.8	0.1	170.7	18	7.8	34.3
TDS	197.4	468.4	276.7	278.2	52.1	100	888	211.3	138.3	160	204.2	502.4	341	344.3	92.6
Ca	13.7	110.6	45	41.7	20.1	4.2	101.6	46.8	44.8	21.6	5.6	86.3	45.2	44.5	16.8
Na	3	61.2	17.5	13.1	13.8	2.6	51.6	18	15.1	13	4.4	63.3	27.1	26.7	13.8
K	0.3	62.5	12	6.5	12.2	0.6	42.5	16.6	15.6	11	1	27.2	11.3	8.6	7.1
Cl^-	0.1	5	1.2	0.7	1.1	0.1	3.3	1	0.8	0.8	0.1	2.5	1	0.6	0.8
Fe	2.3	72.3	38	38.6	17.5	2.4	68.6	25	20	20.3	1.1	83.4	21	17.5	16.5
Mn	bdl	2.4	1	1	0.5	bdl	2.8	1	1	0.7	0.2	2.8	1	1	0.6
Mg	0.1	53.8	17.6	16.4	12.5	0.1	37	10.3	6.5	10.1	0.1	37	14.3	10.2	12.2
SO_4^{-2}	bdl	4	2	2	1	0.1	4.3	1.7	1.6	0.8	0.1	5	1.7	1.3	1
HCO_3^-	40	221.3	90	80.1	35.6	42.2	163	90.2	86.1	31	53.3	152.3	96.7	97.4	29.5
PO_4^{-3}	0.3	6	3	2.5	1.5	0.1	6	2.6	2	1.6	0.3	5.5	2	1.8	1.2

Note: 'a' indicates concentration unit is µg L^{-1}

Table 4. 2 Hydro-geochemical parameters of L*As*CR groundwater samples (n=68) unit is mg L^{-1}.

	Pub-Mangaldai(*n=20*)					Pachim Mangaldai(*n=31*)					Sipajhar(*n=17*)				
	Min	**Max**	**Mean**	**Median**	**S.D**	**Min**	**Max**	**Mean**	**Median**	**SD**	**Min**	**Max**	**Mean**	**Median**	**SD**
pH	6.2	6.6	6.4	6.5	0.1	6.2	7.5	6.6	6.5	0.3	6.7	7.6	7.1	7	0.3
Temperature (°C)	25	27	26	26	0.5	24.6	28	25.6	25.4	0.7	25	26.8	25.7	25.7	0.5
EC (µS cm^{-1})	11	298	140.5	105	100.4	32	348	188	207	87	-108	210	136	173	87.4
DO	0.1	2.1	1.1	1.3	0.6	0.1	3.3	1.5	1.5	1	0.1	5	1.6	1.1	1.7
ORP (mV)	-289	-121	-210.2	-217	48.7	-388	-50	-184	-167	84	-353	-90	-179	-162	70
Eh (mV)	-89	79	-10.2	-17	48.7	-188	150	16	33	84	-153	110	21	39	70
As [a]	3.6	84.6	35	33	24	4	66.5	38.4	36.8	16.6	0.6	21.7	8.7	8.1	7
Na	10.1	32.4	20.2	19.7	6.4	10.4	30	20	18.4	5.3	11.5	34.1	23.3	22.6	6.3
K	0.1	23	8.1	6.3	8.1	0.1	11	1	0.4	2	1	2	1.4	1.5	0.2
Ca	5.3	55.7	36.5	37.1	12.1	19	45.3	34.3	35	6.1	27.1	41	33.2	32.6	3.8
SO_4^{-2}	0.1	1.7	0.6	0.5	0.5	0.1	1.5	0.7	0.6	0.4	0.1	1.2	0.6	0.7	0.4
Cl^-	0.1	3.6	0.4	0.2	0.8	0.1	3	0.7	0.4	0.7	0.1	2.2	0.8	0.6	0.6
HCO_3^-	20	120	70.7	70	23.1	41	73	57	55	7.7	42	76	60	62	9.3
Fe	9.8	39.7	21	18.6	9.3	2.6	18.5	11	11.3	3.7	1.1	8.7	4.8	4.2	2.4
Mn	0.1	2	0.7	0.5	0.5	0.1	1	0.5	0.4	0.3	0.2	1	0.5	0.4	0.3
Mg	0.4	22	3.4	1.2	6	0.1	1.8	0.7	0.6	0.5	0.1	2	1.2	1.3	0.5
TDS	70.8	149.1	119	130	23.5	90	174.1	125.7	122.8	24.5	81.4	190	111.4	105	29.2
PO_4^{-3}	0.1	3.4	0.8	0.5	1	0.1	1.4	0.3	0.2	0.3	0.1	2.1	0.6	0.1	0.7

Note: 'a' indicates concentration unit is µg L^{-1}

Table 4. 3 Hydro-geochemical parameters of groundwater samples.

	H*As*CR (*n= 110*)					L*As*CR (*n=90*)				
	Min	**Max**	**Mean**	**Median**	**SD**	**Min**	**Max**	**Mean**	**Median**	**SD**
pH	5	7.3	6.4	6.7	0.6	5.8	7	6.4	6.4	0.2
ORP (mV)	-169	143	-85	-103.2	69.1	-1007	10.4	-87.2	-77.2	104
Eh (mV)	31	343	116	97	69	42.7	210.4	122.5	123	36.4
Temperature (°C)	23	29.8	24.6	25	2.7	22	26.1	23.2	23	0.8
EC(µS cm^{-1})	64.0	1060	461	524	290.6	30	953	205.3	177	108.7
TDS	35.2	583	254	288	159.8	17	524	113	98	59.8
***As*[a]**	bdl	36.3	12.4	9	10.3	bdl	56.1	15	10.4	13.1
Fe	0.1	23.1	8	5.4	7.1	bdl	81.5	17	12	15.7
Mn	bdl	3.2	0.5	0.4	0.6	bdl	3	0.6	0.1	0.8
Mg	3	97	28	27.3	17.4	2.7	72.5	15.3	13.2	9.1
Pb	bdl	0.4	0.1	0.1	0.1	bdl	3.4	0.5	0.2	0.8
Cr	bdl	0.1	0.1	0.1	bdl	bdl	0.1	bdl	bdl	bdl
Cu	bdl	0.1	bdl	bdl	bdl	bdl	0.5	0.2	0.2	0.2
HCO_3^-	bdl	580	136.4	118	102	34	482	143	108	90
Na	bdl	127.3	28.7	24.6	24.1	2.1	38	12.1	10.2	7.7
Ca	bdl	288.1	70.6	67.6	45.2	14.2	398	117.1	90	81
K	bdl	85.7	16.1	11	18.3	0.2	25	3.2	1.7	4.2
F^-	bdl	0.6	bdl	bdl	0.1	bdl	1.6	0.3	0.2	0.4
Cl^-	bdl	45.3	5.6	2.5	7.7	bdl	0.6	2.1	bdl	2.5
NO_3^-	bdl	75.3	3.6	bdl	11.2	bdl	7.4	1.2	bdl	2
NO_2^-	bdl	9.7	1.4	1.4	134.1	bdl	8	1	bdl	2
PO_4^{-3}	bdl	35.3	2	bdl	1.8	bdl	2.3	0.3	bdl	1
SO_4^{-2}	bdl	30.2	2.7	bdl	6	bdl	29	4.6	2.8	6.4

Note: 'a' indicates concentration unit is µg L^{-1}

The hydro-geochemical results of L*As*CR, HCO_3^- concentration was found to be in the range of bdl; 34 mg L^{-1} to 580; 482 mg L^{-1} (mean 136; 143 ± 102; 90mg L^{-1}) which was highest among other anion concentration whereas, highest cation concentrations Ca^{+2} was found to be in the range bdl; 14.2 mg $L^{-1}$to 288; 398 mg L^{-1} (mean 70; 117 ± 45; 81 mg L^{-1}) in the groundwater sample. Low Fe concentration in H*As*CR groundwater samples can be attributed in groundwater due to alkali mineral desorption (Michael, 2008; Ujević Bošnjak et al., 2013, 2012). Normalized data of Ca^{+2}, Na^+, Mg^{+2}, and HCO_3^- were used for bivariate plots [Figure 4.1(a-f)]. These plots showed predominate three zones (viz. evaporate dissolution, silicate weathering, and carbonate dissolution) with global average groundwater composition which is further used to compare and predicate the local groundwater composition using these plots shown in different zone mechanisms. The

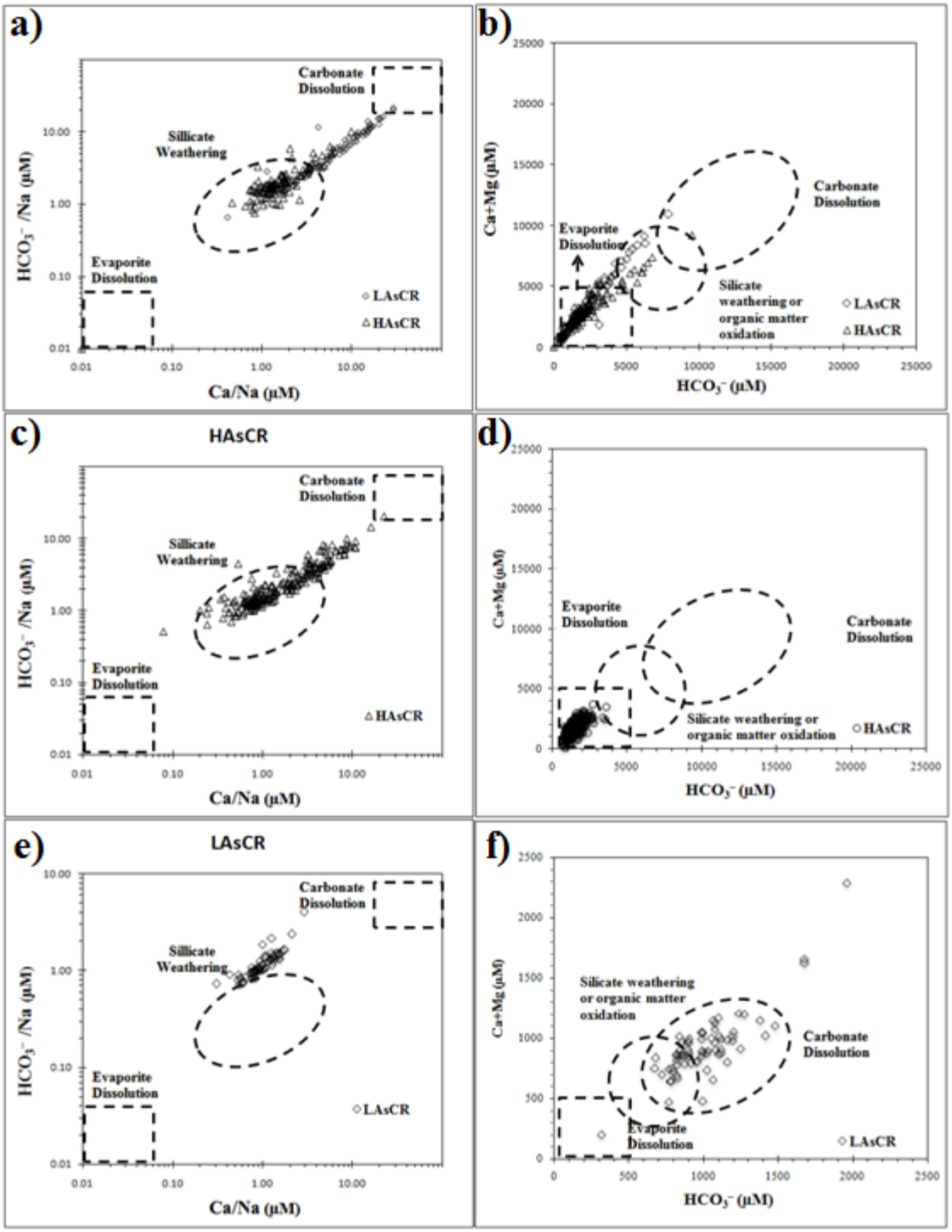

Figure 4. 1 Bi-variant plots of normalized data of H*As*CR a) Na^+, Ca^{2+} versus $HCO_3^-$and b) Ca^{2+} + Mg^{2+} versus HCO_3^- similarly, normalized data of L*As*CR showed in figure c) Na^+, Ca^{2+} versus HCO_3^- and b) Ca^{2+} + Mg^{2+} versus $HCO_3^-$for the year 2013 groundwater samples. The 2017 groundwater samples normalized data showed in the bi-variant plot of e) Na^+, Ca^{2+} versus HCO_3^- and f) Ca^{2+} + Mg^{2+} versus HCO_3^-.

bivariate plot shows a molar ratio (Mukherjee and Fryar 2008) for Ca+2/Na+ vs. HCO3–/Na+ [Figure 4.1(a), (c) and (e)] which indicate silicate mineral weathering was the predominant primary mechanism for higher bicarbonate concentration in groundwater. The average (Ca^{+2} + Mg^{+2})/HCO_3^- ratio was found to be ~0.55 in all the groundwater samples, which was comparable to another *As* contaminated regions of India(Mukherjee and Fryar 2008) and Bangladesh (Dowling et al., 2003). The dissolution of carbonate mineral in L*As*CR suggests the secondary process for alkaline groundwater in all the three studied blocks (Figure 4.1).

4.1.1 Major hydro-geochemical facies

In this study, the hydro-geochemical composition of groundwater showed with major ions composition using a trilinear diagram (also known as a Piper diagram) (Piper 1944, Winston 2000) [Figure 4.2]. Figure 4.2 (a) and (c) showed similar hydro-chemical facies Ca^{+2} – HCO_3^- and Ca^{+2} – Na^+ – HCO_3^- in H*As*CR study area. In figure 4.2 (b) and (d), L*As*CR showed Ca^{+2} – HCO_3^- and Ca^{+2} – Na^+ – HCO_3^- common in both year groundwater samples but few samples showed HCO_3^- – SO_4^{-2} – Na^+ facie in 2017 sample. The diffused hydrochemical facies: (i) shallow aquifers contain admixture of Ca^{2+}– HCO_3^- type (i.e. fresh groundwater) (ii) Ca^{2+}– Na – HCO_3^- type (i.e. cation exchange) water, (iii) whereas, Na^+– HCO_3^-– SO_4^{2-} type water shows a microbial degradation of organic matter and with cation exchange as evidenced by hydrogen sulphide is formed by the bacterial reduction of sulphate. The results were well corroborated by the previous studies performed by Mahanta et al. (2015). Henceforth, these two water facies decipher the weathering, dissolution, precipitation mechanisms, and freshwater recharge in study area aquifer. The concentration of these facies in groundwater depicts that these aquifers are replenished by the surface water bodies or direct rainwater infiltration into the shallow aquifer.

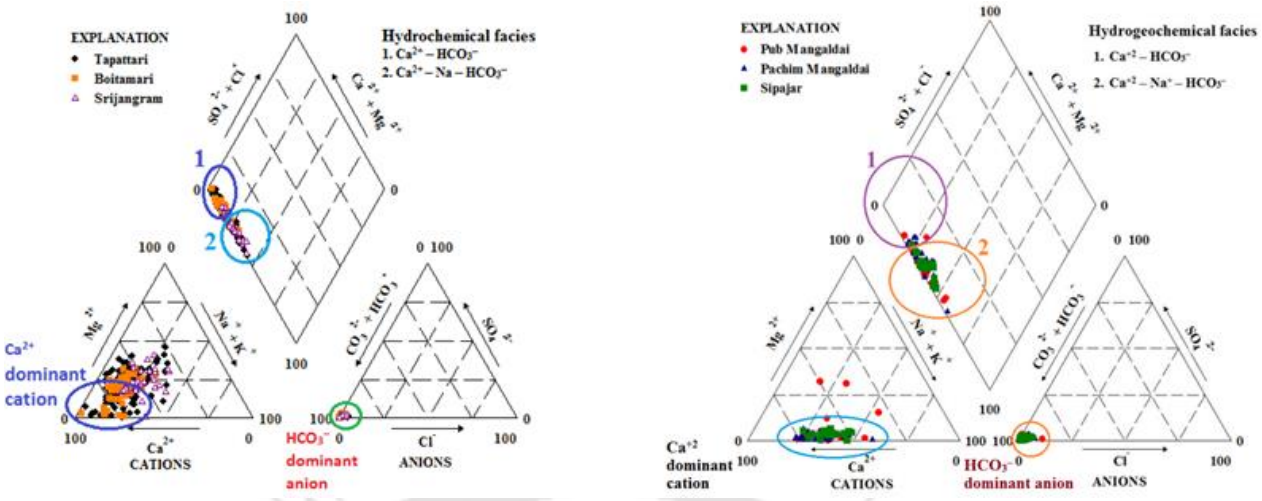

Figure 4. 2 Piper diagrams depicts predominate groundwater facies for the year 2013 [i.e. figure (a) and (b)] and the year 2017 [i.e. figure (c) and (d)] present in H*As*CR and L*As*CR study area.

4.1.2 Statistical correlation

Scatter plot for Fe vs. *As* showed significant positive values with a dissolved concentration in groundwater for both the study areas (Figure 4.3). The Pearson correlation (ρ) values observed between dissolved *As* concentration with Mn and HCO_3^- [Appendix Table A 1.1 to 1.8]. Here, the positive correlation values 0.5,0.64 and 0.69 were observed between dissolved Fe and *As* concentration in Tapatari, Boitamari and Srijangram blocks of H*As*CR groundwater samples [Appendix Table A 1.1, 1.2 and 1.3]. Similarly, in L*As*CR samples 0.65, 0.03 and 0.32 observed in Pub Mangaldai, Pachium Mangaldai and Sipajhar block samples [Appendix Table A 1.4, 1.5

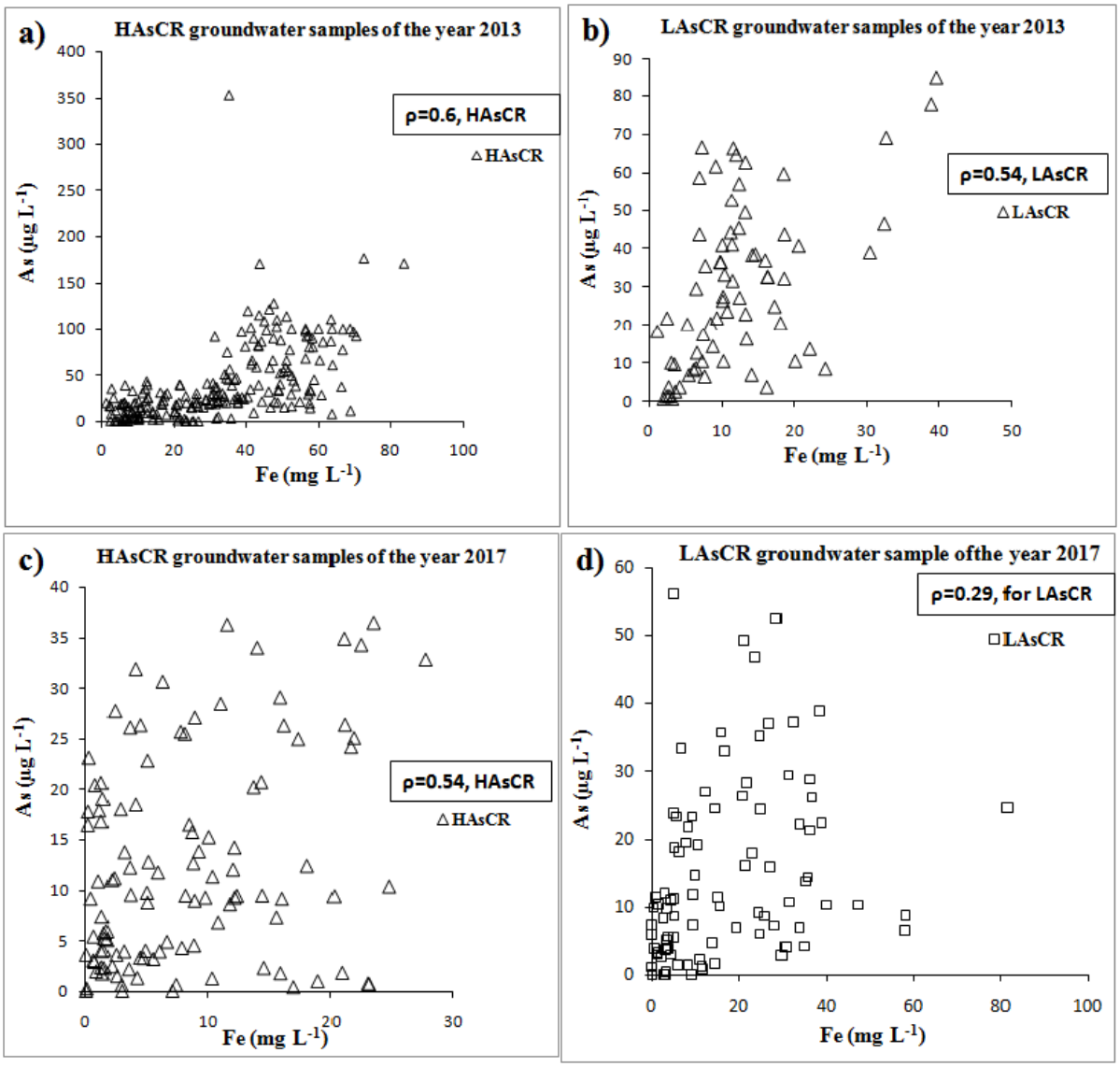

Figure 4. 3 Scatter plot of dissolved Fe and *As* concentration showed Pearson correlation values for H*As*CR and L*As*CR groundwater samples.

and 1.6]. Except the poor correlation values was observed in between *As* with Fe in Pachim Mangaldai (i.e. 0.03) and Sipajhar (i.e. 0.32) block groundwater samples, in other samples the correlation results support the reductive dissolution mechanism of Fe-oxy/hydroxide minerals for *As* mobilization in the H*As*CR and L*As*CR groundwater aquifer (McArthur et al. 2004). Furthermore, in 2013 groundwater samples, insignificant Pearson correlation values for H*As*CR

study area was observed in between dissolved *As* concentration with Mn as 0.22, -0.08 and 0.05 and HCO_3^- as -0.02, 0.34 and 0.19 observed in Boitamari, and Srijangram block, respectively. Similarly, in L*As*CR groundwater samples, correlation values for dissolved *As* with Mn as 0.41, -0.19 and 0.51 and HCO_3^- as -0.01, 0.23 and -0.25 observed in Pub-Mangaldai, Paschim Mangaldai, and Sipajhar blocks respectively.

Therefore, these lack of correlation values observed between *As* with Mn and HCO_3^- especially for Boitamari and Srijangram blocks of H*As*CR [Appendix Table A 1.2, 1.3] and all L*As*CR samples [Appendix Table A1.4,1.6] suggested that the lack of pH-dependent desorption or reductive dissolution mechanism prevailing in this groundwater aquifer whereas, positive value depicts that reductive dissolution (viz. Fe-oxy/hydroxides) mechanism mobilizes *As* at the regional scale (Mukherjee and Fryar 2008). Moreover, weak correlation values were observed between Fe and HCO_3^- as 0.31, 0.11 and -0.3 in Tapatari, Boitamari, and Srijangram block groundwater samples [Appendix Table A 1.1, 1.2 and 1.3]. Similarly, 0.37, 0.05 and -0.4 observed between Fe and HCO_3^-in L*As*CR groundwater samples of Pub Mangaldai, PaschimMagaldi and Sipajhar block respectively.

These correlation results suggest that the condition in the hydrogeochemical condition in the aquifer are favorable for precipitation of siderite, vaterite, goethite and dolomite minerals (Mahanta et al. 2015). The studies over Ganga-Meghana-Brahmaputra floodplain also observed an insignificant correlation between Fe and HCO_3^-, which suggest that non-conservative nature of siderite minerals, leading to lower dissolved iron concentration in the groundwater (Mahanta et al. 2015, Mukherjee and Fryar 2008). Similarly, in groundwater samples from the year,2017 showed a positive *As* correlation values which were observed with Fe as 0.26 and 0.28 for H*As*CR and

L*As*CR groundwater samples respectively. Likewise, *As* correlation with Mn (i.e. 0.01 & -0.2) and HCO_3^- (i.e. 0.1 & 0.2) was observed [Appendix Table A.1.7 and 1.8].

4.1.3 Minerals and gases saturation indices

Visual MINTEQ 3.1 software was used to determine the mineral saturation indices (SI) which show whether the water will tend to dissolve or precipitate a particular mineral. Table 4.4 and 4.5 enlisted the range of SI values for some of the important mineral phases present in groundwater of both study areas. The negative and positive value of SI in Table 4.4 and 4.5 signifies the presence of undersaturated and oversaturated minerals, respectively. In Table 4.4,*As*-bearing minerals mainly realgar (Avg. –58.7 & -42.4), orpiment (Avg. – 151.0 & -111.1), claudetite (Avg. –21.3 & -13) and arsenolite (Avg. –21.3 & -14.5) were found in unsaturated conditions in the year 2013 groundwater samples. Also, the other *As* and Fe associated minerals viz. chalcopyrite (Avg. –74.6 & -49.5) and pyrite (Avg. – 69.8 & -52.3) were found in the unsaturated state and which may dissolve further in the conducive environment in both the study area groundwater aquifers. Chalcocite was a new mineral observed in the year 2017 Groundwater samples compared to the year 2013 groundwater analysis samples. In Table 4.5, chalcocite (Avg. –25 & -27.3), chalcopyrite (Avg. –66.9 & -64.9) and pyrite (Avg. – 71.4 & -67.3) of *As* and Fe associated minerals were observed in the year 2017 groundwater samples.

Similarly, the other unsaturated *As*-bearing minerals such as realgar (Avg. – 55.2 & – 50.7), orpiment (Avg. – 29.3 & – 133.7), claudetite (Avg. – 17.9 & – 11.8) and arsenolite (Avg. – 17.8 & – 11.8) were also found in the year 2017 groundwater samples. The other saturated minerals of iron such as maghemite (Avg. + 5.7 & + 1.2), lepidocrocite (Avg. + 4.7 & + 2.4), magnetite (Avg. + 18.7 & + 13.5), goethite (Avg. + 5.6 & + 3.2), ferrihydrite (Avg. + 3.3 & +0.9), siderite (Avg. +

0.7 & – 0.3), vivianite (Avg. + 4.0 & – 9.3) and hematite (Avg. + 13.6 & + 8.8) were found (Table 4.4). In this analysis, only greigite (Avg. – 165.7 & -106.5), which is Fe-S bearing mineral was the highest unsaturated mineral found amongst the other minerals (Table 4.4) in year 2013groundwater samples of H*As*CR and L*As*CR study area. Results obtained from the geochemical modeling showed that SI values were observed near to saturation for Fe (III) and Mn- oxy/hydroxides minerals in a varying dissolved concentration. The Figure 4.4 a), b) and c) showed bivariate plots for the modeled SI values for rhodochrosite, vivianite and siderite minerals versus dissolved concentration of Fe and Mn in the H*As*CR and L*As*CR groundwater. The figures signify that the minerals saturation trend in the grey color aquifer of H*As*CR was higher than the grey color aquifer of L*As*CR groundwater samples. In Appendix Figure G 1.1 (a–c) siderite minerals showed clear precipitation in both study areas than rhodochrosite and vivianite minerals.

Thus, it further inferred that high adsorption capacity of siderite was the cause for low *As* concentration in L*As*CR groundwater samples (Guo et al., 2013, 2007; Zhao et al., 2014). Moreover, average partial pressure values for dissolved gases were observed in decreasing order of CO_2> H_2 > NH_3 > O_2 > H_2S > CH_4 that showed nearly equilibrium condition. In 2013 groundwater samples, significant average positive value of CO_2 (Avg. + 0.27 & + 0.038) was observed, whereas in 2017, comparatively high CO_2 (Avg. + 6.00 & +4.00) gas value was observed in Table 4.4 and 4.5. It suggests that input from the organic matter oxidation and carbonate mineral dissolution is the primary cause for high CO_2 in groundwater (Mukherjee and Fryar 2008). In the year 2017 groundwater of the study area is in highly undersaturated condition for *As*-bearing minerals such as realgar,orpiment, claudetite, and arsenolite. Except the saturated minerals of iron

Table 4. 4: Summary of saturation indices (SI) calculated by Visual MINTEQ showed possible mineral phases for 2013 groundwater samples

	HAsCR (n = 215)			LAsCR (n = 68)		
Mineral	**Min.**	**Max.**	**Average**	**Min.**	**Max.**	**Average**
Aragonite	-1.5	1.2	-0.5	-24.1	-0.1	-2.2
Arsenolite	-43.9	-10.5	-21.3	-124.2	-6.6	-14.5
Artinite	-20.4	-3.4	-8.3	-14.3	-1.3	-10.9
$As_2O_5(s)$	-37.2	-26.6	-31.6	-59.6	-2.0	-30.6
$As_2S_3(am)$	-295.8	-61.9	-152.4	-300.0	-9.5	-110.8
Atacamite	-31.0	-23.2	-26.0	-43.9	-3.2	-16.6
Azurite	-39.8	-29.0	-32.6	-52.9	1.6	-18.6
Birnessite	-31.7	-8.6	-20.6	-40.6	-2.7	-25.4
Calcite	-1.4	1.3	-0.3	-10.4	0.0	-1.7
Chalcanthite	-22.5	-18.5	-19.9	-19.2	-9.5	-11.3
Chalcopyrite	-155.1	-23.9	-74.6	-152.1	18.5	-49.5
Claudetite	-43.9	-10.5	-21.3	-40.3	-6.6	-13.0
Dolomite	-7.4	2.4	-1.0	-19.5	-1.4	-7.8
Ferrihydrite	-0.9	7.1	3.3	-4.0	6.3	0.9
Goethite	1.6	9.3	5.6	-1.9	8.5	3.2
Greigite	-322.2	-65.6	-165.7	-333.8	-1.5	-106.5
Gypsum	-5.0	-2.9	-3.4	-14.2	-2.9	-4.7
Hematite	5.5	20.9	13.6	-1.4	19.4	8.8
Lepidocrocite	0.7	8.4	4.7	-2.9	7.6	2.4
Maghemite	-2.4	13.1	5.7	-9.4	11.6	1.2
Magnesite	-7.8	-0.1	-1.9	-10.6	-2.1	-3.5
Magnetite	9.6	28.7	18.7	2.3	22.1	13.5
Manganite	-19.5	-4.3	-11.6	-25.7	15.1	-14.9
Orpiment	-294.4	-60.5	-151.0	-298.6	-8.1	-111.1
Pyrite	-142.4	-22.6	-69.8	-147.1	7.2	-52.3
Realgar	-115.1	-23.8	-58.7	-116.5	-3.9	-42.4
Rhodochrosite	-8.6	-2.4	-4.2	-12.3	0.7	-6.4
Siderite	-2.2	2.5	0.7	-10.3	1.4	-0.3
Vaterite	-1.9	0.7	-0.9	-10.4	-0.5	-2.3
Vivianite	-4.7	8.6	4.0	-56.9	4.6	-9.3
Gas partial pressure	**Min.**	**Max.**	**Average**	**Min.**	**Max.**	**Average**
O_2 (g)	7.8E-60	8.3E-20	6.7E-22	1.3E-64	6.4E-47	2.2E-48
H_2 (g)	2.0E-22	2.2E-12	7.9E-14	2.1E-19	9.3E-11	2.7E-12
CH_4 (g)	1.0E-65	4.2E-25	1.3E-26	5.6E-54	2.2E-19	6.3E-21
CO_2 (g)	1.1E-03	2.7E-01	4.3E-02	1.1E-02	9.8E-02	3.8E-02
H_2S (g)	5.0E-65	1.7E-22	3.3E-24	9.2E-63	9.5E-28	2.7E-29
NH_3 (g)	8.3E-22	5.3E-19	3.8E-20	1.1E-21	9.1E-21	4.7E-21

Note: S- Solid phase, am – amorphous phase

Table 4. 5 : Summary of saturation indices (SI) calculated by Visual MINTEQ showed possible mineral phases for 2017 groundwater samples

Minerals saturation Index	HAsCR (*n* = 110)			LAsCR (*n* = 90)		
	Max.	**Min.**	**Avg.**	**Max.**	**Min.**	**Avg.**
Aragonite	-6.2	-0.4	-2.2	-5.3	-0.6	-2.1
Arsenolite	-33.8	-12.6	-17.8	-19.8	-6.6	-11.8
Birnessite	-32.6	-11.6	-19.7	-31.9	-16.5	-20.8
Calcite	-6.1	-0.3	-2.1	-5.1	-0.5	-1.9
Chalcocite	-68.4	-3.7	-25	-54.5	-9.3	-27.3
Chalcopyrite	-139.3	-28.8	-66.9	-102.3	-32	-64.9
Claudetite	-33.8	-12.6	-17.9	-19.9	-6.6	-11.8
Dolomite	-11.2	-0.1	-3.7	-10	-1.3	-3.5
Ferrihydrite	-9.7	5.7	1	-11.4	3.6	0.9
Goethite	-9.6	8	3	-9.2	5.8	3.4
Greigite	-307.2	10.1	-167.8	-241	-82.7	-161.3
Hematite	-43.4	18.3	7.8	-15.9	14	9.2
Lepidocrocite	-8.4	7.1	2.2	-10	5	2.6
Mackinawite	-81.8	-9.2	-45.5	-64.2	-21.9	-43.5
Maghemite	-23.5	10.6	0.5	-23.5	6.4	1.6
Magnesite	-45.7	-0.9	-3.5	-6.1	-1.9	-2.7
Magnetite	-22.4	22.6	11.6	-24.2	19.2	12.9
Manganite	-22.7	-5.7	-10.1	-21.1	-7.3	-11.1
Jarosite	-49.4	-6.6	-29.3	-50.7	-6.3	-23.1
Orpiment	-272.5	-13.9	-144.4	-204.8	-66.7	-133.7
Pyrite	-136.7	-26.3	-71.4	-105.7	-31.9	-67.3
Realgar	-104.5	-5.2	-55.2	-77.4	-24	-50.7
Rhodochrosite	-13.6	1.2	-1.9	-11.8	0.2	-2.8
Siderite	-11.9	1.7	-0.9	-12	1.4	-0.4
Vaterite	-22.7	-0.8	-3	-5.7	-1.1	-2.5
Vivianite	-54.8	8.4	-16.7	-56.2	3.9	-17.9
Wurtzite	-80.2	-2.5	-42.7	-64.4	-28.7	-44.6
Gas partial pressure	**Max.**	**Min.**	**Avg.**	**Max.**	**Min.**	**Avg.**
O_2	1E-03	5E-06	1E-04	1E-06	6E-05	2E-05
H_2	1E+00	2E-03	2E-02	2E-02	9E-01	2E-01
CH_4	1E-03	7E-08	1E-03	6E-05	2E-02	5E-02
CO_2	5E+00	5E-01	6E+00	3E-01	1E+01	4E+00
H_2S	9E-03	3E-09	9E-03	9E-06	9E-03	2E-03
NH_3	3E-02	1E-02	9E-02	1E-02	1E-02	5E-02

Note: S- Solid phase, am – amorphous phase

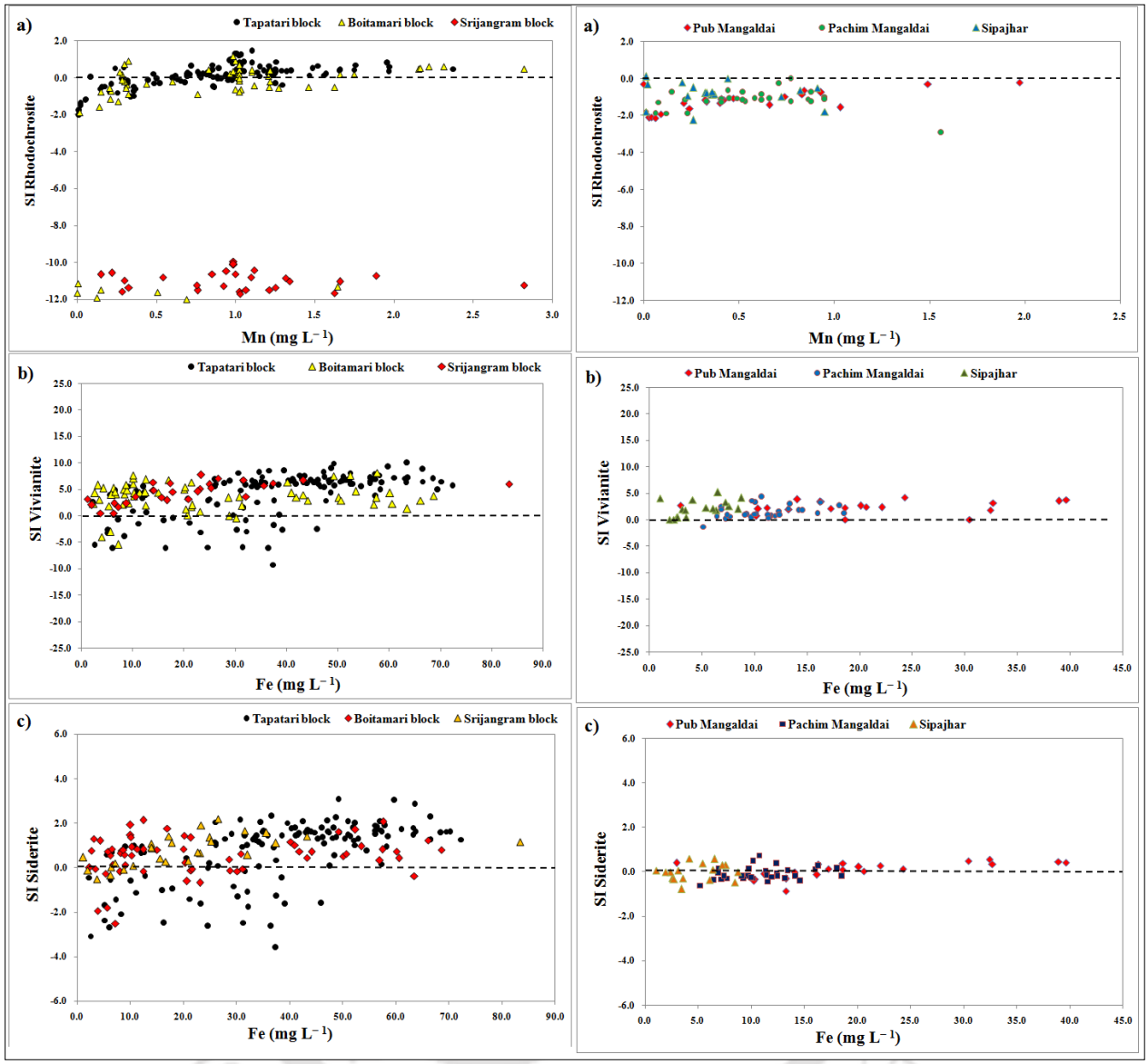

Figure 4. 4 Bivariate plots showed the modeled SI values dependency for a) rhodochrosite vs Mn b) vivianite vs Fe c) siderite vs Fe on dissolved Fe and Mn concentration measured in the 2013 year groundwater samples.

Bearing minerals such as maghemite (Avg. + 0.5 & + 1.6), lepidocrocite (Avg. + 2.2 & + 2.6), magnetite (Avg. + 11.6 & + 12.9), goethite (Avg. + 3.0 & + 3.4), ferrihydrite (Avg . + 1.0 & + 0.9) and hematite (Avg. + 7.8 & + 9.2) no other significant minerals were observed in the 2017 groundwater samples in the saturation state. The highly unsaturated greigite (Avg. – 167.8 & –161.3) mineral was observed in2017 groundwater sample (Table 4.5). Other *As* associated

minerals viz.chalcocite (Avg. –25 & – 27.3), chalcopyrite (Avg. – 66.9 & – 64.9) and pyrite (Avg. – 71.4 & –67.3) were observed in an unsaturated state which are more susceptible to occur in dissolved state in the present conducive aquifer condition (Appendix Figure G 1.1). The saturation index value of carbonate-bearing minerals viz. calcite (Avg. – 2.1 & – 1.9), siderite (Avg. – 0.9 & – 0.4) and vaterite (Avg. – 1.97 & – 17.9) signify that they are in the chemically imbalanced state and are primary cause for alkaline pH for the study area groundwater (Table 4.5).

4.2 Sediment analysis

4.2.1 Munsell color and grain size classification

The order of Munsell color systems helped to develop a logical relationship to distinguish and identify different soil horizon (viz. oxidized and reduced aquifer condition) into a group of soil taxonomy. According to the Munsell sediment color classification, the sediments samples were further classified into 32 and 41 hues (Biswas et al. 2014a, Mahanta et al. 2015) classes. Distinct Munsell color variation or pattern was observed in H*As*CR and L*As*CR aquifer sediments (Figure 4.5a, 4.5b). It also provides a clue for the presence of different mineral content in sediment aquifer depth.

In H*As*CR region, the aquifers near to Manas river were dominated with dark grey to grey color sediments, whereas area near to the hillocks predominantly contains reddish brown to yellow sediment color. In L*As*CR region, even the major study areas near the Brahmaputra river showed comparatively distinct patchy brown, greenish-grey, pale-blue and white color sediments than the H*As*CR study area. Especially in well M1 and M2, a thick 30 feet (depth < 100 feet) layer of brown and white medium sand was observed. It suggests that the rapid

depletion of groundwater table may be due to high pumping rate for irrigation wells or public water supply wells in the high yielding capacity of the aquifer which causes precipitation of ferrous iron deposition over the sediment surface locally.

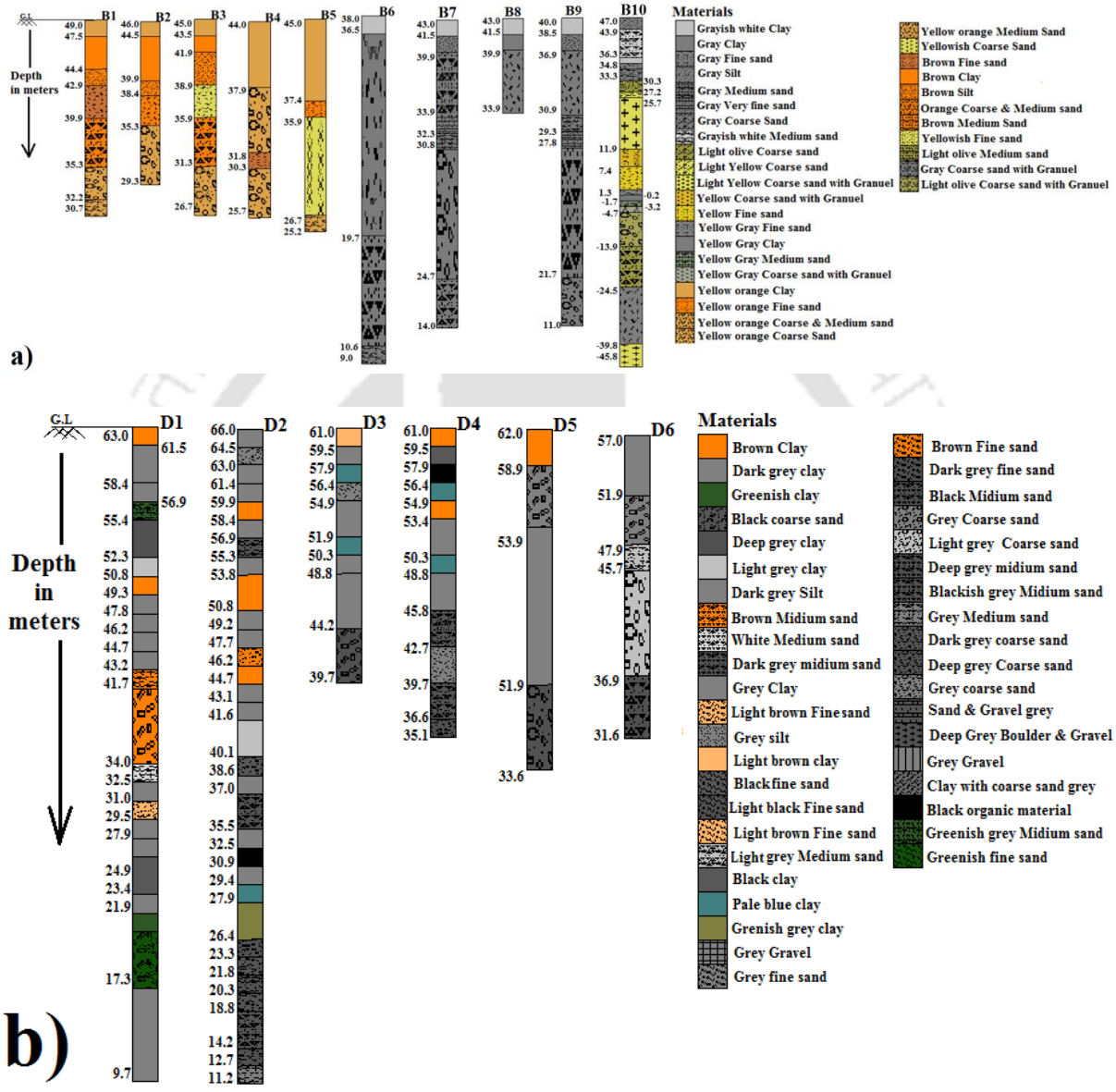

Figure 4. 5 showed detailed lithology for respective wells recorded according to Munsell color classification and texture of sediments a) H*As*CR study area and b) L*As*CR study area samples.

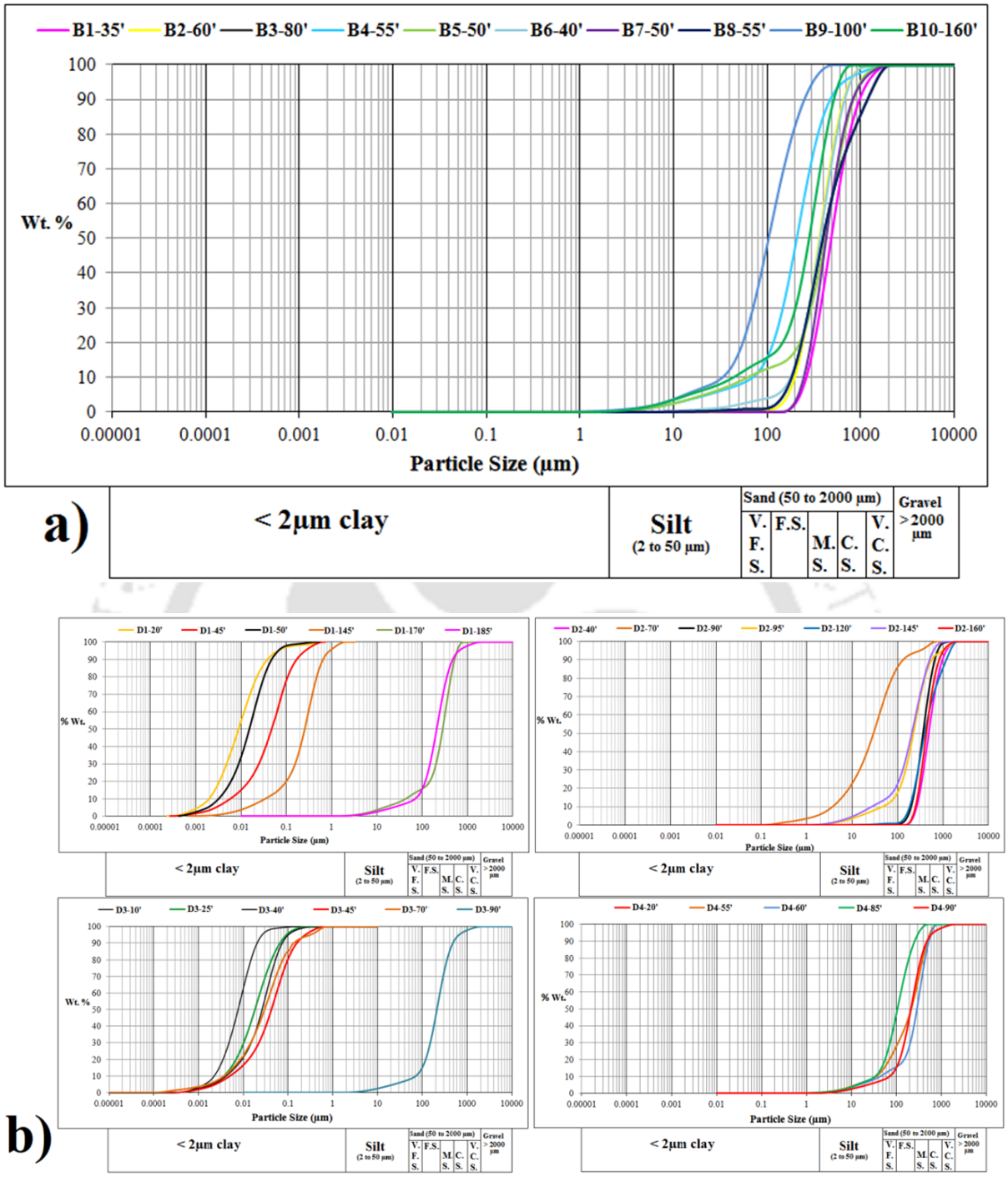

Figure 4. 6 a) and b) showed particle size distribution curves for selective depth sediment samples from H*As*CR study area and b) L*As*CR study area by using laser particlesize analyzer

The yellow to reddish brown color classified sediments samples, predominantly at shallow depth, suggest the precipitation of iron (i.e. ferric form) over sediment particles and suggest a strong oxidation condition prevailing at the shallow depth aquifer. Whereas, blackish, grey, dark grey sediment depicts the presence of high manganese-bearing minerals and organic matter decomposition by the microbiological community which affects on the sediment color at the shallow and deeper depth aquifers. The differentiated sediment colors according to Munsell color code suggested that yellow-brown color of the sandy aquifer is a part of Pleistocene age sediment, whereas grey color sediment suggests Holocene age sediment deposit (Ravenscroft et al. 2005, von Brömssen et al. 2007).

The collected sediments were texturally classified into five class (viz. clay, fine sand, medium sand, coarse sand, and granule) and verified using the LPSA method. The obtained results by LPSA method were plotted on a logarithmic scale (Figure4.6a and 4.6b). The distribution curves for each sediment samples from H*As*CR and L*As*CR study areas were classified according to the U.S Geological survey. The distribution curves in Figure 4.6a) and 4.6b) resembles the alluvium soil distribution curves (Todd and Mays 2005). The distribution curves for H*As*CR sediment samples suggest that they are uniformly graded silty-sandy samples (Figure 4.6a and 4.6b). Similarly, the L*As*CR sample analysis suggested the presence of uniformly graded silty-sandy aquifer sample (Figure 4.6b), whereas top (6 m to21 m) and intermediate layer (~ 44 m) suggest the presence of clayey aquiclude over the aquifers. These results were well corroborated with the recorded lithological data on-field during sediment sample collection. The experimental results showed that the light yellow color coarse sand which was exposed to the H_2S gas for 10 min turned to grey color [Figure 4.7 (a–b)]. It could further be concluded that these aquifers were vulnerable for the precipitation of Fe−S−*As*

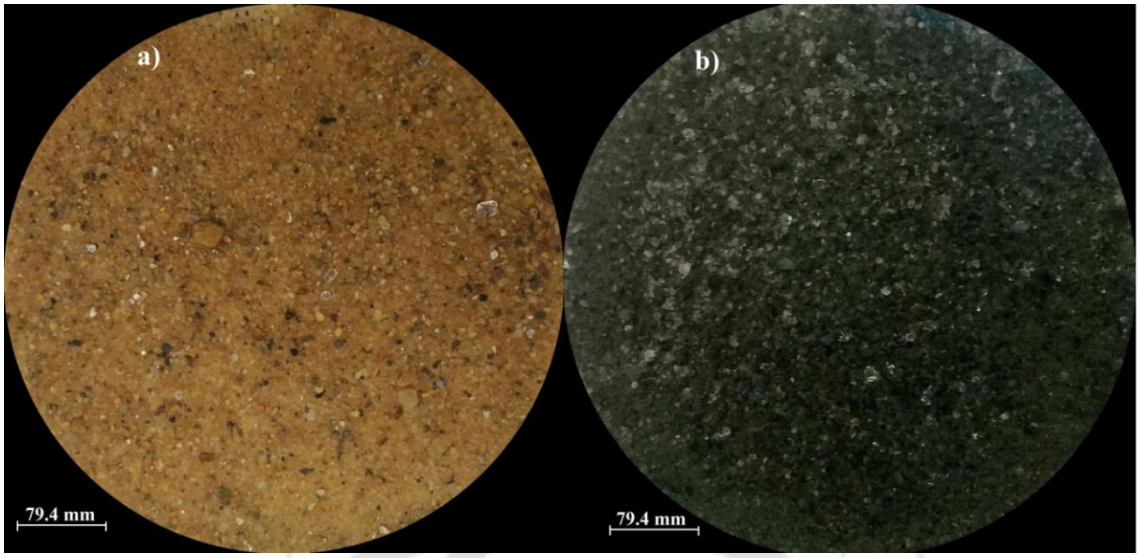

Figure 4. 7 Photographic images of the chemical reaction showed results a) brown colored sediment before experiment b) and after exposing to H_2S gas for 10 minutes.

bearing minerals.

In addition, the aforesaid results also well supported with the presence of low dissolved SO_4^{-2} concentration in shallow aquifer groundwater samples. The sediment samples exposed to H_2S gas, have hypothesized that brown color sand was surface coated by sulfide was the cause for the formation of grey color sand (Hagiwara et al., 2011). Thus, the result inferred that the presence of predominant grey color sandy-clayey at the shallow aquifer was susceptible to color change with respect to the presence of solid phase sulfide in the aquifer.

4.2.2 Sediment pH, TOC and Cation Exchange Capacity

The sediment pH was assessed according to NRCS (1993) classification. It was in the range of strongly acidic (i.e. 5.1) to slightly alkaline (i.e. 7.8) condition (Figure 4.8). A distinct pH was observed in different sediment color. The grey color sediment was observed as acidic (i.e. 5.1) to alkaline (i.e. 7.3) pH condition whereas reddish color sediment was acidic to slightly alkaline (i.e. 7.8) pH condition.

The depth profiles of different sediment pH have shown that shallow depth sediment was acidic in nature, whereas increasing pH trend was observed as the depth increases. The

alkaline sediment results suggested the recharge from the rainfall or surface water bodies, can replace the H^+ ions from the sediment surfaces whereas, acidic sediment condition is more susceptible for exchangeable aluminum, carbonic and organic acids and replace OH^+ ions from sediment surface (Cole, 1957). The above observation suggests that the wide range of sediment pH can increase the solubility of pure elements from sediment to groundwater.

In H*As*CR sediments, high total organic carbon (TOC) content (9%) was observed in grey color clayey–silty–sandy sediment in the shallow depth samples whereas low content (0.35%) was quantified in brownish–reddish color sediment samples (Figure 4.8). In L*As*CR sediments, high TOC content (9.1%) was observed in M2 well (145 feet depth) sample, whereas low content (1.1 %) was observed in M1 (80 feet depth) well sediment sample. Sediment near the river in H*As*CR was rich in TOC content compared to L*As*CR sediment sample. Moreover, the region which is far from the river bank and high in elevation was found to have more reddish color sediment and low in TOC content. It suggested that the aquifer have significant flushing capability than lower elevation region. The content of TOC indicates the presence of freshly deposited leaves, twigs, branches by river water and sediments in the study area aquifer. In the analyzed sediment samples, the highest TOC content of 9.5 % was measured for H*As*CR samples in fine sand sample (viz. yellow-grey colored) of well B10 (at155 feet), whereas, the lowest content (i.e. 0.17%) was measured at 55 feet in the coarse sand (viz. yellowish) aquifer sediment of B5 well (Figure 4.8). Similarly, for L*As*CR sediment samples, 1.1% (minimum) and 9.1 % (maximum) TOC content was measured in the brown and olive black fine sand samples respectively. Higher TOC content was observed in the grey colored fine sand samples compared to yellow-brown sand samples. Moreover, as the depth increases, TOC content was found to be low in the analyzed well sediment samples (Figure 4.8). The high concentration of TOC was observed in H*As*CR (i.e. 6 %) sample than the

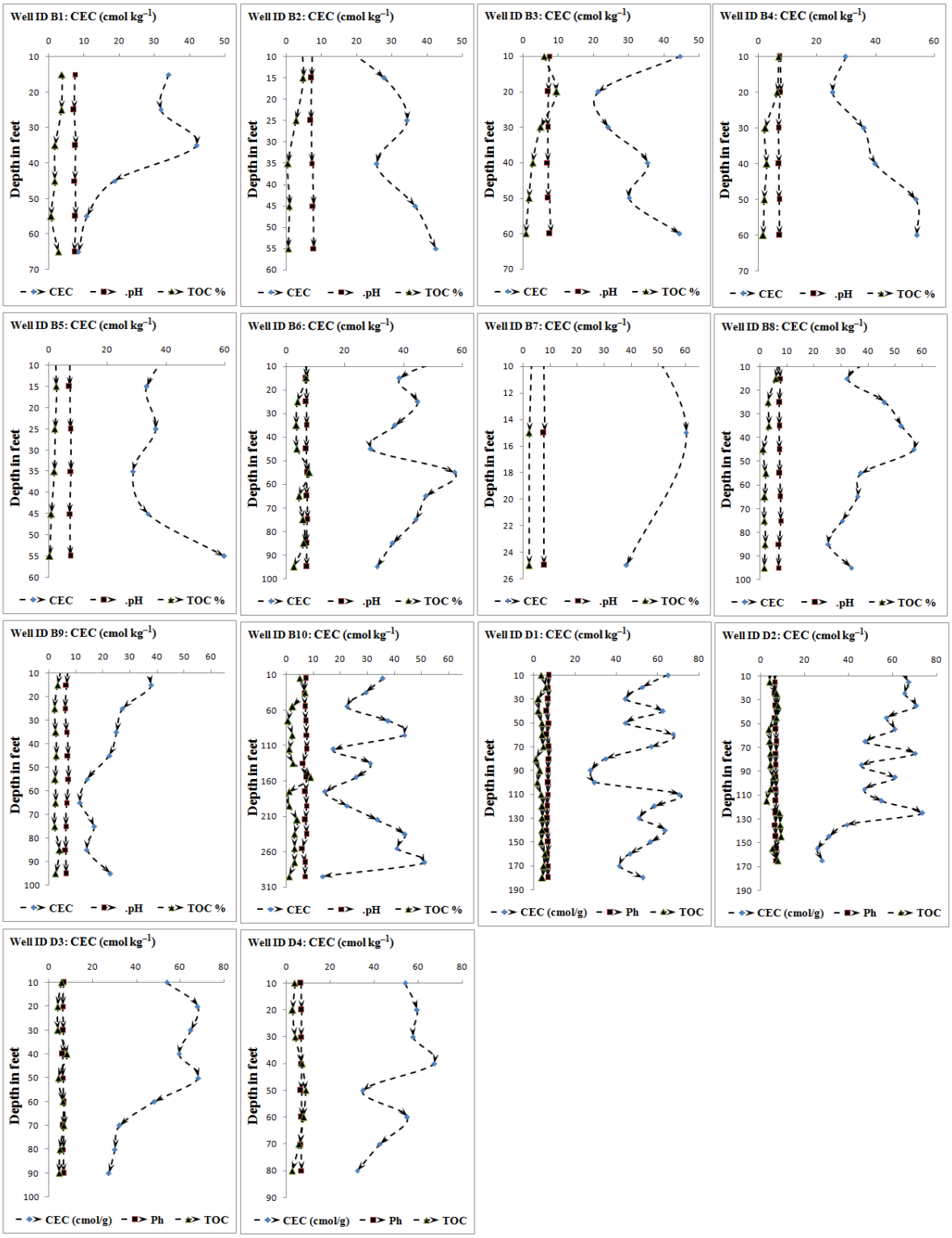

Figure 4. 6 depth wise profile of sediment pH, TOC, and Cation Exchange Capacity.

L*As*CR (i.e. 4.8 %) (Appendix Table A 3.1) sediment sample. The highest concentration was observed in grey color medium sand sediment in H*As*CR whereas in L*As*CR high concentration was observed in grey color fine sand sediment. Grey color sediment aquifer contains high *As* and Fe in groundwater which was caused by prevailing Fe oxy/hydroxides reduction in the shallow aquifer. Brown color on aquifer sediment caused by oxidation of aquifer sediment due to lowering of groundwater level and flushed with oxic water. It further a causes low concentration of *As* and Fe in groundwater (Biswas et al., 2014).

The average concentration of soluble and bound cations 6.5, 13.2, 1.9, 2.53 (in cmol kg^{-1}) and 105.2, 266.1, 28.4, 37.7 (in cmol kg^{-1}) respectively, were measured for Na^{+}, Ca^{+2}, K^{+} and Mg^{+2} cations respectively in H*As*CR sediment samples (Appendix Figure B 3.1,3.2). Similarly, in L*As*CR, the average concentration of soluble and bound cations of respective Na^{+}, Ca^{+2}, K^{+} and Mg^{+2} was 5, 10.7, 1.7, 2.1 (in cmol kg^{-1}) and 64.0, 481.1, 10.2, 8.2 (in cmol kg^{-1}) (Appendix TableB2.1, 2.2). The result shows that bound cations concentration was higher than soluble cations. Highest Ca^{+2} dissolved concentrations were measured in both the study areas than the other cations (Figure 4.8). These results suggest the predominance of calcium carbonate minerals as a possible cause for high calcium and bicarbonate concentration in the groundwater aquifers both the study regions. The results of CEC of selective depth sediment was well corroborated with some depth samples which suggests that the presence of organic carbon, other minerals dissolution have an equal role in controlling the cation exchange capacity in groundwater aquifer condition. The 2D scatter plot showed a Pearson correlation between dissolved *As* and Fe concentration in groundwater (Figure 4.9). Negative Pearson correlation values (viz. B1, B2, B5, B6, B7, B8, B9 and B10 in H*As*CR groundwater samples) indicate dissolution of iron-bearing minerals in groundwater aquifers and positive values

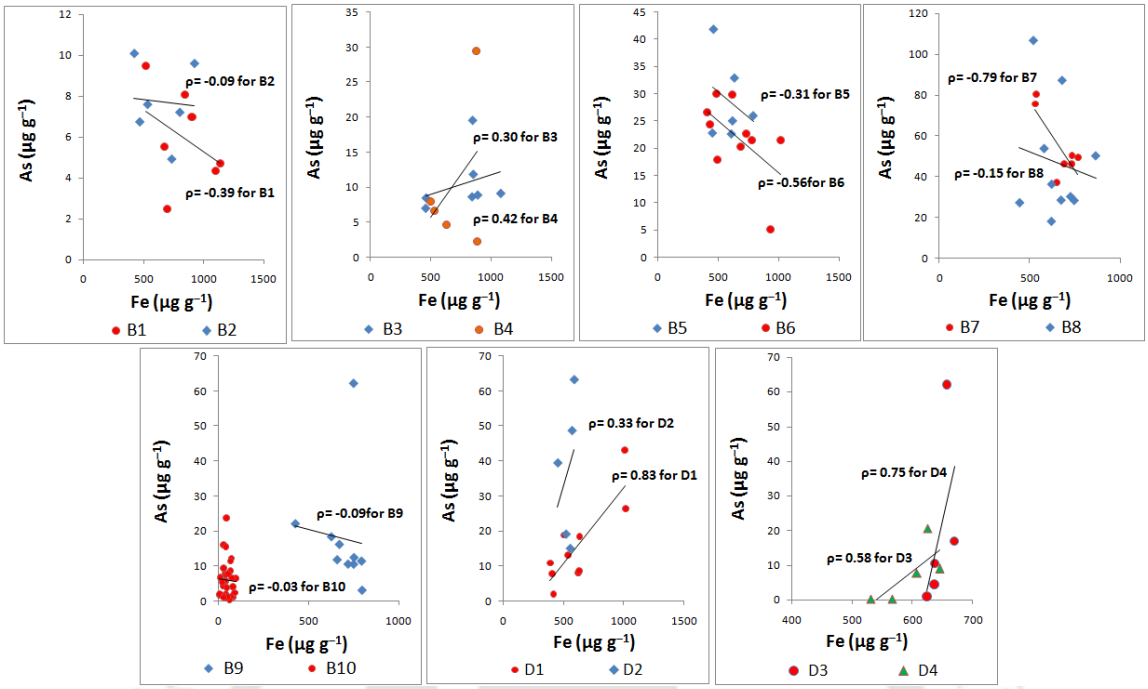

Figure 4. 7Pearson correlation values for *As* and Fe showed possible co-occurrence and inter relationship in sediment samples.

(viz. B3, B4 in H*As*CR whereas in D1, D2, D3 and D4 in L*As*CR in groundwater samples) suggests the physical or chemical sorption phenomenon prevailing in aquifer condition. It controls the solid and liquid phase *As* distribution in the H*As*CR and L*As*CR study area groundwater.

4.2.3 Total nitrogen content

The total nitrogen content was highest for B10 well sediment sample for H*As*CR study area, measured as 43.5 mg g^{-1} at depth of 51.8 m. The sediment color and texture was yellow-grey color coarse sand (i.e. B10) (Table 4.6). For L*As*CR, sediment with granule and light yellow coarse sand sample has measured lowest nitrogen content (i.e. below detection limit) at 27.4 m depth, whereas highest nitrogen concentration (i.e. 19.37 mg g^{-1}) was measured in deeper depth (i.e. 53.3 m in M1 well) than shallow depth (i.e. 27.4 m in M3 well) sediment

samples (i.e. grey, coarse sand) (Table 4.6). Highest content (43.5 mg kg^{-1}) was observed in the coarse sand sediment of B10 borewell at 170 feet depth, which is close to the Manas river, whereas lowest content was observed in grey colored coarse and medium sand samples. The highest nitrogen concentration range was observed in yellowish > grey > brown color sediment samples.

4.2.4 Total elemental analysis

Depth wise different elements concentration variation is shown in Figure 4.10. Results of selective sediments acid digestion method showed that average *As* concentration was measured as 18.9 µg g^{-1} in L*As*CR sediment samples. In H*As*CR and L*As*CR sediment samples, minimum viz. 0.4 & 0.18 µg g^{-1} and maximum viz. 106.8 & 63.2 µg g^{-1} of *As* concentration was measured in the respective study area. In H*As*CR, highest *As* concentration as 106.8 µg g^{-1} was measured in a gray color medium sand sample of B8 well at 85 feet, whereas in L*As*CR study area, highest *As* concentration as 63.16 µg g^{-1}measured in the dark grey color clay sample.

The other metals such as Al, Cr, Cu, Mg, Mn, Ni, Pb, and Zn were also measured in the same sediment samples.The average concentration as 8.8 & 7.9 mg g^{-1}, 619.5 & 375 µg g^{-1}, 55.2 & 65 µg g^{-1}, 213.7 & 747.2 µg g^{-1}, 590.5 & 589. 2 µg g^{-1}, 131.3 & 161.2 µg g^{-1}, 205 & 203.3 µg g^{-1} and 207.4 &259 µg g^{-1} was measured for Al, Cr,Cu, Mg, Mn,Ni, Pb and Zn elements in H*As*CR and L*As*CR sediment samples respectively. Figure 4.15 shows depth wise variation of different elements in selective depth sediment samples from H*As*CR and L*As*CR study area. Appendix Figure C.1.1 and 1.2 showed depth wise concentration profile for both the study area sediment samples. The significant concentration of other elements suggests that these sediments are also contaminated by other toxic and heavy elements in different depth. Depth wise arsenic concentration trend was almost same in till 35ft depth sediment samples

Table 4. 6 Results of Total Kjeldahl Nitrogen analysis of selective depth aquifer sediments

Sample ID	Sediment colour / texture	Total Nitrogen in soil (mg g^{-1})
B1-13.7	Yellow-orange/ Medium Sand	29.3
B2-15.2	Yellow-orange/ Medium Sand	9.7
B3-16.7	Brown/Medium Sand	9.5
B4-15.2	Brown/Fine Sand	19.3
B5-13.7	Yellowish/ Coarse sand	19.9
B6-22.9	Grey/Medium Sand	5
B7-7.6	Grey/Fine Sand	23.3
B8-16.8	Grey/Medium sand	11.2
B9-24.4	Grey/Coarse sand	4.9
B10-27.4	Light yellow/ Coarse sand with Granules	bdl
B10-51.8	Yellow-grey/ Coarse sand with Granules	43.5
D1-7.6	Greenish grey/Medium Sand	18.43
D1-29	White/ Medium sand	14.64
D1-53.3	Deep grey/Medium Sand	19.37
D2-9.1	Black/ Medium sand	14.25
D2-32	Blackish grey/ Medium Sand	9.67
D2-53.3	Deep grey/ coarse sand	4.98
D3-19.8	Dark grey/Fine sand	9.85
D3-22.8	Dark grey/Fine sand	5.62
D3-27.4	Grey/ Coarse sand	4.66
D4-16.8	Dark grey/Medium sand	4.92
D4-22.9	Dark grey/Medium sand	9.58
D4-27.4	Dark grey/Medium sand	4.92

Note ; Below detection level is abbreviated as 'bdl'

of B1,B2, B3 wells, whereas in B4, B5, B6,B7, and B8 well samples increasing trend at the deeper aquifer sediment was observed (Figure 4.10). Significant variation in different elements concentration was observed in all well sediment samples.

4.2.5 X-ray fluorescence (XRF)

The non-destructive X-ray fluorescence (XRF) technique was used to determine the total elemental composition in the sediment samples (Appendix Table D 1.1 and 1.2). The results showed that significant concentration of *As* (Avg. 16.5 mg kg^{-1} and max. 50.4 mg kg

$^{-1}$), Fe (Avg. 12.5 % and max. 18.7 %), Mn (Avg.1.4 % and max. 4 %), P (Avg. 0.7 % and max. 1.1

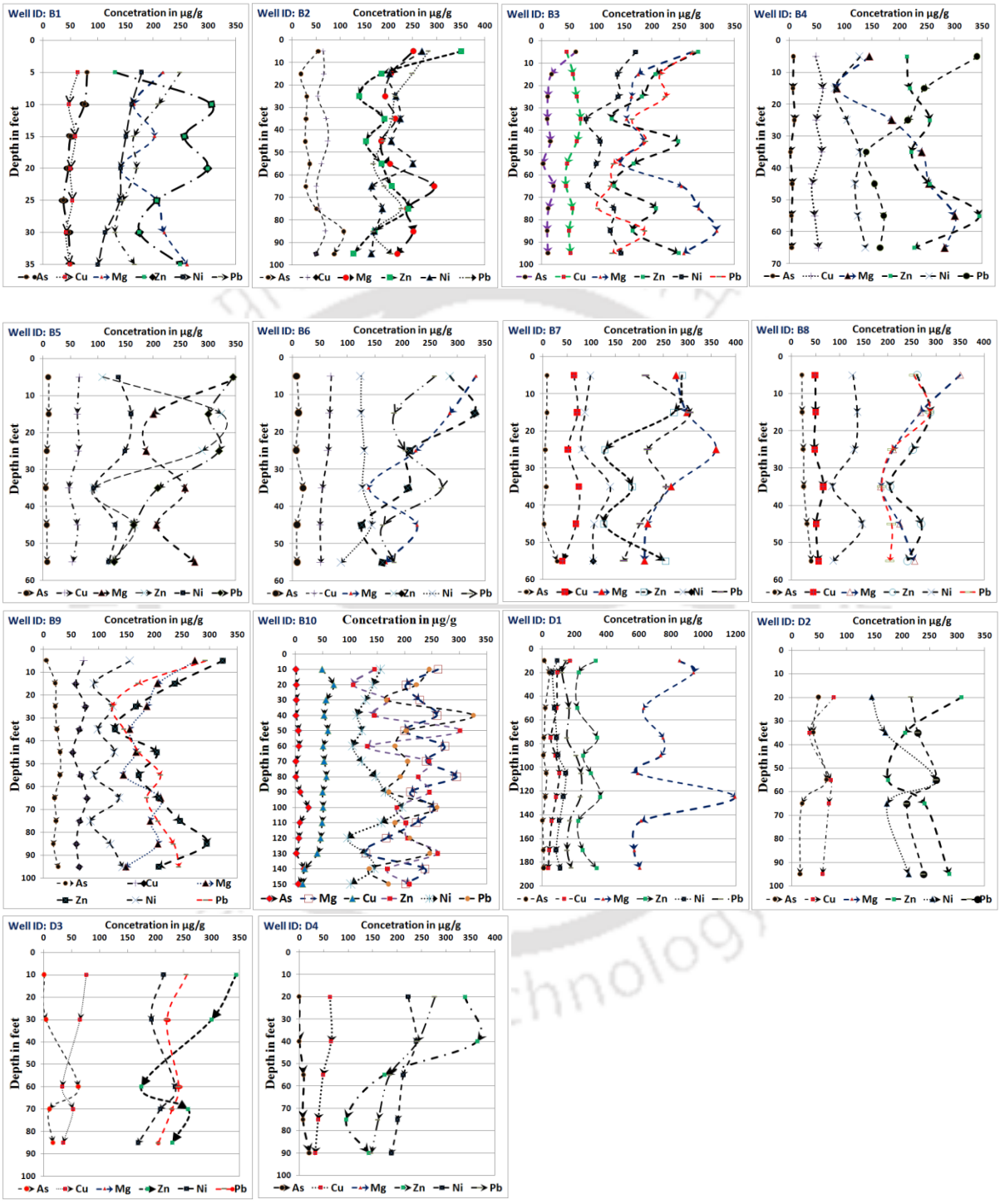

Figure 4. 8 Depth wise concentration variation of *As* with Cu, Mg, Zn, Ni, and Pb showed for H*As*CR and L*As*CR sediment samples.

%) and Ca (Avg. 3.7% and max. 9.7%) was measured in H*As*CR aquifer sediments (Table 4.7). In L*As*CR sediment samples, concentration of *As* (Avg. 17.6 mg kg $^{-1}$and max. 61.0 mg kg $^{-1}$), Fe (Avg. 16.0 % and max. 25 %), Mn (Avg. 2.1 % and max. 3.8 %), P (Avg. 0.6 % and max. 0.7 %) and Ca (Avg. 2.7% and max. 8.7%) was measured (Table 4.7). Compared to H*As*CR, the L*As*CR sediment have a high concentration of *As*, Fe, and Mn which suggests that comparatively slow reductive dissolution mechanism of Fe-Mn bearing minerals and high oxidation condition was the primary cause for low *As* concentration in the groundwater of study area. A high concentration of PO_4^{-3} and Ca in H*As*CR, suggests that the ionic exchange and carbonate dissolution mechanisms were the cause for high *As* groundwater concentration in the H*As*CR study area.

The highest concentration of Fe (Avg. 18.7%) was observed in grayish-black color coarse sand sediments in H*As*CR samples, whereas low concentration (Avg. 7.5 %) was observed in reddish–brown color sediment (Appendix Table D 1.1 and 1.2). Compared to *As* concentration in H*As*CR sediment samples, a contradictory highest 50.4 mg kg^{-1} and lowest concentration 0 (i.e. below detection limit) mg kg^{-1} measured in the grey-colour medium sand sample. Similarly, the highest Fe concentration of 25% was observed in pale blue color clay sample followed by dark grey color silt sample as 24.8 %for L*As*CR study area. Compared to *As* concentration in L*As*CR sediment samples, lowest concentration 0.0 mg kg^{-1} (i.e. below detection limit) in pale blue color clay and highest 61 mg kg^{-1} in dark grey color silt was measured in the sediment sample. The total elemental concentrations of other metals were well corroborated with the above ASTM sediment digestion results. The average concentration in H*As*CR and L*As*CR sediment sample for other metals such as Ni (Avg. 389 and 365.1 mg kg^{-1}), Cr (212.4 and 330.3 mg kg^{-1}), Cu (93.3 and 176 mg kg^{-1}) and Pb (169.6 and 164.3mg kg^{-1}) were measured by XRF analysis (Table 4.7).

Table 4. 7 Total elemental concentrations measured by XRF for selective depth sediments samples in mg kg^{-1}.

Compound	HAsCR				LAsCR			
	Min	Max	Avg.	S.D	Min	Max	Avg.	S.D
Mg %	0.2	0.8	0.4	0.2	0.4	1.2	0.8	0.3
Al %	5.6	12.7	8.2	2.2	8.6	15.7	11.5	2.3
Si %	50.6	73	62.2	8.5	0.7	72.7	48.4	18.7
P %	0.5	1.1	0.7	0.2	0.4	0.7	0.6	0.1
Cl	bdl	1*	375.1	327	bdl	359.1	103	166.3
K %	7.3	13	10	2	8.8	14.5	11.8	2
Ca %	0.6	9.7	3.7	4	bdl	8.7	2.7	3
Ti %	0.5	2.8	1.2	0.6	0.6	2.2	1.5	0.5
V	7.3	330.2	205.8	124.4	bdl	638	322.4	202.5
Cr	0.1	621.5	212.4	159.1	100.7	598	330.3	172
Mn %	0.1	4	1.4	1.6	1	3.8	2.1	1.1
Fe %	7.5	18.7	12.3	4.1	7	25	16	6
Ni	63.5	389	172.4	103	bdl	365.1	173.8	100.3
Cu	bdl	211.2	93.3	61.8	bdl	364.2	176	106.5
Zn	124.5	448.8	268.4	95.8	153.6	673	396.5	173.1
Ga	bdl	170	83	62.2	bdl	168.1	94.7	48.5
As	bdl	50.4	16.5	17.2	bdl	61	17.6	18.3
Rb	0.1	67.8*	6.7*	20.3*	469	2.1*	1.1*	454
Sr	0.3	3*	790	1.1*	0.1	387.8	219.2	157.1
Y	66	279	141.7	77.6	77.4	243.1	160.8	58.8
Zr	0.1	2*	927.6	752.6	0.1	1.3*	428.4	451
Nb	bdl	bdl	bdl	bdl	bdl	111.7	27.5	47.3
Ag %	0.3	0.4	0.3	0.1	0.3	0.5	0.4	0.1
Ba %	bdl	786	139.4	310.2	bdl	2.8	1.1	1.2
Nd	bdl	bdl	bdl	bdl	bdl	637.3	59.7	191.7
Eu	0.1	2*	692.8	550.4	0.1	1.1*	402.8	417.8
Yb	bdl	47.5	13	22	bdl	86.5	10	26.3
Re	bdl	26	16	9.2	bdl	28.6	11.8	10.3
Ir	bdl	16.5	3	6.4	bdl	15.3	3.6	5.7
Pb	90	287.5	169.6	68	94.2	324.1	164.3	69.8
Th	bdl	99.2	9	30	bdl	203	59.3	84

Note: * indicates concentration unit is %

4.2.6 Selective Sequential Extraction (SSE)

The sequential extraction analysis method was used to determine the *As* affinity and cause for heterogeneous enrichment in sediments in each fraction of the analysis and shown its depth wise variation in Figure 4.11 and 4.12. In obtained aliquots of each fraction, the concentration of Fe, Mn, and Al was also determined (Appendix Table E 1.1, 1.2). Following are the results of the sequential extraction for each successive fraction, Fraction 1: in this physisorbed (outer sphere surface complexes) fraction, minimum and maximum extractable *As* fraction was measured between 0.1 to 19.4 mg kg^{-1} for H*As*CR samples whereas, for L*As*CR samples, it was measured between 0.16 to 13.03 mg kg^{-1}. This implies that the adsorbed *As* fraction can easily be released into groundwater and vulnerable to redox aquifer condition and ion exchange capacity.

In Fraction 1 other extractable average fractions of Mn, Fe, Al was 44.3, 1526.1 and 960.6 mg kg^{-1}measured for H*As*CR samples 22.5, 1574.8 and 134.4 mg kg^{-1} for L*As*CR sediment samples respectively. Fraction 2: In chemisorbed extractable fraction (inner sphere surface complexes), the extractable*As*was measured between 0 (i.e., below detection limit) to 6.5 mg kg^{-1} for H*As*CR samples whereas, for L*As*CR it was measured in the range of 0.2 to 4.6 mg kg^{-1}. In this chemisorbed fraction, relatively low proportions of *As* was extracted from physisorbed fractions. In the same fraction the extractable average concentration of Mn, Fe, and Al was measured 4.4 to 48.7 mg kg^{-1}, 763.9 to 142.8 mg $kg^{-1}$and 421.3 to 650.4 mg kg^{-1}, in H*As*CR and L*As*CR sediment samples respectively (Appendix Table E 1.1, 1.2). In fraction 3: the extractable concentration of total non-labile *As* was associated with poorly crystalline and amorphous oxides of Fe, Mn, and Al minerals surfaces which was measured in the range of 0.2 to 36.7 mg kg^{-1} and bdl to 6.5 mg $kg^{-1}$for H*As*CR and L*As*CR sediment samples. Average Fe, Mn and Al concentration was measured as 5860.1 & 6363.4 mg kg^{-1},180.8 & 164.7 mg kg^{-}

[1] and 4449 & 1670.5 mg kg^{-1} for H*As*CR and L*As*CR samples respectively(Appendix Table E1.1, 1.2). Amongst the other two fractions, *As* was found highest in this fraction, which suggested that *As* was co-precipitated and had high affinity with the amorphous Fe, Mn and

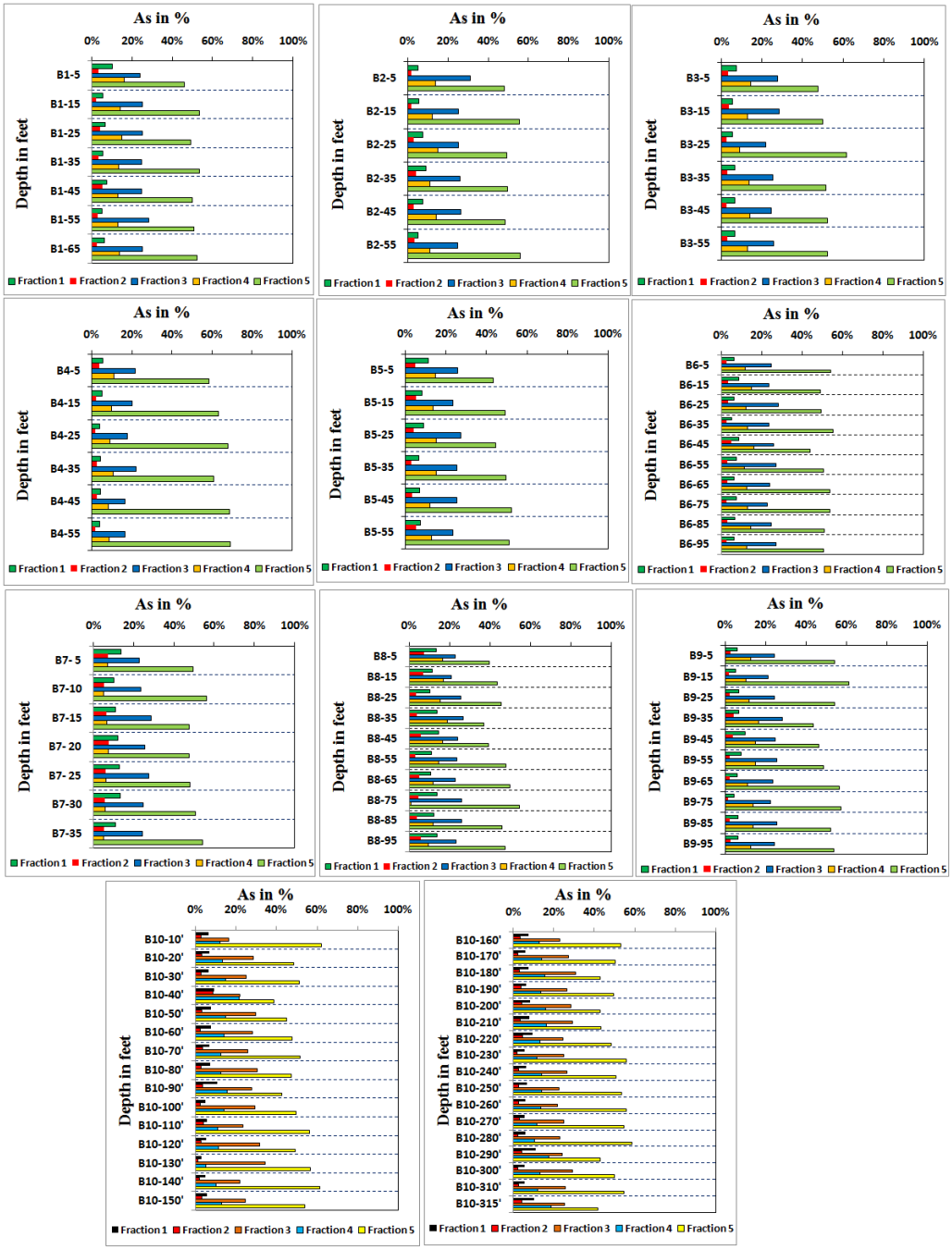

Figure 4. 9Extraction results of *As* and major elements for H*As*CR selective depth sediment.

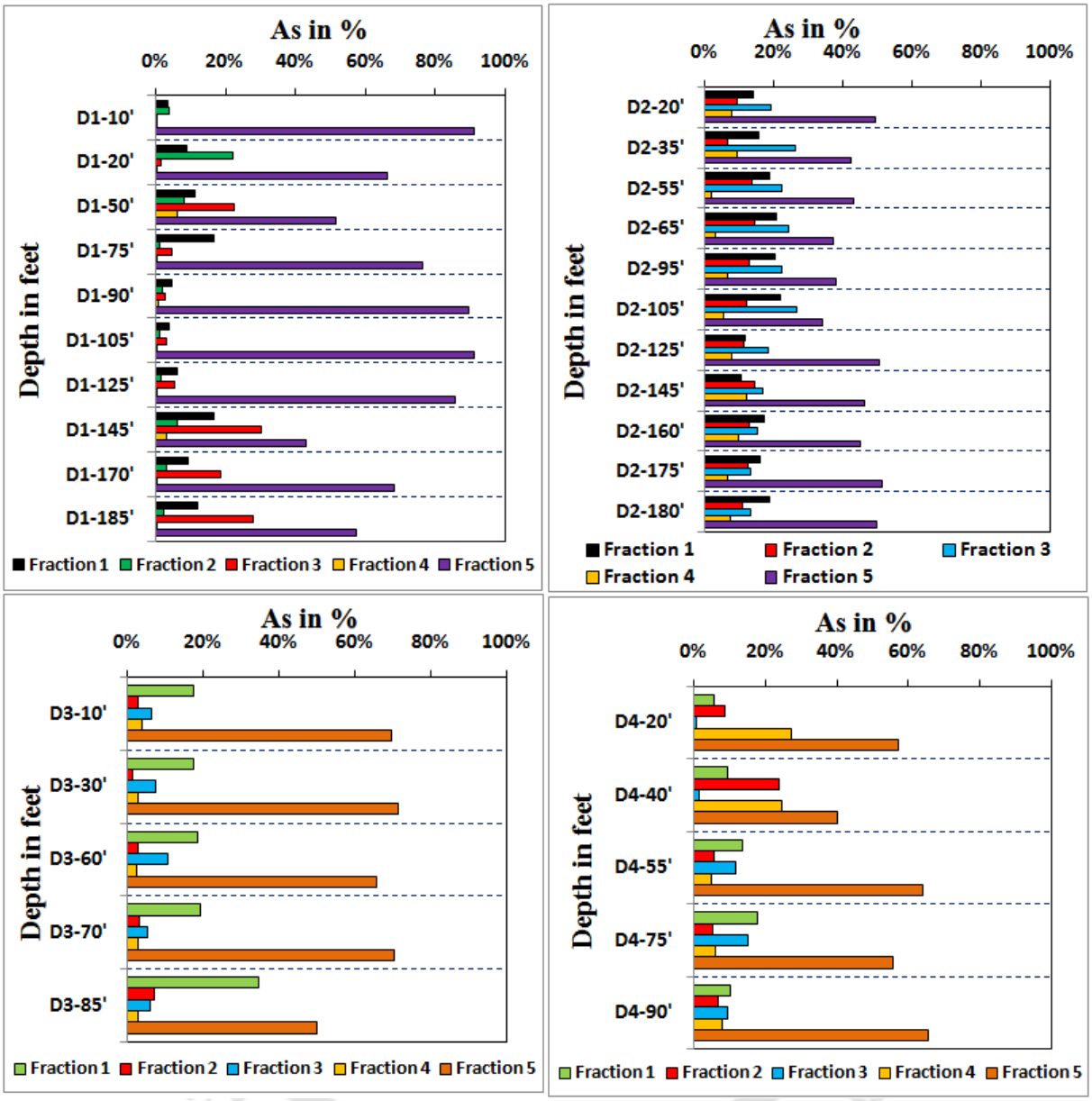

Figure 4. 10Extraction results of *As* and major elements for L*As*CR selective depth sediments.

Al-bearing minerals in this aquifer. Fraction 4: The total extractable concentration of *As*, bound to well crystallized Fe, Mn and Al oxide/hydroxides minerals were measured between the range of 0.1 to 17.5 mg kg^{-1}, 0 to 3.5 mg kg^{-1} for H*As*CR and L*As*CR sediment samples. Moreover, the extracted fraction, measured average concentration of Al, Mn, and Fe was 2124.2 & 3052.3 mg kg^{-1}, 89.4 & 83.9 mg kg^{-1} and 2985.7 & 614.1 mg kg^{-1} for H*As*CR and

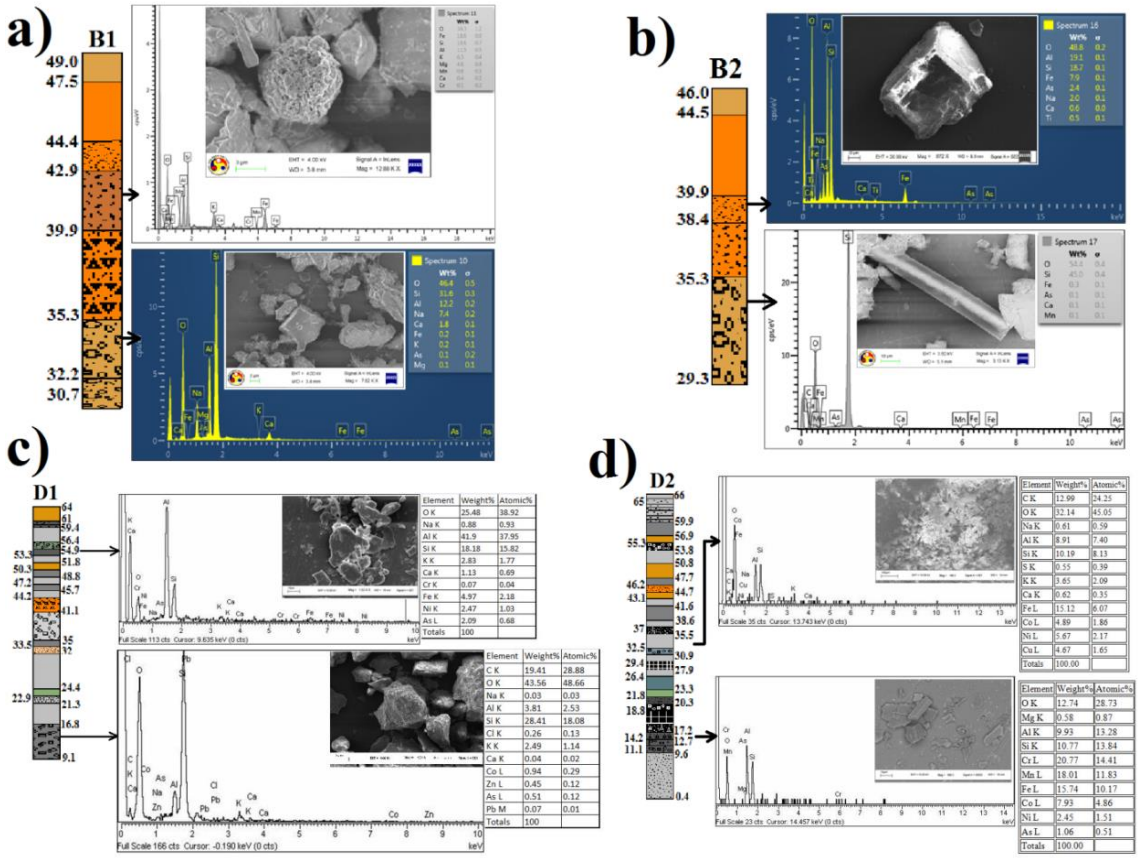

Figure 4. 11Morphological and elemental composition a) B1 well, brown color coarse-medium sand and granule sample showed distorted crystal of magnetite and crystalline Albite mineral, b) B2 well, brown color fine sand and granule sample shows, crystalline shape of scorodite and claudetite mineral, for L*As*CR c) D1 well, dark grey clay and medium sand sample shows flaky muscovite and distorted quartz mineral respectively, d) D2 well, clayey grey sample and coarse sand sample, shows the presence of jarosite and goethite (tubular crystal) mineral respectively, at deeper depth sediment.

L*As*CR samples respectively (Appendix Table E 1.1, 1.2). In this fraction, lowest *As* concentration was extracted amongst the other fraction, suggested that poor crystalline Fe-*As* bearing minerals are present in both the study areas aquifers sediments.

Fraction 5: In this final stage, residual total extractable *As* concentration was measured in the range of 0.4 & 76.8 mg kg^{-1} for H*As*CR and 0.8 & 53.3 mg kg^{-1} for L*As*CR sediment samples. For Mn, Fe, and Al, the average extracted fraction was ranged between 350.6 & 83.9

mg kg^{-1}, 11763.3 & 7562.7 mg $kg^{-1}$and 5984.5 & 8774.5 mg kg^{-1} for H*As*CR and L*As*CR sediment samples respectively (Appendix Table E 1.1, 1.2). It suggested that measured total *As* concentration from aquifer sediments was within a range of (i.e. 0.6 mg kg^{-1} to 490 mg kg^{-1}) the earth crustal materials, which support with the arguments of Hering and Kneebone, (2002) and which is sufficient to produce 1072 nmol kg^{-1} of *As* in groundwater, which was measured in H*As*CR groundwater samples.

4.2.7 FESEM-EDS analysis

A morphological study by FESEM analysis showed the presence of detrital and authigenic mineral crystal in the sediment samples [Figure 4.13 (a-d)]. Here, the grains with broken or round edges were classified as detrital mineral, whereas a grain with sharp edges indicates the presence of authigenic minerals [Appendix Figure H 1.1, 1.2 and1.3]. The elemental composition confirmed the mineral composition and crystal systems for magnetite (i.e. Isometric structure) and albite (i.e. Triclinic structure) minerals observed in well B1 sample [Figure 4. 13(a)]. Similarly, in B2 well sample scorodite (i.e., orthorhombic structure) and claudetite (i.e. monoclinic structure) minerals were observed and confirmed with morphological study for H*As*CR sediment sample. In L*As*CR sediment sample, flaky muscovite (i.e. monoclinic structure) and distorted quartz (i.e. monoclinic structure) was observed in D1 well sediment sample whereas, in D2 well sediment sample, distorted and agglomerated sand was rich in potassium and iron elements suggest that jarosite (trigonal - pyramidal) and goethite (tubular crystal) minerals was confirmed by EDS analysis. A

Table 4. 8 Atomic ratios of Fe, S, and O to *As* in soil particles and matrix determined by SEM-EDS

Well ID	O/Fe	Fe/*As*	*As*/Fe	O/*As*	S/*As*	O/Ca	O/Mn
B1	3.7	nd	nd	nd	nd	123.1	112.5
	404.9	2.7	0.4	1079.9	nd	32.3	nd
B2	10.8	4.4	0.2	47.6	nd	101.9	nd
	316.4	4	0.2	1273.7	nd	681.4	934
B3	157.8	2.2	0.4	352.8	nd	5.1	nd
	9.6	67.8	nd	653.2	nd	233	nd
B4	36	3.9	0.3	139	nd	198.3	407.7
	101	2.7	0.4	271.1	nd	nd	nd
B5	15.5	1.4	0.7	22.2	nd	13.5	nd
	nd	24.3	nd	nd	0.3	nd	nd
B6	nd	24.3	nd	nd	0.3	nd	nd
	11.4	6.5	0.2	74.4	nd	86.2	nd
	101.0	2.7	0.4	271.1	nd	nd	nd
B7	108.6	nd	nd	nd	nd	52	427.5
	32.4	8.7	0.1	282.1	nd	nd	nd
	0.1	71.3	nd	6.6	0.4	0.6	3.43
B8	4.6	4.7	0.2	21.8	nd	39.9	191.4
	157.8	2.2	0.4	352.8	nd	5.1	nd
	1.3	45.8	nd	59.1	78.4	6.2	nd
B9	67.9	3.8	0.3	255.2	nd	nd	nd
	5.6	9.9	0.1	55.6	17	6.7	nd
	14.5	23.7	nd	344.2	nd	276.2	378.6
B10	5.6	23.5	nd	132	nd	20.9	258.1
	15.5	1.4	0.7	22.2	nd	13.5	nd
	5.6	9.9	0.1	55.6	16.9	6.7	nd
	1.3	45.6	nd	59.1	78.7	6.2	nd
	21.5	6	0.2	128	nd	154.1	nd
	21.9	4.1	0.2	90.6	nd	157.5	nd
D1	17.9	3.2	0.3	57.2	nd	2433	nd
	nd	nd	nd	405.5	nd	56.4	nd
D2	7.4	nd	nd	nd	nd	nd	2.4
	2.8	19.9	0.1	56.3	nd	128.7	nd
D3	88.1	0.6	1.7	50.6	nd	nd	nd
	23.6	8.2	0.1	194.4	nd	nd	7.35
D4	7.6	9.4	0.1	71.4	nd	73	nd
	12	38.8	nd	466.9	nd	nd	nd

Note: Not detected is abbreviated as 'nd'

t morphological study by FESEM showed the presence of an authigenic and detrital mineral in the analyzed sediment samples [Figure 4.13 (a-d)]. Also, the grains with broken or round edges

are classified as detrital [Figure 4.13 (a, b and d)] whereas grains with sharp edges indicatehe presence of authigenic minerals [Figure 4.13 (c)]. The morphological and EDS analyses have confirmed the mineral composition and crystals system such as flaky muscovite (monoclinic), quartz (trigonal), jarosite (trigonal), goethite (orthorhombic), birnessite (monoclinic), scorodite (orthorhombic), enargite (orthorhombic), vaterite (hexagonal) in selective depth bore well sediment [Figure 4.13(a-d)]. The FESEM-EDS results depict a close affinity of C, O, Al and Si elements with arsenic, which was common in all the analyzed samples. Significant atomic percentage (at.%) ratio of O vs. Fe, Fe vs. *As*, *As* vs. Fe, O vs. *As* and S vs. *As* shown in Table 4.8 and other elemental such as Co, Ni, Cu, Cr, S, Ti, P, and Pb concentration was also detected in the same sediment samples. Highest atomic percentage (i.e. at. %) ratio for O vs. *As* was observed as 1273.7 % at 60 feet depth sample in B2 well sample for H*As*CR sample. The O vs.*As* ratio was 466.9 % measured in D4 well sample at 75 feet depth grey color sediment sample. In H*As*CR study area sample, O vs.*As* ratio, 352.8 % was found in 55 feet (i.e. 16.8 m) grey color coarse sand sediment sample. The ratio of Fe/*As* found in the range of bdl to 71.3 & 38.8 for H*As*CR and L*As*CR sediment sample. It suggests that *As* oxy-anions are combined with a solid phase of these iron oxy/hydroxides mineral surfaces (Matera et al., 2003). This Fe/*As* ratio further suggest that oxidation condition prevailing in these aquifers and *As* was co-precipitated with ferric oxide, which gets adsorbed on sediment surfaces.

The presence of significant atomic % ratio of O/Fe ranged from bdl to 404.9 % suggested the presence of iron oxy/hydro-oxides mineral such as hematite, siderite, magnetite, scorodite, and goethite in aquifer sediment. Similarly, other average element atomic ratio Fe/*As* (14.6 & 10), *As*/Fe (0.2 & 0.3), O/*As* (216.1 & 162.8) and S/*As* (6.9 & 336.4) was found for H*As*CR and L*As*CR sediment samples, respectively. The results suggest the presence of

primary *As*, Fe and S bearing minerals, similarly as the ratio of O/*As* suggests the presence of secondary *As* bearing claudetite mineral. From table 4.8 it was observed that the particles which are rich in *As* have an O/Fe atomic ratio >1.5. It suggests the presence of magnetite, hematite, goethite, and scorodite structure in the sediment sample. Therefore, the results of L*As*CR aquifer sediment suggests that these regions are high enough to retain *As* in the near future due to the increase in arsenic adsorption capacity (Matera et al., 2003)**.** According to Matera et al., (2003), arsenate oxy-anions ($Hx AsO_4^{x-3}$) can be adsorbed on the surface of iron oxy/hydro-oxides minerals, which are sufficient enough to retain the dissolved *As* and provide the low concentration in groundwater. Also, Mafic and Felsic minerals composition were confirmed by EDS spectrum via the presence of a higher percentage of lighter elements (viz. calcium, magnesium, iron, and sodium, etc.) and a higher percentage of heavier elements (viz. silicon, oxygen, aluminum, and potassium).

4.2.8 X-ray diffraction (XRD)

The mineralogical analysis by XRD (Figure 4.14) method have confirmed using characteristic peaks of primary and secondary minerals with corresponding 2θ angle, for medium sand, coarse sand, and fine sand samples. The primary *As*-bearing minerals mainly enargite (En- 2.28, 3.24 and 3.22), realgar (Re- 2.93 and 3.17), orpiment (Or- 1.37, 2.45, 2.46, 2.55, 3.66, 3.69 and 4.42), armangite (Ar- 1.46, 1.69 and 8.86) were observed at respective *d*-spacing values. The secondary *As*-bearing minerals such as arsenolite (Ar-1.46, 1.69, 8.86), claudetite (Cl- 1.82, 2.25, 2.52, 2.57, 2.98, 3.22, 3.29, 3.52, 4.00 and 4.85) and skutterudite (Sk- 1.37) were observed at respective *d*-spacing values in the sandy yellow-grey aquifer sediments. Other rock-forming, clay and alkaline minerals, mainly comprised by silicates [quartz (Q- 1.54, 1.59,2.26, 3.34 and 4.26)], mica group [biotite (Bi-3.16 and 10.09) and illite

(Il- 5.02, 9.86, 10), montmorillonite (IM- 2.01, 3.33, 9.50,)], muscovite (Mu- 3.33, 3.48,) anorthoclase (An- 2.11, 2.12), dolomite (1.80, 2.41) and kyanite (Ky- 1.37,1.38,4.31) minerals which were found in clayey-silty fine sand samples (Appendix Figure B 1.8 and 1.9). Significant characteristic peak of crystalline Fe-oxy/hydroxides minerals such as, magnetite (Ma-2.97, 3.75, 6.84), hematite (He- 1.35, 1.64), maghemite (Mag- 3.38 and 1.66), siderite (Si- 1.43, 1.51, 2.13), goethite (Go- 1.72, 2.44, 2.45, 2.49, 2.58, 4.19, 4.98), jacobsite (Ja- 2.46, 4.91) were identified in the analyzed sediment samples. Aluminum hydroxide mineral such as gibbsite (Gi) and graphite (i.e. carbon) mineral was not detected in the analyzed sediment samples which may be probably due to amorphous nature.

The crystalline phases of primary and secondary *As*-bearing minerals were detected in the XRD analysis, which further supports the results of the above findings viz. total elemental analysis, SSE, XRF method. The presence of jarosite mineral suggests predominant weathering of primary pyrite mineral, which is stable in oxidizing and acidic aquifer conditions (Matera et al., 2003). The presence of detrital feldspar and quartz minerals suggest a dominant weathering process in Pre-cambrian granite and gneisses minerals in Brahmaputra floodplain. Presence of illite (il), illite- montmorillonite (IM), potassium feldspar (PF) and muscovite (Mu) suggests the weathering of granitic and metamorphic rock, which were physically weathered and carried by the tributary network (i.e. Manas river) of Brahmaputra rivers. The result suggested that more than 80% of clay mineral is dominated by the primary source of *As*-bearing minerals at both the study area aquifer.

4.2.9 Attenuated total reflectance Fourier transform infrared (ATR-FTIR) spectroscopy

In ATR-FTIR spectra, a significant feature of *As* bearing secondary mineral mainly

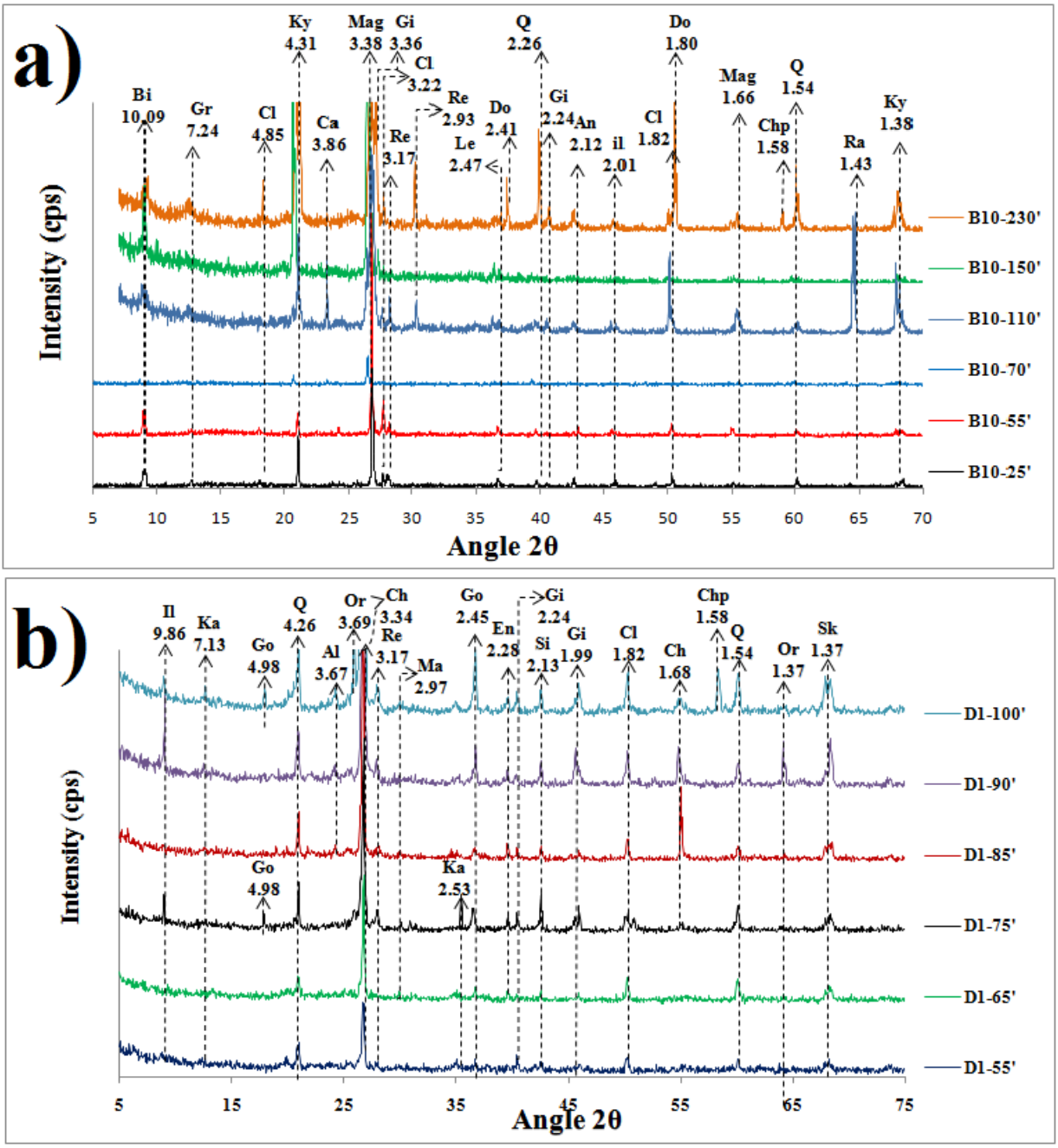

Figure 4. 12 Mineralogy of selective depth sediments showed by d-spacing values for a respective mineral, where; Bi – biotite, Gr – graphite, Cl – claudetite, Kya – kyanite, Ca – calcite, Mag – maghemite, Gi – gibbsite, Si – siderite, Re – realgar, Le – lepidocrocite, Do – dolomite, Q – quartz, An – anorthoclase, il – illite, Chp – chalcopyrite and Ra – ramsdellite, abbreviation indicates mineral name.

arsenolite and claudetite of metal-oxygen stretching modes observed at 795 cm^{-1} and 465 cm^{-1} & 641 cm^{-1} wavelengths (Muller et al., 1964). Arienzo et al., (2002) reported that the wave

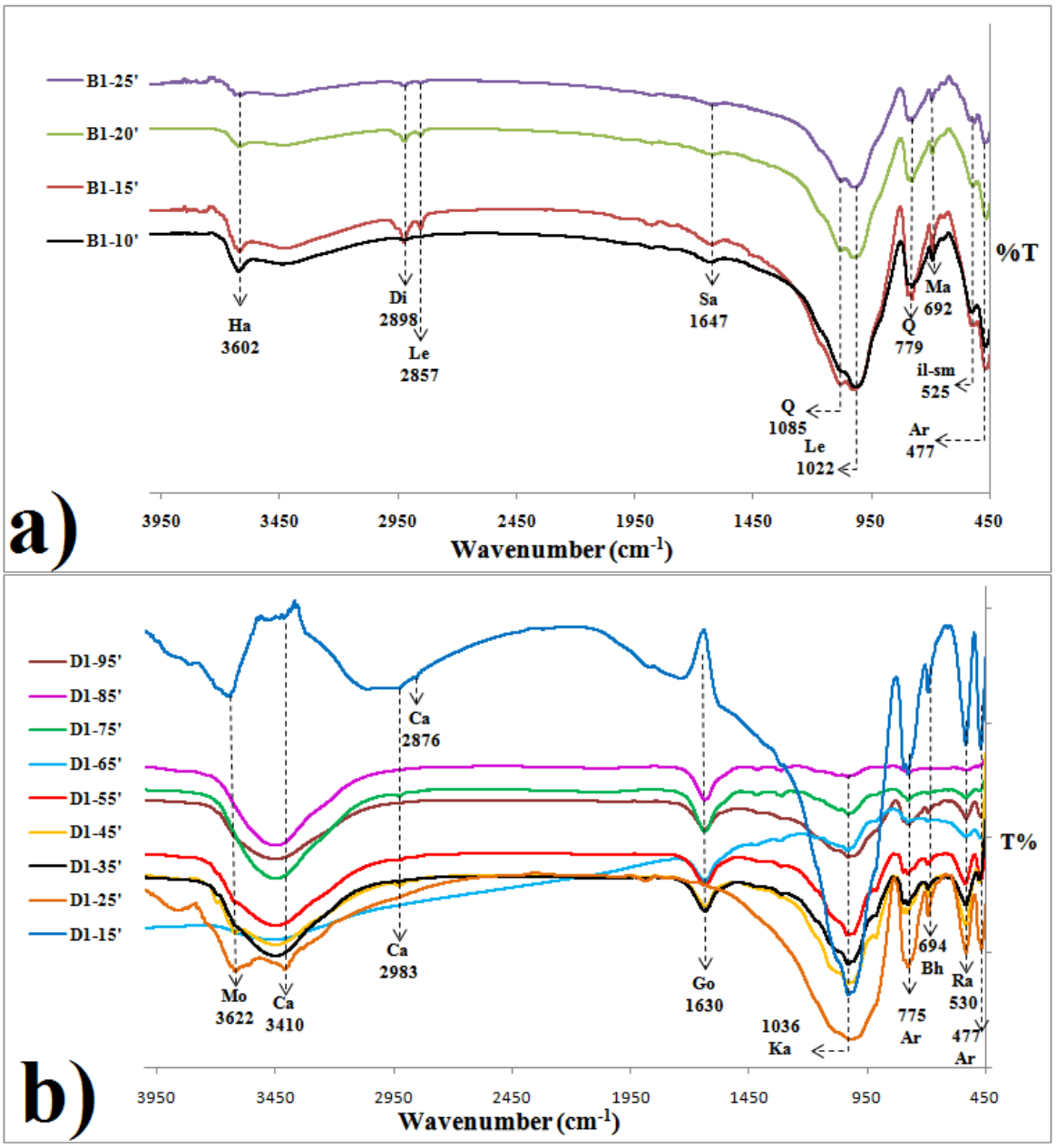

Figure 4. 13 showed FTIR spectra, % T vs. wave number portrayed strong, medium, and weak bands association with a functional group of dominant minerals for H*As*CR and L*As*CR sediment samples. Where arsenolite- Ar, illite-smectite- il-sm, ramsdellite – Ra, boehmite – Bh, kaolinite – Ka, goethite – Go, calcite –Ca, montmorillonite –Mo, quartz – Q, halloysites - Ha, sodium arsenite, Sa, diaspore – Di, lepidocrocite- Le, maghemite – Ma.

the number corresponding to 795 cm^{-1} bands suggests the presence of sodium arsenite ($NaAsO_2$) (Figure 4.15). Moreover, the weak band at 474 cm^{-1} suggest adsorbed phases of *As* on goethite mineral (Lakshmipathiraj et al., 2006). They predominantly belong to *As*-O-Fe groups, which suggested that arsenite binds with Fe-O as well as non-surface complexes of *As*-O metal-oxygen stretching modes (White and Roy 1964). The band at a 795 cm^{-1} was assigned to the symmetric stretching vibration of *As*−O, while the weak feature at 720 cm^{-1} was attributed to *As*–O–Fe (III) stretching vibration (Madejová, 2003). White and Roy, 1964 observed that arsenolite and sodium arsenite are structurally abundant in cubical and monoclinic forms respectively, which supports the above results of FESEM-EDS and XRD for H*As*CR and L*As*CR sediment analysis. The MnO_2 (e.g. ramsdellite) bearing mineral of orthorhombic shape was observed at 682 cm^{-1} and 530 cm^{-1} bands (White and Roy 1964).

Strong intensity band of goethite appeared at 450 cm^{-1} wavelengths. Weak band of boehmite appeared at 694 cm^{-1}wavelength. The infrared spectral band of FeS_2 polymorphs pyrite mineral was appeared at the 418 cm^{-1} wavelength with a shoulder on the low energy side at 412 cm^{-1}wavelength, whereas lepidocrocite band at1013 cm^{-1} was probably appeared due to –OH bending modes (White and Roy 1964). Moreover, dioctahedral minerals (viz. kaolinite, gibbsite) observed in the 800 cm^{-1} to 950 cm^{-1} wavelength regions which suggest that the region to be surrounded by Mg^{+2} or Fe^{+2} cations. Similarly, presence of hydroxyl ion (–OH) of trioctahedral mineral such as brucite indicates the area to be surrounded by two trivalent elements such as Fe^{+3} or Al^{+3} at 700–600 cm^{-1}wavelength range (Klein and Hurlbut, 1999). The Al_2OH bending bands of kaolinite mineral observed near 914 cm^{-1}wavelength, which is probably raised by vibration of inner –OH groups and confirm the presence of trioctahedral minerals presence in sediment samples (Madejová 2003). The ATR-FTIR characteristic peaks

of the primary and secondary forms of iron-bearing minerals viz. hematite, magnetite, lepidocrocite, goethite and siderite in grey and brown color sediments support the identifications and results of FESEM-EDS and XRD analysis for H*As*CR and L*As*CR sediments samples (Appendix Figure J 1.1 and 1.2).

4.2.10 Adsorption Kinetics

The specific surface area of sediment samples was measured using laser particle size analyzer (LPSA)(Master Seizer 2000 Ver. 5.22 Serial Number: MAL100332; Malvern Instruments Ltd. Malvern, UK), for 0.02 to 2000 micron size sediment samples by wet dispersion analysis method. For this test ~500 mg air dried clay to sand (ranges from 0.02 µm to 2000 µm) samples were used, which was dispersed into a double distilled water (ddH_2O) (Millipore Milli-Q 18MΩ) (Song et al. 2006).

4.2.10.1 Arsenic adsorption effect at different pH

The pH of a solution is an important parameter in the adsorption process. Past studies revealed that the removal of *As* (As^{+3}&As^{+5}) ions was strongly dependent on the pH of the solution (Ravenscroft et al., 2005; Sailo and Mahanta, 2016). The adsorption kinetics for the different sand sample was studied at 6.5, 7, and 7.5 pH for As^{+3} and As^{+5}solution. The optimal removal capacity of sediment was found at neutral pH (i.e., pH 7). Further, the increase in pH causes a drastic decrease in the adsorption capacity of *As* was noted. This might be due to the weakening of the electrostatic force of attraction between the oppositely charged adsorbate and adsorbent, which ultimately leads to a reduction in sorption capacity of the adsorbent. Results are shown in Figure 4.16 (a-f), showed that maximum adsorption occurred at 7.5 pH than the 6.5 pH for As^{+3} on brown color sediment sample than grey sediment, whereas for As^{+5}

the optimum pH 7 was observed to be more favorable for adsorption. The brown color sediment has more effective removal capacity than grey color sediment. Presence of high Fe-oxide minerals in brown color sediment affects on point zero charge (pzc) condition of sediment, which was observed in the pH of 6 to 8 range. It prefers more adsorption of As^{+5} than As^{+3}

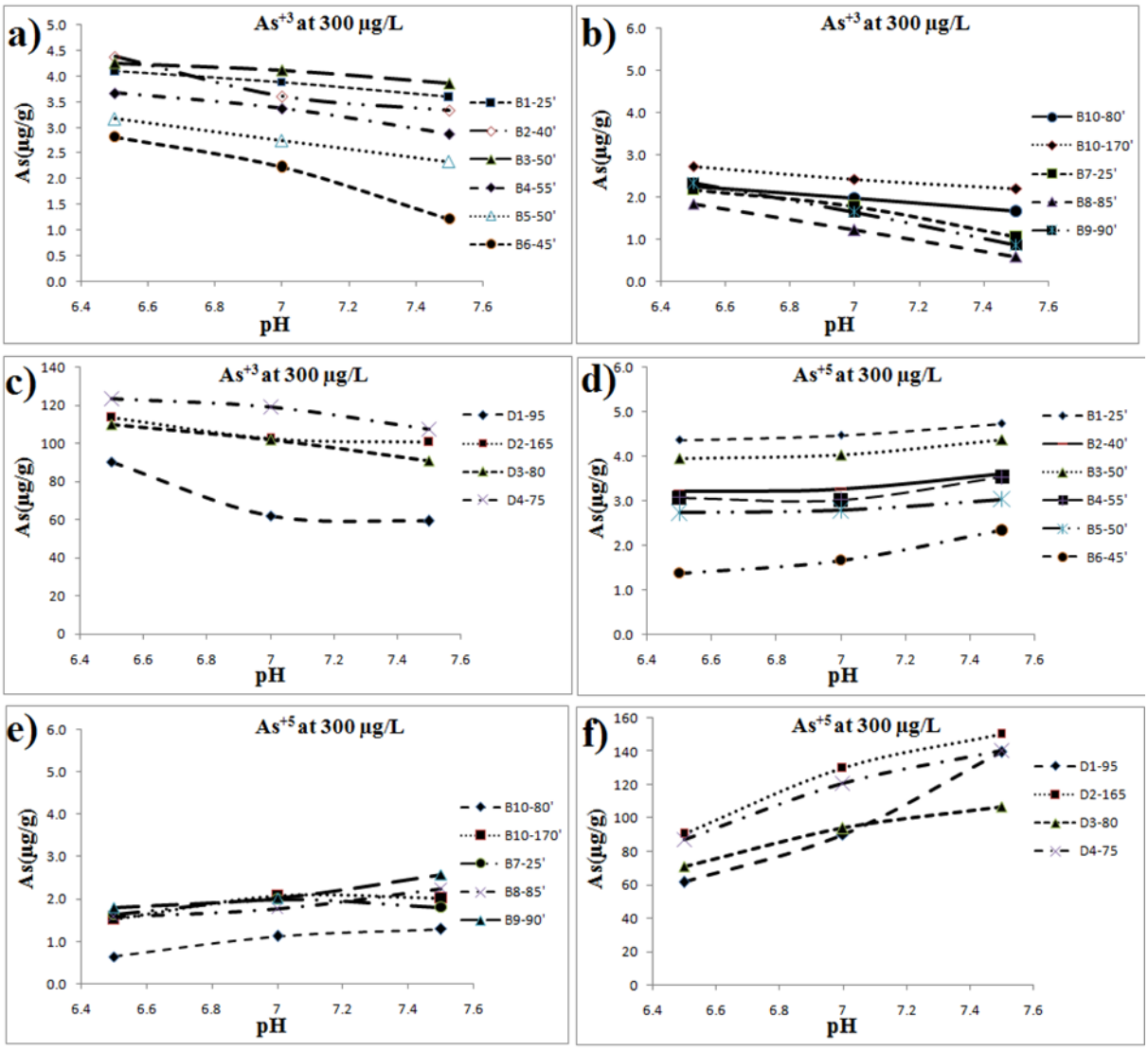

Figure 4. 14 Effect of pH on *As*$^{+3}$ and *As*$^{+5}$ at initial concentrations of 300 µg L^{-1} on sediment adsorption.

sediment surface (Stumm, 1992). However, sediment surface below pcz (i.e., pH 4.6) prefer positive charge and adsorb *As*$^{+5}$ from the solution (Stumm 1992). Therefore, decrease in pH

implies that a decrease in surface charged density (i.e. increase in OH^- anion), which decreases adsorption capacity of As^{+5} on sediment surface (Goldberg, 2002). Ho and McKay, (1999) models using a nonlinear regression method was

used to evaluate the kinetic mechanisms. The adsorption equilibrium time was confirmed from the experimental analysis as 16 h.

4.2.10.2 Pseudo-first order and second order kinetic model

The experimental data were fitted to pseudo-first order (HO, 2004) and pseudo- second-order. The graphical results showed the relationship between the amounts adsorbed by a unit weight of sediments and the amount of adsorbate remaining in a test medium at equilibrium (Appendix Figure K 1.1, 1.2, 1.3, 1.4, 1.5, 1.6, 1.7 and 1.8). The values of q_t predicted by the pseudo-first and second-order model for initial As^{+3} and As^{+5}concentration was 300 and 500 µg L^{-1}concentration solution. This study conducted at room temperature 25°C and samples were collected at 0.15 h, 0.3 h, 1 h, 2 h, 4 h, 8 h, 12 h, 16 h and 24 h time. The results are graphically shown in Appendix Figure K 1.1, 1.2, 1.3, 1.4, 1.5, 1.6, 1.7 and 1.8. The experimental data were fitted to pseudo-first order (HO, 2004) and pseudo-second-order model. The q_t values were observed higher for the pseudo-first-order kinetic model than a second-order kinetic model with decreasing initial As^{+3} and As^{+5}concentration. Compared to the pseudo-first-order kinetic model the results were well fitted with the pseudo-second-order model. The predicted values of q_t by the pseudo-first and second- order model for initial order model, results were found in good agreement with the experimental equilibrium adsorption capacity (q_e) data.

In pseudo-second-order model, highest adsorption rate (K_2) constant was observed for yellowish medium sand sample 0.19 min^{-1} for As^{+3} at 300µg L^{-1} and 500 µg L^{-1} whereas, for As^{+5} at 300 µg L^{-1} and 500 µg L^{-1} it was measured 0.17 min^{-1}. Moreover, in clayey-silty fine sand samples, the presence of aluminum hydroxides and alumino-silicates clay minerals may also retain appreciable concentrations of arsenate, and they exhibit a strong preference for arsenate relative to arsenite (Manning and Goldberg, 1997). Similarly, Mn oxides may impart a strong influence on *As* binding, where reaction of arsenite solutions with Mn oxides such as birnessite mineral results in extensive and rapid uptake, but arsenic was retained as arsenate by surface complexes reaction owing to arsenic oxidation by Mn (III or IV) (Oscarson et al., 1981).

At a higher initial *As* concentration, adsorption is much more competitive, and the rate of adsorption is slower, resulting in lower rate constant values. The results showed that lower arsenic adsorption rate constant (i.e. K_2) was observed for grey color coarse sand samples than brown color fine sand samples. It further inferred that the cause of more availability of active sites on the adsorbent particle. In addition to the equilibrium time, four conclusions were drawn briefly as follows: (1) a low pH value was conducive to *As* adsorption onto sediments, (2) As^{+5} was more readily adsorbed than As^{+3} on the sediment samples, and (3) fine sand sediment have high adsorption capacity than coarse sand sediment sample for *As* because of high surface area. (4) The pseudo-second-order kinetic model fits better than the first-order model. Ho and McKay (1999) state that the adsorption mechanism is mainly followed by chemisorptions when it follows the pseudo-second-order kinetic model. Therefore, arsenate adsorption on respective sediment is chemisorptions in nature.

4.2.10.3 Isotherm study

Langmuir isotherm study for As^{+3} and As^{+5}, shows a plot between the experimental equilibrium adsorption capacity (q_e) and equilibrium concentration (C_e) for adsorption study has shown in Figure 4. 17. The values of the respective parameters are tabulated in Table 4.9 and 4.10. To check the favorable adsorption nature for the studied sediment samples, Adsorbers and Weber, (1974) dimensionless separation factor was used:

$$R_L = \frac{1}{1+bC_0} \quad \ldots (29)$$

Where 'b' is the Langmuir constant and 'C_0' is the initial adsorbate concentration (µg L^{-1}). The physical meaning of different R_L values ranges from $0 < R_L < 1$, the irreversible adsorption observed when $R_L = 0$, the linear adsorption observed when $R_L = 1$ and unfavorable adsorption observed when $R_L > 1$. The dimensionless favorable R_L values for As^{+3} and As^{+5} adsorption on sediment showed favorable adsorption for B1, B2, B3, B4, B5, B6 and B7 samples of H*As*CR, whereas all samples of L*As*CR samples showed favorable adsorption condition. The linear adsorption values were observed only for As+5 to B 9 and B 10 sediment samples of H*As*CR study area. Nath et al., (2009) and Geen et al., (2008) data of all studied samples were observed to be linearly fit and showed significant Pearson correlation values. The studied sediment samples from West Bengal and South-East Asia showed that the condition. The linear adsorption values were observed only for As+5 to B 9 and B 10 sediment samples of H*As*CR study area. Nath et al., (2009) and Geen et al., (2008) data of all studied samples were observed to be linearly fit and showed significant Pearson correlation values. The studied sediment

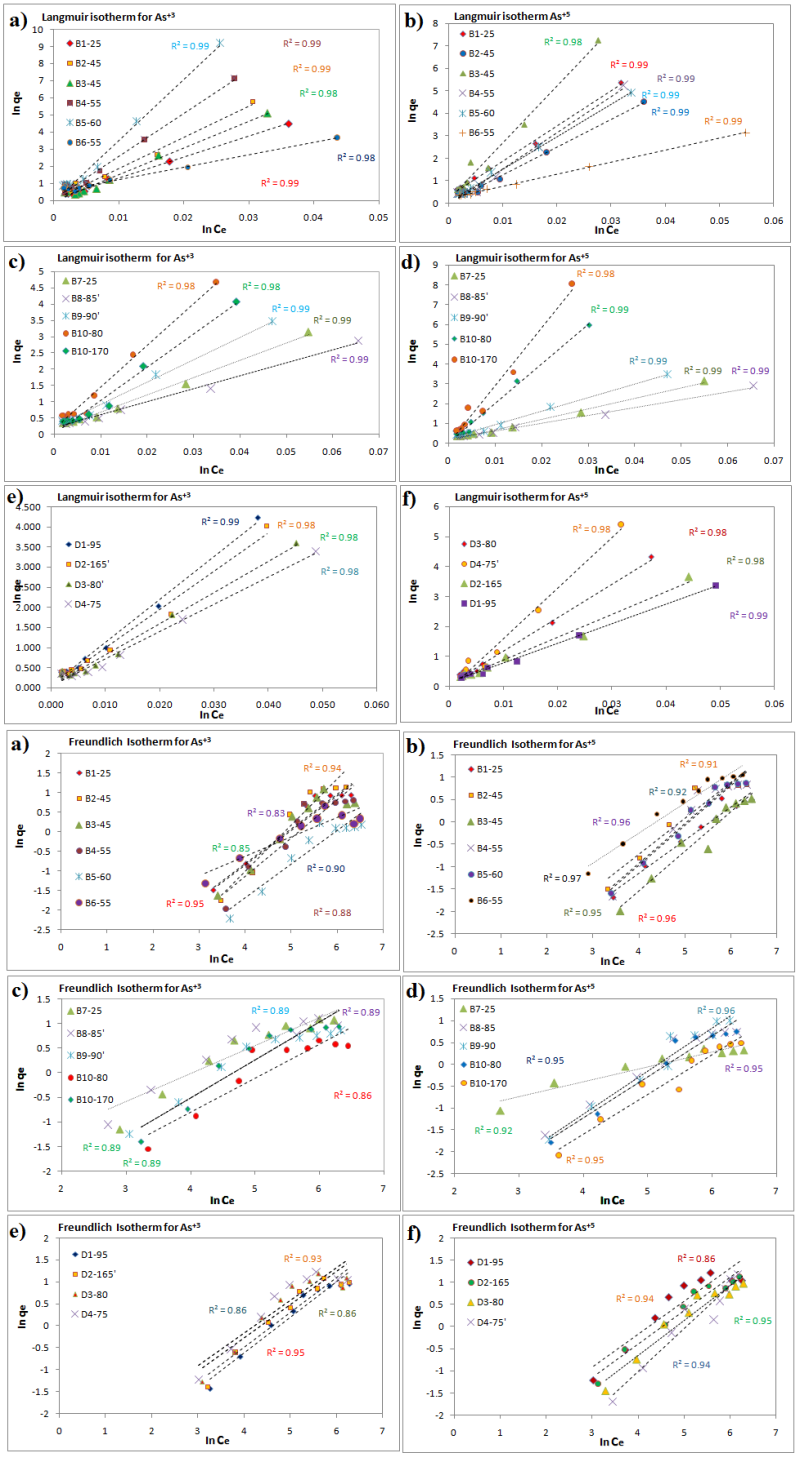

Figure 4. 15 Langmuir isotherm study results have shown in a) to f) and Freundlich isotherm study results and g) to l) for H*As*CR and L*As*CR study area.

Table 4.9 Langmuir isotherm model results showed adsorption capacity values

Sample ID	As^{+3}				As^{+5}			
	q_{max} (ug g^{-1})	b (L μg^{-1})	R^2	R_L	q_{max} (ug g^{-1})	b (L μg^{-1})	R^2	R_L
B1-25’	11.3	0.001	0.99	0.74	3.18	0.002	0.99	0.59
B2-45’	14.37	0.0003	0.99	0.9	21.37	0.0004	0.99	0.87
B3-45’	13.95	0.0005	0.98	0.73	6.93	0.001	0.98	0.7
B4-55’	14.84	0.0003	0.98	0.73	14.1	0.0004	0.99	0.9
B5-60’	17.99	0.0002	0.98	0.93	13.19	0.001	0.99	0.7
B6-55’	2.0	0.007	0.98	0.34	4.59	0.004	0.99	0.5
B7-25’	6.23	0.003	0.99	0.51	1.46	0.021	0.99	0.2
B8-85'	4.53	0.009	0.99	0.16	8.38	0.001	0.99	0.7
B9-90'	4.28	0.003	0.99	0.51	37.45	0.0001	0.99	1.0
B10-80’	5.6	0.001	0.98	0.74	42.02	0.0001	0.99	1.0
B10-170’	34.84	0.0003	0.98	0.90	142.86	0.00002	0.98	1.0
D1-95’	18.76	0.0005	0.99	0.84	7.35	0.00	0.99	0.60
D2-165’	33.67	0.0003	0.98	0.90	8.43	0.002	0.98	0.59
D3-80’	25.19	0.001	0.98	0.74	17.33	0.001	0.98	0.74
D4-75’	22.22	0.001	0.98	0.74	11.51	0.001	0.98	0.74

Table 4. 10 Freundlich isotherm model results showed adsorption capacity values

Sample ID	As^{+3}				As^{+5}			
	n	q_m (ug g^{-1})	K_d (L kg^{-1})	R^2	n	q_m (ug g^{-1})	K_d (L kg^{-1})	R^2
B1-25’	1.13	2.05	7.26	0.95	1.36	1.63	4.28	0.96
B2-45’	0.85	3.74	8.4	0.93	1.24	2.50	7.46	0.91
B3-45’	1.12	2.05	7.19	0.85	1.13	1.93	3.45	0.95
B4-55’	1.02	3.58	6.08	0.88	1.12	2.05	6.67	0.92
B5-60’	1.16	6.61	2.89	0.89	1.11	2.18	6.23	0.96
B6-55’	2.01	1.32	6.15	0.83	1.49	2.65	11.17	0.96
B7-25’	1.56	3.09	12.61	0.92	1.10	2.32	8.01	0.95
B8-85'	1.77	2.89	14.3	0.88	1.19	1.51	5.61	0.95
B9-90'	1.6	2.49	9.05	0.90	1.02	3.58	5.82	0.96
B10-80’	1.44	1.8	6.06	0.86	1.06	2.79	5.07	0.95
B10-170’	1.29	2.93	9.09	0.89	1.10	2.32	3.34	0.95
D1-95’	1.23	2.50	8.2	0.95	1.35	3.25	13.1	0.86
D2-165’	1.26	3.32	9.44	0.93	1.33	1.63	9.99	0.95
D3-80’	1.23	2.50	11.7	0.95	1.26	2.21	7.83	0.94
D4-75’	1.35	3.25	13.14	0.86	1.02	3.58	6.63	0.94

samples from West Bengal and South-East Asia showed that the distribution coefficient. ‘K_d’ values were in the range of 4L kg–1 to 40 L kg–1. Similarly, in this study, the Kd ‘values for As^{+3} was in the range of 6 L kg^{-1} to 13 L kg^{-1}, whereas for As+5, the values ranged from 3L

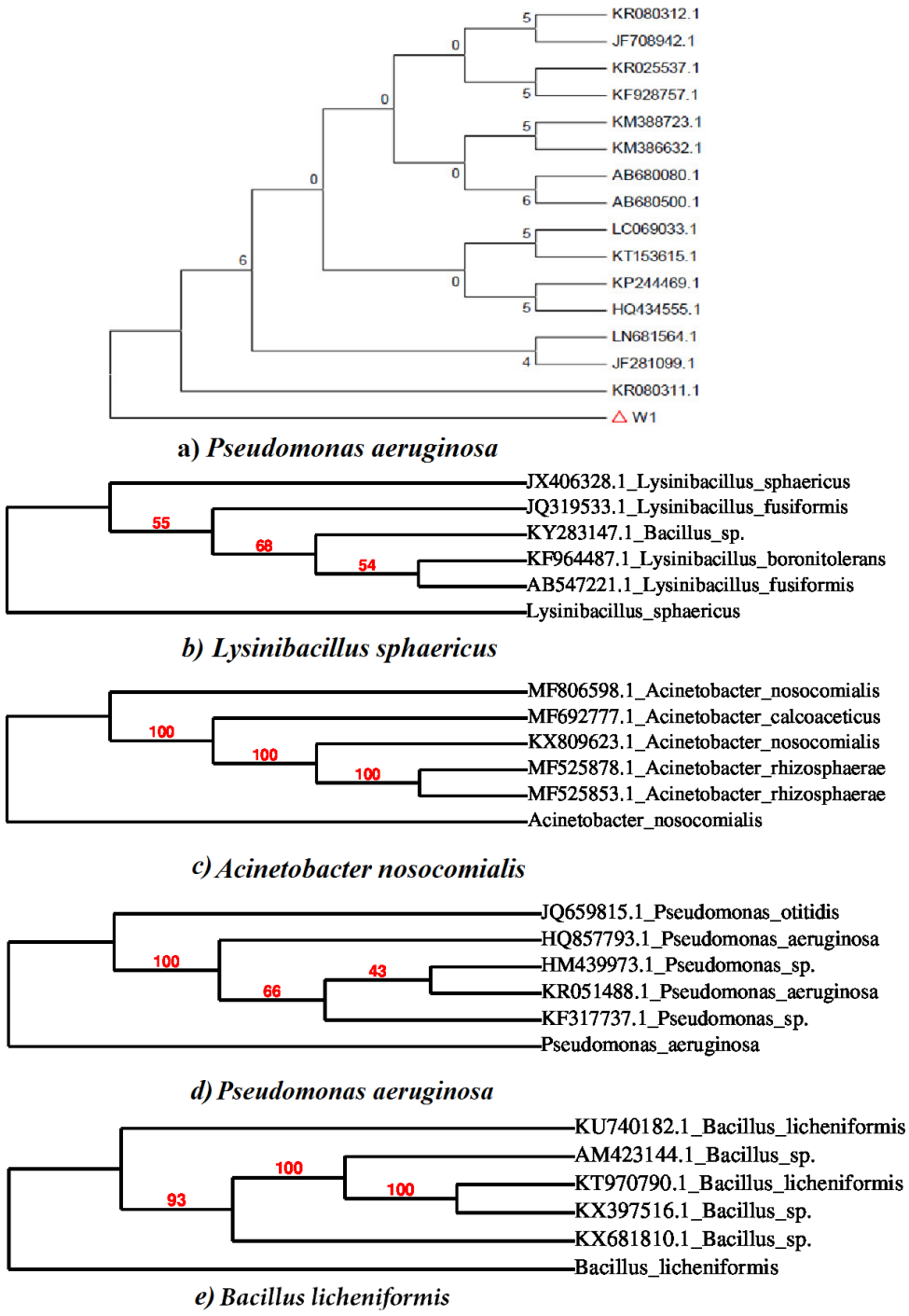

Figure 4. 16S rRNA gene neighbor-joining tree showed the genetic relationship of a) *Pseudomonas aeruginosa* from sediment, where b) *Lysinibacillus sphaericus* and c) *Acinetobacter nosocomialis*from groundwater of H*As*CR sample. Figure d) *Pseudomonas aeruginosa* and e) *Bacillus licheniformis* bacterium from groundwater of L*As*CR samples with the published microbial species in the GenBank.

kg^{-1} to 13.1L kg^{-1},which showed equal distribution coefficient values for each arsenic species. Compared to 'K_d' values with H*As*CR and L*As*CR, high 'K_d 'values were observed for L*As*CR sediment samples which infer that the L*As*CR have high adsorption capacity than the H*As*CR sediment samples.

4.3 Identification and morphology of the isolated bacterium

In a preliminary study, a white color bacterium was isolated from H*As*CR sediment sample and abbreviated as '*W1'*, whereas bacterium isolated from the groundwater samples of H*As*CR were named as BS and BL and in L*As*CR named as DS and DL based on their colony size in the cultured agar plates.

4.3.1 16S rRNA gene sequence and phylogenetic analysis

The indigenous bacterium strain (i.e., W1) was isolated from *As* rich sediment and identified as *Pseudomonas aeruginosa* from the sequence which showed similarity of nearly 99% by the blast analysis of 16S rRNA gene sequences (1453 bp) (Figure 4.18a). Moreover, the isolated bacterium was identified from 16S rRNA gene sequences from the groundwater samples (in 2017) of H*As*CR as *Lysinibacillus sphaericus* (BS) and *Acinetobacter nosocomialis* (BL) whereas, *Bacillus licheniformis* (DS) and *Pseudomonas aeruginosa* (DL) isolated from L*As*CR study areas [Figure 4.18 b),c),d) &e)]. The bootstrap consensus tree, inferred from 1000 replicates was taken to represent the evolutionary history of the taxa analyzed (Felsenstein, 1985). These cultures showed similarity with *Pseudomonas aeruginosa (W1)* [Figure 4.18a)], *Lysinibacillus sphaericus*(BS) [Figure 4.18b)] and *Acinetobacter nosocomialis* (BL) [Figure 4.18c)] from H*As*CR study area, whereas, *Bacillus licheniformis* (DS) [Figure 4.18d)] and *Pseudomonas aeruginosa* (DL) [Figure 4.18e)] from L*As*CR study

4.3.2 Morphology and elemental analysis of isolated *As*-resistant bacterium

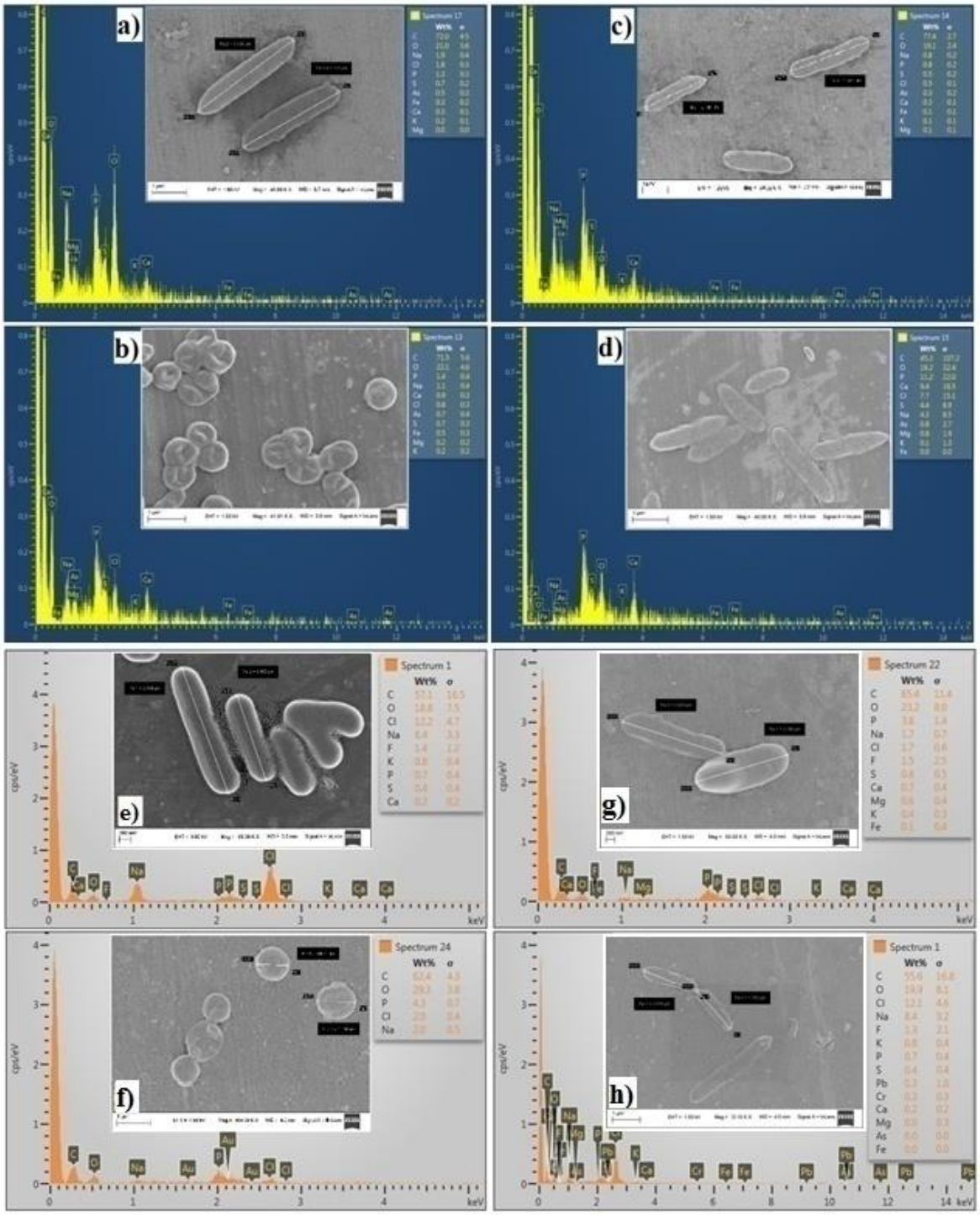

Figure 4. 17 Morphology and EDS of isolated *As* tolerant strains a) *Lysinibacillus sphaericus*, b) *Acinetobacter nosocomialis* of H*As*CR samples, d) *Bacillus licheniformis* and c) *Pseudomonas aeruginosa* bacterium from L*As*CR samples. In similar order e) & f) for H*As*CR and L*As*CR g) & h) showed cell morphology in the presence of high *As* concentration.

areas, which was confirmed based on nucleotide homology and phylogenetic analysis (Jebelli et al., 2017). The morphological analysis by FESEM instrument for the isolated bacteria depicted a rod-shaped morphology which has a length of 1.6–3.2 μm and diameter of 0.5–0.69 μm for

Pseudomonas aeruginosa (*W1*) [Figure 4.19 (a-b)]. The obtained TEM-EDS analysis results showed a rod-shaped morphology and bioaccumulation or precipitation of *As* along with Fe, S, and Mn on a bacterial surface of *Pseudomonas aeruginosa* (*W1*) bacterial cell [Figure 4.19 (c-d)]. Similarly, indigenous bacterium strains isolated from *As* rich groundwater (i.e. H*As*CR) were identified as rod-shaped for *Lysinibacillus sphaericus* (Peña-Montenegro et al., 2015) and coccobacilli shape for *Acinetobacter nosocomialis* (Ghosh and Sar, 2013) (Figure 4.21(a) and (b)). Similarly,the rod-shaped bacterium was observed (Figure 4.21c) and 4.21d)) for *Bacillus licheniformis* (Tripti and Shardendu, 2016) and *Pseudomonas aeruginosa* (Ghosh and Sar 2013) in Darrang district samples which is shown in Figure 4.21 (c) and (d). The EDS results without *As* [Figure 4.21 (a-d)] and with *As* in [Figure 4.21 (e-h)] culture have shown a clear morphology and elemental distribution as per different CDM. The different *As* concentration combination showed distorted morphology for each strains suggesting that its maximum tolerance limit and prevailing condition in a groundwater aquifer environment.

4.3.2.1 Effect of As on bacterial growth

The capability of *Pseudomonas aeruginosa* to grow in the presence of different initial arsenic (As^{+3}) concentration range from 100 to 900 mg L^{-1} was studied and results are shown in Figure 4.20 and 4.22. These results clearly revealed the in the presence of high *As* showed a reduced biomass growth profile. Also, these strain achieved maximum biomass concentrations with a delay of 12 h for all arsenic containing flasks. A clear decline could be

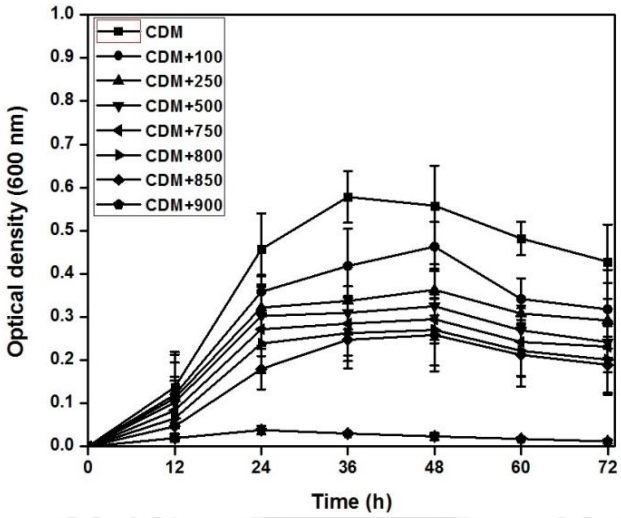

Figure 4. 18 Time profile of optical density showed for Pseudomonas aeruginosa with different initial arsenic concentrations.

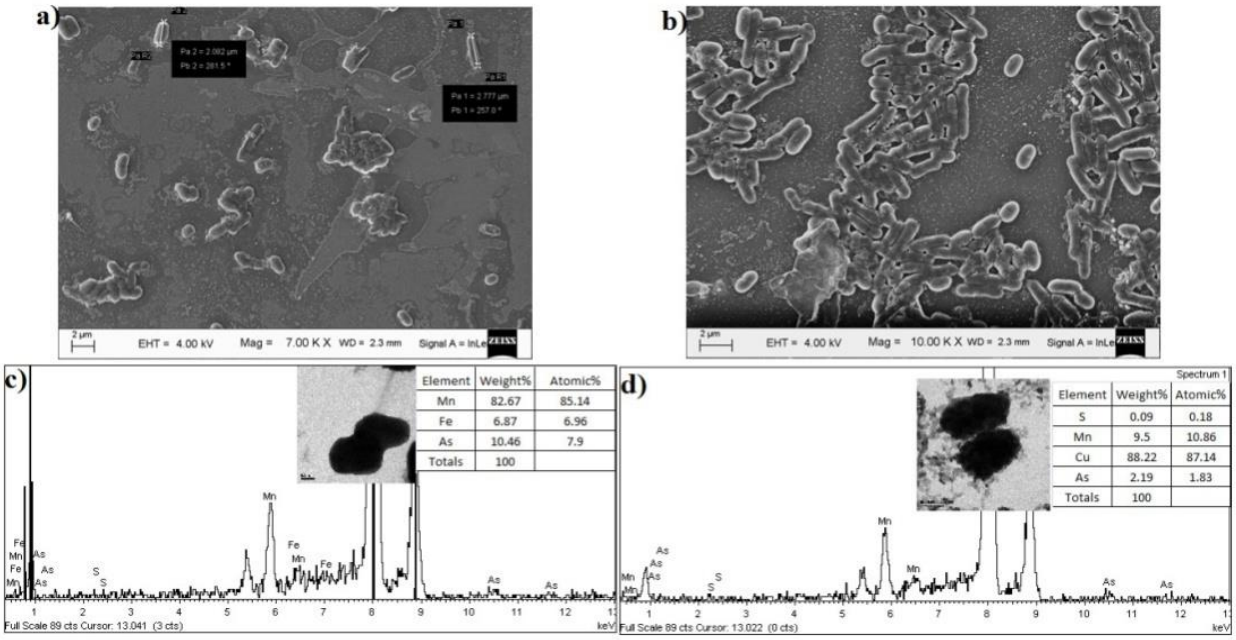

Figure 4. 19(a, b) FESEM images showed the morphology of cultured microbes; (c, d) TEM-EDS showed elemental composition and morphology of cultured microbes.

observed in all the flasks having an initial *As* concentration ranged from 100mg L^{-1} to 850 mg L^{-1}. The culture showed negligible growth in the flask containing an initial *As* concentration of 900 mg L^{-1}, it infers that the bacterial tolerance limit is 850 mg L^{-1}. Beyond this *As* concentration (i.e., 900 mg L^{-1}), the bacteria were not able to grow and it is lethal to the strain.

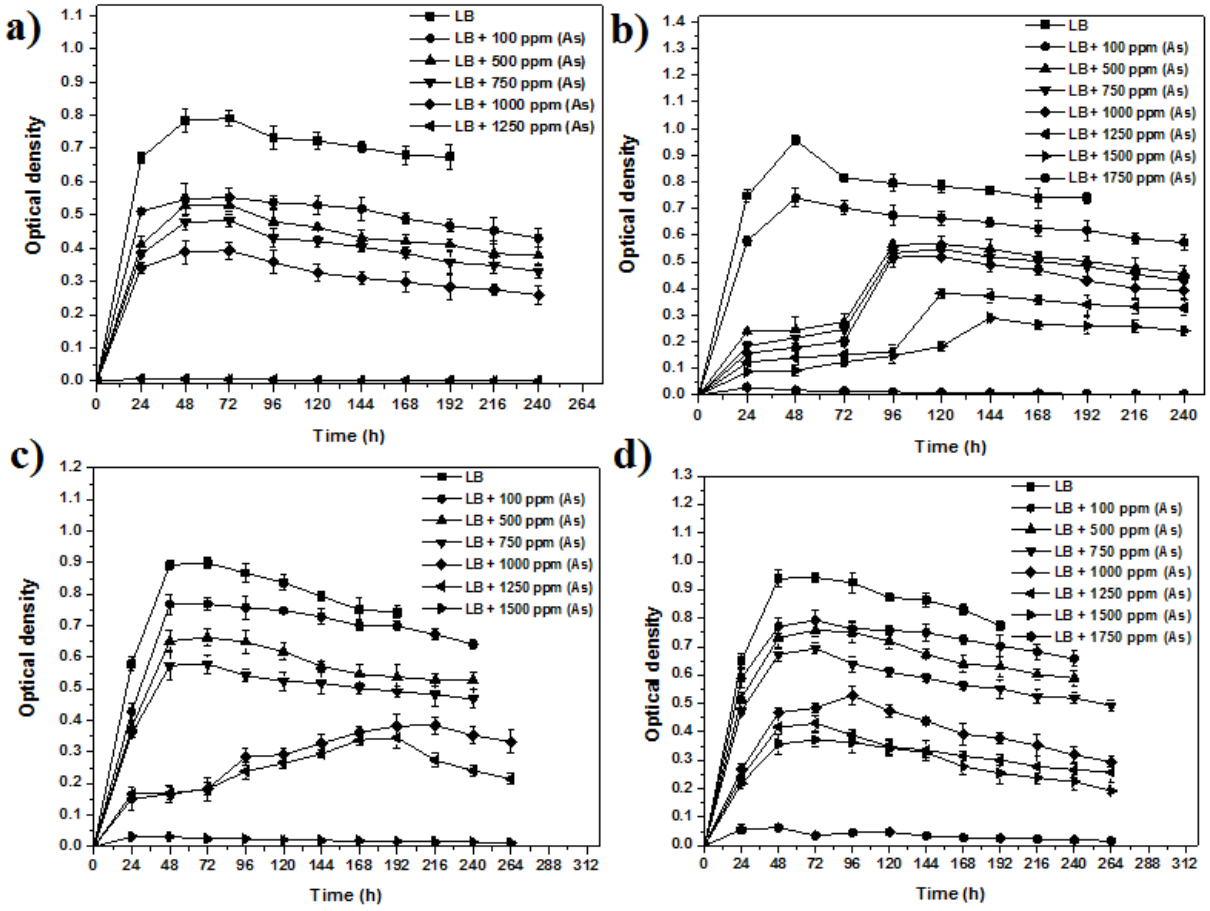

Figure 4. 20 Time profile of optical density with different initial arsenic concentration. a) *Lysinibacillus sphaericus*, b) *Acinetobacter nosocomialis* of HAsCR samples figure c) *Bacillus licheniformis* and d) *Pseudomonas aeruginosa* bacterium from LAsCR samples.

Hence, the strain isolated from the study area, *P. aeruginosa* is capable of tolerating *As* concentration to an initial concentration of 850 mg L^{-1}. In another study performed by Ghosh and Sar (2013), *Acidovorax* strain collected from the groundwater samples of northern part of Brahmaputra river, were found that the hyper-tolerant for *As* (V) as well as *As* (III), whereas *Brevundimonas* sp. was hyper tolerant to both the forms of *As* (i.e., *As* (V) and *As* (III)) and they are capable of tolerating *As* concentration of 550 µg L^{-1} and 50 µg L^{-1} respectively.

Batch experiments were performed for evaluating the effect of different initial arsenic [*As* (III)] concentration on the bacterial growth using LB medium. 1% (w/v) of the inoculum size was taken for conducting each of the experimental runs. Figure 4.22 illustrates the

bacterial biomass growth curve with and without the presence of arsenic in the flasks. For H*As*CR district, bacterium BS was isolated from the shallow aquifer groundwater samples. The growth profile of the bacterium in the presence of *As* concentration was found up to 1000 mg L^{-1} of *As* concentration [Figure 4.22a)],whereas, for BL,the growth profile was observed up to *As* concentration limit of 1500 mg L^{-1}[Figure 4.22 b)]. A lag phase of 48 hours was observed beyond the *As* concentration of 500 mg L^{-1} for DL, and bacterium was able to grow after the lag phase. From Figure 4.22c), it is clear that the bacterium DS was capable of growing and maintaining itself in presence of arsenic concentration up to 1250 mg L^{-1}. Beyond this limit, the bacterium was not able to survive; therefore, no growth was observed in the flask containing 1500 mg L^{-1} of *As* concentration. Similarly, for DL strain, the growth inhibition for the bacterium was found for *As* concentration of 1750 mg L^{-1}. The DL strain was capable of surviving in the media up to the concentration of 1500 mg L^{-1}, and after that, no growth has been observed [Figure 4.22d)]. Although the strain achieved the growth profile even in the presence of arsenic, there was a clear decline in the biomass when it compared with the control flasks (without arsenic). Hence, for DL, DS, BL, and BS, from Figure 4.22, it was clear that arsenic tolerance limit was 1500, 1250, 1500 and 1000 mg L^{-1}, respectively. But, arsenic concentration beyond these for the isolated bacteria showed that these bacteria are not able to grow and are lethal to the strains.

4.3.2.2 The qualitative $KMnO_4$ screening method

The growth of the culture at and above an optical density (OD) of 0.4 value was used for the qualitative screening test (Salmassi et al., 2002). In which this test inferred that a pink color of the mixture indicates a positive arsenite oxidation reaction [formation of *As* (V)], and

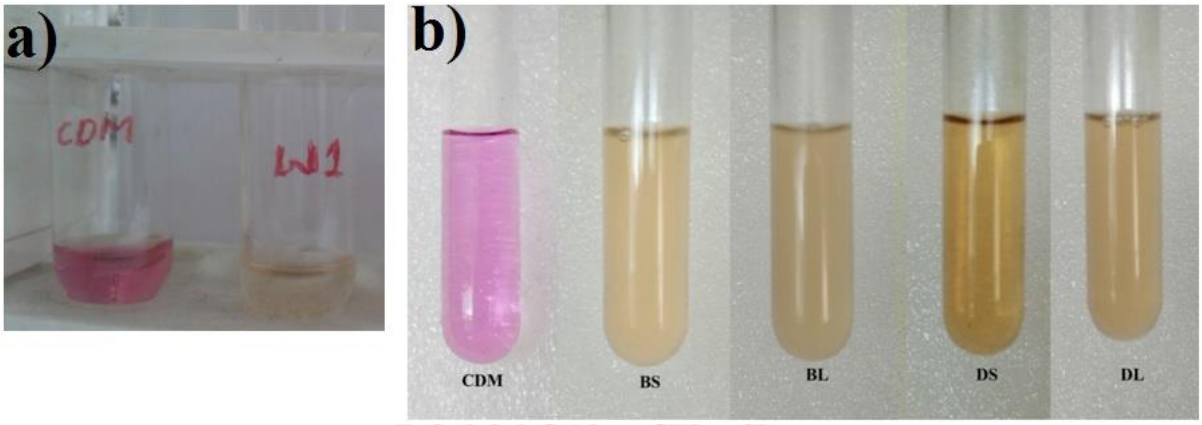

Figure 4. 21Qualitative screening test results showed the presence of Arsenate reducing bacteria were BS- *Lysinibacillus sphaericus*, BL- *Acinetobacter nosocomialis*, DS- *Pseudomonas aeruginosa*, DL- *Bacillus licheniformis* represents, respectively.

yellow color indicates a positive arsenate reduction reaction [formation of *As* (III)] (Fan et al. 2008, Salmassi et al. 2002). The screening test for the entire obtained culture showed a positive yellow color which suggests that arsenate reducing characteristic of the isolated bacterium, which is capable of reducing arsenate (i.e. As^{+5} to As^{+3}) (Figure 4.23).These isolated bacteria viz. *P.aeruginosa,*and *Lysinibacillus sphaericus* microbe are a member of *Pseudomonadaceae* and *Bacillaceae, Moraxellaceae* respectively, whereas the *Acinetobacter nosocomialis* strain is a member of *Moraxellaceae* family, which was found in the study area and is very well known for its respiration and reducing nature of *As* (V), in the natural environment (Cai et al., 1998, 2016). It was also been observed in several other studies that most of *Pseudomonas* sp.,*Bacillaceae* (Paul et al., 2015) and *Moraxellaceae*are a facultative bacteria respectively, whereas the *Acinetobacter nosocomialis* strain is a member of *Moraxellaceae* family, which was found in the study area and is very well known for its respiration and reducing nature of *As* (V), in the natural environment (Cai et al., 1998, 2016a). It has also been observed in several other studies that most of *Pseudomonas sp.* is a facultative anaerobic bacterium which uses

nitrate as an electron acceptor and also belongs to the genera of manganese-reducing bacteria (Gounot 1994).

4.4 Numerical simulation

4.4.1 Stratigraphy model

Stratigraphy 3D model was developed to study a conceptual model (for groundwater flow and contaminant transport modeling), using lithology of both the study areas. Figure 4.24 (a) and (b) showed 3D stratigraphy model, suggesting the presence of complex hydro-stratigraphy framework in the sub-surface of the study area. The results of the stratigraphy model for H*As*CR study area suggested a thick layer of grey colored clay capping over the sandy aquifer, which is observed near the Mansa and Brahmaputra River of H*As*CR. Grey color sandy aquifer was observed at the shallow depth in L*As*CR study area. Appendix Figure L 1.1 and 1.2, showed details of fence diagram and cross-sectional view of sub-surface aquifer for H*As*CR and L*As*CR study areas.

Moreover, the 3D stratigraphy [Figure 4.24 (a) and (b)] view depict a probable lateral and vertical extension of each sandy aquifer in the study areas. It can be inferred from the stratigraphy model is that thick capping of (~6.1 m) clay layer was ubiquitous over the sandy aquifer. The shallow depth aquifers predominately contain medium to coarse sand with clay fraction, it suggests that weathering and erosion of parent rock at the origin of rivers and deposition of suspended sediment on a flat terrain which has formed complex stratigraphy in both the study areas. The 3D stratigraphy model showed aquifer connectivity with the adjoining aquifers, which preliminarily predict the possible groundwater flow and contaminant direction in the deeper and lateral direction. In H*As*CR region stratigraphy model, the results depict the presence of brown sediment near hill locks whereas, the grayish color sediments

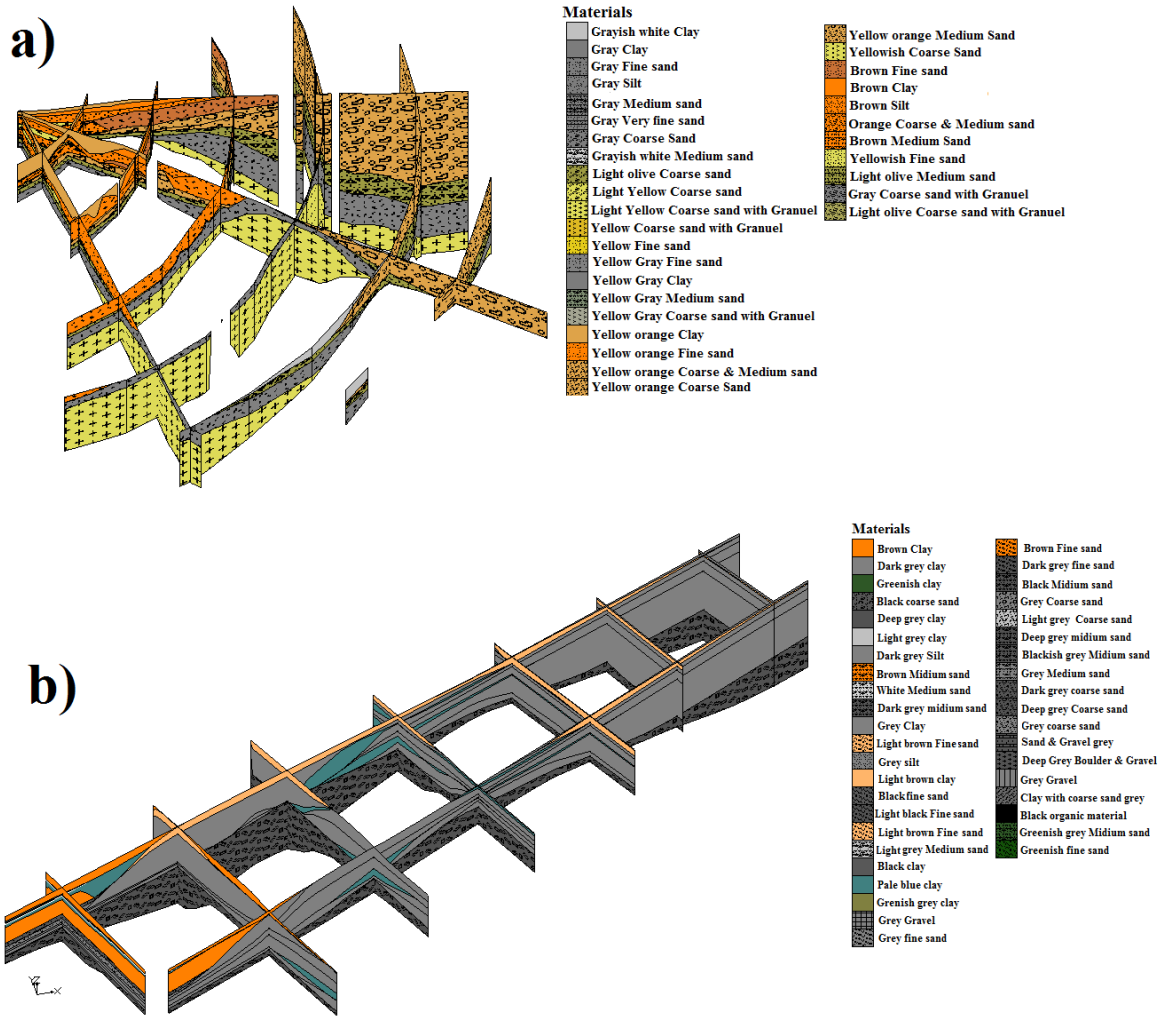

Figure 4. 22 Stratigraphic 3D views showed distribution and extensivity of each aquifer and soil material in the lateral and vertical direction, a) H*As*CR study area stratography b) L*As*CR study area stratigraphy.

predominate near the riverine area [Appendix Figure L 1.1, 1.2]. Moreover, in L*As*CR study area stratigraphy model portrayed, thin (~4.6 m) top layer dominated by brown color whereas successive depth aquifers are dominated by grayish color sediment [Appendix Figure L 1.1, 1.2].

4.4.2 Permeability test

The falling head permeability test was performed on individual and combined soil materials (viz. clay, clay-fine sand, clay-fine-medium sand and coarse sand with gravel) to

estimate the true hydraulic conductivity [Appendix Figure M 1.1, 1.2, 1.3, 1.4]. The average hydraulic conductivity values estimated for the equal thickness of the clay, silty- fine sand, medium sand, clay-medium sand, clay-fine-medium sand, and sandy- gravel was 0.0061 m d^{-1}, 0.08 m d^{-1}, 0.33 m d^{-1}, 0.0031 m d^{-1}, 0.0069m $d^{-1}$and 4.79 m d^{-1}, respectively (Table 4.11).

Table 4. 11 Estimated values for respective soil material properties for transient state MODFLOW simulation

Soil	Initial hydraulic conductivity		Calibrated hydraulic conductivity		V. A.	Ss (1/m)	Sy (%)	L.D (m)	e (%)
	Kx=Ky (m/d)	Kz (m/d)	Kx=Ky (m/d)	Kz (m/d)					
Clay	0.006	0.0006	0.0036	0.00036	10	0.0045	3	198	42
Silt	0.08	0.008	0.078	0.0078	10	0.001	8	50	46
Very fine sand	0.08	0.008	1.5	3	10	0.0005	20	50	40
Fine sand	0.16	0.32	2.5	5	0.5	0.0005	23	50	43
Medium sand	0.33	0.7	35.9	71.8	0.5	0.0008	28	112	39
Coarse sand	2.4	4.8	45	90	0.5	0.0005	27	83	39
Sandy gravel	4.8	9.6	150	300	0.5	0.0005	23	50	28
Coarse with medium sand	40	80	150	300	0.1	0.0005	27	50	39
Coarse sand with granule	150	300	150	300	0.1	0.0087	23	342	28
Gravel	150	300	150	300	0.5	0.0005	23	50	28
Boulder with gravel	150	300	150	300	0.1	0.0005	23	50	28

Note: Kx=Ky and Kz are "Horizontal and Vertical hydraulic conductivity" respectively, V.A. - Vertical anisotropy, Ss - "Specific storage", Sy - "Specific yield," e - "porosity", L.D - "Longitudinal dispersivity".

The hydraulic conductivity results for the combination of clay-medium sand and clay-fine-medium sand materials was observed less due to the presence of equal thickness of the clay layer at the bottom of the mould. The average hydraulic conductivity results for each repacked sediment sample test was in agreement with the reported hydraulic conductivity range for the respective soil materials by Morris and Johnson (1967).

4.4.3 Groundwater flow and sensitivity analysis

An initial head condition, for groundwater flow simulation, calibrations, and groundwater head was calculated by running the model for steady state condition initially and

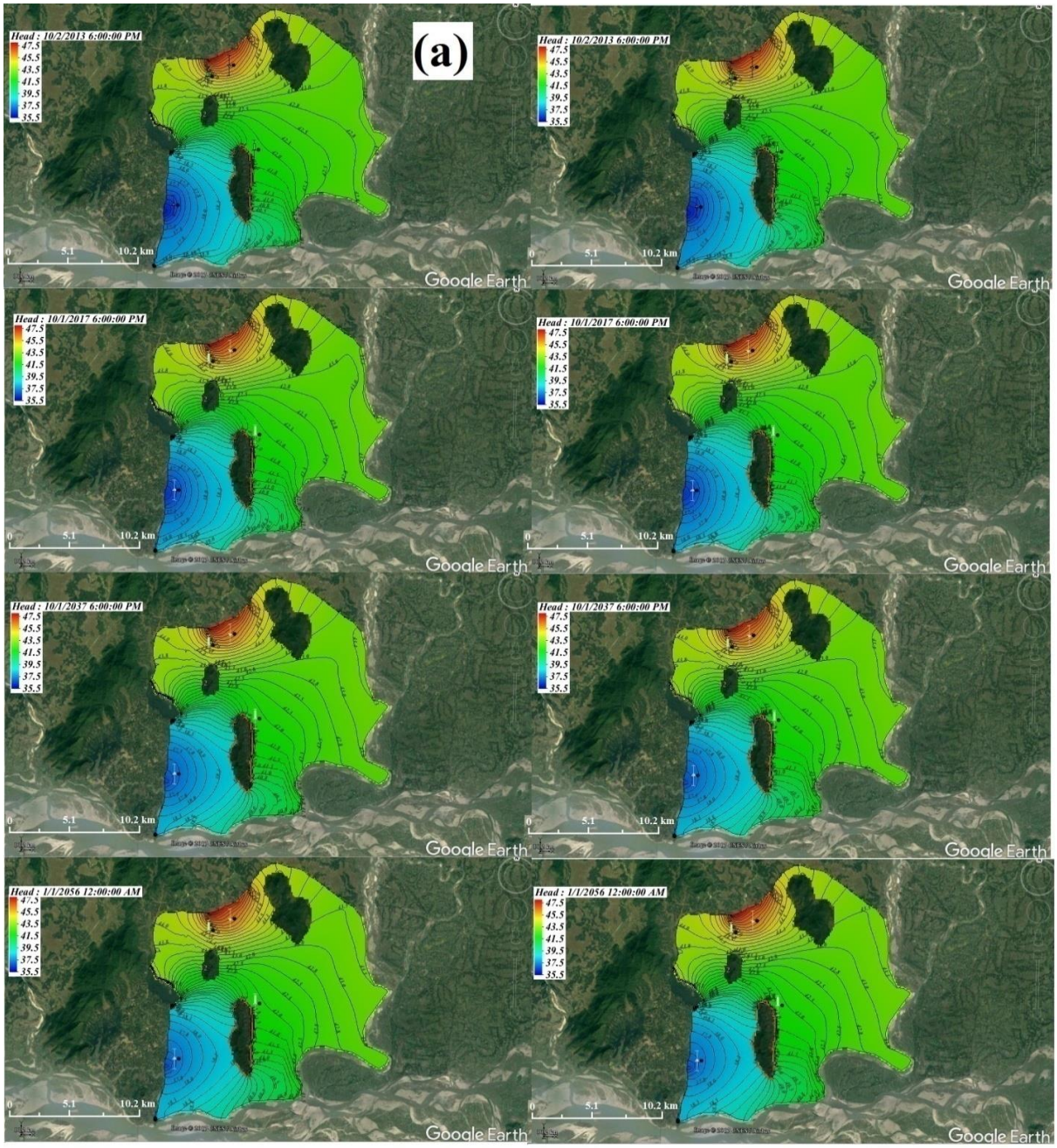

Figure 4. 23 MODFLOW simulation results for selective stress period showed contour distribution for layer 4th and 5th of H*As*CR study area.

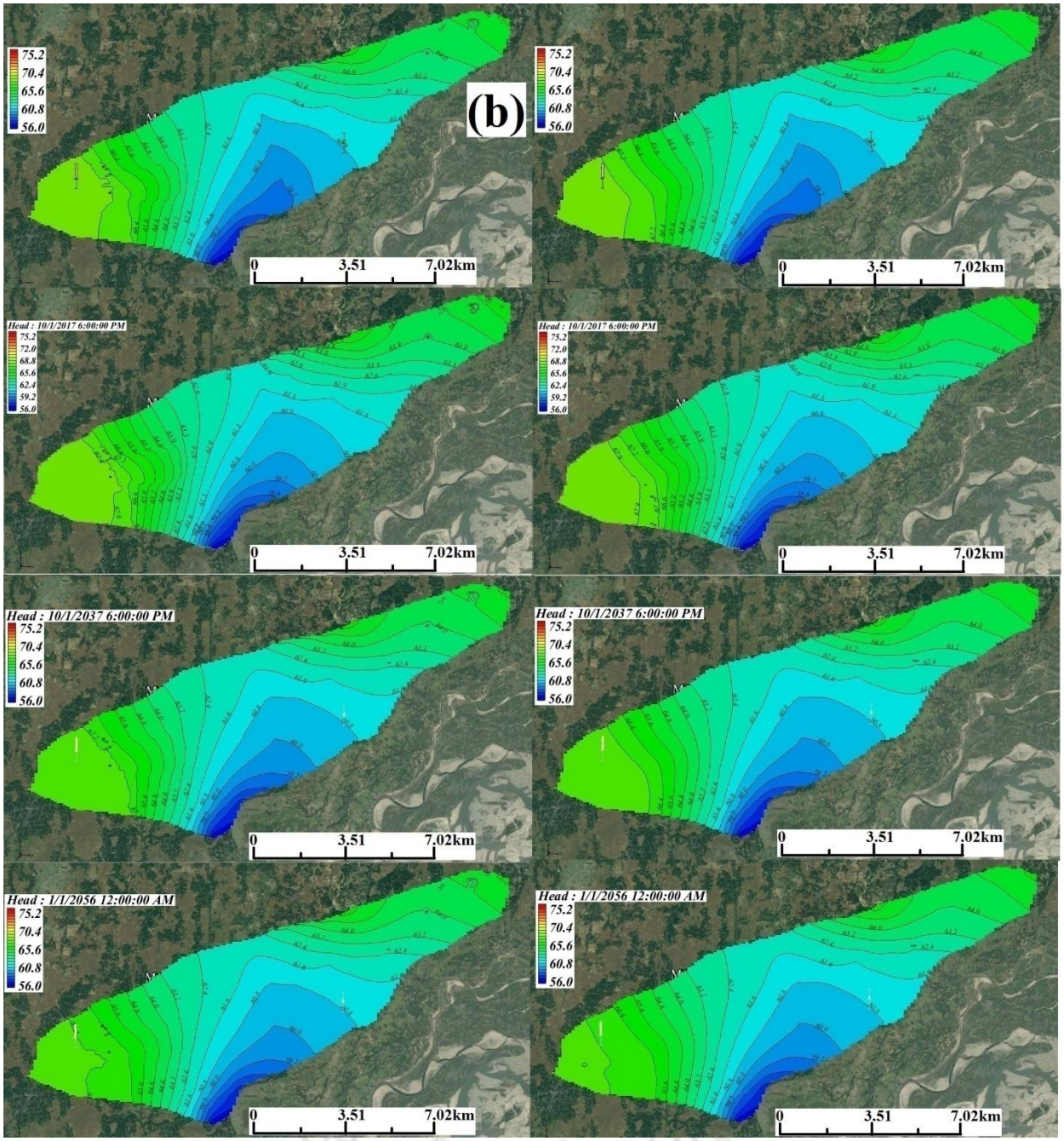

Figure 4. 24MODFLOW simulation results for selective stress period showed contour distribution for layer 9th and 15th of L*As*CR study area.

then run for transient state conditions (viz. since 1st January 2013 to 31st December 2055) (Appendix Table F 1.1). The simulation models were calibrated by changing the values of

hydraulic conductivity (esp. Kx and Kz), specific yield (Sy), storativity (Ss) and well-pumping rate, to obtain a significant reasonable value. The values were adopted for groundwater flow model and cross checked with the empirical values reported by Morris and Johnson, (1967) for the simulations. The vertical hydraulic conductivity (Kz) value for clay and silt was assumed to be 1/10 of horizontal ($K_x = K_y$) hydraulic conductivity for the respective soil (Mukherjee et al., 2007) whereas for sandy aquifer it was assumed twice of horizontal (K_x) hydraulic conductivity (Table 4.11). Todd and Larry, (2005) mentioned empirical values for various soil especially; porosity, specific storage, and specific yield were used for the respective soil materials in MODFLOW simulation (Table 4.11). Finally, the calibrated aquifer parameters and model validation showed reasonable agreement with the present groundwater (viz. observation well data) distribution scenario for H*As*CR and L*As*CR study areas (Figure 4.25 and 4.26). The results depicted that it is the equal success of model calibration and validation. The MODFLOW simulation results for H*As*CR depicted that Manas and Brahmaputra rivers, head stage and its conductance have a major influence on groundwater inflow rate, whereas drain and head-dependent flow boundary on the South - Western side, were acting as a major sink parameter for groundwater flow simulation (Figure 4.26). Similarly, Brahmaputra river inflow rate and meteoric water recharge control the MODFLOW simulation results for L*As*CR study area (Figure 4.25). The drains flowing through the study areas have a major secondary local effect on groundwater flow distribution acting as a sink for groundwater and *As* contaminant.

The predicted simulation results for the L*As*CR study area depicted that the groundwater was flowing from North- Eastern region to South-Western region of the study area. Here, the assigned specified head boundary condition and Brahmaputra River was the major controlling factors for the inflow and outflow rate of groundwater in the study area. The

models were validated using seasonal observation well data obtained from central groundwater board (CGWB) of India for H*As*CR and L*As*CR study area. The validated results were almost matched with the error bar (viz.allowable head difference of ~5m), and observed transient head confidence was 95%, observed transient head standard deviation was 2.6. The model assumption and numerical values achieved reasonable accuracy with the observation well head data within an average of groundwater head difference of ~3m.

4.4.4 Groundwater flow budget and sensitivity analysis

The groundwater tables in these regions occur within ~ 10 m below the ground level, and well corroborated with the observation well data of the study (Enmark and Nordborg 2007, Mahanta et al. 2015). Furthermore, in the observation vs. computed groundwater head plot have shown that, at the middle of each stress period (i.e. July-August), aquifers were replenished by potential recharge sources (viz. rainfall, surface water bodies) (Figure 4.25 and 4.26). The colored error bar used for model calibration, the center of the target bar signifies the observed head value. Top of the target bar corresponds to the observed head value plus the interval, and the bottom corresponds to the observed head value minus the interval. If the bar lies entirely within the target, the color bar is drawn in green. If the bar is outside the target, but the error is less than 200%, the bar is drawn in yellow color. The error greater than 200%, the bar is drawn in red. In this study, we observed error bar was green and yellow for few time steps in both simulation model (Figure 4.25 and 4.26).

The MODFLOW results for both the study areas showed that hydraulic conductivity, the rate of groundwater pumping (i.e. shallow and deeper wells) and stream-bed conductance were observed more sensitive parameters for the net change in the groundwater contour

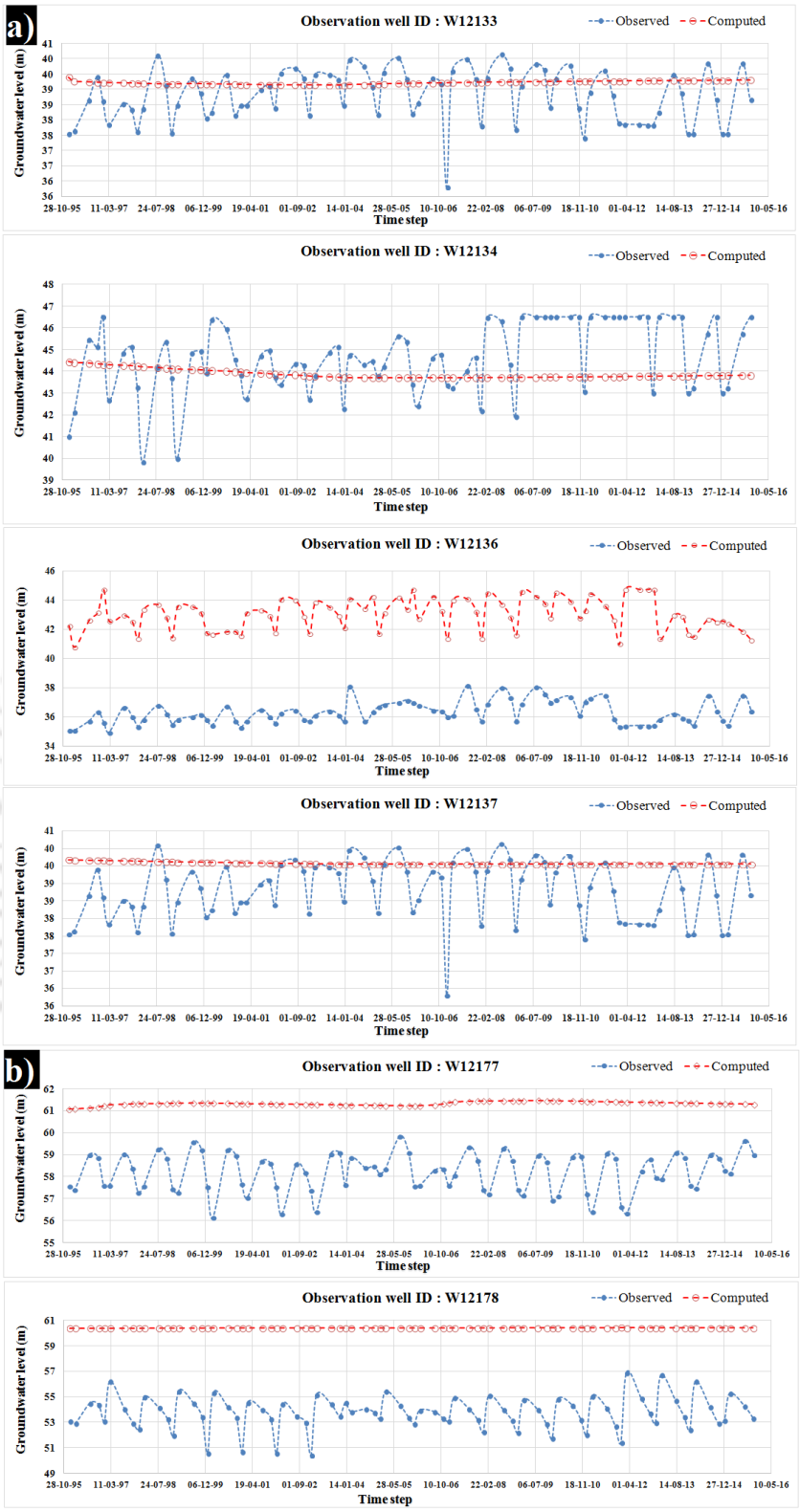

Figure 4. 25 Observed groundwater head and model computed groundwater head for a) H*As*CR and b) L*As*CR study areas

Table 4. 12 Summary of total MODFLOW simulation groundwater flow budget

HAsCR study region		**LAsCR study region**	
In:	**Flow (m^3/d)**	**In:**	**Flow (m^3/d)**
Constant head	1108946.0	Constant head	22769.4
Wells	0.0	Wells	0.0
Drains	0.0	Drains	0.0
River leakage	3726365.6	River leakage	422590.0
ET	0.0	ET	0.0
Head dependent boundary	157314.0	Head dep bounds	13259.6
Recharge	54.7	Recharge	122936.4
Storage	92464.9	Storage	18600.7
Total In	**5085145.2**	**Total In**	**600156.0**
Out:	**Flow (m^3/d)**	**Out:**	**Flow (m^3/d)**
Constant head	0.0	Constant head	2128.9
Wells	63871.6	Wells	14080.0
Drains	403657.0	Drains	44337.9
River leakage	164235.1	River leakage	418819.5
ET	124867.3	ET	110525.7
Head dependent boundary	0.0	Head dep bounds	0.0
Recharge	0.0	Recharge	0.0
Storage	4328602.9	Storage	10024.0
Total out	**5085233.9**	**Total out**	**599916.0**
Summary:	**0.0**	**Summary:**	**0.0**
In - Out	**-88.8**	**In - Out**	**240.0**
Percent Discrepancy	**-0.5**	**Percent Discrepancy**	**7.2**

distribution. The models were less sensitive to porosity, specific yield (Sy) and storativity (Ss) values. The rivers head stage (i.e. specified heads boundary condition) was observed influencing the heads distribution in adjacent cells. The sensitivity analysis trends for both the studied areas were observed almost the same. Figure 4.25 (a) and 4.26 (b) showed groundwater head variation between observed and computed head for each number of time stress periods.

The total flow budget suggests that the regional flow systems mainly control the groundwater level in both the studied areas (Table 4.12), which well corroborate with the conclusion of Harvey et al., (2005) and Mukherjee et al., (2007) for study areas in Bangladesh

and western Bengal, India. The total mass balance for each study area by MODFLOW simulation model was interpreted using the following equation,

Specified head boundary condition $_{(in)}$ + General Head boundary condition $_{(in)}$ + Head dependent flow boundary condition $_{(in)}$ + Storage $_{(in)}$ + River Leakage $_{(in)}$ + Darin $_{(in)}$ + Recharge $_{(in)}$ = Specified head boundary condition $_{(out)}$ + General Head boundary condition $_{(out)}$ + Head dependent flow boundary condition $_{(out)}$ + Storage $_{(out)}$ + Pumping well $_{(out)}$ + Evapotranspiration $_{(out)}$… (30)

Where: river leakage and drain are the potential conductance capacity and head stages which contribute to flow in and out for the modeled study areas. Recharge from meteoric water considered as inflow and outflow as evapotranspiration for the modeled study areas. The average groundwater head contours residuals from the simulation were calculated by taking a difference between the observed head and computed head of the wells, namely W12133, W12134, W12136 and W12137 as -0.5 m, 0.7 m, -5.6 m and -0.8 m respectively, for H*As*CR study area [Figure 4.27 (a)]. In L*As*CR simulation, the average residual head was observed for W12177 and W12178 observation wells, as -3.2 m and -6.7 m, and -6.7 m, respectively [Figure 4.27 (b)]. The values of positive and negative residue suggested that the model is underestimating and overestimating the inflow and outflow rates, respectively.

In H*As*CR region flow budget summary, the major groundwater inflow parameter was river head stage and potential recharge. They have a major contribution to the shallow depth aquifer replenishing in H*As*CR and L*As*CR. The major groundwater outflow sources were drains, river, evapotranspiration and well-pumping rate that balance the groundwater distribution in the shallow depth aquifer in study area regions. Hence, the outflow budget summary depicted that the drains, evapotranspiration, wells and constant head boundary

condition where the major controlling parameters for groundwater level in both the study area. The minimum recharge in H*As*CR, indicates relatively long residence time (low flushing) of groundwater, which suggest that the arsenite diffusivity parameter was the dominating cause for high *As* contamination whereas, in L*As*CR the dynamic flow system (high flushing) suggests that the advection parameter controls the arsenite distribution in groundwater aquifer making the region less contaminated.

4.4.5 Contaminant transport (MT3DMS) model simulation

The objective importance of this study was to understand the effect of hydro-stratigraphy, pumping rate, recharge rate, and rivers head stage and leakage on the movement of potentially high *As* affected groundwater at the regional scale. Both the simulation results have helped to understand the movement of the *As* concentration gradient and delineate the safe zones for groundwater resource in both the studied areas. In H*As*CR study area (Figure 4.28), the results depicted that the shallow depth groundwater near the Brahmaputra River would yield *As*safe groundwater, although comparatively, it has less flushing capacity than L*As*CR study area observed in Figure 4.29. The results of MODFLOW and MT3DMS simulation suggest that *As* transport was mainly controlled by the meteoric water recharge, specified boundary conditions, leakages of the river and drains which were mainly acting as a sink parameter in the model for both the study areas.

In L*As*CR study area, a considerable low *As* concentration variation was observed, suggesting that the hydrology has a potential capacity to flush the present *As* contaminated aquifer at the shallow depth, whereas comparatively less flushing capacity of aquifers was observed in Bongaigaon district study area. The groundwater velocity is comparatively low in

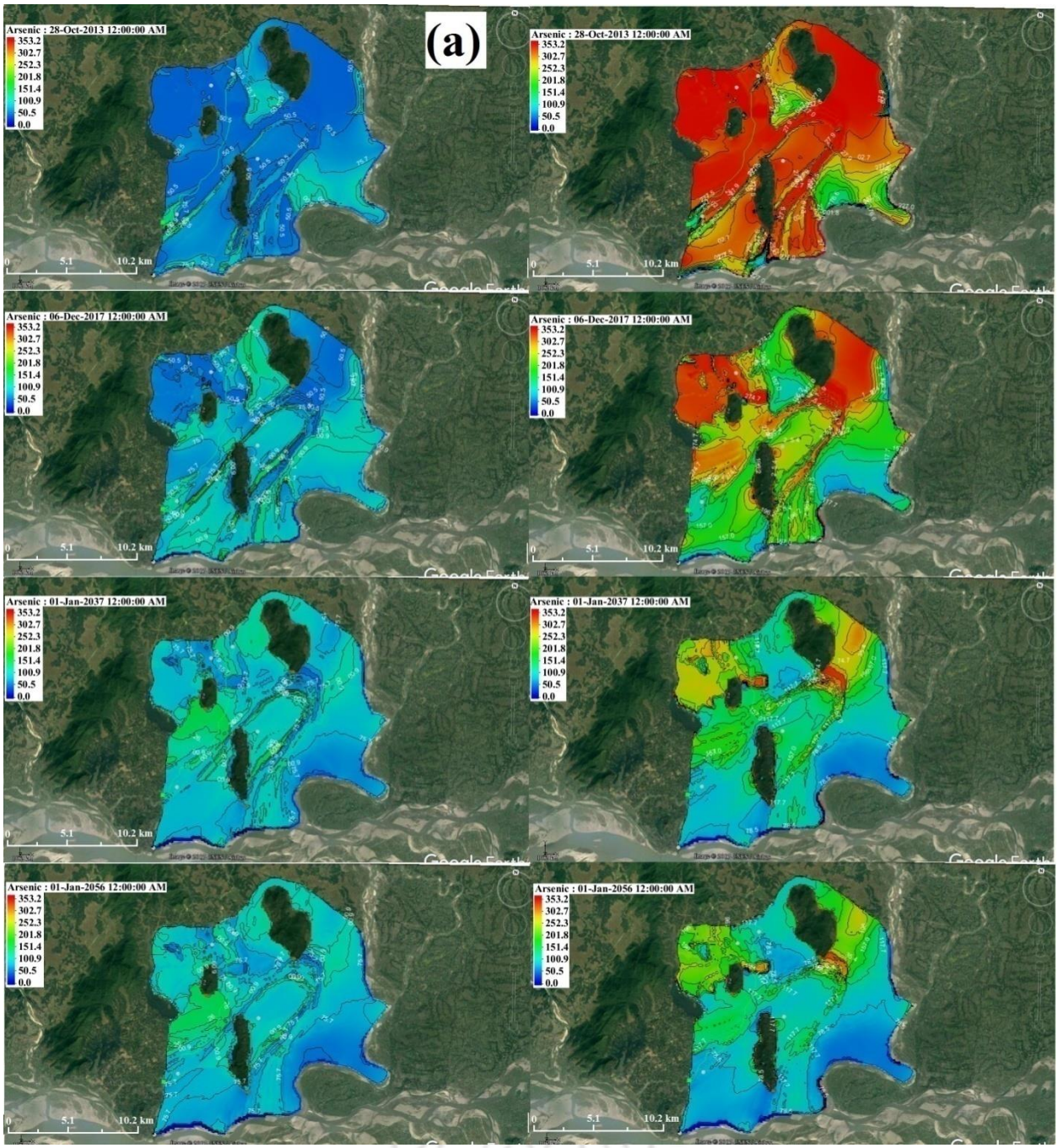

Figure 4. 26MT3DMS simulation results for *As*contaminant transport at the 4th and 5th layer (last) of H*As*CR study area

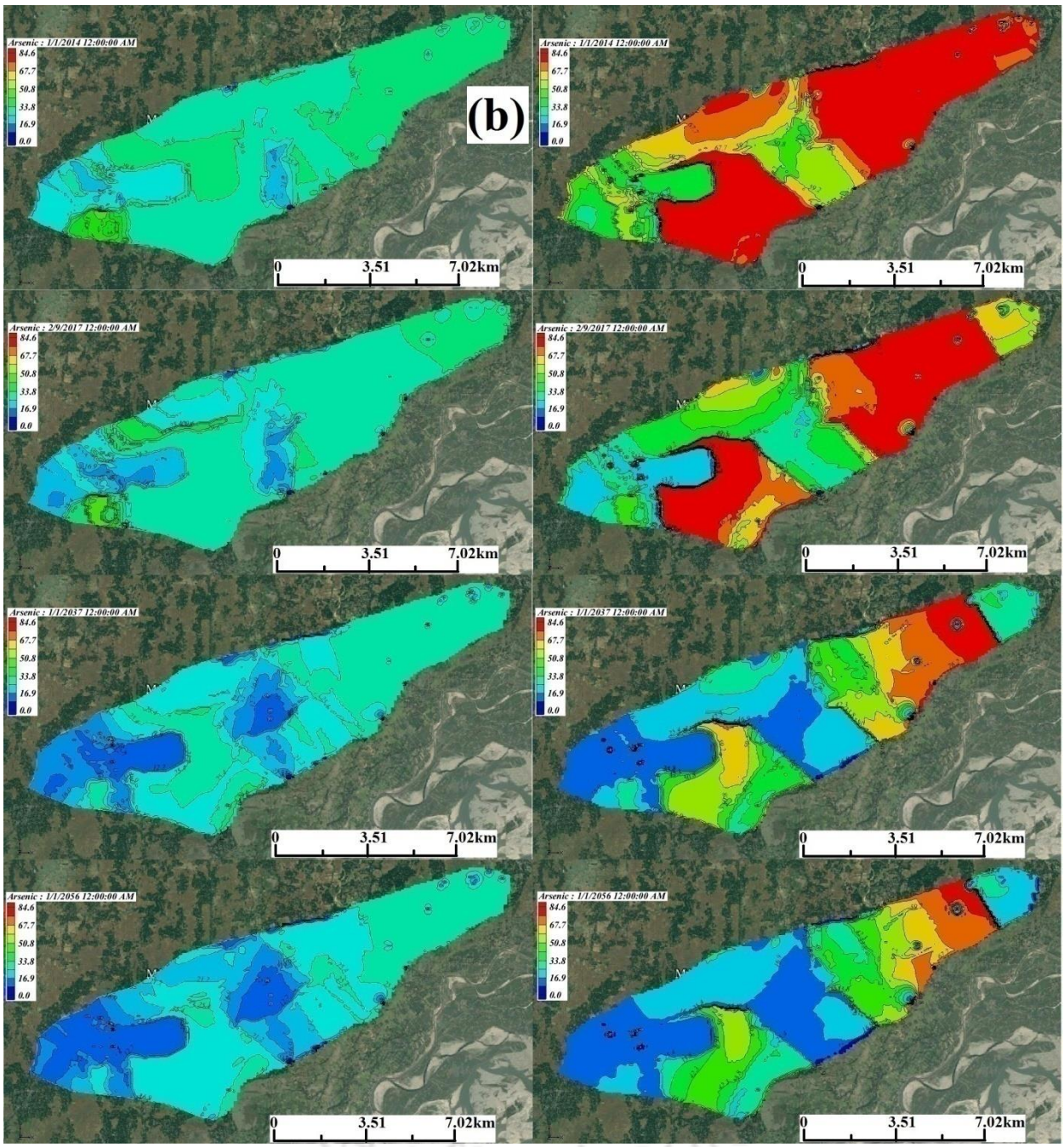

Figure 4. 27 MT3DMS simulation results for *As* contaminant transport at the 9th and 15th layer of L*As*CR study area

HAsCR study area than the LAsCR. Suggesting stagnation of *As* contaminated groundwater over a long period cause for high *As* contamination and more favorable condition for minerals precipitation and formation. This may contaminate deeper aquifers as well. Dynamic

groundwater flow was observed in the L*As*CR study area, which has some patchy high *As* contaminated groundwater regions, suggesting that the presence of low permeable hydro-stratigraphy hinder the movement of dissolved *As* flume in the shallow aquifer. Moreover, the MT3DMS transport simulation results of H*As*CR study area for As^{+3} suggested that dispersion and advection coefficient values were a dominating contaminate transport parameter in the H*As*CR and L*As*CR study area.

Chapter 5

5 Summary and Conclusion

5.1 Summary

5.1.1 Hydro-geochemistry

1. Groundwater samples analyzed in the year of 2013 and 2017 showed acidic to alkaline nature, with a strong to moderate reducing condition in H*As*CR and L*As*CR respectively. Significant concentrations of competing ions such as HCO_3^- (in H*As*CR 89 mg $L^{-1}$to 138 mg L^{-1} and in L*As*CR 57 mg L^{-1} to 142 mg L^{-1}) and PO_4^{-3} (in H*As*CR 1.9 mg $L^{-1}$to 2 mg L^{-1} and in L*As*CR 0.03 mg L^{-1} to 0.8 mg L^{-1}) were observed in both the years groundwater samples. These anions replace the adsorbed *As* from the surface of sediments and increases the dissolved *As* concentration in the groundwater.

2. The bivariate plots depict silicate and carbonate minerals dissolution, along with organic matter oxidation/degradation, prevailing in both the study area aquifers.

3. Based on the Piper plot, water chemistry was classified into two major water facies such as (1) Ca^{2+}–HCO_3^- and (2) Ca^{2+}–Na^+–HCO_3^- observed in the year 2013 of H*As*CR and L*As*CR groundwater samples but in the year 2017 groundwater facie as HCO_3^-– SO_4^{2-}–Na^+ observed only in L*As*CR region.

4. Minerals and gases saturation indices helped to predict the presence of authigenic and detrital minerals in both the study areas. The saturated condition of *As* and Fe bearing minerals suggests that the presence of these minerals was the major cause for heterogeneous *As* distribution over

both the study areas. However, the saturation indices for gases such as CO_2, CH_4, H_2S, O_2, and NH_3 depict the actual groundwater condition with microbial activity prevailing at shallow depth aquifers.

5. The positive Pearson correlation values of *As* with Fe, HCO_3^- and Mn in H*As*CR region depicts that these mineral reductive dissolution and adsorption mechanism was the primary cause for high and low *As* concentration in the H*As*CR and L*As*CR study area.

5.2 Sediment analysis

1. The Munsell color classification system helped to develop a clue for mineral content interpretation. In H*As*CR region, the aquifers near Manas River was dominated with dark grey to light grey color sediments whereas the area near the hillocks predominantly contains reddish brown to yellow sediment color. In L*As*CR region, distinct patchy brown, greenish-grey, pale-blue and white color sediments were observed. The yellowish to reddish brown color sediments (at shallow depth), suggested precipitation of iron (i.e. ferric form) over sediment particles and depicted the strong oxidation condition prevailing at shallow depth. The blackish grey to dark grey sediment depicted the presence of high manganese-bearing minerals, high in organic matter and sulfate-reducing micro-organisms.

2. According to the U.S. Geological Survey soil classification, the distribution curve resembles the alluvium soil distribution curves. It supports the soil color classification, suggesting a presence of Holocene age sediment deposit (carried and deposited by tributaries) in both the study areas. Lithology for representative study area suggests a series of sandy aquifers with intermediate thin and thick clay layers.

3. The pH, TOC and CEC measurements support the findings and causes for the specific soil color present in both the study area. Acidic to alkaline sediment pH was measured, where the grey color sediment was specifically more acidic than brown color sediment. The more acidic sediment was observed in deeper depth aquifers. However, high TOC content was observed in grey color sediment samples than brown-reddish color samples in both the study areas.

4. The TKN results suggest that highest concentration observed in the order of yellowish > grey > brown color sediment irrespective of sediment texture, which signifies nitrogen-consuming bacteria prevailing and availability of organic matter at different depths.

5. Elemental analysis results by ASTM digestion and XRF methods have quantified the significant concentration of *As* in sediment samples, high *As* content was observed in H*As*CR (i.e. 106.8 µg g^{-1}) and low *As* content was observed in L*As*CR (i.e. 63.16 µg g^{-1}) specifically in grey color sediments. Along with *As*, other element concentrations were also measured at a significant concentration.

6. In the sequential extraction analysis results, highest *As* affinity was observed in 3rd fraction, i.e. amorphous phases of Fe, Mn, and Al-bearing minerals surfaces. In 5th fraction, i.e. residual phase, highest *As* concentration was measured than the other fractions. These results suggested that total *As* concentration in aquifer sediments was below the average earth crustal values and can dissolve ~ 80 µg L^{-1} into groundwater aquifer.

7. The detrital and authigenic minerals were observed more in H*As*CR region than the L*As*CR study area. These results suggest that primary solid phase *As*-bearing minerals (i.e., geogenic source) are the main cause for high *As* concentration in the groundwater aquifer of the study areas. The authigenic minerals suggest that in these aquifers, hydro-geochemistry equally

control the *As* mobilization mechanism at different depth. The elemental analyses have verified the mineral composition and results were well corroborated with the obtained results of SSE & XRF analysis. The high concentration of Ca^{+} was observed in H*As*CR and L*As*CR sediment samples, then the other cations (viz. Mg^{+2}, Na^{+}, $K^{+,}$ etc.). It indicates that the primary cause for high calcium and bicarbonate concentrations in both the study area groundwater aquifers.

8. Mineral identification by XRD method confirmed that findings of FESEM-EDS analysis and were confirmed according to the International Centre for Diffraction Data (i.e., ICDD). The d-spacing values confirmed the primary and secondary *As*, Fe, Mn, Al, Cu, Cr, Ca, Zn, Pb, Si, K and Mg-bearing minerals. Moreover, the FTIR analysis further confirmed *As* association with alkane (i.e. – CH_3) and hydroxyl (i.e. – OH) functional group.

9. In the Kinetic study, compared to the pseudo-first-order kinetic reaction model, the pseudo-second-order model rate constant showed high uptake values and is in good agreement with the experimental equilibrium isotherm adsorption results. In equilibrium study, Freundlich isotherm (i.e. chemisorptions or multilayer adsorption) was best fitted than the Langmuir isotherm (i.e. physisorption or monolayer adsorption). The high adsorption capacity of sediment was observed at pH 7 (i.e. at neutral groundwater condition) for As^{+3} and As^{+5} removal. The results of brown color sediment have shown more adsorption capacity than the grey color sediments which suggest that the precipitated Fe-oxy/hydroxide minerals have a significant role on *As* adsorption at oxic aquifer condition.

5.3 Isolation and identification of Microbes

In a preliminary study of microbiology, *Pseudomonas aeruginosa* was isolated from H*As*CR study area showed significant survival limit at a concentration of 850 mg L^{-1} in the presence of

arsenite. In a further study, predominantly four bacteria were isolated namely *Lysinibacillus sphaericus*(BS) *and Acinetobacter nosocomialis*(BL) from H*As*CR whereas, *Bacillus licheniformis* (DS) and *Pseudomonas aeruginosa* (DL) from L*As*CR study areas. The qualitative screening test method, characterized that these bacteria are of reducing nature and can reduce arsenite to arsenate in sub-oxic groundwater aquifer conditions. The presence of these bacteria in H*As*CR and L*As*CR region samples suggest the secondary cause for the heterogeneous distribution of *As* concentration in groundwater aquifer.

5.4 Numerical contaminant modeling

1 The stratigraphy models of both the study areas helped to understand the extensivity and connectivity of water-bearing aquifers in both the study areas. The results of the stratigraphy model for H*As*CR and L*As*CR study area suggested that a thick layer of grey color clay capping present over sandy aquifer near the Manas and Brahmaputra River. It can be inferred from the stratigraphy model that capping of thick (~6.1 m) clay layer was ubiquitous over the sandy aquifer and series of sandy aquifers were present in both study areas. The complex stratigraphy of the study area suggests that these sand deposits are of Holocene age. The permeability test was conducted on repacked sediment samples suggested that this aquifer hydraulic conductivity would be influenced by the presence of clayey-silty sand. Moreover, these test results were well corroborated by the empirical values.

2 The numerical models for groundwater flow estimation and distribution over both the study areas have shown good agreement with observation well data of CGWB India. These results support the assumed boundary and initial conditions depicting the actual hydro-geological and groundwater flow conditions in both the study areas. Furthermore, it discouraged to tap irrigation wells at the deeper depth aquifer. However, the Brahmaputra River on the South-

West boundary of both the study areas was observed to be mostly gaining subsurface water. Consequently, since it may adversely affect the hydro-geochemistry of Brahmaputra river, these sub-surface water was found unsafe for irrigation purposes and aquatic life.

3 In the present study, MT3DMS simulation results simultaneously showed that shallow as well as deeper aquifers, are also vulnerable for *As* contaminant due to extensive groundwater extraction whereas, river water infiltration (due to seasonal fluctuation in head stages, which dilute the *As* concentration) and hydro-stratigraphy (high flushing aquifers) near the riverine region showed possible *As*-safe source of groundwater. The results further depicted that vertical infiltrations of *As* in deeper aquifer will also contaminate the deeper aquifers. The predictive results for *As* contamination transport modeling suggest that, concentration in H*As*CR and L*As*CR will decrease over a period of time due to continuous extraction of groundwater and flushing capability of the adjoin aquifers.

5.5 Conclusion

The analytical results of H*As*CR and L*As*CR groundwater samples revealed that both the study areas are comparatively high and low *As* contaminated. These high *As* concentration region was well affiliated with sub-oxic aquifer conditions. High dissolved Fe concentration was found significantly correlated with *As*, suggesting that reductive dissolution of Fe bearing minerals equally increases dissolved *As* concentration in groundwater aquifer. Presences of the multilayer aquifer were also responsible for the dissolution and precipitation of major and trace elements by multiple mechanisms in both the study areas. Higher *As* contaminated patches were observed in younger alluvium near BFP (i.e. inundation region) whereas low *As* concentration regions were found associated with the older alluvium. The wells tap in reddish-brown sediment were observed to be safe in *As* contaminated region than the grey sediment aquifers, but the wells near of the

Brahmaputra river (contains predominant grey color aquifer sediment) in L*As*CR study area were also observed yielding *As* safe groundwater (i.e. below the permissible limit of WHO standard).

In solid phase sediment characterization, there was no perceptible *As* enrichment differences observed in grey and yellow-brown sand sediments. In the present study, sediment characterizations by various methods suggested that the presence of detrital and authigenic minerals and primary sources of *As* in solid phase at Holocene age aquifer. The concise results of the hydro-geochemistry and geochemical model suggests that these aquifers sediments are highly susceptible to ion-exchange, minerals weathering and dissolution. It suggests the major cause for different facies of *As* in groundwater and mobilizes *As* from solid to liquid phase in the study area aquifer. These results suggested that the partial reducing and oxidation condition was prevailing at the shallow depth aquifer due to degradation of humic substances, which are further mediated by the indigenous microbial consortium.

In this study, the biotic factors for *As* mobilization was observed to be equally responsible as abiotic factors in the *As*-contaminated alluvial aquifers. The isolated microbes suggested that they are facultative anaerobic microbes, which can prevail in these partially oxidizing aquifer conditions. Their qualitative screening test methods suggest that these bacteria were able to reduce arsenate into arsenite in groundwater aquifers. Its phase diagram and qualitative screening test support that these bacteria use arsenate as the terminal electron acceptor and reduce arsenate by dissimilatory reduction mechanisms. This reducing characteristic of these bacteria further inferred that it will increase the dissolved *As* concentration and will help to reduce the solid phase *As* in both the study areas. The findings of this study provide evidenced insights into *As* mobilization, where the reductive dissolution of Fe oxy-hydroxides coupled with the biogeochemical cycle of *As* (III) and *As* (V) point towards the prevalence of sub-oxic to reducing alluvial aquifer conditions.

The above conclusions from groundwater, sediment analysis, and microbiological characterization suggested that these aquifers are contaminated with *As* and unsafe for drinking. The possible reliable and sustainable sources have barely been found and implemented because the mitigation strategies based upon such study will greatly depend upon the availability of precise data and its appropriate interpretation. The transient state groundwater flow and contaminant transport models result concludes that combined implications for strategic groundwater resources management would provide possible *As* safe potable groundwater for these H*As*CR and L*As*CR study areas. Thus, it can be further deduced that the presence of high geogenic sources of *As* in the shallow aquifers is favorable to flushing, which can attenuate *As* pollutants and trace metals. Therefore, taping of irrigation bore well in shallow depth (i.e. < 70 m) and community or private drinking wells at deeper depth (> 70 m) in highly aquifer flushing region, which are present nearer to the Manas river (i.e. Srijangram block) and reddish-brown color sediments (i.e. region in Boitamari block) for H*As*CR would be the possible *As* safe groundwater region. Similarly, areas near Sipajhar block in L*As*CR and proximately to the Brahmaputra river would be the possible *As* safe groundwater region for drinking purposes at the regional scale.

5.6 Future scope

i) Evaluate a source of inorganic carbon and effect on iron reduction in shallow aquifer of the study area,

ii) The vulnerability of deeper aquifers (>70m); causes a significant degree of contaminations, the role of sediment texture and indigenous microbes on *As* mobilization,

iii) Microbiologically reduction of *As* and Fe in sub-anoxic aquifer condition, Effect of surface water infiltration and geomorphology of the study area on temporal variation of groundwater *As* concentration,

Reference

Acharyya, S.K., Shah, B.A., 2007. Groundwater arsenic contamination affecting different geologic domains in India — a review : influence of geological setting , fluvial geomorphology and Quaternary stratigraphy Groundwater arsenic contamination affecting different geologic domains in Indi 4529. https://doi.org/10.1080/10934520701566744

Adsorbers, F., Weber, T.W., 1974. Pore and Solid Diffusion Models for 20.

Ahmed, K.M., Bhattacharya, P., Hasan, M.A., Akhter, S.H., Alam, S.M.M., Bhuyian, M.A.H., Imam, M.B., Khan, A.A., Sracek, O., 2004. Arsenic enrichment in groundwater of the alluvial aquifers in +: an overview. Appl. Geochemistry 19, 181–200. https://doi.org/http://dx.doi.org/10.1016/j.apgeochem.2003.09.006

Akai, J., Kanekiyo, A., Hishida, N., Ogawa, M., Naganuma, T., Fukuhara, H., Anawar, H.N., 2008. Biogeochemical characterization of bacterial assemblages in relation to release of arsenic from South East Asia (Bangladesh) sediments. Appl. Geochemistry 23, 3177–3186. https://doi.org/http://dx.doi.org/10.1016/j.apgeochem.2008.06.018

Anawar, H.M., Akai, J., Sakugawa, H., 2004. Mobilization of arsenic from subsurface sediments by effect of bicarbonate ions in groundwater. Chemosphere 54, 753–762. https://doi.org/http://dx.doi.org/10.1016/j.chemosphere.2003.08.030

Anderson, H., Knobeloch, L., Warzecha, C., 1999. Public Health Hazard Surveillance and Response to Arsenic Contamination, in: Calderon, W.R.C.O.A.L.B.T.-A.E. and H.E.I.I.I. (Ed.), . Elsevier Science Ltd, Oxford, pp. 367–372. https://doi.org/http://dx.doi.org/10.1016/B978-008043648-7/50041-8

Arienzo, M., Adamo, P., Chiarenzelli, J., Bianco, M.R., De Martino, A., 2002. Retention of arsenic on hydrous ferric oxides generated by electrochemical peroxidation. Chemosphere 48, 1009–1018. https://doi.org/http://dx.doi.org/10.1016/S0045-6535(02)00199-6

Bhattacharya, P., Chatterjee, D., Jacks, G., 1997. Occurrence of Arsenic-contaminatedGroundwater in Alluvial Aquifers from Delta Plains, Eastern India: Options for Safe Drinking Water Supply. Int. J. Water Resour. Dev. 13, 79–92. https://doi.org/10.1080/07900629749944

Bhattacharya, P., Jacks, G., Ahmed, K.M., Routh, J., Khan, A.A., 2002. Arsenic in Groundwater of the Bengal Delta Plain Aquifers in Bangladesh. Bull. Environ. Contam. Toxicol. 69, 538–545. https://doi.org/10.1007/s00128-002-0095-5

Biswas, A., Majumder, S., Neidhardt, H., Halder, D., Bhowmick, S., Mukherjee-Goswami, A., Kundu, A., Saha, D., Berner, Z., Chatterjee, D., 2011. Groundwater chemistry and redox processes: Depth dependent arsenic release mechanism. Appl. Geochemistry 26, 516–525. https://doi.org/http://dx.doi.org/10.1016/j.apgeochem.2011.01.010

Biswas, A., Nath, B., Bhattacharya, P., Halder, D., Kundu, A.K., Mandal, U., Mukherjee, A., Chatterjee, D., Mörth, C.-M., Jacks, G., 2012. The hydrogeochemical contrast between brown and grey sand aquifers in shallow depth of Bengal Basin: Consequences for sustainable drinking water supply. Sci. Total Environ. 431, 402–412. https://doi.org/http://dx.doi.org/10.1016/j.scitotenv.2012.05.031

Biswas, A., Bhattacharya, P., Mukherjee, A., Nath, B., Alexanderson, H., Kundu, A.K., Chatterjee, D., Jacks, G., 2014a. Shallow hydrostratigraphy in an arsenic affected region of Bengal Basin: Implication for targeting safe aquifers for drinking water supply. Sci. Total Environ. 485–486, 12–22. https://doi.org/http://dx.doi.org/10.1016/j.scitotenv.2014.03.045

Biswas, A., Neidhardt, H., Kundu, A.K., Halder, D., Chatterjee, D., Berner, Z., Jacks, G., Bhattacharya, P., 2014b. Spatial, vertical and temporal variation of arsenic in shallow aquifers of the Bengal Basin: Controlling geochemical processes. Chem. Geol. 387, 157–169. https://doi.org/http://dx.doi.org/10.1016/j.chemgeo.2014.08.022

Blum, Switzer, J., Allana, Bindi, B., Buzzelli, J., Stolz, J.F., Oremland, R.S., 1998. from Mono Lake, California that respire oxyanions of selenium and arsenic 19–30. https://doi.org/10.1007/s002030050673

Burton, E.D., Bush, R.T., Johnston, S.G., Watling, K.M., Hocking, R.K., Sullivan, L.A., Parker, G.K., 2009. Sorption of arsenic (V) and arsenic (III) to schwertmannite. Environ. Sci. Technol. 43, 9202–9207. https://doi.org/10.1021/es902461x

Cai, J., Salmon, K., DuBow, M.S., 1998. A chromosomal ars operon homologue of Pseudomonas aeruginosa confers increased resistance to arsenic and antimony in Escherichia coli. Microbiology 144, 2705–2713. https://doi.org/10.1099/00221287-144-10-2705

Cai, X., Zhang, Z., Yin, N., Du, H., Li, Z., Cui, Y., 2016. Comparison of arsenate reduction and release by three As(V)-reducing bacteria isolated from arsenic-contaminated soil of Inner Mongolia, China. Chemosphere 161, 200–207. https://doi.org/10.1016/j.chemosphere.2016.06.102

Cao, W., Guo, H., Zhang, Y., Ma, R., Li, Y., Dong, Q., Li, Y., Zhao, R., 2018. Controls of paleochannels on groundwater arsenic distribution in shallow aquifers of alluvial plain in the Hetao Basin, China. Sci. Total Environ. 613–614, 958–968. https://doi.org/https://doi.org/10.1016/j.scitotenv.2017.09.182

Chakraborti, D., Rahman, M., Das, B., Nayak, B., Pal, A., Sengupta, M., Hossain, M.A., Ahamed, S., Sahu, M., Saha, K., Mukherjee, S., Pati, S., Dutta, R., Quamruzzaman, Q., 2013. Groundwater arsenic contamination in Ganga–Meghna–Brahmaputra plain, its health effects and an approach for mitigation. Environ. Earth Sci. 70, 1993–2008. https://doi.org/10.1007/s12665-013-2699-y

Chakraborti, D., Rahman, M.M., Paul, K., Chowdhury, U.K., Sengupta, M.K., Lodh, D., Chanda, C.R., Saha, K.C., Mukherjee, S.C., 2002. Arsenic calamity in the Indian subcontinent: What lessons have been learned? Talanta 58, 3–22. https://doi.org/https://doi.org/10.1016/S0039-9140(02)00270-9

Chatterjee, D., Roy, R.K., Basu, B.B., 2005. Riddle of arsenic in groundwater of Bengal Delta Plain - Role of non-inland source and redox traps. Environ. Geol. 49, 188–206. https://doi.org/10.1007/s00254-005-0011-5

Chen, X., Zeng, X.-C., Wang, J., Deng, Y., Ma, T., Guoji E, Mu, Y., Yang, Y., Li, H., Wang, Y., 2017. Microbial communities involved in arsenic mobilization and release from the deep sediments into groundwater in Jianghan plain, Central China. Sci. Total Environ. 579, 989–999. https://doi.org/https://doi.org/10.1016/j.scitotenv.2016.11.024

Clesceri, L.S., Greenberg, A.E., Eaton, A.D., 1996. Standard Methods for the Examination of Water and Wastewater/Prepared and Published Jointly by American Public Health Association, American Water Works Association, Water Environment Federation. Am. Public Heal. Assoc. Washington, DC.

Cole, C. V, 1957. Hydrogen and calcium relationships of calcareous soils. Soil Sci. 83, 141–150.

Cullen, W.R., Reimer, K.J., 1989. Arsenic speciation in the environment. Chem. Rev. 89, 713–764. https://doi.org/10.1021/cr00094a002

Das, N., Deka, J.P., Shim, J., Patel, A.K., Kumar, A., Sarma, K.P., Kumar, M., 2016. Effect of river proximity on the arsenic and fluoride distribution in the aquifers of the Brahmaputra Floodplains, Assam, Northeast India. Groundw. Sustain. Dev. 2–3, 130–142. https://doi.org/http://dx.doi.org/10.1016/j.gsd.2016.07.001

Dean, W.E., 1974. Determination of carbonate and organic matter in calcareous sediments and sedimentary rocks by loss on ignition; comparison with other methods. J. Sediment. Res. 44, 242–248.

Deng, Y., Zheng, T., Wang, Y., Liu, L., Jiang, H., Ma, T., 2018. Effect of microbially mediated iron mineral transformation on temporal variation of arsenic in the Pleistocene aquifers of the central Yangtze River basin. Sci. Total Environ. 619–620, 1247–1258. https://doi.org/10.1016/j.scitotenv.2017.11.166

Desbarats, A., Koenig, C., 2014. Groundwater flow dynamics and arsenic source characterization in an aquifer system of West Bengal, India. Water Resour. … 4974–5002. https://doi.org/10.1002/2013WR014034.Received

Dey, U., Chatterjee, S., Mondal, N.K., 2016. Isolation and characterization of arsenic-resistant bacteria and possible application in bioremediation. Biotechnol. Reports 10, 1–7. https://doi.org/10.1016/j.btre.2016.02.002

Dixit, S., Hering, J., 2003. Comparison of arsenic (V) and arsenic (III) sorption onto iron oxide minerals: Implications for arsenic mobility. Environ. Sci. Technol. 37, 4182–4189. https://doi.org/10.1021/es030309t

Dowling, C.B., Poreda, R.J., Basu, A.R., 2003. The groundwater geochemistry of the Bengal Basin: Weathering, chemsorption, and trace metal flux to the oceans. Geochim. Cosmochim. Acta 67, 2117–2136. https://doi.org/http://dx.doi.org/10.1016/S0016-7037(02)01306-6

Eiche, E., Berg, M., Hönig, S.M., Neumann, T., Lan, V.M., Pham, T.K.T., Pham, H.V., 2017. Origin and availability of organic matter leading to arsenic mobilisation in aquifers of the Red River Delta, Vietnam. Appl. Geochemistry 77, 184–193. https://doi.org/10.1016/j.apgeochem.2016.01.006

Engelen, G.B., Kloosterman, F.H., 2012. Hydrological systems analysis: methods and applications. Springer Science & Business Media.

Fan, H., Su, C., Wang, Y., Yao, J., Zhao, K., Wang, Y., Wang, G., 2008. Sedimentary arsenite-oxidizing and arsenate-reducing bacteria associated with high arsenic groundwater from Shanyin, Northwestern China. J. Appl. Microbiol. 105, 529–539. https://doi.org/10.1111/j.1365-2672.2008.03790.x

Felsenstein, J., 1985. Confidence Limits on Phylogenies: An Approach Using the Bootstrap. Evolution (N. Y). 39, 783–791. https://doi.org/10.2307/2408678

Fendorf, S., Michael, H.A., van Geen, A., 2010. Spatial and temporal variations of groundwater arsenic in South and Southeast Asia. Science 328, 1123–1127. https://doi.org/10.1126/science.1172974

Freeze, R.A., 1971. Flow in a Groundwater. Water Resour. Res. 7, 347–366. https://doi.org/10.1029/WR007i002p00347

Freeze, R.A., Witherspoon, P.A., 1966. Theoretical Analysis of Regional Groundwater Flow 1. Analytical and Numerical Solutions to the Mathematical Model. Water Resour. Res. 2, 641–656.

Geen, A. Van, Zheng, Y., Jr, S.G., Horneman, A., Aziz, Z., Cheng, Z., Stute, M., Mailloux, B., Weinman, B., Hoque, M.A., Seddique, A.A., Hossain, M.S., Chowdhury, S.H., Ahmed, K.M., 2008. Flushing History as a Hydrogeological Control on the Regional Distribution of Arsenic in Shallow Groundwater of the Bengal Basin Flushing History as a Hydrogeological Control on the Regional Distribution of Arsenic in Shallow Groundwater of the Bengal Bas. Environ. Sci. Technol. 42, 2283–2288. https://doi.org/10.1021/es702316k

Gelhar, L.W., Welty, C., Rehfeldt, K.R., 1992. A critical review of data on field-scale dispersion in aquifers. Water Resour. Res. 28, 1955–1974.

Ghosh, D., Routh, J., Dario, M., Bhadury, P., 2015. Elemental and biomarker characteristics in a Pleistocene aquifer vulnerable to arsenic contamination in the Bengal Delta Plain, India. Appl. Geochemistry 61, 87–98. https://doi.org/10.1016/j.apgeochem.2015.05.007

Ghosh, S., Sar, P., 2013. Identification and characterization of metabolic properties of bacterial populations recovered from arsenic contaminated ground water of North East India (Assam). Water Res. 47, 6992–7005. https://doi.org/http://dx.doi.org/10.1016/j.watres.2013.08.044

Giles, D.E., Mohapatra, M., Issa, T.B., Anand, S., Singh, P., 2011. Iron and aluminium based adsorption strategies for removing arsenic from water. J. Environ. Manage. 92, 3011–3022. https://doi.org/10.1016/j.jenvman.2011.07.018

Goh, K.H., Lim, T.T., 2005. Arsenic fractionation in a fine soil fraction and influence of various anions on its mobility in the subsurface environment. Appl. Geochemistry 20, 229–239. https://doi.org/10.1016/j.apgeochem.2004.08.004

Goldberg, E., 2002. The executive brain: Frontal lobes and the civilized mind. Oxford University Press, USA.

Goswami, D.C., 1985. Brahmaputra River, Assam, India: Physiography, Basin Denudation, and Channel Aggradation. Water Resour. Res. 21, 959–978. https://doi.org/10.1029/WR021i007p00959

Guo, H., Ren, Y., Liu, Q., Zhao, K., Li, Y., 2013. Enhancement of Arsenic Adsorption during Mineral Transformation from Siderite to Goethite: Mechanism and Application. https://doi.org/10.1021/es303503m

Guo, H., Stüben, D., Berner, Z., 2007. Adsorption of arsenic(III) and arsenic(V) from groundwater using natural siderite as the adsorbent. J. Colloid Interface Sci. 315, 47–53. https://doi.org/10.1016/j.jcis.2007.06.035

Guo, H., Wen, D., Liu, Z., Jia, Y., Guo, Q., 2014. A review of high arsenic groundwater in Mainland and Taiwan, China: Distribution, characteristics and geochemical processes. Appl. Geochemistry 41, 196–217. https://doi.org/https://doi.org/10.1016/j.apgeochem.2013.12.016

Hagiwara, H., Akai, J., Terasaki, K., Yoshimura, T., Luo, H., 2011. Black coloured sandy sediments caused by bacterial action, and the mechanism for arsenic enrichment of groundwater in Inner Mongolia. Appl. Geochemistry 26, 380–393. https://doi.org/http://dx.doi.org/10.1016/j.apgeochem.2010.12.011

Han, C., Li, H., Pu, H., Yu, H., Deng, L., Huang, S., Luo, Y., 2013. Synthesis and characterization of mesoporous alumina and their performances for removing arsenic(V). Chem. Eng. J. 217, 1–9. https://doi.org/10.1016/j.cej.2012.11.087

Hao, X., Weihong, L., Xiang, H., Chenggang, Z., Jianxin, M., 2009. Assessment of the groundwater threshold of desert riparian forest vegetation along the middle and lower reaches of the Tarim River, China. Hydrol. Process. 24, 178–186. https://doi.org/10.1002/hyp.7432

Haque, S., Ji, J., Johannesson, K.H., 2008. Evaluating mobilization and transport of arsenic in sediments and groundwaters of Aquia aquifer, Maryland, USA. J. Contam. Hydrol. 99, 68–84. https://doi.org/http://dx.doi.org/10.1016/j.jconhyd.2008.03.003

Harvey, C.F., Swartz, C.H., Badruzzaman, A.B.M., Keon-Blute, N., Yu, W., Ali, M.A., Jay, J., Beckie, R., Niedan, V., Brabander, D., Oates, P.M., Ashfaque, K.N., Islam, S., Hemond, H.F., Ahmed, M.F., 2005. Groundwater arsenic contamination on the Ganges Delta: biogeochemistry, hydrology, human perturbations, and human suffering on a large scale. Comptes Rendus Geosci. 337, 285–296. https://doi.org/https://doi.org/10.1016/j.crte.2004.10.015

Harvey, C.F., Swartz, C.H., Badruzzman, A.B.M., Keon-Blute, N., Yu, W., Ali, M.A., Jay, J., Beckie, R., Niedan, V., Brabander, D., Oates, P.M., Ashfaque, K.N., Islam, S., Hemond, H.F., Ahmed, M.F., 2002. No Title. Science (80-.). 298, 1602.

He, J., Ma, T., Deng, Y., Yang, H., Wang, Y., 2009. Environmental geochemistry of high arsenic groundwater at western Hetao plain, Inner Mongolia. Front. Earth Sci. China 3, 63–72. https://doi.org/10.1007/s11707-009-0004-x

Hering, J.G., Kneebone, P.E., 2002. Biogeochemical controls on arsenic occurrence and mobility in water supplies. Environ. Chem. Arsen. 155–181.

Héry, M., Van Dongen, B.E., Gill, F., Mondal, D., Vaughan, D.J., Pancost, R.D., Polya, D.A., Lloyd, J.R., 2010. Arsenic release and attenuation in low organic carbon aquifer sediments from West Bengal. Geobiology 8, 155–168. https://doi.org/10.1111/j.1472-4669.2010.00233.x

HO, Y.-S., 2004. Citation review ofLagergren kinetic rate equation on adsorption reactions. Scientometrics 59, 171–177. https://doi.org/10.1023/B:SCIE.0000013305.99473.cf

Ho, Y.S., McKay, G., 1999. Pseudo-second order model for sorption processes. Process Biochem. 34, 451–465. https://doi.org/http://dx.doi.org/10.1016/S0032-9592(98)00112-5

Hoque, M.A., McArthur, J.M., Sikdar, P.K., 2014. Sources of low-arsenic groundwater in the Bengal Basin: investigating the influence of the last glacial maximum palaeosol using a 115-km traverse across Bangladesh. Hydrogeol. J. 22, 1535–1547. https://doi.org/10.1007/s10040-014-1139-8

Hossain, M., Bhattacharya, P., Frape, S.K., Jacks, G., Islam, M.M., Rahman, M.M., von Brömssen, M., Hasan, M.A., Ahmed, K.M., 2014. Sediment colour tool for targeting arsenic-safe aquifers for the installation of shallow drinking water tubewells. Sci. Total Environ. 493, 615–625. https://doi.org/https://doi.org/10.1016/j.scitotenv.2014.05.064

Islam, F.S., Gault, A.G., Boothman, C., Polya, D.A., Charnock, J.M., Chatterjee, D., Lloyd, J.R., 2004. Role of metal-reducing bacteria in arsenic release from Bengal delta sediments. Nature 430, 68–71.

Jebelli, M.A., Maleki, A., Amoozegar, M.A., Kalantar, E., Shahmoradi, B., Gharibi, F., 2017. Isolation and identification of indigenous prokaryotic bacteria from arsenic-contaminated water resources and their impact on arsenic transformation. Ecotoxicol. Environ. Saf. 140, 170–176. https://doi.org/10.1016/j.ecoenv.2017.02.051

Jessen, S., Larsen, F., Postma, D., Viet, P.H., Ha, N.T., Nhan, P.Q., Nhan, D.D., Duc, M.T., Hue, N.T.M., Huy, T.D., Luu, T.T., Ha, D.H., Jakobsen, R., 2008. Palaeo-hydrogeological control on groundwater As levels in Red River delta, Vietnam. Appl. Geochemistry 23, 3116–3126. https://doi.org/http://dx.doi.org/10.1016/j.apgeochem.2008.06.015

Klein, C., Hurlbut, C.S., 1999. Manual of Mineralogy (after James D. Dana, revised 21 st edition).

Ko, M.S., Park, H.S., Lee, J.U., 2017. Influence of indigenous bacteria stimulation on arsenic immobilization in field study. Catena 148, 46–51. https://doi.org/10.1016/j.catena.2016.08.022

Kong, S., Wang, Y., Zhan, H., Yuan, S., Yu, M., Liu, M., 2014. Adsorption/Oxidation of Arsenic in Groundwater by Nanoscale Fe-Mn Binary Oxides Loaded on Zeolite. Water Environment Research 86, 147-155.

Kudo, K., Yamaguchi, N., Makino, T., Ohtsuka, T., Kimura, K., Dong, D.T., Amachi, S., 2013. Release of arsenic from soil by a novel dissimilatory arsenate-reducing bacterium, anaeromyxobacter sp. strain PSR-1. Appl. Environ. Microbiol. 79, 4635–4642. https://doi.org/10.1128/AEM.00693-13

Kumar, M., Herbert, R., Jha, P.K., Deka, J.P., Rao, M.S., Ramanathan, A.L., Kumar, B., 2016.

Understanding the Seasonal Dynamics of the Groundwater Hydrogeochemistry in National Capital Territory (NCT) of India Through Geochemical Modelling. Aquat. Geochemistry 22, 211–224. https://doi.org/10.1007/s10498-016-9289-z

Lachaal, F., Mlayah, A., Bédir, M., Tarhouni, J., Leduc, C., 2012. Implementation of a 3-D groundwater flow model in a semi-arid region using MODFLOW and GIS tools: The Zéramdine–Béni Hassen Miocene aquifer system (east-central Tunisia). Comput. Geosci. 48, 187–198. https://doi.org/http://dx.doi.org/10.1016/j.cageo.2012.05.007

Lakshmipathiraj, P., Narasimhan, B.R. V, Prabhakar, S., Bhaskar Raju, G., 2006. Adsorption of arsenate on synthetic goethite from aqueous solutions. J. Hazard. Mater. 136, 281–287. https://doi.org/http://dx.doi.org/10.1016/j.jhazmat.2005.12.015

Leupin, O.X., Hug, S.J., 2005. Oxidation and removal of arsenic (III) from aerated groundwater by filtration through sand and zero-valent iron. Water Res. 39, 1729–1740. https://doi.org/10.1016/j.watres.2005.02.012

Liao, V.H.-C., Chu, Y.-J., Su, Y.-C., Hsiao, S.-Y., Wei, C.-C., Liu, C.-W., Liao, C.-M., Shen, W.-C., Chang, F.-J., 2011. Arsenite-oxidizing and arsenate-reducing bacteria associated with arsenic-rich groundwater in Taiwan. J. Contam. Hydrol. 123, 20–29. https://doi.org/http://dx.doi.org/10.1016/j.jconhyd.2010.12.003

Lièvremont, D., N'negue, M.A., Behra, P., Lett, M.C., 2003. Biological oxidation of arsenite: Batch reactor experiments in presence of kutnahorite and chabazite. Chemosphere 51, 419–428. https://doi.org/10.1016/S0045-6535(02)00869-X

Livesey, N.T., Huang, P.M., 1981. Adsorption of arsenate by soils and its relation to selected chemical properties and anions. Soil Sci. v. 131, p. 88-94.

Madejová, J., 2003. FTIR techniques in clay mineral studies. Vib. Spectrosc. 31, 1–10. https://doi.org/http://dx.doi.org/10.1016/S0924-2031(02)00065-6

Mahanta, C., Enmark, G., Nordborg, D., Sracek, O., Nath, B., Nickson, R.T., Herbert, R., Jacks, G., Mukherjee, A., Ramanathan, A.L., Choudhury, R., Bhattacharya, P., 2015. Hydrogeochemical controls on mobilization of arsenic in groundwater of a part of Brahmaputra river floodplain, India. J. Hydrol. Reg. Stud. 4, Part A, 154–171. https://doi.org/http://dx.doi.org/10.1016/j.ejrh.2015.03.002

Mailloux, B.J., Trembath-Reichert, E., Cheung, J., Watson, M., Stute, M., Freyer, G.A., Ferguson, A.S., Ahmed, K.M., Alam, M.J., Buchholz, B.A., Thomas, J., Layton, A.C., Zheng, Y., Bostick, B.C., van Geen, A., 2013. Advection of surface-derived organic carbon fuels microbial reduction in Bangladesh groundwater. Proc. Natl. Acad. Sci. 110, 5331–5335. https://doi.org/10.1073/pnas.1213141110

Mallick, S., Rajagopal, N.R., 1996. Groundwater development in the arsenic-affected alluvial belt of West Bengal–some questions. Curr. Sci. 70, 956–958.

Malmström, V.H., 1969. A New Approach To The Classification Of Climate. J. Geog. 68, 351–357. https://doi.org/10.1080/00221346908981131

Mandal, B.K., Suzuki, K.T., 2002. Arsenic round the world: a review. Talanta 58, 201–235. https://doi.org/https://doi.org/10.1016/S0039-9140(02)00268-0

Manning, B.A., Goldberg, S., 1997. Arsenic (III) and arsenic (V) adsorption on three California soils. Soil Sci. 162, 886–895.

Matera, V., Le Hécho, I., Laboudigue, A., Thomas, P., Tellier, S., Astruc, M., 2003. A methodological approach for the identification of arsenic bearing phases in polluted soils. Environ. Pollut. 126, 51–64. https://doi.org/http://dx.doi.org/10.1016/S0269-7491(03)00146-5

McArthur, J.M., Banerjee, D.M., Hudson-Edwards, K.A., Mishra, R., Purohit, R., Ravenscroft, P., Cronin, A., Howarth, R.J., Chatterjee, A., Talukder, T., Lowry, D., Houghton, S., Chadha, D.K., 2004. Natural organic matter in sedimentary basins and its relation to arsenic in anoxic ground water: the example of West Bengal and its worldwide implications. Appl. Geochemistry 19, 1255–1293. https://doi.org/https://doi.org/10.1016/j.apgeochem.2004.02.001

Meharg, A.A., 2004. Arsenic in rice - Understanding a new disaster for South-East Asia. Trends Plant Sci. 9, 415–417. https://doi.org/10.1016/j.tplants.2004.07.002

Meng, X., Dupont, R.R., Sorensen, D.L., Jacobson, A.R., McLean, J.E., 2017. Mineralogy and geochemistry affecting arsenic solubility in sediment profiles from the shallow basin-fill aquifer of Cache Valley Basin, Utah. Appl. Geochemistry 77, 126–141. https://doi.org/https://doi.org/10.1016/j.apgeochem.2015.12.011

Michael G. McDonald, Harbaugh, A.W., 1988. A modular three-dimensional fl n ite-di fference ground-water flow model 1–2.

Michael, G.G., 2008. Biosorption: critical review of scientific rationale, environmental importance and significance for pollution treatment. J. Chem. Technol. Biotechnol. 84, 13–28. https://doi.org/10.1002/jctb.1999

Mirza, B.S., Muruganandam, S., Meng, X., Sorensen, D.L., Dupont, R.R., McLean, J.E., 2014. Arsenic(V) Reduction in Relation to Iron(III) Transformation and Molecular Characterization of the Structural and Functional Microbial Community in Sediments of a Basin-Fill Aquifer in Northern Utah. Appl. Environ. Microbiol. 80, 3198–3208. https://doi.org/10.1128/AEM.00240-14

Morris, D.A., Johnson, A.I., 1967. Summary of hydrologic and physical properties of rock and soil materials, as analyzed by the hydrologic laboratory of the US Geological Survey, 1948-60. US Govt. Print. Off.,.

Mukherjee, A., Bhattacharya, P., Fryar, A.E., 2011. Arsenic and other toxic elements in surface and groundwater systems. Appl. Geochemistry 26, 415–420. https://doi.org/http://dx.doi.org/10.1016/j.apgeochem.2011.01.001

Mukherjee, A., Bhattacharya, P., Savage, K., Foster, A., Bundschuh, J., 2008a. Distribution of geogenic arsenic in hydrologic systems: Controls and challenges. J. Contam. Hydrol. 99, 1–7. https://doi.org/http://dx.doi.org/10.1016/j.jconhyd.2008.04.002

Mukherjee, A., Fryar, A.E., 2008b. Deeper groundwater chemistry and geochemical modeling of the arsenic affected western Bengal basin, West Bengal, India. Appl. Geochemistry 23, 863–894. https://doi.org/http://dx.doi.org/10.1016/j.apgeochem.2007.07.011

Mukherjee, A., Fryar, A.E., Howell, P.D., 2007a. Regional hydrostratigraphy and groundwater flow modeling in the arsenic-affected areas of the western Bengal basin, West Bengal, India. Hydrogeol. J. 15, 1397–1418. https://doi.org/10.1007/s10040-007-0208-7

Mukherjee, A., Fryar, A.E., Rowe, H.D., 2007b. Regional-scale stable isotopic signatures of recharge and deep groundwater in the arsenic affected areas of West Bengal, India. J. Hydrol. 334, 151–161. https://doi.org/https://doi.org/10.1016/j.jhydrol.2006.10.004

Mukherjee, A., Fryar, A.E., Thomas, W.A., 2009. Geologic, geomorphic and hydrologic framework and evolution of the Bengal basin, India and Bangladesh. J. Asian Earth Sci. 34, 227–244. https://doi.org/10.1016/j.jseaes.2008.05.011

Mukherjee, A., Verma, S., Gupta, S., Henke, K.R., Bhattacharya, P., 2014. Influence of tectonics, sedimentation and aqueous flow cycles on the origin of global groundwater arsenic: Paradigms from three continents. J. Hydrol. 518, Part, 284–299. https://doi.org/http://dx.doi.org/10.1016/j.jhydrol.2013.10.044

Mukherjee, A., von Brömssen, M., Scanlon, B.R., Bhattacharya, P., Fryar, A.E., Hasan, M.A., Ahmed, K.M., Chatterjee, D., Jacks, G., Sracek, O., 2008. Hydrogeochemical comparison and effects of overlapping redox zones on groundwater arsenic near the Western (Bhagirath

sub-basin, India) and Eastern (Meghna sub-basin, Bangladesh) margins of the Bengal Basin. J. Contam. Hydrol. 99, 31–48. https://doi.org/https://doi.org/10.1016/j.jconhyd.2007.10.005

Mukhopadhyay, S., Hoidal, J.R., Mukherjee, T.K., 2006. Role of TNFα in pulmonary pathophysiology. Respir. Res. 7, 1–9. https://doi.org/10.1186/1465-9921-7-125

Muller, O., White, W.B., Roy, R., 1964. Crystal chemistry of some technetium-containing oxides. J. Inorg. Nucl. Chem. 26, 2075–2086.

Nath, B., Berner, Z., Basu Mallik, S., Chatterjee, D., Charlet, L., Stueben, D., 2005. Characterization of aquifers conducting groundwaters with low and high arsenic concentrations: a comparative case study from West Bengal, India. Mineral. Mag. 69, 841–854.

Nath, B., Chakraborty, S., Burnol, A., Stüben, D., Chatterjee, D., Charlet, L., 2009. No Title. J. Hydrol. 364, 236.

Neidhardt, H., Berner, Z.A., Freikowski, D., Biswas, A., Majumder, S., Winter, J., Gallert, C., Chatterjee, D., Norra, S., 2014. Organic carbon induced mobilization of iron and manganese in a West Bengal aquifer and the muted response of groundwater arsenic concentrations. Chem. Geol. 367, 51–62. https://doi.org/10.1016/j.chemgeo.2013.12.021

Nickson, R.T., Mcarthur, J.M., Ravenscroft, P., Burgess, W.G., Ahmed, K.M., 2000. Mechanism of arsenic release to groundwater, Bangladesh and West Bengal. Appl. Geochemistry 15, 403–413. https://doi.org/10.1016/S0883-2927(99)00086-4

Nordborg, D., 2007. Arsenic in the groundwater of the Brahmaputra floodplains , Assam , India – Source , distribution and release mechanisms.

Ohtsuka, T., Yamaguchi, N., Makino, T., Sakurai, K., Kimura, K., Kudo, K., Homma, E., Dong, D.T., Amachi, S., 2013. Arsenic dissolution from Japanese paddy soil by a dissimilatory arsenate-reducing bacterium geobacter sp. OR-1. Environ. Sci. Technol. 47, 6263–6271. https://doi.org/10.1021/es400231x

Oremland, R.S., Stolz, J.F., 2005. Arsenic, microbes and contaminated aquifers. Trends Microbiol. 13, 45–49. https://doi.org/http://dx.doi.org/10.1016/j.tim.2004.12.002

Oremland, R.S., Stolz, J.F., 2003. The Ecology of Arsenic. Sci. 300, 939–944.

Osborne, T.H., Santini, J.M., 2012. Prokaryotic aerobic oxidation of arsenite. Metab. arsenite 61–72.

Oscarson, D.W., Huang, P.M., Liaw, W.K., 1981. role of manganese in the oxidation of arsenite

by fresh water lake sediments 1 29, 219–225.

Pal, T., Mukherjee, P.K., Sengupta, S., Bhattacharyya, A.K., Shome, S., 2002. Arsenic Pollution in Groundwater of West Bengal, India - An Insight into the Problem by Subsurface Sediment Analysis. Gondwana Res. 5, 501–512. https://doi.org/http://dx.doi.org/10.1016/S1342-937X(05)70738-3

Parsons, C., Margui Grabulosa, E., Pili, E., Floor, G.H., Roman-Ross, G., Charlet, L., 2013. Quantification of trace arsenic in soils by field-portable X-ray fluorescence spectrometry: Considerations for sample preparation and measurement conditions. J. Hazard. Mater. 262, 1213–1222. https://doi.org/http://dx.doi.org/10.1016/j.jhazmat.2012.07.001

Paul, D., Kazy, S.K., Banerjee, T. Das, Gupta, A.K., Pal, T., Sar, P., 2015. Arsenic biotransformation and release by bacteria indigenous to arsenic contaminated groundwater. Bioresour. Technol. 188, 14–23. https://doi.org/http://dx.doi.org/10.1016/j.biortech.2015.02.039

Peña-Montenegro, T.D., Lozano, L., Dussán, J., 2015. Genome sequence and description of the mosquitocidal and heavy metal tolerant strain Lysinibacillus sphaericus CBAM5. Stand. Genomic Sci. 10, 2. https://doi.org/10.1186/1944-3277-10-2

Pike, J.G., 1964. The estimation of annual run-off from meteorological data in a tropical climate. J. Hydrol. 2, 116–123.

Plant, J.A., Kinniburgh, D.G., Smedley, P.L., Fordyce, F.M., Klinck, B.A., 2003. Arsenic and Selenium, in: Treatise on Geochemistry. Elsevier, pp. 17–66. https://doi.org/10.1016/B0-08-043751-6/09047-2

Postma, D., Larsen, F., Minh Hue, N.T., Duc, M.T., Viet, P.H., Nhan, P.Q., Jessen, S., 2007. Arsenic in groundwater of the Red River floodplain, Vietnam: Controlling geochemical processes and reactive transport modeling. Geochim. Cosmochim. Acta 71, 5054–5071. https://doi.org/http://dx.doi.org/10.1016/j.gca.2007.08.020

Postma, D., Larsen, F., Thai, N.T., Trang, P.T.K., Jakobsen, R., Nhan, P.Q., Long, T.V., Viet, P.H., Murray, A.S., 2012. Groundwater arsenic concentrations in Vietnam controlled by sediment age. Nat. Geosci 5, 656–661.

Radloff, K.A., 2010. Geochemical and hydrologic determinants of arsenic distribution in sedimentary aquifers in Bangladesh. ProQuest Diss. Theses. Columbia University, Ann Arbor.

Radloff, K.A., Zheng, Y., Michael, H.A., Stute, M., Bostick, B.C., Mihajlov, I., Bounds, M., Huq, M.R., Choudhury, I., Rahman, M.W., Schlosser, P., Ahmed, K.M., Van Geen, A., 2011. Arsenic migration to deep groundwater in Bangladesh influenced by adsorption and water demand. Nat. Geosci. 4, 793–798. https://doi.org/10.1038/ngeo1283

Radu, T., Subacz, J.L., Phillippi, J.M., Barnett, M.O., 2005. Effects of dissolved carbonate on

arsenic adsorption and mobility. Environ. Sci. Technol. 39, 7875–7882. https://doi.org/10.1021/es050481s

Ravenscroft, P., Brammer, H., Richards, K., 2009. References, in: Arsenic Pollution. Wiley-Blackwell, pp. 528–580. https://doi.org/10.1002/9781444308785.refs

Ravenscroft, P., Burgess, W.G., Ahmed, K.M., Burren, M., Perrin, J., 2005. Arsenic in groundwater of the Bengal Basin, Bangladesh: Distribution, field relations, and hydrogeological setting. Hydrogeol. J. 13, 727–751.

Rhine, E.D., Garcia-Dominguez, E., Phelps, C.D., Young, L.Y., 2005. Environmental microbes can speciate and cycle arsenic. Environ. Sci. Technol. 39, 9569–9573. https://doi.org/10.1021/es051047t

Rosen, B.P., 2002. Biochemistry of arsenic detoxi ¢ cation. Science (80-.). 529, 86–92. https://doi.org/http://dx.doi.org/10.1016/S0014-5793(02)03186-1

Rosen, B.P., 1999. Families of arsenic transporters. Trends Microbiol. 7, 207–212. https://doi.org/https://doi.org/10.1016/S0966-842X(99)01494-8

Rowland, H.A.L., Gault, A.G., Lythgoe, P., Polya, D.A., 2008. Geochemistry of aquifer sediments and arsenic-rich groundwaters from Kandal Province, Cambodia. Appl. Geochemistry 23, 3029–3046. https://doi.org/http://dx.doi.org/10.1016/j.apgeochem.2008.06.011

Rowland, H.A.L., Pederick, R.L., Polya, D.A., Pancost, R.D., Van Dongen, B.E., Gault, A.G., Vaughan, D.J., Bryant, C., Anderson, B., Lloyd, J.R., 2007. The control of organic matter on microbially mediated iron reduction and arsenic release in shallow alluvial aquifers, Cambodia. Geobiology 5, 281–292. https://doi.org/10.1111/j.1472-4669.2007.00100.x

Sahu, S., Saha, D., 2015. Role of shallow alluvial stratigraphy and Holocene geomorphology on groundwater arsenic contamination in the Middle Ganga Plain, India. Environ. Earth Sci. 73, 3523–3536. https://doi.org/10.1007/s12665-014-3637-3

Sailo, L., Mahanta, C., 2016. Natural attenuation processes of arsenic in the groundwater of the Brahmaputra floodplain of Assam, India. Environ. Sci. Process. Impacts 18, 115–125. https://doi.org/10.1039/C5EM00401B

Sailo, L., Mahanta, C., 2014. Arsenic mobilization in the Brahmaputra plains of Assam: groundwater and sedimentary controls. Environ. Monit. Assess. 186, 6805–6820. https://doi.org/10.1007/s10661-014-3890-7

Sailo, L., Mahanta, C., 2013. Hydrogeochemical factors affecting the mobilization of As into the

groundwater of the Brahmaputra alluvial plains of Assam, Northeast India. Environ. Sci. Process. Impacts 15, 1775–1782. https://doi.org/10.1039/C3EM00156C

Salmassi, T.M., Venkateswaren, K., Satomi, M., Newman, D.K., Hering, J.G., 2002. Oxidation of Arsenite by Agrobacterium albertimagni , AOL15, sp. nov., Isolated from Hot Creek, California. Geomicrobiol. J. 19, 53–66. https://doi.org/10.1080/014904502317246165

Santini, J.M., Sly, L.I., Schnagl, R.D., Macy, J.M., 2000. A New Chemolithoautotrophic Arsenite-Oxidizing Bacterium Isolated from a Gold Mine: Phylogenetic, Physiological, and Preliminary Biochemical Studies. Appl. Environ. Microbiol. 66, 92–97.

Santini, J.M., Streimann, I.C.A., Hoven, R.N., 2004. Bacillus macyae sp . nov ., an arsenate-respiring bacterium isolated from an Australian gold mine 2241–2244. https://doi.org/10.1099/ijs.0.63059-0

Sarkar, A., Kazy, S., Sar, P., 2013. Characterization of arsenic resistant bacteria from arsenic rich groundwater of West Bengal, India. Ecotoxicology 22, 363–376. https://doi.org/10.1007/s10646-012-1031-z

Sathe, S.S., Mahanta, C., Mishra, P., 2018. Simultaneous influence of indigenous microorganism along with abiotic factors controlling arsenic mobilization in Brahmaputra floodplain, India. J. Contam. Hydrol. 0–1. https://doi.org/10.1016/j.jconhyd.2018.03.005

Schaefer, M. V., Ying, S.C., Benner, S.G., Duan, Y., Wang, Y., Fendorf, S., 2016. Aquifer Arsenic Cycling Induced by Seasonal Hydrologic Changes within the Yangtze River Basin. Environ. Sci. Technol. 50, 3521–3529. https://doi.org/10.1021/acs.est.5b04986

Schaefer, M. V, Guo, X., Gan, Y., Benner, S.G., Griffin, A.M., Gorski, C.A., Wang, Y., Fendorf, S., 2017. Redox controls on arsenic enrichment and release from aquifer sediments in central Yangtze River Basin. Geochim. Cosmochim. Acta 204, 104–119. https://doi.org/https://doi.org/10.1016/j.gca.2017.01.035

Sharma, A.K., Tjell, J.C., Sloth, J.J., Holm, P.E., 2014. Review of arsenic contamination, exposure through water and food and low cost mitigation options for rural areas. Appl. Geochemistry 41, 11–33. https://doi.org/https://doi.org/10.1016/j.apgeochem.2013.11.012

Silver, S., Phung, L.T., 2005. Genes and Enzymes Involved in Bacterial Oxidation and Reduction of Inorganic Arsenic. Appl. Environ. Microbiol. 71, 599–608. https://doi.org/10.1128/AEM.71.2.599-608.2005

Singh, A., 2004. Arsenic contamination in groundwater of North Eastern India. Natl. Semin. Hydrol. Roorkee.

Singh, A.K., 2004. Published in Proceedings of National seminar on Hydrology with focal theme on " Water Quality " held at National Institute of Arsenic Contamination in Groundwater of North Eastern India. Hydrology.

Smedley, P.L., Kinniburgh, D.G., 2002. A review of the source, behaviour and distribution of arsenic in natural waters. Appl. Geochemistry 17, 517–568. https://doi.org/http://dx.doi.org/10.1016/S0883-2927(02)00018-5

Smedley, P.L., Kinniburgh, D.G., Macdonald, D.M.J., Nicolli, H.B., Barros, A.J., Tullio, J.O., Pearce, J.M., Alonso, M.S., 2005. Arsenic associations in sediments from the loess aquifer of La Pampa, Argentina. Appl. Geochemistry 20, 989–1016. https://doi.org/10.1016/j.apgeochem.2004.10.005

Smedley, P.L., Zhang, M., Zhang, G., Luo, Z., 2003. Mobilisation of arsenic and other trace elements in fluviolacustrine aquifers of the Huhhot Basin, Inner Mongolia. Appl. Geochemistry 18, 1453–1477. https://doi.org/https://doi.org/10.1016/S0883-2927(03)00062-3

Smith, E., Naidu, R., Alston, A.M., 2002. Chemistry of inorganic arsenic in soils: II. Effect of phosphorus, sodium, and calcium on arsenic sorption. J. Environ. Qual. 31, 557–563.

Smith, J.V.S., Jankowski, J., Sammut, J., 2003. Vertical distribution of As(III) and As(V) in a coastal sandy aquifer: factors controlling the concentration and speciation of arsenic in the Stuarts Point groundwater system, northern New South Wales, Australia. Appl. Geochemistry 18, 1479–1496. https://doi.org/https://doi.org/10.1016/S0883-2927(03)00063-5

Song, S., Lopez-Valdivieso, A., Hernandez-Campos, D.J., Peng, C., Monroy-Fernandez, M.G., Razo-Soto, I., 2006. Arsenic removal from high-arsenic water by enhanced coagulation with ferric ions and coarse calcite. Water Res. 40, 364–372. https://doi.org/http://dx.doi.org/10.1016/j.watres.2005.09.046

Stahl., O.M., F., H.C., Alexander, van G., Jing, S., Pham, T.K.T., Vi, M.L., Thao, M.P., Pham, H.V., C., B.B., 2016. River bank geomorphology controls groundwater arsenic concentrations in aquifers adjacent to the Red River, Hanoi Vietnam. Water Resour. Res. 52, 6321–6334. https://doi.org/10.1002/2016WR018891

Standardization, I.O. for, 1995. Catalogue. International Organization for Standardization.

Stollenwerk, K.G., Breit, G.N., Welch, A.H., Yount, J.C., Whitney, J.W., Foster, A.L., Uddin, M.N., Majumder, R.K., Ahmed, N., 2007. Arsenic attenuation by oxidized aquifer sediments in Bangladesh. Sci. Total Environ. 379, 133–150. https://doi.org/http://dx.doi.org/10.1016/j.scitotenv.2006.11.029

Stolz, J.F., 2012. Overview of microbial arsenic metabolism and resistance. Metab. Arsenite 55–60.

Stumm, W., 1992. Chemistry of the solid-water interface: processes at the mineral-water and particle-water interface in natural systems. John Wiley & Son Inc.

Sun, H., 1997. A two-dimensional analytical solution of groundwater response to tidal loading in an estuary. Water Resour. Res. 33, 1429–1435.

Sun, J., Quicksall, A.N., Chillrud, S.N., Mailloux, B.J., Bostick, B.C., 2016. Arsenic mobilization from sediments in microcosms under sulfate reduction. Chemosphere 153, 254–261. https://doi.org/http://dx.doi.org/10.1016/j.chemosphere.2016.02.117

Tanaka, M., Takahashi, Y., Yamaguchi, N., Kim, K.-W., Zheng, G., Sakamitsu, M., 2013. The difference of diffusion coefficients in water for arsenic compounds at various pH and its dominant factors implied by molecular simulations. Geochim. Cosmochim. Acta 105, 360–371. https://doi.org/https://doi.org/10.1016/j.gca.2012.12.004

Tauhid-Ur-Rahman, M., Mano, A., Udo, K., Ishibashi, Y., 2011. Exploring sustainability of aquifers based on predictive modeling of sorption characteristics of arsenic enriched Holocene sediments in Bangladesh. Appl. Geochemistry 26, 636–647. https://doi.org/http://dx.doi.org/10.1016/j.apgeochem.2011.01.020

Tesfahunegn, G.B., Vlek, P.L.G., Tamene, L., 2013. Application of SWAT model to assess erosion hotspot for sub-catchment management at Mai-Negus catchment in northern Ethiopia. East African J. Sci. Technol. 2, 97–123.

Todd, D.K., Larry, W., 2005. Mays, groundwater hydrology.

Toth, J., 1963. A Theoretical Analysis of Groundwater Flow in Small Drainage Basins 1 of phe - low order stream and having similar t he outlet of lowest impounded body of a relatively. J. Geophys. Res. 68, 4795–4812. https://doi.org/10.1029/JZ068i016p04795

Tripti, K., Shardendu, 2016. PH modulates arsenic toxicity in Bacillus licheniformis DAS-2. Ecotoxicol. Environ. Saf. 130, 240–247. https://doi.org/10.1016/j.ecoenv.2016.04.029

Turner, A.W., 1949. Bacterial Oxidation of Arsenite. Nature 164, 76.

Ujević Bošnjak, M., Capak, K., Jazbec, A., Casiot, C., Sipos, L., Poljak, V., Dadić, Ž., 2012. Hydrochemical characterization of arsenic contaminated alluvial aquifers in Eastern Croatia using multivariate statistical techniques and arsenic risk assessment. Sci. Total Environ. 420, 100–110. https://doi.org/http://dx.doi.org/10.1016/j.scitotenv.2012.01.021

Ujević Bošnjak, M., Casiot, C., Duić, Ž., Fazinić, S., Halamić, J., Sipos, L., Santo, V., Dadić, Ž., 2013. Sediment characterization and its implications for arsenic mobilization in deep aquifers of eastern Croatia. J. Geochemical Explor. 126–127, 55–66. https://doi.org/http://dx.doi.org/10.1016/j.gexplo.2012.12.017

van Geen, A., Zheng, Y., Goodbred, S., Horneman, A., Aziz, Z., Cheng, Z., Stute, M., Mailloux, B., Weinman, B., Hoque, M.A., Seddique, A.A., Hossain, M.S., Chowdhury, S.H., Ahmed, K.M., 2008. Flushing History as a Hydrogeological Control on the Regional Distribution of Arsenic in Shallow Groundwater of the Bengal Basin. Environ. Sci. Technol. 42, 2283–2288. https://doi.org/10.1021/es702316k

van Geen, A., Zheng, Y., Versteeg, R., Stute, M., Horneman, A., Dhar, R., Steckler, M., Gelman, A., Small, C., Ahsan, H., Graziano, J.H., Hussain, I., Ahmed, K.M., 2003. Spatial variability of arsenic in 6000 tube wells in a 25 km2 area of Bangladesh. Water Resour. Res. 39, 1140. https://doi.org/10.1029/2002WR001617

Verma, S., Mukherjee, A., Choudhury, R., Mahanta, C., 2015. Brahmaputra river basin groundwater: Solute distribution, chemical evolution and arsenic occurrences in different geomorphic settings. J. Hydrol. Reg. Stud. 4, Part A, 131–153. https://doi.org/http://dx.doi.org/10.1016/j.ejrh.2015.03.001

von Brömssen, M., Häller Larsson, S., Bhattacharya, P., Hasan, M.A., Ahmed, K.M., Jakariya, M., Sikder, M.A., Sracek, O., Bivén, A., Doušová, B., Patriarca, C., Thunvik, R., Jacks, G., 2008. Geochemical characterisation of shallow aquifer sediments of Matlab Upazila, Southeastern Bangladesh — Implications for targeting low-As aquifers. J. Contam. Hydrol. 99, 137–149. https://doi.org/https://doi.org/10.1016/j.jconhyd.2008.05.005

von Brömssen, M., Jakariya, M., Bhattacharya, P., Ahmed, K.M., Hasan, M.A., Sracek, O., Jonsson, L., Lundell, L., Jacks, G., 2007. Targeting low-arsenic aquifers in Matlab Upazila, Southeastern Bangladesh. Sci. Total Environ. 379, 121–132. https://doi.org/https://doi.org/10.1016/j.scitotenv.2006.06.028

Wang, J., Zeng, X.C., Zhu, X., Chen, X., Zeng, X., Mu, Y., Yang, Y., Wang, Y., 2017. Sulfate enhances the dissimilatory arsenate-respiring prokaryotes-mediated mobilization, reduction and release of insoluble arsenic and iron from the arsenic-rich sediments into groundwater. J. Hazard. Mater. 339, 409–417. https://doi.org/10.1016/j.jhazmat.2017.06.052

Wang, S., Mulligan, C.N., 2006. Occurrence of arsenic contamination in Canada: Sources, behavior and distribution. Sci. Total Environ. 366, 701–721. https://doi.org/http://dx.doi.org/10.1016/j.scitotenv.2005.09.005

Weeger D., W.A.-L., 1999. Oxidation of arsenite to arsenate by a bacterium isolated from an aquatic environment: RN - Biometals, v. 12, p. 141-149. 141–149.

Wei, L.H., Zhou, W.G., 1992. Development of arsenic mineral resources and environment control. Hunan Geol 11, 259–262.

Wen, D., Zhang, F., Zhang, E., Wang, C., Han, S., Zheng, Y., 2013. Arsenic, fluoride and iodine in groundwater of China. J. Geochemical Explor. 135, 1–21. https://doi.org/http://dx.doi.org/10.1016/j.gexplo.2013.10.012

Wenzel, W.W., Kirchbaumer, N., Prohaska, T., Stingeder, G., Lombi, E., Adriano, D.C., 2001a. Arsenic fractionation in soils using an improved sequential extraction procedure. Anal. Chim. Acta 436, 309–323. https://doi.org/http://dx.doi.org/10.1016/S0003-2670(01)00924-2

Wenzel, W.W., Kirchbaumer, N., Prohaska, T., Stingeder, G., Lombi, E., Adriano, D.C., 2001b. Arsenic fractionation in soils using an improved sequential extraction procedure 436, 309–323.

W.H.O., 2015. Guidelines for Drinking-Water Quality, Geneva: World Health Organization; 2011.

Winkel, L.H.E., Trang, P.T.K., Lan, V.M., Stengel, C., Amini, M., Ha, N.T., Viet, P.H., Berg, M., 2011. Arsenic pollution of groundwater in Vietnam exacerbated by deep aquifer exploitation for more than a century. Proc. Natl. Acad. Sci. 108, 1246–1251. https://doi.org/10.1073/pnas.1011915108

Xu, M., Eckstein, Y., 1995. Use of weighted least-squares method in evaluation of the relationship between dispersivity and field scale. Groundwater 33, 905–908.

Zhang, L., Qin, X., Tang, J., Liu, W., Yang, H., 2017. Review of arsenic geochemical characteristics and its significance on arsenic pollution studies in karst groundwater, Southwest China. Appl. Geochemistry. https://doi.org/10.1016/j.apgeochem.2016.05.014

Zhang, Z., Yin, N., Cai, X., Wang, Z., Cui, Y., 2016. Arsenic redox transformation by Pseudomonas sp. HN-2 isolated from arsenic-contaminated soil in Hunan, China. J. Environ. Sci. 47, 165–173. https://doi.org/https://doi.org/10.1016/j.jes.2015.11.036

Zhao, K., Guo, H., Zhou, X., 2014. Adsorption and heterogeneous oxidation of arsenite on modified granular natural siderite: Characterization and behaviors. Appl. Geochemistry 48, 184–192. https://doi.org/10.1016/j.apgeochem.2014.07.016

Appendix A1

Appendix Table A 1. 1: Summary of hydro-chemical parameters of H*As*CR groundwater samples.

ID	Latitude	Longitude	pH	Temp.	EC	DO	ORP	Eh	Well depth	Filter Length	As	TDS	Ca	Na	K	Cl^-	Fe	Mn	Mg	SO_4^{-2}	HCO_3^-	PO_4^{-3}
				°C	µS cm^{-1}	mg L^{-1}	mV	mV	(feet)	(feet)	µg L^{-1}	mg L^{-1}										
B1-1	90.7214°	26.3239°	7.3	25.6	104.0	1	-276.3	-76.3	86	6	352.7	204.2	64.2	54.6	33.8	0.4	35.0	1.8	13.9	2.8	170	2.2
B1-2	90.7305°	26.3264°	7.1	25.3	409.0	1.1	-289.3	-89.3	66	6	108.3	207.0	64.5	36.2	22.5	0.1	44.8	1.1	29.5	1.7	150	3.1
B1-3	90.68°	26.309°	7.3	25.4	268.0	1	-98.3	101.7	80	6	30.3	231.6	16.4	27.3	32.6	0.4	18.0	0.8	23.8	0.6	104	1.3
B1-4	90.68°	26.312°	7.1	25.3	256.0	0.9	-104.1	95.9	86	6	33.2	237.4	40.4	4.7	5.7	1.0	8.4	0.5	27.5	0.1	82	1.8
B1-5	90.679°	26.314°	7.1	25.4	322.0	0.9	-271.2	-71.2	86	6	20.1	269.2	78.2	31.3	10.1	2.5	23.3	0.6	28.2	0.1	153	1.1
B1-6	90.6809°	26.3239°	7.2	25.1	432.0	1	-125.4	74.6	86	6	17.1	304.2	26.4	10.5	3.6	1.3	6.5	0.8	16.8	0.0	50	3.1
B1-7	90.68°	26.321°	7.1	25.1	412.0	1.2	-176.4	23.6	86	6	19.2	287.1	34.8	27.9	13.4	1.4	5.7	0.8	27.3	0.9	107	1.3
B1-8	90.689°	26.329°	7.3	25.3	566.0	1.1	-146.3	53.7	36	6	20.1	295.4	42.7	38.1	29.9	2.9	6.1	0.8	30.1	0.2	128	1.2
B1-9	90.69°	26.328°	7.0	25.1	412.0	1.2	-188.4	11.6	36	6	43.3	271.2	58.2	15.6	5.1	1.3	12.3	0.8	17.7	1.0	94	1.3
B1-10	90.686°	26.322°	7.4	25.1	558.0	1.1	-233.4	-33.4	57	6	20.2	243.7	44.1	13.5	4.0	0.3	34.3	0.8	16.3	0.0	78	1.8
B1-11	90.687°	26.322°	7.2	25.2	512.0	1.1	-142.4	57.6	26	6	15.2	278.2	48.3	28.3	22.5	1.4	10.7	0.7	17.6	1.2	112	1.2
B1-12	90.685°	26.321°	7.1	25.1	556.0	0.9	-221.8	-21.8	80	6	16.3	317.2	46.2	34.6	13.0	1.4	26.6	0.7	19.5	1.3	103	1.8
B1-13	90.692°	26.319°	7.0	25.1	452.0	0.8	-236.4	-36.4	80	6	18.4	322.2	56.0	15.3	6.2	2.7	29.5	0.7	14.2	1.9	88	1.8
B1-14	90.687°	26.317°	7.0	25	348.0	0.8	-296.3	-96.3	85	6	61.0	267.4	27.8	5.1	8.3	2.4	63.7	1.7	26.3	2.8	60	5.5
B1-15	90.703°	26.314°	7.1	24.8	299.0	0.9	-103.7	96.3	66	6	20.3	298.1	34.6	26.1	8.3	3.2	9.2	0.7	22.4	0.8	91.3	5.4
B1-16	90.7°	26.315°	7.8	24.15	284.0	0.7	-284.9	-84.9	60	5	20.3	278.3	70.3	46.1	36.6	2.3	21.2	0.9	18.9	1.3	162	1.8
B1-17	90.701°	26.322°	7.6	25.3	219.0	0.6	-269.8	-69.8	80	5	20.1	260.1	72.3	61.2	56.8	1.4	16.3	1.2	16.5	0.2	217	1.9
B1-18	90.689°	26.3°	6.9	25.1	224.0	0.9	-260.7	-60.7	80	6	45.1	241.4	16.0	36.3	42.0	4.0	58.6	1.0	10.5	1.9	106	2.4
B1-19	90.695°	26.311°	6.9	25.1	184.0	1	-366.7	-166.7	80	6	20.3	244.6	45.7	7.9	7.1	4.6	26.1	0.6	37.6	1.2	93	4.8
B1-20	90.694°	26.308°	7.0	25.2	233.0	0.9	-273.6	-73.6	80	6	15.3	227.4	75.2	18.6	8.0	1.8	24.6	0.6	24.9	0.2	124	5.9
B1-21	90.686°	26.292°	7.0	25.3	182.0	0.9	-287.3	-87.3	75	6	22.2	388.6	55.1	5.5	5.8	3.7	12.1	0.7	11.3	2.8	72	6.0
B1-22	90.685°	26.287°	7.0	25.4	147.0	0.8	-295.0	-95.0	80	6	19.3	361.2	54.9	3.9	5.5	3.0	26.1	2.4	13.6	1.9	72	4.0
B1-23	90.684°	26.286°	7.0	25.3	121.0	1	-280.0	-80.0	80	6	15.3	204.7	47.6	6.3	5.1	2.2	27.9	0.7	11.3	2.5	64	4.3
B1-24	90.684°	26.285	7.2	25.3	155.0	1.1	-244.6	-44.6	76	6	86.2	197.4	16.9	5.1	2.0	2.6	61.0	2.0	35.3	2.7	52	3.3
B1-25	90.686°	26.288°	7.1	25.1	112.0	1.3	-217.1	-17.1	80	6	98.2	203.5	33.2	25.6	12.5	2.4	56.2	1.3	33.7	3.8	89	3.9
B1-26	90.683°	26.284°	7.2	25	133.0	1.1	-216.5	-16.5	80	6	90.2	281.5	31.4	26.9	17.4	2.2	47.3	0.3	23.0	3.1	80	4.6
B1-27	90.686°	26.284°	7.3	25.1	362.0	1.2	-234.7	-34.7	76	6	90.3	230.3	14.1	10.6	22.7	1.4	58.0	0.3	34.2	2.0	78	5.5
B1-28	90.679°	26.285°	7.1	25.2	456.0	0.9	-234.2	-34.2	76	6	30.2	243.4	53.6	38.8	44.2	2.6	26.1	0.2	1.8	1.2	144	2.1
B1-29	90.68°	26.275°	6.7	25	301.7	1.1	-262.8	-62.8	80	6	176.2	327.1	48.2	33.1	26.5	1.3	72.3	1.3	36.3	3.7	137	2.1
B1-30	90.679°	26.274°	6.8	25.3	568.0	1	-141.3	58.7	100	6	35.2	311.7	46.0	5.9	4.0	3.2	12.0	1.5	10.2	2.1	61.6	1.0
B1-31	90.677°	26.281°	6.4	25.4	649.0	1.1	-289.2	-89.2	60	6	17.3	298.4	35.5	15.8	2.2	2.6	20.6	0.9	8.5	3.9	58	1.5
B1-32	90.677°	26.277°	6.9	25.1	761.0	1	-283.6	-83.6	60	5	25.4	330.4	30.2	14.5	1.2	3.9	12.8	1.0	0.1	2.8	40	1.5
B1-33	90.677°	26.279°	7.4	25.1	788.0	0.9	-202.6	-2.6	80	6	20.3	362.9	19.1	30.1	2.3	3.1	37.6	0.7	17.5	2.7	62	1.2
B1-34	90.68°	26.279°	7.0	25.3	692.0	0.9	-227.9	-27.9	80	6	170.4	252.3	14.3	21.0	1.7	4.9	43.5	1.6	31.3	3.7	60	4.1
B1-35	90.696°	26.306°	6.9	25.1	682.0	1.3	-216.7	-16.7	110	6	20.3	208.2	13.7	16.5	17.9	1.2	48.5	0.7	8.3	2.7	57	1.8
B1-36	90.705°	26.298°	7.1	25.1	538.0	1.2	-284.3	-84.3	80	6	21.3	306.2	43.3	13.1	4.9	1.3	47.6	0.6	23.6	1.6	82	3.7
B1-37	90.725°	26.302°	7.8	25.2	661.0	1.4	-264.4	-64.4	60	6	81.3	384.6	57.7	23.7	12.4	0.9	39.5	0.7	18.3	0.7	112.3	4.2
B1-38	90.722°	26.3°	6.8	25.1	793.0	1.1	-258.0	-58.0	40	6	15.2	370.1	72.1	3.8	6.5	0.7	46.5	0.3	16.2	2.0	93.1	1.8

B1-39	90.707°	26.286°	7.3	24.8	487.0	1.7	-130.2	69.8	80	6	82.2	405.1	66.9	9.2	2.3	0.3	43.1	0.2	2.4	2.1	80	2.1
B1-40	90.706°	26.282°	7.2	25.5	614.0	1.3	-275.0	-75.0	60	6	34.3	215.4	72.7	7.8	2.4	1.3	57.3	0.0	2.3	2.1	87	2.1
B1-41	90.718°	26.284°	6.9	25	353.0	0.9	-124.6	75.4	80	6	15.4	231.5	50.1	11.7	1.2	2.0	50.4	0.4	35.5	3.2	93	4.1
B1-42	90.708°	26.28°	6.7	25	336.0	0.8	-77.7	122.4	80	6	16.3	274.6	39.1	3.8	5.2	0.3	52.4	0.4	33.3	2.2	82	4.1
B1-43	90.714°	26.277°	6.4	25.4	567.0	0.8	-66.4	133.6	80	6	19.4	294.6	61.5	11.7	0.3	0.9	57.4	0.4	4.7	2.2	76	5.5
B1-44	90.716°	26.277°	6.8	25.1	597.0	0.9	-28.8	171.2	65	6	29.3	288.2	49.6	3.0	5.6	0.5	52.2	0.2	6.6	2.6	63	5.5
B1-45	90.702°	26.279°	6.4	25	651.0	1.2	-50.7	149.3	65	6	21.3	220.2	47.6	5.0	6.0	0.2	54.6	0.3	2.4	1.2	58	5.9
B1-46	90.7°	26.281°	6.9	25.2	737.0	0.8	-68.5	131.6	60	6	47.1	384.2	57.2	8.1	3.5	0.3	37.1	bdl	8.3	2.9	74	3.8
B1-47	90.7°	26.28°	7.4	25.2	453.0	0.8	-39.8	160.2	60	6	100.2	361.2	33.4	9.6	4.2	0.7	56.2	1.2	26.5	3.2	73	1.8
B1-48	90.704°	26.28°	7.0	25.1	714.0	1.2	-105.4	94.6	60	6	34.4	204.7	75.9	5.1	3.7	0.6	48.7	0.1	23.1	1.0	112	3.6
B1-49	90.691°	26.283°	6.9	25.1	676.0	0.9	-277.6	-77.6	60	6	58.0	197.4	42.4	7.3	13.9	0.5	46.3	0.1	24.2	2.0	87	2.7
B1-50	90.701°	26.284°	7.1	25.3	546.0	0.8	-211.6	-11.6	45	6	97.2	203.5	53.4	5.5	5.6	0.4	38.5	0.1	3.6	3.6	70	1.3
B1-51	90.702°	26.292°	7.7	25.2	718.0	0.9	-110.4	89.6	80	6	75.0	281.5	62.4	38.4	23.9	0.2	34.6	1.1	6.5	2.1	127.2	5.7
B1-52	90.692°	26.273°	8.1	25.3	764.0	1	-113.4	86.6	60	6	45.1	230.3	90.4	5.7	6.9	2.2	36.6	0.1	4.7	1.5	117	3.7
B1-53	90.687°	26.271°	8.3	25.4	694.0	0.8	-70.6	129.4	40	6	100.2	243.4	87.5	43.2	13.7	0.7	63.5	1.0	38.1	3.2	167	6.0
B1-54	90.686°	26.266°	7.6	25.3	834.0	2.4	-147.1	52.9	80	6	59.0	327.1	41.8	8.8	3.8	0.2	42.6	1.3	2.4	1.2	57	3.1
B1-55	90.668°	26.28°	8.4	25.3	597.0	1	-189.4	10.6	60	6	19.0	237.4	24.1	32.1	15.2	0.3	31.4	1.0	6.3	1.2	80	4.1
B1-56	90.659°	26.278°	8.7	25.1	584.0	0.9	-210.6	-10.6	80	6	27.0	269.2	62.6	7.0	4.9	0.2	37.4	1.0	8.5	1.3	82	3.5
B1-57	90.669°	26.276°	7.8	25	664.0	0.9	-217.1	-17.1	80	6	100.0	304.2	61.1	4.6	5.6	0.5	66.5	1.0	14.9	2.1	86.1	3.7
B1-58	90.668°	26.273°	7.6	25.1	761.0	0.8	-216.5	-16.5	80	6	66.0	287.1	109	7.6	7.0	0.3	47.1	1.1	2.3	2.1	126	4.8
B1-59	90.667°	26.262°	8.8	25.2	820.0	0.9	-234.7	-34.7	65	6	52.0	295.4	106	7.4	6.9	0.5	49.2	1.1	1.5	1.0	117	3.5
B1-60	90.669°	26.261°	6.9	25	674.0	0.9	-234.2	-34.2	65	6	51.0	271.2	92.5	4.9	6.0	0.8	33.9	0.9	3.3	1.3	97	4.1
B1-61	90.669°	26.26°	7.1	25.3	364.0	1	-100.3	99.7	45	6	66.0	243.7	38.4	6.7	6.5	0.3	41.5	1.1	9.5	1.8	55	3.4
B1-62	90.67°	26.259°	7.1	25.4	448.0	0.9	-98.3	101.7	80	6	27.0	278.2	55.7	6.6	6.7	0.3	33.8	0.8	4.2	3.5	73	2.9
B1-63	90.671°	26.259°	6.9	25.1	874.0	1.2	-104.1	95.9	80	6	68.0	317.2	47.3	19.0	62.5	0.5	56.2	1.2	36.2	2.6	167	2.5
B1-64	90.671°	26.258°	6.9	25.6	942.0	1.1	-171.2	28.8	60	6	66.0	278.2	28.5	13.2	8.9	0.2	50.9	1.0	17.6	3.2	62	4.7
B1-65	90.6709°	26.2549°	7.0	25.3	961.0	1.3	-125.4	74.6	40	6	24.0	317.2	41.6	39.0	25.3	0.2	37.5	1.2	26.4	2.3	133	1.8
B1-66	90.6819°	26.2549°	7.0	25.4	535.0	1.2	-176.4	23.6	80	6	26.0	322.2	38.7	28.6	20.7	0.2	38.6	1.4	18.4	3.3	111	1.4
B1-67	90.6809°	26.2549°	7.0	25.3	453.0	1.4	-146.3	53.7	60	6	28.0	267.4	22.4	30.6	38.2	0.4	31.5	1.0	19.2	2.7	108	1.5
B1-68	90.662°	26.256°	7.0	25.4	249.0	1.3	-188.4	11.6	80	6	22.0	298.1	61.0	7.6	1.5	0.5	33.3	1.3	21.2	2.1	91	1.8
B1-69	90.6669°	26.256°	7.2	25.1	374.0	1.1	-210.4	-10.4	80	6	15.0	278.3	38.1	6.4	1.3	0.2	24.9	1.0	32.6	2.7	76	4.7
B1-70	90.6569°	26.2639°	7.1	25.1	246.0	1.2	-90.0	110.0	80	6	39.0	260.1	44.8	19.4	17.2	0.4	35.8	1.0	22.1	2.5	89	2.2
B1-71	90.662°	26.2609°	7.2	25.3	231.0	1.3	-125.9	74.1	65	6	37.0	241.4	39.2	16.4	10.3	0.5	31.6	1.0	14.4	3.4	71	3.1
B1-72	90.679°	26.263°	7.3	25.1	247.0	1.1	-116.0	84.0	65	6	87.0	244.6	34.9	6.3	5.5	0.3	63.2	1.3	52.2	1.8	99	2.1
B1-73	90.678°	26.2619°	7.1	25.1	986.0	1.2	-125.9	74.1	80	6	25.0	227.4	98.2	6.7	5.2	0.1	26.0	1.0	16.1	1.8	131	3.7
B1-74	90.645°	26.25°	6.7	25.2	862.0	1.1	-88.0	112.0	60	6	92.0	388.6	36.8	5.9	5.8	0.6	31.1	1.0	20.1	1.8	63	2.1
B1-75	90.6449°	26.249°	6.9	25.1	794.0	0.8	-70.0	130.0	40	6	29.2	361.2	50.7	8.3	4.6	0.3	32.0	1.0	17.2	1.8	76	3.1
B1-76	90.65°	26.253°	8.1	25.1	862.0	0.9	-110.4	89.6	80	6	33.2	204.7	111	12.9	10.1	0.4	48.8	1.0	11.6	1.9	126	3.7
B1-77	90.651°	26.249°	7.4	25	776.0	0.8	-113.4	86.6	60	6	100.1	197.4	18.0	9.5	1.0	0.5	52.4	2.0	33.6	2.9	56	4.8
B1-78	90.651°	26.25°	6.8	24.8	844.0	0.9	-70.6	129.4	80	6	110.3	231.6	17.6	9.5	1.8	1.1	63.3	2.0	32.2	3.0	58	3.5
B1-79	90.652°	26.2479°	6.8	25.1	684.0	0.7	-147.1	52.9	80	6	45.4	237.4	30.4	4.3	11.1	0.2	34.9	1.0	13.6	3.7	54.2	4.1
B1-80	90.652°	26.2469°	6.4	25	424.0	1.3	-189.4	10.6	80	6	80.4	269.2	36.1	18.9	11.5	0.5	58.2	0.9	3.2	1.3	71.2	3.4
B1-81	90.6529°	26.246°	6.9	25.1	335.0	1.2	-210.6	-10.6	65	6	21.1	304.2	52.6	6.5	3.9	0.7	32.0	1.0	13.2	1.2	74.2	2.9
B1-82	90.6529°	26.243°	7.4	25.2	682.0	0.8	-216.5	-16.5	65	6	22.7	287.1	53.9	9.8	10.9	0.6	32.1	0.9	2.6	0.9	81	2.5
B1-83	90.6529°	26.242°	7.0	25	538.0	0.8	-138.0	62.0	80	6	30.3	295.4	37.6	9.9	10.2	0.3	33.2	0.9	1.5	0.2	60	4.7
B1-84	90.6529°	26.2409°	6.9	25.3	661.0	0.9	-147.4	52.6	60	6	46.9	271.2	52.0	5.8	3.6	0.5	34.3	1.0	30.4	2.5	93	1.8

B1-85	90.653°	26.239°	7.1	25.4	793.0	0.8	-164.8	35.2	40	6	92.5	243.7	36.4	8.6	1.6	0.6	70.2	1.7	1.5	1.1	49.8	1.4
B1-86	90.6159°	26.242°	7.8	25.1	487.0	1	-130.2	69.8	80	6	15.6	361.2	43.6	12.5	3.6	2.0	24.7	0.9	3.7	1.3	57	1.5
B1-87	90.619°	26.235°	6.8	25.1	614.0	0.9	-68.5	131.6	60	6	25.9	204.7	26.3	22.3	16.5	1.0	12.6	0.9	4.2	1.0	59.1	1.5
B1-88	90.622°	26.234°	7.3	25.3	353.0	0.7	-39.8	160.2	80	6	77.5	197.4	29.5	14.3	6.5	0.4	51.9	1.0	2.3	1.5	54.3	1.5
B1-89	90.6149°	26.233°	7.2	25.2	336.0	0.7	-105.4	94.6	80	6	92.2	203.5	31.3	14.2	5.6	0.4	56.5	1.2	6.5	1.0	59.5	1.2
B1-90	90.6119°	26.234°	6.9	25.3	567.0	0.8	-277.6	-77.6	80	6	100.2	281.5	23.1	13.3	4.2	0.4	68.5	1.2	31.3	2.6	71.2	4.1
B1-91	90.611°	26.235°	7.3	25.4	597.0	0.7	-211.6	-11.6	65	6	113.5	230.3	18.2	17.0	3.3	1.1	51.0	1.0	36.2	2.5	76.1	1.8
B1-92	90.61°	26.236°	7.4	25.3	651.0	0.7	-110.4	89.6	65	6	93.3	243.4	42.1	10.3	1.3	1.6	57.1	0.9	1.3	2.5	52	3.7
B1-93	90.605°	26.235°	7.9	25.3	737.0	0.8	-113.4	86.6	80	6	41.3	327.1	44.2	6.5	1.4	0.2	30.7	1.0	2.6	2.5	53.3	4.2
B1-94	90.625°	26.229°	8.4	25.1	453.0	0.6	-70.6	129.4	80	6	100.2	237.4	20.3	13.3	7.6	0.3	59.8	1.0	31.5	2.6	68	1.8
B1-95	90.669°	26.288°	8.1	25	714.0	0.7	-147.1	52.9	65	6	19.7	269.2	36.1	16.6	12.4	0.3	30.3	0.3	3.2	2.8	57.6	2.1
B1-96	90.669°	26.291°	8.4	25.1	676.0	0.6	-189.4	10.6	65	6	24.1	304.2	60.5	34.2	23.5	0.8	36.5	1.0	1.2	1.5	110.2	2.1
B1-97	90.7°	26.328°	7.6	25.2	546.0	0.6	-210.6	-10.6	65	6	32.1	287.1	56.3	7.6	6.1	0.7	46.0	1.0	2.2	1.7	58.1	4.1
B1-98	90.707°	26.315°	7.5	25	718.0	1.1	-217.1	-17.1	25	6	24.1	295.4	56.1	43.6	19.6	1.8	39.2	1.0	6.9	3.2	116.3	4.1
B1-99	90.701°	26.318°	6.9	25.3	764.0	0.9	-216.5	-16.5	80	6	16.0	197.4	48.7	11.4	7.2	1.5	7.2	1.0	2.7	2.1	69.2	5.5
B1-100	90.716°	26.322°	7.2	25.4	631.0	1	-234.7	-34.7	25	6	18.4	203.5	40.2	22.3	18.6	0.1	5.2	0.9	16.1	2.5	95.6	5.5
B1-101	90.708°	26.331°	7.2	25.1	592.0	0.8	-234.2	-34.2	26	6	8.1	281.5	58.6	34.3	13.6	0.1	2.5	1.7	3.7	2.8	101.4	5.9
B1-102	90.714°	26.333°	7.2	25.5	358.0	2.4	-100.3	99.7	26	6	16.4	230.3	40.3	22.8	11.4	0.2	2.3	1.2	7.9	2.2	81.2	3.8
B1-103	90.725°	26.317°	7.4	25.4	793.0	1	-98.3	101.7	86	6	41.1	243.4	33.9	21.5	10.3	1.2	29.0	1.0	7.0	1.7	75.1	1.8
B1-104	90.718°	26.319°	7.4	25.5	603.0	0.9	-104.1	95.9	26	6	20.2	327.1	23.7	56.2	34.3	1.3	6.2	0.5	33.5	3.2	136.2	1.5
B1-105	90.709°	26.328°	7.1	25.6	334.0	0.9	-171.2	28.8	80	6	31.2	204.7	20.4	16.5	4.7	0.1	16.1	1.3	14.3	2.2	54	1.5
B1-106	90.718°	26.331°	6.8	25.1	423.0	1.2	-188.5	11.6	80	6	31.0	291.4	52.3	60.3	38.1	0.8	11.2	1.6	53.8	1.3	221.3	1.2
B1-107	90.724°	26.317°	6.4	25	210.0	1.3	-175.6	24.4	25	6	21.1	305.4	68.4	59.8	43.2	0.3	10.1	1.3	23.0	1.3	206.1	4.1
B1-108	90.72°	26.331°	6.9	25.1	946.0	0.8	-193.7	6.3	26	6	18.5	266.4	42.7	37.3	24.7	0.6	5.2	1.0	44.6	2.0	162	1.8
B1-109	90.724°	26.3°	7.4	25.2	882.0	0.7	-185.6	14.4	26	6	56.3	301.6	37.1	22.4	36.3	0.9	35.2	1.5	24.0	2.2	118.4	3.7
B1-110	90.72°	26.319°	7.0	25	726.0	0.6	-177.4	22.6	100	6	62.2	279.6	29.6	16.4	22.5	3.2	41.2	1.3	2.0	2.2	63.1	4.2
B1-111	90.719°	26.314°	6.9	25.3	713.0	0.8	-164.6	35.5	80	6	44.3	288.2	38.2	27.1	22.6	1.2	52.9	0.5	28.8	1.7	116.5	1.8
B1-112	90.7102°	26.3097°	7.3	26.1	392.1	1	-268.9	-68.9	80	6	80.6	257.3	49.7	14.2	2.4	0.6	57.2	0.0	18.7	1.3	81.5	2.1
B1-113	90.698°	26.2994°	7.0	25.1	453.8	0.9	-216.5	-16.5	80	6	86.4	340.2	15.1	42.9	36.2	0.2	44.0	0.0	29.1	1.5	113	1.5
B1-114	90.7025°	26.3072°	7.0	25.9	390.0	0.7	-198.5	1.5	80	6	90.1	302.0	31.5	14.4	16.3	0.6	41.9	1.0	26.5	2.5	84.3	1.3
B1-115	90.7042°	26.3102°	7.1	25.1	735.0	0.7	-201.1	-1.1	80	6	102.3	291.4	32.7	6.1	6.4	3.5	48.2	1.2	33.7	0.2	80.2	1.8
B1-116	90.7058°	26.3043°	6.9	25.2	402.7	0.8	-223.2	-23.2	80	6	77.6	310.3	37.0	16.2	1.2	1.5	66.5	0.4	3.4	0.9	56.9	2.2
B1-117	90.6942°	26.3075°	7.1	25.8	360.6	0.7	-225.0	-25.0	80	6	54.7	280.9	35.4	8.1	4.3	2.0	51.4	0.9	10.3	0.1	50	2.6
B1-118	90.7142°	26.3152°	7.0	25.7	399.6	1.1	-210.3	-10.3	80	6	96.9	300.3	29.6	4.4	5.2	2.5	69.5	0.3	11.2	0.1	52	0.3
B1-119	90.7104°	26.3177°	7.1	25.4	697.0	1.3	-278.6	-78.6	80	6	114.6	280.7	29.6	7.4	6.7	1.0	43.4	1.0	30.9	2.6	69.3	1.0
B1-120	90.7137°	26.3104°	7.2	25.7	553.0	1.2	-257.6	-57.6	80	6	101.3	264.4	29.8	10.3	5.6	1.5	41.1	1.2	21.8	1.2	64.8	1.4
B1-121	90.6995°	26.2954°	7.1	25.4	522.0	0.8	-206.2	-6.2	80	6	88.1	271.6	37.8	5.7	4.9	2.0	49.3	0.2	9.7	1.4	60.3	1.1
B1-122	90.6966°	26.2917°	7.2	26.1	357.2	0.7	-191.5	8.5	80	6	109.7	386.7	31.1	13.2	3.2	1.5	48.3	1.5	9.3	1.4	54.3	1.8
B1-123	90.7011°	26.2994°	7.1	25.9	429.8	0.6	-250.4	-50.4	80	6	98.7	263.2	31.8	8.5	6.4	2.0	45.4	0.5	6.6	0.9	54.3	1.4
B1-124	90.7064°	26.3073°	7.1	25.1	556.0	1.4	-235.8	-35.8	80	6	127.6	287.9	31.5	4.0	1.8	0.5	47.4	1.2	30.8	0.6	72.2	0.5
B1-125	90.7001°	26.3036°	7.1	25.3	503.0	1.3	-215.7	-15.7	80	6	121.1	254.3	28.7	3.5	3.5	2.0	46.2	0.5	39.5	1.1	76.3	1.5
B1-126	90.7°	26.3109°	7.2	25.3	233.7	1.1	-209.1	-9.1	80	6	119.4	468.4	38.0	10.0	4.5	0.5	40.3	0.2	38.1	1.5	89.1	1.7
B1-127	90.649°	26.34°	6.7	24.3	905.0	0.9	-188.4	11.6	80	6	7.2	104.3	23.7	24.9	1.6	0.1	20.7	0.2	12.5	1.5	64.3	2.2
B1-128	90.651°	26.341°	6.9	24.4	820.0	0.9	-210.4	-10.4	100	6	0.3	109.8	55.6	8.3	0.6	1.2	5.6	0.3	0.0	1.9	61.3	3.1
B1-129	90.654°	26.344°	6.3	24.8	830.0	1	-231.7	-31.7	80	6	9.4	118.6	34.2	22.9	16.2	2.7	41.9	0.2	6.7	1.8	73.6	1.3
B1-130	90.653°	26.344°	6.9	24	897.0	1	-164.8	35.2	120	6	10.7	164.3	39.2	26.3	20.6	1.5	20.0	0.3	16.2	1.5	102.6	1.8

B1-131	90.644°	26.359°	6.3	26	708.0	0.9	-146.1	53.9	80	6	8.0	137.2	44.4	28.4	18.3	1.3	63.5	0.1	17.8	1.7	113.6	1.1
B1-132	90.652°	26.367°	6.8	25.6	833.0	1	-134.9	65.1	100	6	9.1	224.2	78.8	16.1	37.0	0.1	12.5	0.6	12.7	1.6	153.3	3.1
B1-133	90.65°	26.369°	7.1	25.4	678.0	1	-164.3	35.7	120	6	10.1	119.0	62.1	6.3	5.7	1.2	8.3	2.2	28.3	3.2	102.5	1.3
B1-134	90.657°	26.377°	7.1	25.1	716.0	1.2	-136.3	63.7	80	6	0.3	127.7	86.3	15.7	7.2	0.1	7.2	2.2	19.3	1.3	123.9	1.2
B1-135	90.656°	26.377°	7.1	24.9	580.0	1	-90.0	110.0	100	6	0.6	137.3	59.2	10.8	5.7	0.5	3.9	2.3	16.3	2.5	94.5	1.3
B1-136	90.654°	26.375°	7.0	25.3	662.0	1	-125.9	74.1	120	6	9.3	167.1	49.8	5.5	4.6	0.1	11.4	2.2	12.3	2.3	72.1	1.8
B1-137	90.629°	26.364°	7.3	25.4	745.0	0.9	-116.0	84.0	100	6	10.1	107.4	57.3	4.5	5.7	1.5	20.2	0.8	14.6	1.5	84.1	1.2
B1-138	90.625°	26.362°	7.0	25.6	518.0	0.9	-125.9	74.1	100	6	0.3	110.4	58.1	12.3	7.1	2.2	4.3	1.0	16.3	3.7	88.8	1.8
B1-139	90.625°	26.37°	6.9	25	200.0	0.8	-88.0	112.0	100	6	7.9	101.6	66.0	15.1	7.4	2.5	15.1	1.2	18.3	0.7	111.6	1.8
B1-140	90.62°	26.362°	7.0	25	212.0	0.9	-70.0	130.0	120	6	10.1	138.3	70.1	6.1	6.6	0.8	8.2	1.0	31.1	2.1	108.9	5.5
B1-141	90.625°	26.373°	6.9	25.3	471.0	0.9	-110.4	89.6	120	6	6.7	122.5	57.7	7.2	8.6	1.4	8.9	1.0	4.5	2.1	76.2	5.4
B1-142	90.631°	26.369°	6.8	25.3	667.0	0.8	-113.4	86.6	120	6	5.4	138.4	49.9	16.7	10.9	0.3	10.3	1.7	29.9	1.6	110.2	1.8
B1-143	90.632°	26.37°	7.9	25.1	349.0	0.9	-70.6	129.4	100	6	8.6	130.5	22.5	2.6	5.5	0.4	10.0	1.0	26.4	1.7	53.1	1.9
B1-144	90.593°	26.312°	7.3	24.6	410.0	0.8	-147.1	52.9	80	6	4.1	276.1	22.4	30.5	17.8	0.6	21.4	1.0	3.7	4.3	74.1	2.4
B1-145	90.576°	26.33°	6.2	25.4	532.0	0.7	-189.4	10.6	80	6	2.1	304.3	27.2	11.4	9.6	0.3	5.4	1.2	18.2	1.1	60.3	4.8
B1-146	90.579°	26.326°	6.1	25.8	615.0	0.8	-210.6	-10.6	45	6	2.4	394.3	48.1	24.6	7.6	0.3	8.1	1.0	11.2	0.3	86.1	5.9
B1-147	90.583°	26.322°	6.7	25.1	862.0	1.1	-216.5	-16.5	86	6	4.6	378.0	36.5	12.6	4.5	1.4	6.7	1.2	16.3	2.2	64.1	6.0
B1-148	90.603°	26.353°	7.2	25.3	734.0	1.2	-138.0	62.0	80	6	3.2	348.2	39.2	10.4	8.2	1.0	6.2	1.0	3.6	2.2	52.6	4.0
B1-149	90.599°	26.349°	7.3	25.1	435.0	0.8	-147.4	52.6	100	6	3.1	127.7	21.2	22.7	14.0	2.4	8.7	1.1	1.5	1.0	56.1	4.3
B1-150	90.584°	26.339°	6.8	25.4	963.0	1.2	-164.8	35.2	120	6	0.6	137.3	59.2	3.2	1.6	0.6	3.5	1.0	2.1	2.1	65	3.3
B1-151	90.607°	26.35°	7.8	25.3	461.0	0.7	-130.2	69.8	100	6	2.3	167.1	33.1	16.3	15.2	1.4	10.1	1.0	1.6	1.0	63.1	3.9
B1-152	90.612°	26.354°	8.2	25.4	532.0	1.2	-275.0	-75.0	120	6	3.3	107.4	14.3	16.2	20.3	0.4	10.0	1.0	2.3	1.4	51.3	4.6
B1-153	90.592°	26.239°	8.4	25.6	635.0	0.9	-117.6	82.4	75	6	25.3	110.4	11.2	26.3	10.3	0.5	3.1	0.3	0.7	2.2	44.2	5.5
B1-154	90.59°	26.238°	7.6	25.1	864.0	1.1	-146.4	53.7	75	6	35.4	101.6	54.2	40.3	26.6	3.3	2.6	0.3	1.2	2.5	126.3	2.1
B1-155	90.591°	26.238°	8.7	25.2	716.0	0.8	-164.8	35.2	45	6	39.7	138.3	60.3	32.1	26.3	0.3	12.5	0.3	9.1	1.0	120	1.8
B1-156	90.592°	26.238°	6.9	24.8	621.9	0.8	-177.7	22.4	70	6	37.7	122.5	52.2	36.3	15.6	0.2	31.2	0.2	1.6	1.1	107.2	1.4
B1-157	90.592°	26.233°	6.8	23.1	500.4	1.2	-134.4	65.6	60	6	39.7	138.4	62.3	42.2	20.7	1.5	21.4	1.7	26.7	1.9	160.2	1.5
B1-158	90.596°	26.233°	6.9	24.2	335.0	1.3	-188.4	11.6	80	6	39.1	130.5	38.6	24.6	13.5	0.8	21.6	2.8	30.1	1.8	101.3	1.8
B1-159	90.599°	26.237°	6.1	24.5	257.0	1.2	-126.5	73.6	100	6	27.4	276.1	60.2	42.6	13.3	2.6	23.1	1.6	0.5	1.6	117.4	4.7
B1-160	90.597°	26.237°	6.1	25.6	934.0	1.3	-195.4	4.6	120	6	53.9	304.3	36.1	23.4	10.1	0.5	50.1	0.8	37.0	3.2	105.2	2.2
B1-161	90.6°	26.237°	6.2	25.4	512.0	1.2	-162.4	37.7	60	6	66.2	394.3	56.2	43.5	16.2	0.2	60.1	1.0	0.1	1.0	116.2	3.1
B1-162	90.601°	26.236°	6.3	25.3	674.0	1.4	-174.6	25.4	40	6	30.2	378.0	60.1	48.6	32.8	0.1	30.8	1.1	24.8	3.3	163	2.1
B1-163	90.603°	26.236°	7.2	25.1	832.0	0.8	-138.0	62.0	50	6	40.1	370.3	22.1	5.5	18.3	1.4	49.2	1.2	11.2	1.4	54	5.9
B1-164	90.603°	26.239°	6.8	24.6	754.0	0.6	-147.4	52.6	60	6	26.3	110.4	4.2	4.5	37.0	0.4	40.2	1.0	16.3	2.2	53.2	6.0
B1-165	90.598°	26.237°	7.3	25.4	415.0	1.1	-164.8	35.2	100	6	49.7	101.6	40.3	12.3	5.7	0.5	52.4	1.1	3.6	1.0	62.1	4.0
B1-166	90.596°	26.237°	6.1	25.8	913.0	0.98	-130.2	69.8	80	6	39.3	124.3	36.1	15.1	7.2	3.3	43.3	1.0	1.5	2.1	56.4	4.3
B1-167	90.592°	26.24°	7.6	25.1	361.0	1.3	-146.4	53.7	120	6	32.6	348.2	60.5	6.1	5.5	0.3	57.7	1.0	2.1	1.0	76.1	3.3
B1-168	90.637°	26.311°	7.2	25.3	562.0	1.5	-164.8	35.2	75	6	6.4	127.7	16.3	7.2	17.8	0.3	5.9	1.0	1.6	1.4	42.2	1.4
B1-169	90.635°	26.309°	7.1	25.1	645.0	1.4	-177.7	22.4	75	6	2.5	138.3	56.1	16.7	9.6	0.4	10.3	0.3	6.7	2.2	86.3	1.5
B1-170	90.637°	26.31°	7.3	25.4	834.0	1.7	-210.4	-10.4	80	6	2.1	122.5	38.7	2.6	7.6	0.6	6.6	0.3	16.2	0.7	68.1	1.8
B1-171	90.636°	26.309°	6.4	25.3	726.0	0.9	-231.7	-31.7	100	6	3.5	138.4	40.2	6.9	4.5	0.3	9.1	0.3	17.8	2.1	71.3	1.8
B1-172	90.616°	26.293°	6.1	25.4	597.0	0.6	-164.8	35.2	120	6	58.3	130.5	58.6	24.6	21.6	0.3	50.6	0.3	12.7	2.1	113	1.1
B1-173	90.637°	26.334°	6.8	25.6	604.0	0.7	-146.1	53.9	100	6	0.7	137.3	40.3	38.4	20.1	0.9	2.3	0.4	28.3	1.6	127.1	3.1
B1-174	90.589°	26.275°	6.0	25.1	778.0	1.1	-134.9	65.1	80	6	21.6	167.1	33.9	39.4	18.7	1.6	44.2	1.5	1.5	1.4	96.4	1.3
B1-175	90.592°	26.273°	6.2	25.2	683.0	1.8	-164.3	35.7	120	6	24.1	110.4	44.8	51.6	20.2	2.2	28.6	1.3	2.1	2.2	113.6	2.6
B1-176	90.593°	26.272°	6.9	24.6	700.0	1.1	-136.3	63.7	80	6	15.4	106.3	39.2	14.2	30.6	0.5	12.5	0.2	0.0	1.6	87.4	2.3

B1-177	90.5939°	26.2353°	7.8	27	331.8	1	-169.9	30.1	50	6	22.3	390.0	34.9	17.6	21.0	0.5	17.0	0.3	4.4	2.3	71	2.0
B1-178	90.5926°	26.234°	6.6	26	236.9	1.2	-270.6	-70.6	60	6	34.7	140.0	98.2	3.5	36.7	1.0	41.0	0.0	2.4	1.0	134	1.1
B1-179	90.5881°	26.233°	6.1	27	66.3	1.1	-213.2	-13.2	80	6	18.1	300.0	36.8	4.9	42.5	1.0	20.4	0.0	0.0	2.5	88.1	0.6
B1-180	90.5899°	26.233°	5.6	26.7	86.6	1.2	-212.2	-12.2	120	6	27.9	260.0	50.7	4.5	20.8	1.5	30.2	0.0	2.4	1.0	79.8	0.4
B1-181	90.5881°	26.238°	6.6	27	66.3	1.2	-303.2	-130	100	6	37.4	270.0	102	2.6	36.0	2.0	66.1	0.0	1.5	1.2	141.2	0.1
B1-182	90.5837°	26.237°	5.6	27.5	39.5	1	-256.3	-56.3	80	6	22.8	888.0	8.0	12.3	32.1	0.5	28.7	0.0	3.1	1.9	50	0.8
B1-183	90.5771°	26.24°	5.8	26.4	130.7	0.8	-376.1	-176	60	6	28.5	530.0	17.6	12.8	41.1	1.9	60.6	0.1	0.0	2.8	71.2	1.7
B1-184	90.5777°	26.237°	6.2	26.7	115.0	0.9	-246.3	-46.3	100	6	14.6	100.0	30.4	5.1	30.4	1.6	57.5	0.2	0.0	0.2	67.4	1.3
B1-185	90.5813°	26.237°	6.1	26.5	114.5	1	-259.5	-59.5	120	6	11.5	114.0	55.6	8.1	21.1	1.5	68.6	0.5	6.4	0.3	86.1	2.4
B1-186	90.5985°	26.237°	5.7	26.4	179.4	0.9	-275.6	-75.6	80	6	29.4	850.0	94.6	19.2	33.3	0.5	57.0	0.7	1.9	0.7	137.4	2.1
B1-187	90.6061°	26.236°	6.4	27	397.0	1.3	-283.3	-83.3	100	6	38.4	220.0	87.3	19.3	20.2	1.0	53.5	1.6	6.5	0.1	142	2.7
B1-188	90.7214°	26.3641°	7.8	24.6	350.0	0.6	-60.5	139.5	80	6	20.0	204.2	23.7	26.3	7.2	0.1	1.1	1.0	2.3	1.0	58.4	2.1
B1-189	90.7222°	26.3572°	6.9	24.7	346.0	0.9	-70.5	129.6	100	6	17.0	207.0	5.6	40.3	5.7	1.2	2.0	0.3	0.7	3.7	54.2	1.5
B1-190	90.7104°	26.3624°	6.4	26	754.0	1.5	-103.6	96.4	120	6	19.0	231.6	44.6	32.1	4.6	0.1	8.8	0.3	1.2	1.3	84.1	1.3
B1-191	90.7057°	26.368°	6.5	25.7	653.0	1.7	-94.6	105.4	80	6	39.0	237.4	39.2	36.3	5.7	0.5	6.4	0.3	9.1	1.2	89.3	1.8
B1-192	90.7162°	26.3663°	7.3	24.9	663.0	0.7	-284.6	-84.6	80	6	81.7	269.2	44.4	42.2	7.1	0.1	43.3	0.2	1.6	4.9	96.1	2.2
B1-193	90.7316°	26.3558°	6.9	24.2	187.0	0.6	-207.5	-7.5	120	6	170.7	267.4	78.8	24.6	7.4	1.5	83.4	1.7	26.7	3.2	126.3	2.6
B1-194	90.738°	26.357°	6.7	25.8	744.0	1.1	-88.9	111.1	100	6	12.0	298.1	62.1	42.6	6.6	2.2	7.2	2.8	30.1	2.5	147.1	0.3
B1-195	90.726°	26.366°	6.3	25.7	164.0	1.4	-87.3	112.7	100	6	12.0	278.3	86.3	23.4	8.6	2.5	3.7	1.6	0.5	1.1	122	1.0
B1-196	90.73°	26.361°	6.4	24.7	155.0	0.8	-81.6	118.4	80	6	18.0	260.1	59.2	43.5	10.9	0.8	16.7	0.8	37.0	1.3	139	1.4
B1-197	90.7°	26.378°	7.2	24.9	137.0	1.3	-77.6	122.4	120	6	11.0	361.2	49.8	63.3	5.5	1.4	14.0	1.0	0.1	1.0	116.3	1.1
B1-198	90.704°	26.348°	7.5	25.1	199.0	1.5	-64.0	136.0	120	6	27.9	204.7	57.3	26.8	17.8	0.3	17.3	1.1	24.8	0.7	127	1.8
B1-199	90.7106°	26.3675°	7.0	25.2	526.0	1.8	-270.6	-70.6	80	6	20.1	284.4	37.4	18.6	21.6	0.4	37.4	1.3	11.2	2.0	84.6	2.2
B1-200	90.6964°	26.3783°	6.7	25.4	330.0	1.2	-247.1	-47.1	80	6	0.4	267.4	55.6	7.6	1.0	0.6	23.1	0.9	16.3	2.2	76.9	3.1
B1-201	90.7022°	26.3714°	7.3	25.5	293.0	1.3	-289.4	-89.4	60	4	0.1	294.1	53.3	5.9	14.5	1.0	24.9	0.9	3.6	1.5	76.2	1.3
B1-202	90.6876°	26.3789°	6.9	25.1	326.0	1.7	-210.6	-10.6	40	4	0.2	327.4	28.0	8.2	5.8	0.3	25.2	0.5	13.5	1.9	53.3	1.8
B1-203	90.7051°	26.3552°	7.1	24.7	341.0	2.1	-216.5	-16.5	60	5	3.2	368.2	55.4	4.4	2.0	0.2	35.6	0.2	4.2	1.2	68.9	1.1
B1-204	90.6957°	26.3607°	7.2	25.8	319.0	1.2	-138.0	62.0	100	6	3.2	421.7	33.7	6.5	8.7	1.5	31.6	0.9	6.4	2.3	53.4	3.1
B1-205	90.6931°	26.3727°	7.8	24.6	246.0	1.1	-147.4	52.6	120	6	0.3	418.6	33.3	22.6	4.2	0.6	26.6	1.0	6.9	1.5	69.8	1.3
B1-206	90.7074°	26.3714°	6.9	26	585.0	1.1	-164.8	35.2	80	6	6.9	460.1	32.1	26.7	18.2	0.2	17.8	1.9	5.7	1.0	83.6	1.2
B1-207	90.7151°	26.3604°	6.4	25.7	841.0	0.8	-130.2	69.8	80	6	5.1	386.1	28.3	16.5	7.6	1.4	32.1	1.2	7.7	2.0	61.2	1.3
B1-208	90.6976°	26.3695°	6.5	24.9	860.0	1	-275.0	-75.0	80	6	2.1	502.4	38.2	22.8	13.3	2.5	15.7	1.3	29.3	1.3	108	1.8
B1-209	90.7161°	26.3685°	7.1	24.2	373.0	1.2	-117.6	82.4	80	6	8.7	487.3	41.6	30.1	17.4	1.4	14.1	1.3	21.5	1.6	103.3	1.2
B1-210	90.6987°	26.3842°	6.7	25.8	588.0	1	-266.5	-66.5	80	6	2.8	416.3	63.1	40.2	27.2	2.4	22.7	0.8	6.7	1.0	124	1.8
B1-211	90.6892°	26.4006°	6.3	25.9	531.0	0.9	-170.8	29.2	50	4	1.0	428.6	48.2	33.7	27.2	0.4	20.9	1.0	16.5	1.2	132	1.8
B1-212	90.7069°	26.364°	6.4	25.7	520.0	1.4	-183.5	16.5	60	5	12.4	361.3	30.6	27.6	15.5	0.2	10.6	1.1	28.3	1.0	98.7	5.5
B1-213	90.6842°	26.395°	7.2	24.7	468.0	1.2	-174.7	25.4	60	5	2.1	466.9	38.1	17.4	11.4	0.7	14.0	1.1	34.3	1.0	99.4	5.4
B1-214	90.6889°	26.3925°	7.8	24.9	361.0	1.7	-213.5	-13.5	80	5	0.6	437.8	52.3	38.4	20.6	1.5	23.4	1.0	36.4	1.0	152.3	3.7
B1-215	90.6941°	26.3993°	6.1	25.9	453	1.6	-146.6	53.4	80	5	2.5	398.4	44.8	31.3	12.4	0.3	6.3	1.0	18.6	1.3	102.3	1.2

Appendix Table A 1. 2: Summary of hydro-chemical parameters of L*As*CR groundwater samples.

ID	Latitude	Longitude	pH	Temp.	EC	DO	ORP	Eh	Well depth	Filter depth	As	Na	K	Ca	SO_4^{-2}	Cl^-	F	HCO_3^-	Pb	Fe	Mn	Mg	TDS	PO_4^{-3}	Al	Cr	Cu
				°C	µS/cm	mg L^{-1}	mV	mV	(ft)	(ft)	µg L^{-1}	mg L^{-1}																
D1-1	26.472833°	92.069750°	6.6	25.9	258	1.3	-208	-8	80	5	62.6	10.1	1.7	5.3	0.5	0.2	0.5	20	0.1	13.3	1.0	1.6	128.9	0.2	0.01	bdl	bdl
D1-2	26.473011°	92.068725°	6.6	26.0	143	1.6	-188	12	120	6	43.6	28.5	11.4	54.7	0.6	0.1	0.5	102	0.9	18.7	2.0	7.1	71.3	0.4	0.01	bdl	bdl
D1-3	26.472814°	92.067392°	6.5	25.4	142	1.6	-250	-50	140	5	38.9	11.2	20.7	55.7	0.7	0.5	0.6	120	0.8	30.5	bdl	21.9	70.8	0.3	0.01	bdl	bdl
D1-4	26.473164°	92.069767°	6.5	25.5	298	1.5	-217	-17	125	6	46.4	20.7	22.3	36.0	0.5	0.2	0.6	102	0.8	32.5	0.8	17.6	149.1	0.1	0.04	bdl	bdl
D1-5	26.472008°	92.069947°	6.6	26.1	269	1.4	-217	-17	145	6	69.0	13.5	12.3	33.4	0.6	0.4	0.6	55	0.7	32.7	0.4	0.4	134.6	0.3	0.10	bdl	bdl
D1-6	26.472547°	92.070803°	6.5	25.7	280	1.5	-235	-35	120	6	84.6	11.3	23.0	25.1	1.3	0.3	0.2	65	bdl	39.7	0.8	0.8	139.9	0.9	0.03	bdl	bdl
D1-7	26.472842°	92.071457°	6.5	25.2	284	2.1	-234	-34	160	6	77.7	20.0	14.6	36.7	0.2	0.1	0.2	73	0.1	38.9	0.9	1.6	142.0	0.6	0.03	bdl	bdl
D1-8	26.47107°	92.06964°	6.6	26.1	58	0.3	-263	-63	65	10	32.6	29.9	10.8	39.9	0.1	0.6	1.6	86	0.4	16.3	1.5	0.7	130.0	0.9	bdl	bdl	bdl
D1-9	26.47084°	92.06968°	6.4	26.9	161	0.1	-141	59	75	10	24.8	23.4	13.7	44.3	0.2	0.1	1.4	90	0.3	17.3	bdl	bdl	130.0	0.5	0.02	bdl	bdl
D1-10	26.46981°	92.05711°	6.5	26.0	47	1.3	-289	-89	36	10	33.2	19.4	11.3	18.2	1.0	0.1	0.4	47	0.3	10.4	0.4	0.4	130.0	0.7	0.01	bdl	bdl
D1-11	26.47147°	92.05731°	6.4	26.0	68	0.4	-284	-84	75	10	32.2	18.4	13.3	40.4	1.3	0.4	0.3	73	0.6	18.6	0.3	1.1	130.0	0.5	0.01	bdl	bdl
D1-12	26.435822°	91.945730°	6.4	26.3	81	1.5	-203	-3	60	10	40.6	15.4	1.0	32.7	0.5	3.6	0.3	52	0.5	20.6	0.1	1.2	100.0	0.4	0.02	0.1	bdl
D1-13	26.46332°	92.05216°	6.2	25.9	78	1.3	-228	-28	48	10	22.9	18.4	1.4	24.3	0.2	0.1	0.4	48	0.6	13.3	0.7	1.1	110.0	1.1	0.10	bdl	bdl
D1-14	26.46196°	92.05122°	6.2	25.5	129	1.4	-217	-17	65	10	10.4	23.6	1.2	37.5	0.1	0.7	0.4	64	0.3	10.2	0.2	1.7	100.0	0.4	bdl	bdl	bdl
D1-15	26.46185°	92.05216°	6.5	25.9	11	0.2	-179	21	100	10	13.7	32.4	1.8	44.0	0.4	0.3	0.1	84	0.4	22.1	0.2	1.2	130.0	0.3	bdl	bdl	bdl
D1-16	26.47231°	92.07054°	6.5	26.3	71	0.2	-196	4	75	10	10.4	20.3	0.1	46.5	0.6	0.2	0.3	76	0.6	20.1	0.3	1.2	100.0	0.5	bdl	bdl	bdl
D1-17	26.47475°	92.07507°	6.5	26.4	42	0.3	-156	44	120	6	8.4	18.7	0.6	32.1	0.2	0.4	0.1	50	0.1	24.3	0.7	1.7	90.0	2.2	bdl	bdl	bdl
D1-18	26.47343°	92.07759°	6.3	26.2	37	0.4	-257	-57	80	10	3.6	23.4	0.7	32.1	1.7	bdl	0.1	60	0.4	16.2	0.1	1.3	140.0	2.9	bdl	bdl	bdl
D1-19	26.46853°	92.07942°	6.5	26.5	72	1.1	-121	79	45	10	6.8	16.2	0.2	46.3	1.0	0.1	0.1	67	0.7	14.1	0.4	0.4	110.0	3.4	bdl	bdl	bdl
D1-20	26.442111°	92.013833°	6.3	25.0	285	2.0	-122	78	120	6	36.5	29.0	0.7	45.6	0.2	0.2	0.9	78	0.2	9.8	0.8	1.5	142.3	0.2	bdl	bdl	bdl
D1-21	26.442722°	92.013547°	6.6	25.5	207	1.9	-143	57	160	8	29.5	26.0	0.6	40.1	1.1	0.4	0.8	73	0.2	6.4	0.2	0.4	103.5	0.1	bdl	bdl	bdl
D1-22	26.442581°	92.013939°	6.5	25.0	214	2.3	-94	106	80	6	21.8	21.9	0.4	32.0	1.0	0.2	0.1	58	0.3	9.3	0.6	0.1	107.1	0.2	bdl	bdl	bdl
D1-23	26.442047°	92.014103°	6.5	25.4	194	1.6	-50	150	60	6	27.4	24.5	0.8	26.2	1.3	0.4	0.1	50	0.3	10.2	0.7	0.5	97.2	0.2	bdl	bdl	bdl
D1-24	26.441636°	92.013386°	6.6	25.6	219	2.9	-102	98	100	6	35.4	21.0	1.9	31.2	0.5	0.4	0.7	56	0.2	7.7	0.3	0.4	109.3	0.1	bdl	bdl	bdl
D1-25	26.437050°	92.013517°	7.3	25.3	211	1.4	-133	67	150	6	23.6	25.1	0.3	24.6	1.1	0.2	0.8	48	0.2	10.7	0.8	0.8	105.3	0.2	bdl	bdl	bdl
D1-26	26.437833°	92.013883°	7.5	25.2	196	1.6	-142	58	140	5	26.3	25.2	11.0	18.9	0.3	0.4	0.1	61	0.8	10.1	0.7	0.2	97.8	0.2	bdl	bdl	bdl
D1-27	26.438283°	92.013933°	7.3	26.2	220	1.4	-122	78	100	5	58.6	18.4	1.0	42.2	1.0	0.3	0.5	66	1.0	6.9	0.5	1.8	110.2	0.2	bdl	bdl	bdl
D1-28	26.438300°	92.014383°	6.8	25.3	180	1.3	-136	64	80	6	61.6	14.8	0.3	45.3	0.1	0.1	0.4	65	bdl	9.2	0.2	0.5	90.2	0.3	bdl	bdl	bdl
D1-29	26.437933°	92.014533°	6.5	25.0	213	1.5	-186	14	80	6	66.3	25.5	0.1	35.0	1.1	0.4	0.7	60	1.0	11.6	0.1	0.4	106.4	0.2	bdl	bdl	bdl
D1-30	26.440911°	91.951600°	6.4	25.0	333	1.8	-100	100	60	5	40.8	10.4	0.4	27.8	0.7	1.1	0.6	41	0.9	10.1	bdl	1.5	166.3	0.2	bdl	bdl	bdl
D1-31	26.441217°	91.950850°	6.4	25.0	246	2.9	-98	102	60	6	31.6	18.3	0.6	33.3	0.7	1.2	0.6	51	0.9	11.5	bdl	1.6	122.8	0.2	bdl	bdl	bdl
D1-32	26.441217°	91.950517°	6.4	25.1	261	3.3	-104	96	100	5	36.8	27.4	0.2	39.5	1.1	0.2	0.7	60	0.8	16.0	0.1	1.7	130.4	0.1	bdl	bdl	bdl
D1-33	26.440667°	91.950800°	6.4	25.3	256	2.6	-171	29	120	5	59.6	29.9	0.3	32.7	0.9	1.1	0.5	68	0.9	18.5	0.1	1.5	128.1	0.1	bdl	bdl	bdl
D1-34	26.440600°	91.950500°	6.3	24.8	348	2.9	-125	75	100	6	32.5	14.8	0.5	39.3	1.5	1.0	0.6	51	0.9	16.3	0.5	0.9	174.1	0.2	bdl	bdl	bdl
D1-35	26.441306°	91.952033°	7.0	24.9	287	2.1	-176	24	80	5	57.0	19.6	0.7	27.7	0.7	1.9	0.7	49	0.9	12.4	0.2	0.7	143.7	0.2	bdl	bdl	bdl
D1-36	26.442064°	91.952031°	7.1	25.0	255	2.4	-146	54	120	6	52.7	17.1	0.7	33.9	0.4	1.1	0.7	55	0.3	11.3	0.4	0.8	127.6	bdl	bdl	bdl	bdl
D1-37	26.442075°	91.952578°	6.6	25.1	318	1.2	-188	12	140	5	64.6	27.9	0.5	37.1	0.7	3.0	0.9	66	1.0	12.0	0.5	0.9	159.1	0.1	bdl	bdl	bdl
D1-38	26.442661°	91.952131°	6.2	24.6	244	1.6	-210	-10	160	5	66.5	21.1	0.8	35.4	0.6	1.6	0.7	61	0.1	7.2	0.9	bdl	121.9	0.2	bdl	bdl	bdl
D1-39	26.442739°	91.952500°	6.4	24.9	286	1.7	-232	-32	100	6	43.6	18.2	0.4	29.0	0.4	0.6	0.1	49	0.1	6.9	0.5	0.7	143.2	0.1	bdl	bdl	bdl
D1-40	26.43945°	91.91874°	6.7	25.9	108	0.4	-285	-85	50	10	41.0	14.1	0.4	37.6	0.6	0.1	1.1	55	0.2	11.4	0.4	0.6	140.0	0.3	bdl	bdl	bdl
D1-41	26.44261°	91.94099°	6.5	26.0	88	0.6	-270	-70	120	6	45.3	18.2	0.1	34.4	0.2	0.8	0.5	52	0.4	12.4	0.6	0.2	140.0	0.1	bdl	bdl	bdl
D1-42	26.43853°	91.93831°	6.5	26.3	63	0.8	-261	-61	80	10	38.2	15.6	0.4	41.6	0.7	0.7	1.3	61	bdl	14.2	1.0	0.2	120.0	0.2	bdl	bdl	bdl

D1-43	26.46382°	91.93542°	6.4	27.0	107	0.1	-367	-167	120	10	49.4	13.2	1.0	33.8	0.8	0.1	1.2	50	0.3	13.2	0.9	0.3	160.0	0.4	bdl	bdl	bdl
D1-44	26.43985°	91.92643°	6.5	25.9	129	0.2	-274	-74	120	10	36.3	12.6	1.4	26.7	0.2	0.3	0.9	44	0.6	9.8	0.4	0.8	140.0	0.6	bdl	bdl	bdl
D1-45	26.43898°	91.93214°	6.6	25.6	125	0.2	-287	-87	80	10	38.4	26.4	0.2	36.1	bdl	0.1	1.1	66	bdl	14.6	1.0	0.1	140.0	1.4	bdl	bdl	bdl
D1-46	26.39752°	91.97461°	6.9	26.8	32	0.7	-125	75	120	6	20.2	17.3	0.4	38.7	0.6	0.7	0.3	52	0.7	5.2	0.4	0.2	120.0	0.7	bdl	bdl	bdl
D1-47	26.39233°	91.97442°	6.2	27.9	107	0.8	-388	-188	65	10	17.4	12.6	0.1	38.3	0.4	0.1	0.4	54	0.6	7.4	0.6	0.6	170.0	0.1	bdl	bdl	bdl
D1-48	26.386650°	91.974819°	6.4	25.8	40	0.1	-304	-104	70	10	27.1	25.7	0.3	26.7	0.6	0.3	0.4	50	0.8	12.4	0.5	0.6	140.0	0.1	bdl	bdl	bdl
D1-49	26.38155°	91.97456°	6.6	26.4	100	1.0	-167	33	60	10	16.3	16.8	0.4	38.4	0.2	1.4	0.9	55	0.4	13.4	0.9	0.9	90.0	0.7	bdl	bdl	bdl
D1-50	26.38093°	91.97414°	6.5	26.0	70	1.1	-171	29	90	10	20.5	17.2	0.5	41.6	0.3	1.7	1.1	61	0.1	18.1	bdl	0.1	100.0	0.5	bdl	bdl	bdl
D1-51	26.405709°	91.908498°	6.9	25.9	186	2.2	-140	60	120	6	3.6	22.0	1.5	38.1	0.4	0.2	0.6	68	1.0	2.6	0.3	1.2	93.2	0.1	bdl	bdl	bdl
D1-52	26.405827°	91.908527°	6.8	24.9	163	2.1	-165	35	80	5	2.5	19.3	1.5	41.0	0.9	0.4	0.6	66	0.9	3.6	0.4	1.3	81.4	0.1	bdl	bdl	bdl
D1-53	26.406050°	91.908164°	6.9	25.3	175	1.1	-146	54	80	6	1.4	27.3	1.7	34.3	1.1	2.1	0.6	68	0.9	2.7	0.3	1.2	87.6	0.1	bdl	bdl	bdl
D1-54	26.405691°	91.908549°	6.9	25.4	173	2.0	-135	65	100	5	0.6	24.1	1.4	37.4	0.8	0.1	0.7	71	0.9	3.1	0.4	1.4	86.4	0.1	bdl	bdl	bdl
D1-55	26.406113°	91.909347°	6.7	25.1	176	2.6	-164	36	80	6	6.4	31.8	1.5	33.6	0.4	1.4	0.7	63	1.0	7.6	0.4	1.6	88.2	0.2	bdl	bdl	bdl
D1-56	26.405961°	91.908386°	7.2	26.8	188	4.7	-136	64	60	8	8.6	24.7	1.1	32.6	0.7	2.2	0.6	54	0.8	6.4	0.2	1.0	93.8	0.1	bdl	bdl	bdl
D1-57	26.405595°	91.910164°	7.0	26.0	173	1.8	-90	110	80	5	6.8	22.6	1.3	36.5	0.3	1.0	0.6	60	0.1	5.4	0.2	1.9	86.6	0.1	bdl	bdl	bdl
D1-58	26.406327°	91.911440°	7.6	25.2	210	4.9	-126	74	120	6	1.3	32.1	1.8	32.1	0.3	1.1	0.7	71	bdl	2.4	0.3	0.1	105.0	0.1	bdl	bdl	bdl
D1-59	26.407961°	91.910242°	7.1	26.0	180	1.4	-116	84	140	5	0.7	20.3	1.3	35.7	0.2	0.2	0.7	55	0.1	1.9	bdl	0.3	90.1	0.1	bdl	bdl	bdl
D1-60	26.404181°	91.908232°	7.6	25.2	210	4.9	-126	74	100	6	3.6	12.0	1.9	28.9	0.7	0.3	2.0	47	0.2	4.2	bdl	0.5	105.0	0.1	bdl	bdl	bdl
D1-61	26.39805°	91.90449°	7.6	26.1	150	0.3	-353	-153	70	10	10.4	11.5	1.0	31.3	0.7	0.2	0.4	42	0.7	7.3	1.0	1.4	190.0	0.1	bdl	bdl	bdl
D1-62	26.39698°	91.90472°	7.4	25.6	160	0.1	-188	12	70	10	12.6	22.2	1.5	38.7	0.1	0.8	0.3	67	0.4	6.6	bdl	1.3	120.0	0.2	bdl	bdl	bdl
D1-63	26.38772°	91.90649°	7.3	26.0	182	0.2	-181	19	36	10	14.3	29.3	1.5	27.1	0.3	0.7	0.4	62	0.4	8.7	0.4	1.4	110.0	1.2	bdl	bdl	bdl
D1-64	26.40137°	91.90462°	7.1	25.7	164	0.4	-156	44	80	10	8.1	20.3	1.7	30.3	0.4	0.8	0.5	53	0.8	6.1	0.8	0.9	100.0	1.4	bdl	bdl	bdl
D1-65	26.40321°	91.91801°	6.7	25.8	-25	0.1	-284	-84	60	6	9.6	34.1	1.4	33.4	0.3	0.6	0.2	76	0.6	3.4	0.7	2.0	150.0	1.5	bdl	bdl	bdl
D1-66	26.40322°	91.91837°	6.9	25.9	37	0.1	-264	-64	60	6	18.3	21.8	1.5	30.7	0.8	0.6	0.1	58	0.8	1.1	0.3	1.1	140.0	2.1	bdl	bdl	bdl
D1-67	26.40144°	91.91961°	6.9	25.7	102	0.1	-258	-58	80	10	20.3	19.7	1.1	28.3	1.2	0.5	0.5	50	0.5	8.4	0.9	1.8	140.0	1.3	bdl	bdl	bdl
D1-68	26.39984°	91.91874°	6.8	25.5	-108	0.3	-162	39	120	10	21.7	22.6	1.3	32.4	1.2	0.2	0.4	62	0.2	2.4	0.9	1.7	120.0	1.1	bdl	bdl	bdl

Appendix Table A 1. 3: Summary of hydro-chemical parameters of H*As*CR groundwater samples.

ID	Latitude	Longitude	Well depth	Filter length	pH	ORP	Eh	Temp	EC	TDS	*As*	Fe	Mn	Mg	Pb	Cr	Cu	Zn	HCO_3^-	Na	Ca	K	F^-	Cl^-	NO_3^-	Br	NO_2^-	PO_4^{-3}	SO_4
			(feet)	(feet)		mV	mV	°C	µS cm^{-1}	mg L^{-1}	µg L^{-1}	mg L^{-1}																	
B2-1	26.291°	90.614°	100	20	6.6	-105.2	94.8	24.9	176.9	97.3	26.3	16.2	0.5	23.0	0.2	bdl	bdl	0.1	128	24.2	76.5	11.3	bdl	bdl	bdl	bdl	2.1	-1.0	3.9
B2-2	26.240°	90.542°	120	20	6.0	-57.0	143.0	25.8	235.1	129.3	36.3	11.5	bdl	18.3	0.3	bdl	bdl	0.1	90	11.2	61.3	0.8	bdl	bdl	bdl	bdl	2.1	bdl	3.6
B2-3	26.239°	90.543°	100	20	6.1	-104.0	96.0	25.0	145.1	79.8	2.4	1.2	0.3	10.2	0.1	bdl	bdl	bdl	82	31.7	88.0	15.7	bdl	bdl	71.6	bdl	2.6	bdl	5.0
B2-4	26.239°	90.546°	80	20	5.9	-102.4	97.6	24.4	114.5	63.0	7.4	1.3	bdl	14.1	0.3	bdl	bdl	bdl	74	11.0	31.5	20.9	bdl	0.2	bdl	bdl	1.7	bdl	2.9
B2-5	26.241°	90.543°	95	10	5.7	-70.3	129.7	24.0	130.7	71.9	9.2	0.4	bdl	8.5	0.3	0.1	bdl	bdl	56	10.7	34.6	11.0	bdl	0.8	bdl	60.6	bdl	0.6	6.9
B2-6	26.242°	90.542°	100	20	5.9	-93.1	106.9	24.2	97.1	53.4	5.2	1.5	bdl	11.0	0.1	0.1	bdl	bdl	66	8.0	47.4	0.9	bdl	0.2	bdl	bdl	1.8	bdl	3.4
B2-7	26.238°	90.543°	120	15	6.1	-99.9	100.1	25.3	94.7	52.1	10.9	1.0	bdl	8.5	0.3	0.1	bdl	bdl	86	9.6	82.4	5.7	bdl	0.1	0.3	bdl	8.5	bdl	bdl
B2-8	26.236°	90.544°	130	20	6.1	-136.8	63.2	26.0	107.2	59.0	5.4	0.6	bdl	18.2	0.1	0.1	bdl	bdl	92	10.4	62.0	0.8	bdl	0.2	bdl	bdl	1.8	bdl	bdl
B2-9	26.236°	90.545°	150	20	5.9	-145.2	54.8	25.2	117.6	64.7	5.7	1.5	bdl	11.1	0.2	bdl	bdl	bdl	66	10.1	46.2	0.6	bdl	bdl	bdl	bdl	2.4	bdl	4.1
B2-10	26.245°	90.544°	120	20	5.5	-36.8	163.2	27.0	65.7	36.1	3.6	2.4	bdl	9.7	0.3	bdl	bdl	0.1	54	4.1	42.4	1.5	bdl	2.0	bdl	bdl	1.8	bdl	3.2
B2-11	26.247°	90.547°	30	10	7.3	49.9	249.9	23.8	73.7	40.5	17.9	1.1	bdl	10.9	0.3	bdl	bdl	bdl	40	3.5	23.9	1.2	bdl	bdl	bdl	bdl	bdl	bdl	bdl
B2-12	26.239°	90.552°	70	10	5.0	36.0	236.0	25.6	64.0	35.2	17.8	0.2	bdl	7.5	0.2	0.1	bdl	0.1	28	4.8	20.3	1.0	bdl	4.4	bdl	bdl	1.4	bdl	bdl
B2-13	26.258°	90.551°	80	20	5.4	40.6	240.6	25.5	102.6	56.4	14.2	12.1	bdl	10.2	0.2	0.1	bdl	bdl	46	7.2	34.5	1.2	bdl	4.4	bdl	bdl	1.8	bdl	3.6
B2-14	26.264°	90.546°	90	10	5.2	59.9	259.9	25.2	69.6	38.3	20.6	1.2	bdl	8.1	0.3	0.1	bdl	bdl	44	5.1	38.0	1.2	0.1	5.8	1.6	bdl	1.8	bdl	bdl
B2-15	26.262°	90.529°	80	10	5.2	42.0	242.0	24.3	104.9	57.7	18.0	2.7	0.1	8.5	0.1	0.1	bdl	bdl	34	8.8	31.0	3.0	11.3	6.4	1.6	1.0	1.8	bdl	bdl
B2-16	26.261°	90.590°	110	6	5.3	56.9	256.9	25.6	117.1	64.4	1.8	20.9	0.1	19.1	0.1	0.1	bdl	0.3	44	5.6	32.8	3.3	0.1	17.6	bdl	0.76	bdl	1.5	bdl
B2-17	26.276°	90.601°	140	30	6.7	-88.6	111.4	25.6	239.8	131.9	11.0	2.1	bdl	27.0	0.2	0.1	bdl	0.1	126	14.6	86.3	5.0	bdl	0.6	2.0	0.38	3.1	bdl	bdl
B2-18	26.291°	90.631°	120	20	6.6	142.9	342.9	24.0	618.0	339.9	0.7	23.1	0.2	33.4	0.2	0.1	bdl	0.0	104	15.0	48.8	14.5	0.4	0.6	bdl	bdl	1.8	bdl	bdl
B2-19	26.298°	90.619°	140	10	6.2	-142.9	57.1	24.4	90.3	49.7	16.5	0.1	0.3	21.5	0.2	0.1	bdl	0.2	82	12.6	37.3	11.3	0.2	0.5	18.2	bdl	bdl	bdl	bdl
B2-20	26.341°	90.651°	100	20	5.5	-92.5	107.5	24.7	81.0	44.6	20.4	0.7	bdl	5.5	0.1	0.1	bdl	bdl	38	7.5	24.6	1.2	bdl	4.0	bdl	bdl	1.4	bdl	bdl
B2-21	26.341°	90.651°	100	20	6.8	48.6	248.6	24.5	74.4	40.9	9.5	3.6	bdl	6.9	0.1	0.1	bdl	0.1	26	6.9	13.7	2.3	bdl	3.5	bdl	bdl	1.7	bdl	bdl
B2-22	26.352°	90.651°	80	20	5.4	-45.3	154.7	25.1	74.1	40.8	23.1	0.2	bdl	10.9	0.3	0.1	bdl	0.1	44	14.8	23.0	3.3	bdl	bdl	11.3	bdl	bdl	bdl	bdl
B2-23	26.344°	90.659°	40	5	5.9	-22.5	177.5	24.6	95.7	52.6	26.4	4.4	0.1	12.2	0.4	0.1	bdl	0.1	82	17.5	41.5	11.0	bdl	1.6	bdl	bdl	1.3	bdl	bdl
B2-24	26.347°	90.661°	60	10	6.6	16.8	216.8	25.0	117.2	64.5	9.1	16.0	0.1	12.4	0.1	0.1	bdl	0.1	28	10.4	24.1	1.4	bdl	15.0	4.0	bdl	1.8	bdl	bdl
B2-25	26.349°	90.661°	80	10	5.3	-128.1	71.9	24.2	154.6	85.0	3.3	4.3	0.2	13.5	0.1	0.1	bdl	bdl	28	5.1	8.2	1.6	bdl	bdl	bdl	bdl	bdl	bdl	bdl
B2-26	26.349°	90.659°	50	10	4.8	37.9	237.9	26.1	138.9	76.4	bdl	7.0	bdl	3.0	bdl	bdl	bdl	bdl	22	7.6	9.9	1.9	bdl	bdl	bdl	bdl	bdl	bdl	bdl
B2-27	26.351°	90.660°	100	20	6.0	103.7	303.7	25.1	76.6	42.1	2.0	0.8	bdl	7.0	0.1	0.1	bdl	bdl	34	9.5	20.6	1.8	0.1	0.4	6.6	bdl	bdl	bdl	bdl
B2-28	26.353°	90.660°	40	5	5.0	-19.7	180.3	24.5	86.3	47.5	1.3	4.1	bdl	6.1	0.2	0.1	bdl	bdl	16	5.3	24.4	1.0	0.1	13.9	3.6	bdl	1.4	bdl	bdl
B2-29	26.349°	90.659°	50	10	5.1	19.2	219.2	24.7	65.2	35.9	1.7	1.3	bdl	5.5	0.2	0.1	bdl	bdl	16	7.2	10.0	1.2	bdl	1.5	2.7	0.39	bdl	1.7	1.1
B2-30	26.345°	90.660°	60	20	5.7	7.1	207.1	24.9	65.4	36.0	11.8	5.8	bdl	7.7	0.1	0.1	bdl	bdl	42	10.1	22.4	2.8	bdl	1.2	bdl	bdl	1.2	bdl	1.2
B2-31	26.342°	90.659°	50	10	5.4	-90.9	109.1	23.9	110.0	60.5	3.9	3.0	0.1	9.2	bdl	0.1	bdl	bdl	32	11.7	9.6	1.9	bdl	bdl	bdl	bdl	bdl	bdl	bdl
B2-32	26.341°	90.660°	70	10	6.1	47.0	247.0	24.7	172.6	94.9	2.3	1.5	0.2	14.6	0.1	0.1	bdl	bdl	30	12.6	18.5	5.1	bdl	17.2	5.9	8.6	1.0	bdl	bdl
B2-33	26.329°	90.673°	40	5	5.2	bdl	200.0	25.2	112.0	bdl	3.9	1.2	0.1	13.3	0.1	0.1	bdl	bdl	18	9.0	13.1	1.3	bdl	12.0	2.9	bdl	2.0	bdl	bdl
B2-34	26.311°	90.668°	50	10	6.5	44.5	244.5	24.5	106.0	58.3	bdl	2.9	3.2	15.5	0.1	0.1	bdl	bdl	38	9.6	14.1	1.4	0.2	0.8	2.3	bdl	1.3	bdl	bdl
B2-35	26.315°	90.670°	80	20	5.3	13.9	213.9	25.1	157.4	86.6	1.0	19.0	0.6	14.4	0.1	0.1	bdl	bdl	34	9.2	18.5	1.9	bdl	13.4	0.1	bdl	1.0	bdl	bdl
B2-36	26.307°	90.675°	50	10	6.8	-98.7	101.3	23.4	111.8	61.5	3.0	0.6	0.5	46.7	0.1	0.1	bdl	bdl	190	28.6	86.0	23.3	bdl	6.9	1.6	bdl	3.0	bdl	bdl
B2-37	26.305°	90.675°	40	5	6.9	-54.5	145.5	24.6	569.0	313.0	0.6	7.3	0.5	77.0	0.1	0.1	bdl	bdl	236	41.8	92.2	32.3	bdl	11.9	2.7	bdl	5.6	7.5	bdl
B2-38	26.301°	90.675°	40	5	6.4	-132.7	67.3	23.9	662.0	364.1	15.8	8.6	1.2	34.4	0.1	0.1	bdl	bdl	68	10.3	29.1	5.2	bdl	4.4	1.3	bdl	1.7	1.0	bdl
B2-39	26.299°	90.674°	60	5	6.9	-139.7	60.3	24.7	528.0	290.4	16.5	8.4	0.5	40.6	0.1	0.1	bdl	bdl	208	42.0	88.4	30.0	bdl	10.1	4.3	bdl	bdl	1.4	bdl
B2-40	26.295°	90.675°	40	5	6.8	-147.7	52.3	24.8	677.0	372.4	27.8	2.3	0.4	56.2	0.1	0.1	bdl	0.1	302	73.4	94.0	55.3	bdl	3.1	bdl	bdl	1.7	1.2	bdl
B2-41	26.289°	90.675°	80	20	6.6	-73.8	126.2	27.8	663.0	364.7	0.4	17.0	0.4	52.3	bdl	0.1	0.1	0.1	244	57.5	77.3	35.6	bdl	1.9	bdl	bdl	1.4	0.1	bdl
B2-42	26.284°	90.676°	80	20	7.1	-160.5	39.5	25.1	441.2	242.7	31.9	4.0	0.3	35.1	0.1	0.1	bdl	bdl	210	55.2	84.8	34.6	bdl	9.5	2.3	bdl	1.6	0.5	bdl
B2-43	26.281°	90.677°	50	10	6.7	-121.1	78.9	25.6	557.0	306.4	2.3	14.5	0.5	58.8	0.1	0.1	bdl	0.2	226	57.2	79.2	24.5	bdl	bdl	bdl	bdl	bdl	bdl	bdl

B2-44	26.268°	90.679°	80	20	6.5	-155.6	44.4	29.8	806.0	443.3	26.1	3.5	0.6	52.4	bdl	0.1	bdl	0.3	218	50.5	88.9	25.1	5.9	3.5	0.4	bdl	bdl	bdl	10.0
B2-45	26.275°	90.678°	20	5	7.2	-138.7	61.3	24.4	838.0	460.9	0.8	23.0	0.8	63.9	bdl	bdl	0.1	bdl	288	62.3	106	50.1	bdl	5.0	2.1	bdl	9.7	bdl	2.2
B2-46	26.273°	90.667°	40	5	6.4	-78.2	121.8	23.4	801.0	440.6	bdl	21.6	bdl	97.1	bdl	bdl	bdl	bdl	396	82.3	119	65.2	bdl	2.1	1.4	bdl	0.2	0.1	bdl
B2-47	26.266°	90.680°	50	10	6.8	-158.5	41.5	25.8	764.0	420.2	34.0	14.0	0.2	36.0	0.1	0.1	bdl	bdl	276	55.8	129	48.6	bdl	1.3	0.1	bdl	bdl	bdl	12.1
B2-48	26.263°	90.680°	55	5	6.9	-133.7	66.3	25.5	781.0	429.6	22.8	5.0	1.0	28.8	bdl	0.1	bdl	bdl	216	52.9	96.6	37.3	bdl	0.5	0.2	bdl	bdl	bdl	2.7
B2-49	26.258°	90.680°	40	5	7.3	-129.1	70.9	25.1	400.8	220.4	19.1	1.3	1.3	35.9	0.1	0.1	bdl	bdl	154	33.0	72.6	10.8	bdl	3.2	bdl	bdl	8.7	3.2	bdl
B2-50	26.284°	90.680°	100	20	6.7	-169.0	31.0	26.4	223.5	122.9	32.9	27.7	0.6	67.7	bdl	0.1	bdl	bdl	376	77.1	152	56.9	bdl	1.8	0.2	bdl	bdl	1.8	bdl
B2-51	26.288°	90.680°	120	20	6.7	-156.0	44.0	25.0	798.0	438.9	25.1	21.8	0.6	36.9	bdl	0.1	bdl	bdl	352	70.8	152	57.8	bdl	2.4	bdl	bdl	1.5	bdl	bdl
B2-52	26.290°	90.680°	80	20	6.8	-154.0	46.0	25.5	625.0	343.8	4.9	6.6	0.3	36.7	0.1	0.1	bdl	bdl	322	65.3	183	24.6	bdl	1.4	bdl	bdl	1.2	1.4	bdl
B2-53	26.293°	90.682°	50	10	6.7	65.9	265.9	25.2	888.0	488.4	12.2	3.5	0.8	56.9	0.1	0.1	bdl	bdl	368	81.6	153	65.4	bdl	2.4	2.5	bdl	2.0	bdl	6.4
B2-54	26.293°	90.683°	20	5	6.9	-134.7	65.3	25.3	635.0	349.3	9.7	4.9	0.4	68.8	bdl	0.1	bdl	bdl	288	66.4	107	54.7	bdl	10.8	2.6	bdl	1.7	bdl	11.0
B2-55	26.291°	90.687°	40	5	6.6	-98.8	101.2	25.5	958.0	526.9	2.2	3.4	2.0	77.0	bdl	0.1	bdl	bdl	414	90.5	170	74.6	bdl	19.0	3.9	bdl	1.4	bdl	12.5
B2-56	26.295°	90.689°	40	5	6.9	-167.2	32.8	24.9	692.0	380.6	1.8	15.9	0.2	65.2	0.1	0.1	bdl	bdl	338	76.4	147	44.7	0.1	4.1	bdl	bdl	1.6	4.2	bdl
B2-57	26.298°	90.689°	30	5	6.5	-150.0	50.0	25.3	874.0	480.7	10.4	24.7	0.8	52.1	0.1	0.1	bdl	bdl	372	96.6	160	55.7	bdl	2.3	bdl	bdl	1.4	2.3	bdl
B2-58	26.301°	90.690°	75	20	6.5	-158.0	42.0	25.4	167.0	91.9	12.4	18.1	0.8	48.8	bdl	0.1	bdl	0.1	580	127	288	85.7	bdl	2.6	1.9	bdl	bdl	bdl	10.1
B2-59	26.304°	90.690°	80	20	6.7	-104.5	95.5	26.4	595.0	327.3	4.1	1.4	0.6	17.2	bdl	0.1	bdl	bdl	206	48.2	124	24.5	0.1	10.2	bdl	bdl	1.4	bdl	18.3
B2-60	26.307°	90.694°	40	5	6.8	-141.4	58.6	25.2	545.0	299.8	1.2	10.3	0.5	10.3	bdl	0.1	bdl	bdl	144	44.7	83.1	5.8	0.1	4.8	1.9	bdl	bdl	bdl	bdl
B2-61	26.306°	90.696°	30	5	6.4	-111.9	88.1	25.8	582.0	320.1	3.9	5.9	1.0	10.5	0.1	0.1	bdl	bdl	158	60.1	152	4.0	bdl	19.8	bdl	bdl	1.4	bdl	25.8
B2-62	26.296°	90.697°	40	5	6.8	-152.7	47.3	24.6	694.0	381.7	27.1	8.8	0.3	33.2	bdl	0.1	bdl	0.1	159	6.0	103	3.8	bdl	4.3	0.1	bdl	1.2	bdl	bdl
B2-63	26.284°	90.695°	20	5	6.7	-55.4	144.6	24.9	541.0	297.6	11.3	10.3	0.4	36.9	bdl	bdl	bdl	bdl	178	47.8	143	15.4	0.1	23.2	bdl	bdl	2.2	bdl	30.0
B2-64	26.283°	90.696°	30	5	7.0	-66.4	133.6	25.6	581.0	319.6	16.8	1.2	0.9	31.8	bdl	0.1	bdl	0.1	132	33.7	82.5	4.2	bdl	2.3	bdl	bdl	2.2	bdl	11.4
B2-65	26.281°	90.683°	40	5	6.8	-137.0	63.0	25.4	848.0	466.4	12.0	12.0	0.7	31.5	bdl	0.1	bdl	bdl	182	50.5	124	10.4	0.1	26.9	0.5	bdl	3.4	bdl	19.0
B2-66	26.280°	90.700°	80	20	6.4	-168.0	32.0	25.3	789.0	434.0	34.3	22.4	1.7	32.5	bdl	bdl	bdl	bdl	178	45.9	81.3	7.9	0.2	3.1	bdl	bdl	1.0	bdl	bdl
B2-67	26.279°	90.703°	40	20	6.8	-90.6	109.4	25.1	850.0	467.5	8.8	4.9	1.2	34.0	0.1	bdl	bdl	bdl	162	25.1	120	16.4	bdl	12.5	bdl	bdl	1.6	bdl	30.2
B2-68	26.282°	90.706°	60	20	6.9	-117.9	82.1	25.4	917.0	504.4	13.8	3.1	0.6	35.7	bdl	bdl	bdl	0.1	150	31.6	134	18.6	bdl	45.3	0.4	bdl	1.4	bdl	18.5
B2-69	26.282°	90.706°	55	10	7.0	-99.9	100.1	25.8	759.0	417.5	11.2	2.2	0.3	34.0	0.1	bdl	bdl	bdl	112	14.3	71.8	9.0	bdl	13.9	bdl	bdl	1.5	bdl	6.0
B2-70	26.306°	90.703°	30	5	6.6	-114.3	85.7	25.7	819.0	450.5	4.3	7.8	1.3	34.2	0.1	bdl	bdl	bdl	154	34.5	86.3	20.2	bdl	13.5	bdl	bdl	1.4	bdl	8.4
B2-71	26.307°	90.708°	40	5	6.9	-119.6	80.4	25.7	401.9	221.0	3.6	bdl	1.2	23.6	bdl	bdl	bdl	bdl	86	12.4	70.1	4.0	bdl	bdl	18.7	bdl	bdl	bdl	bdl
B2-72	26.309°	90.711°	20	5	7.2	-87.2	112.8	24.9	466.3	256.5	4.0	4.8	0.4	33.4	bdl	bdl	bdl	bdl	100	22.2	49.4	4.2	bdl	1.1	bdl	bdl	1.5	bdl	7.0
B2-73	26.312°	90.718°	30	5	6.7	-111.5	88.5	25.4	912.0	501.6	9.4	20.2	0.5	36.5	0.1	bdl	bdl	bdl	152	23.6	75.4	14.3	bdl	5.2	0.5	bdl	1.1	bdl	3.3
B2-74	26.314°	90.719°	40	10	6.8	-147.7	52.3	24.6	657.0	361.4	34.9	21.0	0.8	32.5	bdl	bdl	bdl	bdl	106	6.5	64.7	3.3	bdl	9.5	bdl	bdl	2.0	bdl	bdl
B2-75	26.316°	90.721°	150	10	7.0	-115.7	84.3	26.8	665.0	365.8	29.1	15.9	0.8	36.3	0.1	bdl	bdl	0.1	144	29.3	82.1	26.9	0.4	34.6	bdl	bdl	1.4	bdl	3.9
B2-76	26.317°	90.724°	100	20	6.8	-135.0	65.0	25.5	627.0	344.9	9.4	12.3	1.1	35.5	0.1	bdl	bdl	bdl	134	25.4	61.3	15.1	bdl	bdl	6.5	bdl	2.5	bdl	bdl
B2-77	26.318°	90.724°	20	5	6.7	-150.7	49.3	24.4	901.0	495.6	36.5	23.4	0.5	37.3	bdl	bdl	bdl	bdl	170	11.1	39.9	10.3	bdl	bdl	17.8	bdl	0.8	bdl	bdl
B2-78	26.322°	90.728°	70	10	6.7	-154.7	45.3	24.0	640.0	352.0	24.2	21.6	0.4	32.6	bdl	bdl	bdl	bdl	118	28.6	66.1	15.5	bdl	bdl	19.8	bdl	9.6	bdl	bdl
B2-79	26.323°	90.729°	100	20	6.7	-141.9	58.1	25.2	645.0	354.8	20.7	14.3	0.7	31.0	bdl	bdl	bdl	bdl	134	26.0	76.1	6.5	bdl	2.5	10.3	bdl	bdl	bdl	bdl
B2-80	26.322°	90.730°	120	20	6.8	-141.5	58.5	24.2	673.0	370.2	26.4	21.1	0.7	30.4	bdl	0.1	bdl	bdl	138	36.5	57.6	24.8	bdl	1.5	bdl	bdl	1.7	bdl	bdl
B2-81	26.325°	90.983°	40	5	6.8	-93.9	106.1	25.5	739.0	406.5	12.8	5.0	0.9	32.5	bdl	0.1	bdl	bdl	102	13.7	78.6	5.1	0.2	15.4	0.8	bdl	1.3	bdl	bdl
B2-82	26.325°	90.973°	30	5	7.2	-136.9	63.1	25.8	686.0	377.3	15.3	10.0	0.7	31.8	bdl	0.1	bdl	0.1	132	28.0	65.3	17.4	bdl	15.4	bdl	bdl	1.4	bdl	bdl
B2-83	26.323°	90.733°	80	20	7.0	-77.0	123.0	24.3	313.0	172.2	7.3	15.6	0.5	23.7	0.1	0.1	bdl	0.2	68	13.6	34.6	3.5	bdl	0.8	bdl	bdl	1.6	bdl	9.6
B2-84	26.319°	90.700°	100	20	6.8	-78.4	121.6	24.8	310.6	170.8	9.3	12.1	0.4	34.2	bdl	0.1	bdl	bdl	184	34.7	109	13.6	0.3	16.8	bdl	bdl	1.7	bdl	bdl
B2-85	26.318°	90.716°	50	5	6.9	-142.9	57.1	25.0	516.0	283.8	9.0	8.8	0.5	28.2	bdl	0.1	bdl	0.2	102	10.5	66.4	5.8	bdl	10.7	bdl	bdl	1.7	bdl	bdl
B2-86	26.320°	90.715°	80	20	6.6	-89.1	110.9	25.3	1060.0	403.7	0.2	0.1	0.8	32.1	bdl	0.1	bdl	0.3	146	28.0	85.8	13.7	bdl	10.3	bdl	bdl	1.2	bdl	bdl
B2-87	26.323°	90.709°	30	5	6.1	-34.6	165.4	24.3	734.0	346.5	0.6	2.8	2.9	30.9	bdl	0.1	bdl	0.1	84	26.4	80.4	16.6	bdl	bdl	75.3	bdl	1.2	bdl	bdl
B2-88	26.323°	90.706°	30	5	6.7	-46.1	153.9	25.9	630.0	274.7	2.4	2.0	1.4	27.0	bdl	0.1	bdl	bdl	80	31.5	57.0	3.0	bdl	0.1	39.7	bdl	1.4	bdl	bdl
B2-89	26.325°	90.684°	55	5	6.0	-118.9	81.1	24.6	499.5	126.1	5.9	1.6	bdl	18.9	bdl	0.1	bdl	bdl	43	5.0	40.6	2.2	bdl	2.7	bdl	bdl	bdl	18.7	bdl
B2-90	26.325°	90.701°	60	10	6.7	-59.2	140.8	24.5	229.2	102.7	8.6	11.7	0.9	20.4	bdl	bdl	bdl	bdl	116	21.4	69.4	14.7	bdl	5.8	bdl	bdl	bdl	15.3	bdl
B2-91	26.328°	90.693°	100	20	6.4	-47.4	152.6	25.4	186.8	285.5	5.0	1.7	0.8	27.8	bdl	bdl	bdl	0.7	116	47.0	53.9	5.4	bdl	bdl	8.3	bdl	bdl	14.9	bdl

B2-92	26.318°	90.690°	100	20	6.9	-66.8	133.2	24.6	519.0	244.0	25.7	7.7	0.6	27.3	bdl	bdl	bdl	0.8	94	10.8	16.9	3.8	bdl	bdl	2.0	bdl	bdl	8.9	bdl
B2-93	26.325°	90.687°	40	5	7.1	-50.6	149.4	25.3	443.6	273.5	2.9	0.7	0.3	25.5	bdl	bdl	bdl	0.1	120	36.8	73.1	23.7	bdl	bdl	9.4	bdl	bdl	34.0	bdl
B2-94	26.325°	90.683°	50	5	6.9	-71.3	128.7	24.0	497.3	283.8	30.7	6.2	1.3	24.6	0.1	bdl	bdl	0.1	120	9.7	79.4	24.2	bdl	bdl	3.6	bdl	bdl	24.2	bdl
B2-95	26.322°	90.686°	25	55	7.1	-41.7	158.3	25.1	516.0	413.6	18.5	4.0	0.3	26.0	bdl	bdl	bdl	0.1	118	10.3	38.6	38.8	bdl	bdl	24.3	bdl	bdl	35.3	bdl
B2-96	26.322°	90.687°	80	20	6.9	-82.2	117.8	25.0	752.0	368.0	25.5	8.0	0.5	30.8	bdl	bdl	0.1	0.2	144	25.1	87.6	15.9	bdl	bdl	8.1	bdl	bdl	9.4	bdl
B2-97	26.319°	90.692°	100	20	6.9	-146.4	53.6	23.7	669.0	331.1	13.8	9.2	0.3	30.1	bdl	bdl	bdl	bdl	126	24.6	62.5	16.6	bdl	6.9	bdl	0.51	bdl	4.0	bdl
B2-98	26.319°	90.692°	100	20	7.1	-144.0	56.0	24.9	602.0	299.2	20.2	13.7	0.6	27.0	bdl	0.1	bdl	0.5	108	25.9	54.9	3.5	bdl	5.1	bdl	bdl	bdl	bdl	bdl
B2-99	26.319°	90.692°	60	20	7.0	-129.8	70.2	25.2	544.0	391.6	3.3	4.6	0.6	30.8	bdl	0.1	bdl	bdl	142	17.9	72.7	35.5	bdl	22.9	bdl	bdl	1.4	bdl	6.3
B2-100	26.316°	90.697°	80	5	6.7	-142.5	57.5	23.2	712.0	315.2	4.5	8.8	0.4	29.7	bdl	0.1	bdl	bdl	130	29.7	62.0	4.3	bdl	1.6	bdl	bdl	1.5	bdl	bdl
B2-101	26.317°	90.697°	100	20	6.8	-143.5	56.5	23.0	573.0	264.6	25.0	17.3	0.6	19.7	bdl	0.1	bdl	0.1	96	25.2	54.1	2.4	0.1	2.3	bdl	bdl	1.8	bdl	bdl
B2-102	26.316°	90.699°	80	20	7.0	-128.3	71.7	24.1	481.0	388.9	12.7	8.7	0.6	25.9	bdl	0.1	bdl	0.2	160	35.8	83.2	14.6	bdl	4.1	bdl	bdl	2.0	bdl	bdl
B2-103	26.316°	90.699°	85	15	7.0	-129.8	70.2	26.5	707.0	372.4	28.5	11.0	1.7	28.2	0.1	0.1	bdl	0.1	166	30.9	88.8	15.0	bdl	3.3	bdl	bdl	2.3	bdl	bdl
B2-104	26.315°	90.700°	70	20	6.8	-64.9	135.1	25.1	677.0	418.0	9.5	8.1	1.1	26.5	bdl	0.1	bdl	bdl	162	35.4	76.7	15.5	bdl	2.9	bdl	bdl	bdl	3.3	bdl
B2-105	26.315°	90.708°	65	10	6.9	-152.8	47.2	25.2	760.0	441.7	9.3	9.7	0.6	29.9	bdl	0.1	bdl	0.1	150	30.8	75.1	15.7	bdl	9.5	bdl	bdl	bdl	bdl	bdl
B2-106	26.314°	90.708°	80	20	6.6	-124.1	75.9	24.4	803.0	413.6	9.5	14.4	1.4	29.8	bdl	bdl	bdl	0.1	70	5.2	34.1	5.4	bdl	1.1	bdl	bdl	2.3	bdl	bdl
B2-107	26.324°	90.681°	100	20	6.7	-104.1	95.9	24.0	752.0	201.0	3.2	5.4	0.2	19.9	0.1	0.1	bdl	bdl	86	14.5	45.7	13.4	0.2	2.8	bdl	0.85	bdl	5.1	bdl
B2-108	26.324°	90.680°	40	5	6.8	-107.5	92.5	25.1	365.5	200.9	1.5	2.4	0.5	22.5	0.2	bdl	bdl	bdl	120	26.1	58.9	13.9	bdl	5.0	bdl	bdl	bdl	bdl	bdl
B2-109	26.330°	90.697°	110	15	6.0	-83.3	116.7	24.8	365.2	82.7	6.8	10.8	0.2	21.6	0.1	bdl	bdl	0.1	110	19.3	72.6	14.6	bdl	10.2	bdl	0.43	bdl	3.3	bdl
B2-110	26.318°	90.716°	60	5	6.7	-127.8	72.8	26.3	150.4	583	bdl	bdl	bdl	bdl	bdl	bdl	bdl	bdl	75.4	11.05	68.8	4.12	0.34	16.9	bdl	bdl	bdl	bdl	bdl

Appendix Table A 1. 4: Summary of hydro-chemical parameters of L*As*CR groundwater samples.

ID	Latitude	Longitude	pH	EC	ORP	Eh	Temp.	TDS	*As*	Ca	Na	K	HCO_3^-	Fe	Mn	F	Cl	SO_4^{-2}	NO_3^-	NO_2^-	PO_4^{-2}	Ni	Cu	Pb	Mg	Cr	Hg
				µS cm^{-1}	mV	mV	°C	mg L^{-1}	µg L^{-1}	mg L^{-1}																		
D2-1	26.390°	91.019°	6.1	466.1	-116.4	83.6	25.2	256.4	bdl	109.2	38.0	15.6	238	3.0	bdl	0.6	0.6	11.9	5.4	bdl	bdl	bdl	bdl	0.1	72.5	bdl	0.4
D2-2	26.391°	91.021°	6.6	405.6	-69.1	130.9	25.0	223.1	8.7	24.2	12.2	24.9	92	5.3	1.4	0.4	bdl	8.1	bdl	6.5	bdl	bdl	bdl	0.1	32.0	bdl	bdl
D2-3	26.417°	91.026°	6.7	346.7	-108.2	91.8	25.0	190.7	3.7	122.6	31.1	14.4	174	3.3	1.9	bdl	bdl	5.1	bdl	bdl	bdl	bdl	0.3	0.1	9.1	bdl	bdl
D2-4	26.444°	91.044°	6.8	118.5	-75.8	124.2	21.9	65.2	3.9	97.4	6.7	5.3	138	3.6	bdl	0.4	bdl	7.7	7.4	3.1	bdl	bdl	0.5	0.1	33.1	bdl	bdl
D2-5	26.453°	92.045°	6.9	953.0	-77.2	122.8	23.1	524.2	10.4	80.6	7.5	5.7	118	1.7	bdl	bdl	bdl	bdl	5.3	bdl	bdl	bdl	0.4	0.1	31.6	bdl	1.3
D2-6	26.464°	92.053°	6.8	183.3	-81.3	118.7	22.1	100.8	2.7	52.5	10.2	3.8	70	2.3	bdl	bdl	bdl	bdl	bdl	bdl	bdl	bdl	bdl	0.1	9.6	bdl	0.8
D2-7	26.468°	92.053°	6.8	166.4	-81.6	118.4	22.1	91.5	2.9	49.1	7.1	2.9	68	29.8	bdl	0.3	0.9	bdl	bdl	3.0	bdl	bdl	bdl	0.2	14.9	bdl	bdl
D2-8	26.467°	92.033°	6.7	235.8	-99.5	100.5	23.1	129.7	12.0	55.6	3.7	2.9	68	3.1	bdl	bdl	bdl	8.6	0.7	4.8	bdl	bdl	bdl	0.1	8.1	bdl	bdl
D2-9	26.481°	92.030°	6.6	168.8	-85.1	114.9	22.5	92.8	23.3	25.5	2.7	0.5	34	5.7	2.1	0.4	3.6	7.8	bdl	bdl	bdl	bdl	bdl	0.2	5.8	bdl	bdl
D2-10	26.494°	92.030°	6.5	206.9	-88.6	111.4	23.1	113.8	11.5	81.7	2.9	0.5	88	15.3	1.2	0.1	1.9	18.2	bdl	3.7	bdl	bdl	bdl	0.2	11.9	bdl	bdl
D2-11	26.510°	92.022°	6.5	163.7	-89.3	110.7	24.4	90.0	14.7	18.7	9.7	12.0	48	10.0	bdl	bdl	2.6	bdl	0.5	4.2	bdl	bdl	bdl	0.1	10.0	bdl	bdl
D2-12	26.520°	92.018°	6.5	174.0	-71.2	128.8	22.2	95.7	1.5	183.9	11.0	1.6	194	6.1	2.4	0.4	1.8	bdl	bdl	bdl	bdl	bdl	bdl	0.1	10.6	bdl	bdl
D2-13	26.529°	92.009°	6.6	270.1	-107.2	92.8	23.1	148.6	37.1	98.6	3.4	0.5	106	32.3	bdl	bdl	bdl	bdl	bdl	bdl	bdl	bdl	bdl	0.2	14.1	bdl	bdl
D2-14	26.536°	92.003°	6.4	210.0	-114.6	85.4	23.8	115.5	14.3	50.7	10.2	3.6	70	35.7	1.4	0.6	1.8	bdl	bdl	bdl	bdl	bdl	bdl	0.1	5.3	bdl	bdl
D2-15	26.547°	91.990°	6.5	153.5	-94.1	105.9	23.2	84.4	1.5	96.3	8.8	1.3	110	8.5	3.0	bdl	0.8	bdl	bdl	bdl	bdl	bdl	bdl	0.1	10.1	bdl	bdl
D2-16	26.398°	91.904°	6.6	167.8	-111.9	88.1	22.1	92.3	33.4	109.0	3.2	0.2	108	6.9	bdl	bdl	0.6	3.8	bdl	bdl	bdl	bdl	bdl	0.2	6.1	bdl	bdl
D2-17	26.388°	91.906°	6.4	181.1	-117.0	83.0	23.0	99.6	18.7	94.1	3.8	0.3	94	5.2	bdl	bdl	1.3	bdl	bdl	bdl	bdl	bdl	bdl	0.2	7.7	bdl	1.8
D2-18	26.376°	91.905°	6.6	201.0	-37.7	162.3	23.6	110.6	56.1	79.5	4.1	0.3	100	5.1	bdl	bdl	0.5	bdl	bdl	2.6	bdl	Bdl	bdl	0.1	8.7	bdl	0.5
D2-19	26.347°	91.910°	6.4	224.6	-140.4	59.6	23.6	123.5	18.1	101.3	3.9	0.9	108	6.3	bdl	1.4	bdl	bdl	bdl	bdl	bdl	2.3	bdl	0.2	10.4	bdl	0.2
D2-20	26.329°	91.907°	6.4	330.3	-93.2	106.8	23.2	181.7	0.8	132.6	3.7	0.3	150	11.7	1.4	bdl	bdl	13.6	bdl	bdl	bdl	bdl	bdl	0.2	19.6	bdl	bdl
D2-21	26.410°	91.928°	6.4	266.4	-140.0	60.0	23.6	146.5	28.8	82.1	8.7	2.0	96	36.2	0.9	bdl	0.4	bdl	0.3	bdl	bdl	bdl	bdl	0.2	11.7	bdl	bdl
D2-22	26.416°	91.930°	6.4	220.6	-157.3	42.7	23.8	121.3	4.8	69.7	7.0	1.8	88	13.9	0.8	bdl	0.6	4.1	bdl	bdl	bdl	bdl	bdl	0.2	7.9	bdl	bdl
D2-23	26.436°	91.925°	6.3	201.0	-122.3	77.7	24.4	110.6	2.3	82.4	6.0	1.4	94	11.2	bdl	bdl	0.8	4.8	0.1	bdl	bdl	bdl	bdl	0.2	4.4	bdl	bdl
D2-24	26.440°	91.932°	6.3	281.3	-124.8	75.2	23.8	154.7	6.1	101.1	5.0	1.8	120	24.9	bdl	bdl	1.4	bdl	bdl	bdl	bdl	bdl	bdl	0.1	10.1	bdl	bdl
D2-25	26.438°	91.968°	6.2	253.3	-123.5	76.5	25.1	139.3	22.4	81.8	10.8	1.9	96	38.8	0.3	bdl	bdl	bdl	bdl	bdl	bdl	bdl	bdl	0.1	7.8	bdl	bdl
D2-26	26.423°	91.971°	6.2	258.1	-116.8	83.2	26.1	142.0	10.3	80.0	10.4	1.4	94	47.3	1.0	bdl	1.0	1.3	bdl	bdl	bdl	bdl	bdl	0.1	6.1	bdl	bdl
D2-27	26.396°	91.975°	6.3	138.6	-109.8	90.2	25.4	76.2	9.1	60.0	3.0	7.8	78	24.6	0.2	1.3	1.1	29.0	bdl	bdl	bdl	bdl	bdl	0.2	11.9	bdl	bdl
D2-28	26.378°	91.970°	6.3	261.9	-132.8	67.2	22.8	144.0	11.3	76.5	2.8	5.3	94	1.1	bdl	bdl	1.7	bdl	bdl	bdl	bdl	bdl	bdl	0.2	8.9	bdl	bdl
D2-29	26.350°	91.825°	6.2	209.7	-42.1	157.9	23.1	115.3	11.2	89.5	3.8	1.4	104	5.3	bdl	1.6	3.0	bdl	bdl	bdl	bdl	bdl	bdl	0.1	11.2	bdl	bdl
D2-30	26.425°	92.000°	6.6	229.1	-113.6	86.4	25.5	126.0	1.2	30.6	10.6	1.6	46	11.6	bdl	bdl	2.2	bdl	1.4	bdl	bdl	bdl	bdl	0.1	8.9	bdl	bdl
D2-31	26.433°	91.026°	6.3	189.0	-111.2	88.8	24.6	104.0	bdl	119.9	11.3	5.6	168	9.3	bdl	0.4	1.7	bdl	5.5	bdl	bdl	bdl	bdl	0.1	23.0	bdl	bdl
D2-32	26.413°	91.024°	6.4	334.4	-112.7	87.3	24.0	183.9	bdl	117.5	9.9	3.8	158	3.2	0.1	0.5	9.7	bdl	bdl	bdl	bdl	bdl	bdl	0.2	21.4	bdl	2.6
D2-33	26.578°	91.972°	6.8	350.6	-77.7	122.3	23.3	192.8	24.5	94.8	5.3	1.8	116	14.5	0.4	bdl	2.1	bdl	bdl	bdl	bdl	bdl	bdl	0.1	19.1	bdl	bdl
D2-34	26.581°	91.963°	6.4	122.7	-79.5	120.5	24.3	67.5	1.6	24.8	7.1	2.6	38	14.5	0.6	bdl	4.7	bdl	bdl	bdl	bdl	bdl	bdl	0.2	6.3	bdl	bdl
D2-35	26.588°	91.936°	6.3	234.4	-70.3	129.7	23.0	128.9	13.7	83.9	3.4	1.7	96	35.1	0.4	bdl	bdl	bdl	bdl	bdl	bdl	bdl	bdl	0.1	5.7	bdl	bdl
D2-36	26.642°	91.913°	6.4	123.2	-1007	-807	22.5	67.8	10.3	29.4	5.6	2.2	40	40.0	bdl	bdl	bdl	bdl	bdl	bdl	bdl	bdl	bdl	0.1	5.8	bdl	bdl
D2-37	26.654°	91.912°	5.9	206.0	-90.7	109.3	22.9	113.3	4.1	54.4	2.1	5.9	78	30.7	bdl	bdl	2.2	bdl	bdl	bdl	bdl	bdl	bdl	0.2	9.2	bdl	bdl
D2-38	26.645°	91.914°	6.4	30.0	-112.6	87.4	23.3	16.5	24.5	73.3	10.8	1.7	106	81.5	1.5	bdl	2.3	4.0	bdl	2.1	bdl	bdl	bdl	bdl	12.1	bdl	bdl
D2-39	26.628°	91.914°	6.0	212.4	-101.8	98.2	23.3	116.8	4.2	42.9	2.7	3.5	58	34.8	0.3	bdl	1.7	9.9	0.5	bdl	bdl	bdl	bdl	0.1	6.6	bdl	bdl
D2-40	26.581°	91.911°	6.1	188.0	-127.5	72.5	23.1	103.4	15.9	78.5	3.0	1.6	80	27.3	0.1	0.2	4.4	2.8	bdl	bdl	bdl	bdl	bdl	0.1	2.7	bdl	bdl
D2-41	26.395°	91.899°	6.1	170.9	-106.3	93.7	22.8	94.0	5.2	213.6	18.9	3.5	258	3.6	0.1	0.6	0.6	11.9	bdl	bdl	bdl	0.2	bdl	0.7	17.7	bdl	0.3
D2-42	26.395°	91.900°	6.6	172.0	-66.7	133.3	22.7	94.6	8.4	74.2	17.9	1.6	92	2.7	bdl	0.4	bdl	8.1	6.5	bdl	bdl	0.2	bdl	0.2	14.7	bdl	0.1
D2-43	26.391°	91.901°	6.7	132.6	-68.4	131.6	22.1	72.9	5.5	130.5	18.9	1.5	164	5.1	bdl	bdl	bdl	bdl	bdl	bdl	bdl	0.2	bdl	0.8	16.4	bdl	0.2

D2-44	26.389°	91.903°	6.8	173.5	-58.7	141.3	22.9	95.4	3.9	173.4	17.7	1.3	188	0.7	bdl	0.4	bdl	7.7	3.1	bdl	bdl	0.3	bdl	0.3	14.3	bdl	0.2
D2-45	26.376°	91.905°	6.9	184.0	-117.1	82.9	22.7	101.2	0.4	114.2	18.5	1.6	140	3.4	bdl	bdl	bdl	bdl	bdl	7.9	bdl	0.2	bdl	0.1	16.8	bdl	0.2
D2-46	26.385°	91.912°	6.8	170.1	-72.8	127.2	22.7	93.6	3.0	53.5	17.4	1.3	70	4.5	bdl	bdl	bdl	bdl	bdl	5.4	bdl	0.3	bdl	0.2	15.4	bdl	0.1
D2-47	26.393°	91.905°	6.8	165.6	-5.5	194.5	23.0	91.1	3.3	52.9	17.0	1.3	68	1.5	bdl	0.3	0.9	bdl	3.0	bdl	bdl	0.2	bdl	0.2	15.1	bdl	0.07
D2-48	26.400°	91.904°	6.7	138.7	-38.2	161.8	22.8	76.3	3.9	51.4	17.3	1.4	68	3.9	bdl	bdl	bdl	8.6	4.8	bdl	bdl	0.2	bdl	0.4	14.3	bdl	0.07
D2-49	26.404°	91.910°	6.6	142.8	-62.5	137.5	22.9	78.5	7.4	14.2	19.4	1.6	34	9.5	bdl	0.4	3.6	7.8	bdl	bdl	bdl	0.2	bdl	0.1	10.7	bdl	0.05
D2-50	26.404°	91.921°	6.5	231.7	1.9	201.9	23.1	127.4	8.6	69.0	20.1	1.2	88	26.0	bdl	0.1	1.9	18.2	3.7	bdl	bdl	0.2	bdl	1.6	24.2	bdl	0.1
D2-51	26.408°	91.928°	6.5	176.1	-33.8	166.2	23.1	96.9	17.9	181.2	14.3	7.1	187	23.1	bdl	bdl	2.6	bdl	4.2	bdl	bdl	0.2	bdl	1.6	14.9	bdl	0.22
D2-52	26.416°	91.931°	6.5	193.8	-71.3	128.7	22.7	106.6	28.3	192.7	7.2	1.9	214	22.0	bdl	0.4	1.8	bdl	bdl	bdl	bdl	0.3	bdl	1.5	21.0	0.1	0.24
D2-53	26.426°	91.928°	6.6	167.9	-63.2	136.8	22.9	92.3	19.4	86.3	22.1	0.9	106	8.0	bdl	bdl	bdl	bdl	bdl	bdl	bdl	0.2	bdl	0.2	17.0	0.1	0.11
D2-54	26.426°	91.926°	6.4	237.1	-65.0	135.0	22.9	130.4	23.3	36.4	27.2	1.3	70	9.4	bdl	0.6	1.8	bdl	bdl	bdl	bdl	0.2	bdl	1.7	19.8	0.1	0.081
D2-55	26.426°	91.921°	6.5	174.9	-14.4	185.6	22.9	96.2	27.0	87.4	27.0	0.9	110	12.3	bdl	bdl	0.8	bdl	bdl	bdl	bdl	0.2	bdl	2.0	13.4	0.1	0.12
D2-56	26.437°	91.925°	6.6	175.1	-59.0	141.0	22.9	96.3	21.7	78.7	26.9	1.1	108	8.4	bdl	bdl	0.6	3.8	bdl	bdl	bdl	0.2	bdl	0.1	10.2	0.1	0.12
D2-57	26.441°	91.912°	6.4	180.6	-56.6	143.4	22.6	99.3	33.0	66.9	23.6	1.1	94	16.8	bdl	bdl	1.3	bdl	bdl	bdl	bdl	0.2	bdl	0.3	13.8	0.1	0.1
D2-58	26.444°	91.899°	6.6	142.0	-71.4	128.6	23.0	78.1	10.9	83.6	21.3	0.8	100	4.6	bdl	bdl	0.5	2.9	2.6	bdl	bdl	0.2	bdl	1.2	9.7	0.1	0.11
D2-59	26.446°	91.892°	6.4	167.1	-10.3	189.7	22.9	91.9	26.4	75.4	22.7	1.0	108	21.0	bdl	1.4	bdl	bdl	bdl	1.9	2.3	0.2	bdl	0.1	15.4	0.1	0.13
D2-60	26.456°	91.893°	6.4	158.1	-57.3	142.7	22.7	87.0	10.1	125.4	21.6	1.1	150	15.7	bdl	bdl	bdl	bdl	3.2	bdl	bdl	0.2	bdl	0.2	11.4	0.1	0.17
D2-61	26.464°	91.895°	6.4	192.0	-72.0	128.0	22.7	105.6	24.4	216.1	21.4	0.9	256	25.0	bdl	bdl	0.4	bdl	bdl	bdl	bdl	0.2	bdl	0.5	13.6	0.1	0.28
D2-62	26.473°	91.896°	6.4	130.2	-91.7	108.3	22.7	71.6	35.7	146.0	25.0	1.0	188	16.0	bdl	bdl	0.6	4.1	bdl	bdl	bdl	0.3	bdl	1.2	12.9	0.1	0.21
D2-63	26.483°	91.895°	6.3	172.9	-60.0	140.0	22.7	95.1	46.8	184.4	21.6	1.3	194	23.9	bdl	bdl	0.8	4.8	bdl	bdl	bdl	0.3	bdl	0.3	12.3	0.1	0.22
D2-64	26.490°	91.894°	6.3	157.6	-44.8	155.2	22.5	86.7	49.1	183.8	23.1	1.2	220	21.4	bdl	bdl	1.4	bdl	bdl	bdl	bdl	0.2	bdl	0.2	11.1	0.1	0.24
D2-65	26.504°	91.893°	6.2	163.0	-114.9	85.1	22.8	89.7	35.1	183.2	20.5	1.7	226	24.9	bdl	bdl	bdl	bdl	bdl	bdl	bdl	0.2	bdl	0.1	11.6	0.1	0.25
D2-66	26.515°	91.891°	6.2	161.9	-57.6	142.4	22.8	89.0	52.4	252.7	17.9	1.4	257	28.5	bdl	bdl	1.0	1.3	bdl	bdl	bdl	0.2	bdl	0.2	14.3	0.1	0.3
D2-67	26.501°	91.915°	6.3	164.9	-107.0	93.0	22.8	90.7	16.1	56.9	12.0	3.6	78	21.6	bdl	1.3	1.1	29.0	bdl	bdl	bdl	0.2	0.1	bdl	10.9	0.1	0.1
D2-68	26.494°	91.922°	6.3	152.2	-29.3	170.7	22.8	83.7	29.4	241.6	18.8	2.4	280	31.2	bdl	bdl	1.7	bdl	bdl	bdl	bdl	0.2	bdl	0.1	12.8	0.1	0.32
D2-69	26.497°	91.941°	6.2	124.9	-78.8	121.2	22.8	68.7	22.2	254.3	7.5	2.4	304	33.8	bdl	1.6	3.0	bdl	bdl	bdl	bdl	0.2	bdl	2.0	22.3	0.1	0.34
D2-70	26.490°	91.956°	6.6	125.5	-19.1	180.9	23.0	69.0	7.0	45.2	6.2	2.0	190	19.5	bdl	bdl	2.2	bdl	bdl	bdl	bdl	0.2	bdl	1.1	16.6	0.1	0.21
D2-71	26.490°	91.957°	6.3	150.0	-19.5	180.5	22.9	82.5	38.8	288.2	12.6	2.3	328	38.4	0.1	0.4	1.7	bdl	bdl	bdl	bdl	0.2	bdl	0.1	19.7	0.1	0.37
D2-72	26.479°	91.852°	6.4	167.0	-114.2	85.8	22.8	91.9	26.1	304.4	6.1	6.3	351	36.7	bdl	0.5	9.7	bdl	bdl	bdl	bdl	0.2	bdl	0.2	20.2	0.1	0.39
D2-73	26.479°	91.985°	6.8	90.9	-52.0	148.0	22.8	50.0	10.7	293.0	5.9	1.3	316	31.4	bdl	bdl	2.1	bdl	bdl	bdl	bdl	0.2	bdl	0.2	11.9	0.1	0.35
D2-74	26.473°	91.992°	6.4	206.3	-102.8	97.2	22.9	113.5	23.8	19.2	13.8	1.4	38	5.1	bdl	bdl	4.7	bdl	bdl	bdl	bdl	0.2	bdl	0.8	26.6	0.1	0.04
D2-75	26.475°	92.005°	6.3	208.9	-47.2	152.8	22.9	114.9	11.8	128.5	11.5	1.5	156	9.5	bdl	bdl	bdl	bdl	bdl	bdl	bdl	0.2	bdl	1.4	25.9	0.1	0.17
D2-76	26.463°	91.998°	6.4	209.1	10.4	210.4	22.9	115.0	9.8	29.3	14.8	0.4	40	3.6	bdl	bdl	bdl	bdl	bdl	bdl	bdl	0.2	bdl	3.4	25.0	0.1	0.04
D2-77	26.456°	91.989°	5.9	120.6	-72.3	127.7	22.9	66.3	5.7	72.2	4.5	1.4	78	3.8	bdl	bdl	2.2	bdl	bdl	bdl	bdl	0.3	bdl	0.5	19.2	0.1	0.08
D2-78	26.454°	91.986°	6.4	95.8	-34.0	166.0	23.0	52.7	5.9	102.1	6.9	1.5	106	bdl	0.1	bdl	2.3	4.0	2.1	bdl	bdl	0.2	bdl	0.1	10.8	0.1	0.12
D2-79	26.452°	91.984°	6.0	98.2	-41.9	158.1	23.1	54.0	6.9	152.8	6.6	1.1	158	33.8	bdl	bdl	1.7	9.9	bdl	bdl	bdl	0.2	bdl	1.2	12.4	0.1	0.19
D2-80	26.448°	91.981°	6.1	441.1	-113.5	86.5	22.7	242.6	bdl	46.1	22.6	13.8	80	0.2	bdl	0.2	4.4	2.8	bdl	bdl	bdl	0.2	bdl	0.2	32.3	0.1	0.09
D2-81	26.445°	91.996°	6.0	95.4	-44.6	155.4	23.0	52.5	bdl	42.5	8.0	1.7	50	1.5	bdl	bdl	1.6	1.7	bdl	bdl	bdl	0.3	bdl	0.6	11.3	0.1	0.05
D2-82	26.445°	91.996°	6.6	91.1	-37.0	163.0	23.0	50.1	bdl	132.7	6.8	1.5	134	bdl	bdl	bdl	2.2	2.2	bdl	bdl	bdl	0.2	bdl	0.1	10.8	0.1	0.14
D2-83	26.445°	92.002°	6.6	169.0	-34.2	165.8	22.9	93.0	8.7	322.4	9.4	2.7	385	58.2	bdl	bdl	4.7	4.9	bdl	bdl	bdl	0.2	bdl	1.5	11.9	0.1	0.45
D2-84	26.444°	92.011°	6.0	177.1	-35.0	165.0	22.7	97.4	36.9	335.0	8.8	6.0	380	27.0	bdl	1.1	1.5	5.3	bdl	bdl	bdl	0.2	bdl	0.3	19.4	0.1	0.41
D2-85	26.447°	92.017°	6.2	172.9	-74.6	125.4	22.9	95.1	21.3	257.8	8.9	3.7	284	36.3	bdl	bdl	9.7	5.1	bdl	bdl	bdl	0.2	bdl	bdl	15.9	0.1	0.32
D2-86	26.448°	92.026°	6.1	244.3	-97.6	102.4	22.8	134.4	7.2	139.0	15.0	5.0	147	28.2	bdl	bdl	12.7	14.8	bdl	bdl	bdl	0.2	bdl	0.1	23.0	0.1	0.18
D2-87	26.441°	92.045°	6.4	324.9	-16.0	184.0	23.1	178.7	19.1	173.5	9.5	4.3	186	10.6	0.1	bdl	0.9	bdl	bdl	bdl	bdl	0.2	bdl	0.2	25.3	0.1	0.20
D2-88	26.437°	92.045°	5.8	318.8	-36.3	163.7	23.1	175.3	9.9	186.3	14.6	22.2	241	0.5	0.1	bdl	8.0	bdl	bdl	bdl	bdl	0.2	bdl	0.1	27.2	0.1	0.26
D2-89	26.467°	92.055°	5.9	273.0	-64.4	135.6	23.0	150.2	6.6	398.0	14.2	5.2	482	58.1	bdl	0.4	6.8	bdl	bdl	bdl	bdl	0.2	bdl	2.3	24.0	0.1	0.55
D2-90	26.473°	92.070°	6.2	195.6	-102.0	98.0	22.6	107.6	7.3	187.5	9.4	2.2	213	bdl	0.1	0.3	2.8	bdl	bdl	bdl	bdl	0.3	bdl	bdl	19.6	0.1	0.22
D2-91	26.473°	92.070°	6.2	194.3	-198.0	122.6	23.4	187.5	7.3	467.8	16.7	2.4	110	bdl	0.2	0.8	3.1	bdl	bdl	7.3	bdl	0.1	0.3	2.8	18.2	0.1	0.076

Appendix A2

Appendix Table A 2. 5: Person correlation for 2013 groundwater samples of Tapatari block

	Ph	Temp.	EC	ORP	DO	TDS	*As*	Ca^{+2}	Na^{+}	K^{+}	Cl^{-}	Fe	Mn	Mg^{+2}	SO_4^{-2}	HCO_3^{-}	PO_4^{-3}
Ph	1.00																
Temp.	-0.04	1.00															
EC	0.15	-0.09	1.00														
ORP	-0.09	-0.21	0.04	1.00													
DO	-0.14	-0.01	-0.04	0.06	1.00												
TDS	-0.03	-0.03	0.08	0.00	0.06	1.00											
As	0.02	0.23	-0.10	-0.12	-0.03	-0.06	1.00										
Ca^{+2}	0.28	-0.14	0.15	-0.01	0.00	0.04	-0.17	1.00									
Na^{+}	0.10	-0.09	-0.13	-0.07	0.01	-0.01	0.01	0.04	1.00								
K^{+}	0.01	-0.14	-0.08	-0.04	0.00	-0.03	-0.02	0.00	0.77	1.00							
Cl^{-}	-0.16	-0.04	-0.23	-0.05	-0.16	0.07	-0.03	-0.17	0.00	-0.03	1.00						
Fe	0.03	0.06	0.07	0.07	-0.11	-0.08	**0.50**	-0.10	-0.32	-0.22	-0.10	1.00					
Mn	0.05	0.01	0.00	0.02	-0.01	-0.08	0.22	-0.13	0.14	0.08	0.01	-0.03	1.00				
Mg^{+2}	-0.16	-0.08	-0.19	-0.02	0.07	-0.02	0.22	-0.25	0.21	0.18	0.06	0.07	0.14	1.00			
SO_4^{-2}	-0.08	-0.03	0.12	0.26	-0.01	-0.03	0.17	-0.14	-0.01	-0.03	-0.05	0.18	0.18	0.09	1.00		
HCO_3^{-}	0.11	-0.17	-0.05	-0.08	0.05	0.00	-0.02	**0.50**	0.76	0.73	-0.10	-0.25	0.05	0.36	-0.11	1.00	
PO_4^{-3}	0.04	-0.23	0.04	0.19	-0.05	-0.14	-0.14	0.24	-0.11	-0.12	-0.03	0.05	0.07	-0.11	0.23	-0.03	1.00

Appendix Table A 2. 6: Person correlation for 2013 groundwater samples of Boitamari block

	Ph	Temp.	EC	ORP	DO	TDS	*As*	Ca^{+2}	Na^{+}	K^{+}	Cl^{-}	Fe	Mn	Mg^{+2}	SO_4^{-2}	HCO_3^{-}	PO_4^{-3}
Ph	1.00																
Temp.	-0.33	1.00															
EC	0.24	-0.52	1.00														
ORP	0.22	-0.21	-0.02	1.00													
DO	-0.06	0.02	0.05	-0.28	1.00												
TDS	-0.42	0.46	-0.36	-0.14	-0.01	1.00											
As	-0.19	0.11	-0.14	-0.10	0.13	0.21	1.00										
Ca^{+2}	-0.13	0.11	-0.15	-0.01	0.20	-0.01	0.16	1.00									
Na^{+}	-0.09	-0.33	0.21	0.04	0.13	0.02	0.33	0.00	1.00								
K^{+}	-0.28	0.41	-0.40	-0.23	-0.01	0.35	0.35	0.05	0.13	1.00							
Cl^{-}	-0.18	0.01	-0.08	0.10	0.01	-0.16	0.03	0.03	0.13	0.06	1.00						
Fe	-0.49	0.37	-0.32	-0.16	0.03	0.28	**0.64**	0.15	0.05	0.42	0.13	1.00					
Mn	0.12	-0.38	0.12	0.35	0.13	-0.14	-0.08	0.11	0.08	-0.42	-0.06	-0.22	1.00				
Mg^{+2}	0.04	-0.31	0.23	0.22	-0.09	-0.17	-0.11	0.07	0.02	-0.28	-0.24	-0.23	0.41	1.00			
SO_4^{-2}	0.06	-0.18	0.23	0.13	0.00	0.03	-0.07	-0.20	0.12	-0.04	0.04	-0.26	0.11	0.24	1.00		
HCO_3^{-}	-0.23	-0.03	-0.08	0.02	0.18	0.03	**0.34**	0.76	0.49	0.36	0.03	0.20	0.10	0.29	-0.04	1.00	
PO_4^{-3}	0.21	-0.22	0.22	0.13	-0.22	0.02	-0.09	-0.28	-0.01	-0.27	0.00	-0.20	0.21	-0.04	-0.07	-0.35	1.00

Appendix Table A 2. 7: Person correlation for 2013 groundwater samples of Srijangram block.

	Ph	Temp.	EC	ORP	DO	TDS	*As*	Ca^{+2}	Na^{+}	K^{+}	Cl^{-}	Fe	Mn	Mg^{+2}	SO_4^{-2}	HCO_3^{-}	PO_4^{-3}
Ph	1.00																
Temp.	-0.55	1.00															
EC	-0.39	0.45	1.00														
ORP	-0.01	0.18	-0.13	1.00													
DO	-0.02	0.20	-0.08	-0.05	1.00												
TDS	-0.01	0.03	0.23	-0.28	0.05	1.00											
As	0.04	-0.36	-0.12	-0.20	-0.37	-0.38	1.00										
Ca^{+2}	-0.16	0.05	-0.29	-0.04	0.06	-0.10	0.33	1.00									
Na^{+}	-0.08	-0.04	0.05	0.47	-0.26	-0.10	0.15	0.08	1.00								
K^{+}	-0.06	0.22	0.13	0.29	0.00	0.40	-0.17	0.09	0.16	1.00							
Cl^{-}	-0.13	-0.01	0.05	-0.04	-0.23	0.27	-0.03	0.40	0.18	0.13	1.00						
Fe	0.18	-0.32	-0.13	-0.48	-0.17	0.03	**0.69**	0.30	-0.28	-0.02	-0.01	1.00					
Mn	-0.08	0.14	0.07	0.08	-0.20	0.23	**0.05**	0.32	0.05	0.21	0.44	0.01	1.00				
Mg^{+2}	-0.08	-0.23	0.01	0.01	-0.02	0.26	0.07	0.21	0.07	0.28	0.14	0.07	0.37	1.00			
SO_4^{-2}	0.06	-0.22	0.11	-0.27	-0.40	-0.30	**0.54**	-0.12	0.04	-0.34	0.02	**0.46**	-0.12	-0.19	1.00		
HCO_3^{-}	-0.15	0.00	-0.05	0.25	-0.07	0.11	0.19	0.68	**0.57**	**0.46**	0.39	0.01	**0.43**	0.61	-0.21	1.00	
PO_4^{-3}	0.14	-0.10	-0.02	0.12	0.03	0.18	0.06	-0.17	-0.21	0.15	-0.19	0.12	-0.11	**0.44**	-0.06	0.00	1.00

Appendix Table A 2. 8: Person correlation for 2013 groundwater samples of Pub-Mangaldai block.

	pH	Temp.	EC	DO	ORP	Eh	Na^{+}	K^{+}	Ca^{+2}	SO_4^{-2}	Cl^{-}	F	HCO_3^{-}	Pb	Fe	*As*	Mn	Mg^{+2}	TDS	Al	Cr	Cu	PO_4^{-3}
pH	1.00																						
Temp.	-0.01	1.00																					
EC	0.27	-0.32	1.00																				
DO	-0.01	-0.49	0.64	1.00																			
ORP	0.06	0.30	0.09	-0.13	1.00																		
Eh	0.06	0.30	0.09	-0.13	1.00	1.00																	
Na^{+}	-0.05	0.26	-0.37	-0.34	-0.11	-0.11	1.00																
K^{+}	0.29	-0.35	0.60	0.38	-0.27	-0.27	-0.15	1.00															
Ca^{+2}	0.04	0.12	-0.19	-0.14	0.18	0.18	0.42	0.17	1.00														
SO_4^{-2}	-0.02	0.04	-0.10	-0.06	-0.18	-0.18	-0.27	0.11	-0.08	1.00													
Cl	-0.04	0.14	-0.13	0.16	0.03	0.03	-0.13	-0.19	-0.01	-0.13	1.00												
F	0.28	0.27	0.15	-0.20	0.06	0.06	0.27	0.30	0.14	-0.45	-0.05	1.00											
HCO_3^{-}	0.13	-0.09	0.06	0.01	-0.03	-0.03	0.42	0.56	0.85	-0.08	-0.12	0.31	1.00										
Pb	0.01	0.10	-0.13	0.10	-0.21	-0.21	0.22	0.12	0.57	0.07	0.05	0.06	0.54	1.00									
Fe	0.20	-0.16	0.65	0.43	-0.04	-0.04	-0.09	0.62	0.19	0.02	0.01	-0.07	0.37	-0.02	1.00								
As	0.40	-0.34	0.79	0.65	-0.33	-0.33	-0.32	0.65	-0.28	-0.02	0.04	0.08	-0.01	-0.12	**0.65**	1.00							
Mn	0.47	-0.07	0.30	0.29	-0.09	-0.09	0.31	0.21	-0.01	-0.25	-0.21	0.27	0.12	0.04	0.19	**0.41**	1.00						
Mg^{+2}	0.13	-0.41	0.30	0.36	-0.06	-0.06	-0.14	0.54	0.38	-0.02	-0.04	0.07	**0.66**	0.45	0.35	0.12	0.04	1.00					
TDS	0.10	-0.16	0.27	-0.14	-0.27	-0.27	-0.02	0.23	-0.48	0.22	-0.25	0.06	-0.26	-0.31	0.09	0.30	-0.11	-0.32	1.00				
Al	0.11	-0.23	0.32	0.53	-0.20	-0.20	-0.28	0.27	-0.20	0.02	-0.16	0.07	-0.03	0.27	0.03	0.39	0.21	0.39	-0.22	1.00			
Cr	-0.36	0.33	-0.37	0.10	-0.12	-0.12	-0.04	-0.38	-0.15	-0.09	0.77	-0.16	-0.29	0.13	-0.21	-0.14	-0.31	-0.24	-0.20	-0.12	1.00		
Cu	-0.33	0.54	-0.78	-0.61	-0.13	-0.13	0.27	-0.50	-0.04	-0.03	0.32	0.05	-0.22	0.05	-0.55	**-0.57**	-0.47	-0.46	0.04	-0.38	0.67	1.00	
PO_4^{-3}	-0.20	0.33	-0.39	-0.26	0.26	0.26	-0.05	-0.43	0.00	0.43	-0.16	-0.31	-0.24	-0.12	-0.22	**-0.49**	-0.15	-0.28	0.00	-0.41	0.01	0.16	1.00

Appendix Table A 2. 9 : Person correlation for 2013 groundwater samples of Paschim-Mangaldai block

	pH	Temp.	EC	DO	ORP	Eh	Na^{+}	K^{+}	Ca^{+2}	SO_4^{-2}	Cl^{-}	F	HCO_3^{-}	Pb	Fe	*As*	Mn	Mg^{+2}	TDS	Al	Cr	Cu	PO_4^{-3}
pH	1.00																						
Temp.	-0.03	1.00																					
EC	-0.02	-0.75	1.00																				
DO	-0.03	-0.60	0.74	1.00																			
ORP	0.26	-0.58	0.53	0.72	1.00																		
Eh	0.26	-0.58	0.53	0.72	1.00	1.00																	
Na^{+}	0.05	-0.42	0.24	0.27	0.29	0.29	1.00																
K^{+}	0.49	-0.09	0.03	0.05	0.13	0.13	0.13	1.00															
Ca^{+2}	-0.26	0.23	-0.11	0.01	-0.02	-0.02	-0.10	-0.48	1.00														
SO_4^{-2}	-0.03	-0.22	0.36	0.42	0.37	0.37	0.22	-0.17	-0.07	1.00													
Cl^{-}	-0.05	-0.29	0.33	0.18	0.15	0.15	0.04	-0.09	0.03	-0.02	1.00												
F	-0.13	0.22	-0.21	-0.3	-0.37	-0.37	-0.13	-0.30	0.38	-0.13	0.14	1.00											
HCO_3^{-}	0.00	-0.11	0.09	0.15	0.14	0.14	0.58	0.06	**0.60**	-0.07	-0.01	0.16	1.00										
Pb	0.12	-0.07	0.31	0.24	0.14	0.14	0.11	0.15	-0.20	0.35	0.28	-0.25	-0.16	1.00									
Fe	-0.18	-0.10	-0.02	0.08	-0.10	-0.10	0.15	-0.12	0.08	0.10	0.25	0.42	0.05	0.14	1.00								
As	0.04	-0.39	0.41	0.08	-0.06	-0.06	0.11	-0.15	0.14	0.05	0.29	0.11	0.23	0.18	0.03	1.00							
Mn	0.01	0.30	-0.33	-0.48	-0.38	-0.38	0.03	0.15	-0.01	-0.19	-0.19	0.20	0.08	-0.43	-0.10	-0.19	1.00						
Mg^{+2}	0.00	-0.22	0.54	0.47	0.35	0.35	0.10	-0.18	0.13	0.23	0.07	0.00	0.07	0.52	0.13	0.16	**-0.40**	1.00					
TDS	-0.41	0.10	0.24	-0.11	-0.48	-0.48	-0.27	-0.25	-0.01	0.01	0.15	0.17	-0.29	0.29	0.14	0.15	0.03	0.23	1.00				
Al	0.05	-0.05	0.01	0.17	0.17	0.17	-0.05	0.12	-0.22	0.16	-0.12	-0.05	-0.15	0.03	-0.09	-0.16	0.05	-0.09	-0.11	1.00			
Cr	0.10	-0.21	0.13	-0.06	-0.20	-0.20	-0.21	0.09	-0.07	-0.17	0.40	-0.04	-0.18	0.00	-0.04	0.31	0.14	-0.24	0.34	-0.23	1.00		
Cu	-0.22	0.22	-0.18	-0.04	-0.35	-0.35	-0.31	-0.21	0.09	-0.11	0.37	0.08	-0.28	0.14	0.25	-0.05	0.11	-0.06	0.32	-0.24	0.45	1.00	
PO_4^{-3}	0.07	0.24	-0.40	-0.47	-0.19	-0.19	-0.06	-0.03	0.08	-0.39	-0.12	0.33	0.02	-0.20	0.17	-0.22	0.30	-0.25	-0.07	0.00	-0.16	-0.11	1.00

Appendix Table A 2. 10 : Person correlation for 2013 groundwater samples of Sipajhar block

	pH	Temp.	EC	DO	ORP	Eh	Na^{+}	K^{+}	Ca^{+2}	SO_4^{-2}	Cl^{-}	F	HCO_3^{-}	Pb	Fe	*As*	Mn	Mg^{+2}	TDS	Al	Cr	Cu	PO_4^{-3}
pH	1																						
Temp.	0.18	1.00																					
EC	0.47	-0.04	1.00																				
DO	0.34	-0.13	0.54	1.00																			
ORP	-0.02	-0.19	0.44	0.57	1.00																		
Eh	-0.02	-0.19	0.44	0.57	1.00	1.00																	
Na^{+}	-0.40	-0.09	-0.13	0.03	0.15	0.15	1.00																
K^{+}	0.15	-0.61	0.29	0.32	0.42	0.42	0.16	1.00															
Ca^{+2}	-0.32	-0.23	0.14	0.06	0.33	0.33	0.04	-0.02	1.00														
SO_4^{-2}	-0.29	-0.24	-0.35	-0.09	-0.20	-0.20	-0.31	-0.17	-0.19	1.00													
Cl^{-}	-0.03	0.17	0.29	0.32	0.26	0.26	0.47	0.09	-0.06	-0.03	1.00												
F	0.36	-0.34	0.48	0.68	0.46	0.46	-0.36	0.49	-0.13	0.06	-0.05	1.00											
HCO_3^{-}	-0.47	-0.34	-0.16	-0.04	0.25	0.25	0.77	0.32	0.51	-0.23	0.13	-0.31	1.00										
Pb	-0.50	-0.04	0.05	-0.12	-0.23	-0.23	0.08	-0.07	0.27	0.29	0.20	-0.24	0.17	1.00									
Fe	0.26	0.23	0.26	-0.15	-0.25	-0.25	-0.06	-0.34	-0.37	-0.10	0.20	-0.04	-0.40	0.01	1.00								
As	-0.08	0.29	-0.68	-0.58	-0.53	-0.53	-0.07	-0.44	**-0.49**	**0.32**	-0.16	-0.48	-0.25	-0.13	**0.32**	1.00							
Mn	-0.21	0.07	-0.53	-0.52	-0.62	-0.62	-0.05	-0.39	-0.39	0.42	-0.23	-0.42	-0.20	0.19	0.31	**0.51**	1.00						
Mg^{+2}	-0.53	0.10	-0.48	-0.57	-0.39	-0.39	0.17	-0.51	0.08	0.23	-0.01	-0.44	0.16	0.26	0.38	**0.48**	**0.50**	1.00					
TDS	0.27	0.28	-0.46	-0.48	-0.92	-0.92	-0.25	-0.40	-0.44	0.12	-0.33	-0.35	-0.36	-0.08	0.21	0.58	0.58	0.27	1.00				
Al	-0.05	0.09	-0.33	-0.56	-0.23	-0.23	-0.30	-0.37	-0.04	0.12	-0.23	-0.24	-0.30	-0.17	0.17	**0.54**	0.16	0.29	0.30	1.00			
Cr	-0.37	0.05	-0.16	-0.21	-0.18	-0.18	0.21	-0.09	0.10	0.01	0.32	-0.14	0.16	0.13	-0.06	-0.04	-0.02	0.51	0.11	0.00	1.00		
Cu	-0.04	0.08	-0.33	-0.46	-0.25	-0.25	0.26	0.04	0.11	-0.24	0.13	-0.45	0.33	0.02	0.21	0.29	0.30	0.32	0.26	0.17	-0.01	1.00	
PO_4^{-3}	-0.33	0.17	-0.65	-0.60	-0.50	-0.50	0.17	-0.07	-0.54	0.17	-0.18	-0.49	0.00	0.03	0.00	**0.72**	**0.48**	0.28	0.45	0.12	0.13	0.20	1.00

Appendix Table A 2. 11: Person correlation for 2017 groundwater samples of HAsCR

	pH	ORP	Eh	Temp	EC	TDS	*As*	Fe	Mn	Mg^{+2}	Pb	Cr	Cu	HCO_3^-	Na^+	Ca^{+2}	K^+	F	Cl^-	NO_3^-	NO_2^-	PO_4^{-3}	SO_4^{-2}
pH	1.0																						
ORP	-0.5	1.0																					
Eh	-0.5	1.0	1.0																				
Temp	0.0	-0.1	-0.1	1.0																			
EC	0.7	-0.5	-0.5	0.2	1.0																		
TDS	0.7	-0.5	-0.5	0.2	1.0	1.0																	
As	0.2	-0.3	-0.3	0.1	0.2	0.2	1.0																
Fe	0.3	-0.3	-0.3	0.0	0.4	0.4	0.26	1.0															
Mn	0.4	-0.2	-0.2	0.1	0.5	0.5	0.01	0.1	1.0														
Mg^{+2}	0.5	-0.4	-0.4	0.1	0.6	0.6	0.0	0.4	0.3	1.0													
Pb	-0.6	0.5	0.5	-0.1	-0.7	-0.7	-0.1	-0.4	-0.5	-0.4	1.0												
Cr	-0.2	0.0	0.0	0.1	-0.1	-0.1	-0.1	0.0	0.0	0.1	0.1	1.0											
Cu	0.0	0.1	0.1	0.1	0.2	0.2	0.0	0.1	0.2	0.3	-0.2	0.3	1.0										
HCO_3^-	0.5	-0.5	-0.5	0.1	0.6	0.6	0.1	0.4	0.2	0.8	-0.4	0.2	0.2	1.0									
Na^+	0.4	-0.4	-0.4	0.1	0.5	0.5	0.0	0.3	0.3	**0.7**	-0.4	0.3	0.3	**0.9**	1.0								
Ca^{+2}	0.4	-0.5	-0.5	0.2	0.5	0.5	0.1	0.3	0.3	**0.6**	-0.4	0.1	0.1	**0.9**	**0.9**	1.0							
K^+	0.4	-0.3	-0.3	0.1	0.5	0.5	0.1	0.3	0.2	0.8	-0.3	0.2	0.3	**0.9**	**0.9**	**0.7**	1.0						
F^-	-0.2	0.1	0.1	0.1	0.0	0.0	0.1	-0.1	-0.1	0.0	0.1	0.1	0.2	-0.1	0.0	-0.1	0.0	1.0					
Cl^-	0.1	0.0	0.0	0.1	0.3	0.3	-0.1	0.0	0.1	0.1	-0.2	0.0	0.2	0.0	0.1	0.2	0.0	0.0	1.0				
NO_3^-	0.0	-0.1	-0.1	0.0	-0.1	-0.1	-0.1	-0.1	-0.1	-0.1	-0.1	-0.2	-0.1	-0.1	-0.1	-0.1	-0.1	0.0	-0.2	1.0			
NO_2^-	0.1	-0.1	-0.1	0.0	0.0	0.0	0.0	0.1	0.0	0.1	0.1	0.1	0.1	0.1	0.0	0.1	0.0	0.0	0.1	0.0	1.0		
PO_4^{-3}	0.2	0.0	0.0	-0.1	0.1	0.1	0.1	-0.1	0.0	0.1	-0.2	-0.4	0.0	0.0	0.0	-0.1	0.1	0.0	-0.2	0.1	-0.2	1.0	
SO_4^{-2}	0.1	-0.1	-0.1	0.1	0.3	0.3	0.0	-0.1	0.1	0.1	-0.1	-0.1	0.0	0.2	0.3	0.4	0.1	0.0	**0.5**	-0.1	0.0	-0.1	1.0

Appendix Table A 2. 12 : Person correlation for 2017 groundwater samples of L*As*CR

	pH	EC	ORP	Eh	Temp.	TDS	Ca^{+2}	Na^{+}	K^{+}	HCO_3^{-}	*As*	Fe	Mn	F	Cl^{-}	SO_4^{-2}	NO_3^{-}	NO_2^{-}	PO_4^{-3}	Cu	Pb	Mg^{+2}	Cr
pH	1.0																						
EC	0.1	1.0																					
ORP	0.0	0.0	1.0																				
Eh	0.0	0.0	1.0	1.0																			
Temp.	-0.1	0.3	0.0	0.0	1.0																		
TDS	0.1	1.0	0.0	0.0	0.3	1.0																	
Ca^{+2}	-0.3	-0.1	0.2	0.2	-0.2	-0.1	1.0																
Na^{+}	0.1	0.1	0.2	0.2	0.0	0.1	0.1	1.0															
K^{+}	-0.2	0.4	0.0	0.0	0.4	0.4	0.0	0.2	1.0														
HCO_3^{-}	-0.2	0.0	0.2	0.2	-0.2	0.0	1.0	0.2	0.1	1.0													
As	-0.1	-0.1	0.1	0.1	-0.2	-0.1	0.3	0.1	-0.2	0.2	1.0												
Fe	-0.3	-0.2	-0.2	-0.2	0.1	-0.2	0.4	-0.2	-0.1	0.4	0.28	1.0											
Mn	0.1	0.1	0.0	0.0	0.2	0.1	-0.1	-0.1	0.1	-0.1	-0.2	0.1	1.0										
F	-0.2	0.0	0.0	0.0	0.1	0.0	0.1	0.0	0.1	0.1	0.0	0.0	0.0	1.0									
Cl^{-}	-0.3	-0.1	0.1	0.1	0.0	-0.1	0.1	-0.2	0.0	0.1	-0.1	0.2	0.0	0.1	1.0								
SO_4^{-2}	0.0	-0.1	0.1	0.1	0.0	-0.1	0.0	0.0	0.1	0.0	-0.1	0.0	0.1	0.0	0.0	1.0							
NO_3^{-}	0.3	0.1	0.1	0.1	0.0	0.1	-0.1	0.2	0.0	-0.1	-0.3	-0.2	-0.2	0.0	-0.2	0.2	1.0						
NO_2^{-}	0.3	0.0	0.0	0.0	0.0	0.0	-0.2	-0.1	0.1	-0.2	-0.1	-0.1	0.1	0.0	-0.2	0.1	0.0	1.0					
PO_4^{-3}	0.0	0.0	0.1	0.1	0.0	0.0	-0.1	0.1	-0.1	0.0	0.1	0.0	0.0	0.3	-0.1	-0.1	0.0	0.2	1.0				
Cu	-0.1	0.0	0.3	0.3	-0.4	0.0	0.3	0.4	0.0	0.4	0.1	-0.1	-0.4	0.1	0.0	0.1	0.2	-0.2	0.1	1.0			
Pb	0.0	-0.1	0.1	0.1	-0.1	-0.1	-0.1	0.0	-0.1	-0.2	0.1	-0.2	-0.1	-0.1	0.1	0.0	0.3	-0.1	0.0	0.1	1.0		
Mg^{+2}	-0.1	**0.5**	0.1	0.1	0.1	**0.5**	0.1	0.4	**0.5**	0.3	-0.1	-0.2	-0.2	0.2	-0.1	-0.1	0.3	0.1	0.0	0.3	0.0	1.0	
Cr	-0.3	-0.2	0.3	0.3	-0.4	-0.2	**0.5**	0.3	0.0	**0.5**	0.3	0.1	-0.4	0.0	0.2	0.0	-0.1	-0.3	0.1	**0.8**	0.1	0.2	1.0

Appendix B1

Appendix Table B 1. 1 shows results of total organic carbon (TOC) analysis for selective depth aquifer sediments

Sr. no.	Sample ID	Sediment color / texture	TOC (%)
1	B1-25	Brown/Fine sand	3.58
2	B1-65	Orange/Coarse & Medium sand	2.68
3	B2-25	Yellowish/Fine sand	2.74
4	B2-55	Yellow orange/Coarse Sand	0.56
5	B3-25	Yellowish/Fine sand	4.96
6	B3-55	Yellow orange/Coarse Sand	0.7
7	B4-25	Yellow orange/Coarse Sand	2.31
8	B4-55	Yellow orange/Medium Sand	1.59
9	B5-25	Yellow orange/Fine sand	2.07
10	B5-55	Yellowish/Coarse Sand	0.35
11	B6-45	Gray/Fine sand	3.61
12	B6-85	Gray/Medium Sand	6.04
13	B7-35	Gray/Fine sand	2.76
14	B8-35	Gray/Medium sand	3.23
15	B8-85	Gray/Medium Sand	1.95
16	B9-45	Gray/Medium Sand	2.7
17	B9-85	Gray/Medium Sand	3.9
18	B10-45	Gray/Fine sand	4.15
19	B10-105	Light Yellow/Coarse sand with Granuel	1.13
20	B10-165	Yellow Gray/Medium sand	0.25
21	B10-225	light olive/Medium sand	0.23
22	B10-285	Yellow Gray/Fine sand	0.22
23	B10-305	Light Yellow/Coarse sand with Granuel	0.17

24	D1-85	White Medium sand	2.82
25	D1-185	Deep grey midium sand	4.56
26	D2-110	Blackish grey Midium sand	2.52
27	D2-180	Grey medium sand	4.21
28	D3-65	Dark grey fine sand	4.83
29	D3-85	Grey Coarse sand	2.76
30	D4-55	Dark grey midium sand	2.44
31	D4-75	Dark grey midium sand	3.65

Appendix B2

Appendix Table B 2. 1 results of soluble and bound cation exchange capacity and Cation Exchange Capacity of H*As*CR fine grained soils samples

Sample ID	Soluble Cations (cmol/kg)				Bound Cations (cmol/kg)				Cation Exchange Capacity (cmol/g)
	Na	Ca	K	Mg	Na	Ca	K	Mg	
B1-10'	10.0	15.3	2.2	1.1	151.2	327.7	41.5	65.5	34.0
B1-20'	3.4	6.4	0.8	3.1	138.3	261.3	48.9	53.1	31.8
B1-30'	5.5	9.9	2.3	2.1	142.0	289.3	63.4	48.7	42.1
B2-10'	17.5	23.2	5.8	8.2	160.4	415.2	53.2	50.7	18.7
B2-20'	13.2	21.9	3.4	8.6	151.9	341.0	48.2	69.0	10.8
B2-30'	11.3	17.7	2.2	3.8	132.9	290.3	38.9	59.1	8.4
B2-40'	13.7	17.0	3.6	6.1	121.9	260.4	35.5	43.3	11.3
B2-50'	11.3	15.5	5.6	7.0	122.7	223.0	35.2	65.7	27.8
B2-60'	9.0	23.3	2.2	1.9	100.1	279.4	26.1	37.9	34.3
B2-70'	5.6	18.6	2.0	3.7	95.2	331.4	22.1	34.5	25.6
B2-80'	4.9	9.2	2.6	6.2	75.6	289.5	17.1	30.1	36.6
B2-90'	6.0	20.2	1.5	1.9	65.5	197.6	18.8	26.6	42.5
B2-100'	6.5	14.5	2.1	2.4	72.2	166.8	20.2	36.5	44.6
B3-10'	5.6	15.5	2.1	4.3	151.6	380.8	42.3	69.9	21.3
B3-20'	9.2	23.2	3.4	3.5	131.8	358.8	51.2	66.0	24.2
B3-30'	10.8	5.9	5.5	1.5	109.2	276.0	34.6	50.3	35.4
B3-45'	5.9	10.8	1.6	6.2	130.2	297.0	37.9	67.1	30.1
B3-50'	4.9	13.5	2.7	1.2	92.0	234.8	21.2	30.5	44.4
B3-60'	4.8	8.3	2.2	12.6	69.9	167.7	18.8	22.8	29.8
B3-70'	5.1	11.4	1.4	7.3	95.9	184.9	25.8	33.9	25.3
B3-80'	5.8	16.4	2.1	4.9	102.8	205.0	27.6	18.7	35.9
B3-90'	5.0	12.4	1.8	1.2	67.3	160.3	18.8	29.4	39.8

B3-100'	5.9	17.7	2.0	3.3	73.1	173.8	17.3	25.2	53.7
B4-10'	3.0	6.6	0.6	0.9	257.0	441.9	49.0	66.6	54.0
B4-20'	5.8	19.8	2.3	2.7	142.9	392.3	37.1	56.0	43.4
B4-30'	3.2	9.1	0.9	1.5	124.8	341.2	30.5	38.5	33.4
B4-40'	3.4	10.3	0.5	0.5	111.0	331.5	28.4	33.8	36.5
B4-50'	6.6	20.8	0.8	0.8	88.7	293.3	26.9	26.9	28.7
B4-60'	11.4	22.3	1.3	2.4	96.9	226.8	21.9	30.5	33.8
B5-10'	5.6	24.8	2.6	3.2	144.1	409.2	42.5	72.5	59.9
B5-20'	2.3	6.5	1.0	1.8	129.9	372.4	39.3	52.5	58.1
B5-30'	4.9	7.3	1.2	0.4	113.0	376.1	39.7	51.7	38.6
B5-40'	4.7	16.1	0.1	2.0	90.4	306.6	25.7	34.3	44.8
B5-50'	2.6	9.0	1.0	1.7	70.6	210.4	20.9	36.5	37.0
B5-55'	3.2	5.6	1.2	3.2	65.4	196.9	16.6	32.1	28.8
B6-10	9.0	21.5	4.3	1.4	173.8	405.6	54.7	24.8	57.3
B6-20	7.8	15.4	1.8	0.3	139.7	308.8	43.3	68.7	47.7
B6-30	7.6	19.2	4.8	1.6	84.8	267.4	25.0	38.3	44.1
B6-40	4.5	7.7	1.1	3.4	110.3	259.9	28.1	27.8	36.3
B6-50	3.1	11.4	0.6	2.9	70.6	165.3	18.7	22.6	30.9
B6-55	7.0	10.5	1.4	1.5	67.0	157.0	22.5	29.5	36.7
B7-10	8.6	19.3	1.8	3.2	166.6	378.5	40.0	73.9	60.2
B7-20	6.1	9.0	2.5	1.6	94.5	287.6	25.2	39.5	38.2
B7-30	5.1	12.8	0.8	1.1	83.8	241.7	21.3	26.0	44.5
B7-40	5.6	10.3	0.4	0.6	67.0	174.5	17.1	20.3	32.3
B7-50	3.4	6.3	1.3	1.8	57.0	156.4	11.7	16.0	46.0
B7-60	2.9	6.2	1.4	0.8	61.8	143.4	20.2	38.2	52.2
B8-10	9.2	62.1	2.5	0.7	293.0	450.5	46.8	59.7	56.8
B8-20	6.7	42.9	2.0	1.9	169.5	382.4	42.2	74.1	37.3
B8-30	6.4	15.1	1.8	2.1	106.3	312.4	24.4	28.6	36.0

B8-40	6.1	12.5	1.7	1.6	83.2	260.2	21.1	27.4	30.4
B8-50	5.5	9.7	1.5	0.2	75.6	236.9	18.6	19.2	25.2
B8-60	2.5	6.4	0.6	3.5	85.5	225.9	20.3	26.8	33.8
B9-10'	9.2	21.8	4.2	3.1	149.8	427.3	44.4	48.1	31.9
B9-20'	25.1	12.7	5.0	1.8	114.4	351.8	28.7	38.2	37.8
B9-30'	16.4	21.6	4.0	2.4	97.6	291.5	25.2	33.8	27.2
B9-45'	13.5	8.9	1.9	2.1	141.4	255.7	39.1	54.2	24.9
B9-50'	15.3	8.8	3.1	3.8	84.5	276.2	21.3	27.5	22.3
B9-60'	8.9	16.9	3.0	2.5	77.7	192.9	17.9	22.6	14.1
B9-70'	5.8	7.1	0.9	1.8	54.5	160.8	13.6	15.4	11.4
B9-80'	7.7	6.7	3.4	3.4	69.3	174.2	16.6	18.9	16.7
B9-90'	8.6	23.3	3.3	3.8	51.2	146.4	12.2	15.6	14.0
B9-100'	9.8	9.4	2.1	1.7	38.1	118.9	8.7	11.4	22.7
B10-20'	3.2	6.2	0.8	1.2	125.6	279.3	34.4	29.7	35.6
B10-40’	5.7	10.3	1.6	1.5	93.5	246.6	23.6	15.7	29.4
B10-60’	2.5	4.4	0.8	1.1	86.5	259.0	21.4	27.8	22.3
B10-80’	2.0	3.3	0.5	0.8	61.6	224.4	19.4	23.1	37.7
B10-100’	2.0	4.2	0.6	1.1	56.4	201.1	12.9	15.6	43.6
B10-120’	1.7	3.7	0.5	0.6	45.7	112.1	11.2	18.6	17.5
B10-140’	1.5	2.9	0.5	0.5	94.1	226.6	22.4	26.3	31.0
B10-160’	2.1	4.5	0.6	1.0	79.4	193.0	17.9	17.0	25.7
B10-180’	2.6	5.3	1.0	1.5	65.9	163.6	18.9	23.2	14.4
B10-200’	2.2	5.0	0.5	0.7	87.4	226.6	21.5	27.2	22.5
B10-220’	3.3	7.3	0.8	1.0	95.2	251.3	27.9	34.1	33.6
B10-240’	5.0	10.0	1.6	2.2	124.9	286.9	32.3	51.4	43.8
B10-260’	3.4	7.7	1.1	1.8	128.4	314.7	29.9	37.8	40.8
B10-280’	2.8	6.1	0.8	1.3	110.9	294.6	28.3	47.0	51.1
B10-300’	3.0	5.2	1.1	1.6	90.4	254.9	21.1	28.2	13.5

Appendix Table B 2. 2 results of soluble and bound cation exchange capacity and cation exchange capacity of L*As*CR fine grained soils

Sample ID	Soluble Cations (cmol/kg)				Bound Cations (cmol/kg)				Cation Exchange Capacity (cmol/g)
	Na	Ca	K	Mg	Na	Ca	K	Mg	
D1-10'	7.3	12.4	2.0	1.4	79.7	469.8	18.0	14.9	64.7
D1-20'	4.4	9.5	1.8	2	93.3	499.6	20.2	22.3	52.5
D1-30'	4.4	7.3	2.8	2.7	59	389.2	13.1	13.1	44.4
D1-40'	3.9	7.2	0.7	1.2	86.1	555.4	19.7	13.6	62.3
D1-50'	4.4	7.7	0.9	1.5	44.9	400.0	11.5	10.9	44.4
D1-60'	2.9	8.9	0.9	0.7	53.1	499.5	9.0	12.4	67.3
D1-70'	7.8	11.0	2.0	4.5	64.1	516.3	17.3	25.6	56.6
D1-80'	3.2	7.7	1.2	1.8	42.3	353.4	7.2	10.8	35
D1-90'	3.4	8.1	1.2	2.4	40	253.2	10.9	12.1	27.6
D1-100'	6.9	9.7	2.8	3.7	41.1	268.4	8.3	13.6	29.3
D1-110'	6.2	11.4	2.4	1.9	60	490.6	6.1	6.8	70.3
D1-120'	7.8	9.5	2.9	2.2	94.7	525.5	13.9	14.7	58.3
D1-130'	2.0	3.9	0.6	0.8	69.2	478.8	15.4	13.2	50.8
D1-140'	7.6	11.7	1.8	3.2	55.8	535.6	8.5	12.7	63.4
D1-150'	2.8	6.5	1.3	1.9	52.5	517.7	9.9	14.5	56.5
D1-165'	6.9	9	2	2.4	49.4	262.4	8.1	7.9	46.4
D1-170'	5.7	12.4	2.6	2.9	56.6	289.6	9.3	8.1	41.2
D1-180'	5.1	13.8	2	2.7	27.8	216.7	4.7	5	52.7
D2-10'	5.4	10.2	1.7	2.1	88.3	565.8	4.7	4.3	63.4
D2-20'	3.5	9	0.9	1.2	103.2	595.0	5.3	4.7	67.1
D2-30'	5.9	14.6	2.1	2.6	112.7	618.6	5.9	5	65.3
D2-40'	5.0	11.9	1.6	3.2	91.1	606.5	5.4	4.9	70.7
D2-50'	10.0	16.6	2.2	2.7	69.9	517.7	3.7	3.4	57.3
D2-60'	5.7	14.5	1.7	2.4	80.2	648.6	7.5	6.4	60.8
D2-70'	4.5	11.6	1.0	1.6	68.4	504.7	2.9	1.7	47.4
D2-80'	3.8	9.4	1.1	1.5	61.5	600.2	5.3	4.5	70.1
D2-90'	3.5	7.6	0.7	1.3	53.1	527.9	3.4	2.5	45.6

D2-100'	6.1	8.8	2.3	2.5	69.2	605.9	5.2	4.5	60.9
D2-110'	3.5	9.9	1.0	1.5	63.3	525.5	2.9	1.6	44.0
D2-130'	4.5	13.1	1.1	1.4	61.3	560.2	4.9	3.9	54.8
D2-140'	3.5	9.6	0.7	1.0	65.4	481.2	2.3	1.4	73.4
D2-150'	3.9	8.0	0.5	0.8	56.5	326.0	2.2	1.3	39.1
D2-160'	6.1	12.6	1.7	2.5	44.5	301.7	1.7	1.3	31.0
D2-170'	3.6	10.2	0.7	1.4	39.2	272.6	1.6	1.1	25.3
D2-180'	3.6	5.9	0.6	0.8	34.1	242.6	1.4	0.6	27.9
D3-10'	4.7	14.2	1.0	1.1	71.0	538.3	24.9	12.4	53.9
D3-20'	5.9	16.3	3.3	2.2	65.8	521.6	22.2	10.9	67.9
D3-30'	6.5	11.5	2.9	2.9	85.9	568.6	28.7	19.4	64.7
D3-40'	5.7	16.7	2.8	4.0	80.4	547.9	25.9	14.7	59.4
D3-50'	3.9	12.0	1.5	1.7	76.2	523.0	19.1	9.5	68.3
D3-60'	6.0	20.0	2.0	3.0	82.8	507.9	24.3	10.7	48.3
D3-70'	3.6	7.7	1.4	1.5	85.0	516.9	23.6	12.2	32.4
D3-80'	4.4	10.8	1.1	1.1	68.8	485.1	20.6	10.1	30.2
D3-90'	6.6	10.2	2.4	1.2	62.9	470.7	18.6	9.1	27.6
D4-10'	3.5	9.8	1.9	2.8	63.9	556.3	6.3	4.2	53.9
D4-20'	4.8	9.3	1.3	1.9	49.4	517.7	4.5	2.7	59.4
D4-30'	7.0	15.8	3.8	3.2	87.3	613.8	7.9	6.4	57.4
D4-50'	2.9	8.1	1.6	2.0	57.1	580.7	6.7	5.3	67.3
D4-60'	4.7	9.9	2.7	1.2	69.2	555.7	4.9	4.0	34.5
D4-70'	7.0	20.7	3.1	3.8	44.6	568.9	7.4	5.8	54.8
D-4-80'	4.1	6.2	1.4	1.6	44.1	471.3	4.2	2.1	42.4
D4-90'	3.0	8.2	1.9	2.5	0.0	452.6	3.6	1.3	32.2

Appendix B3

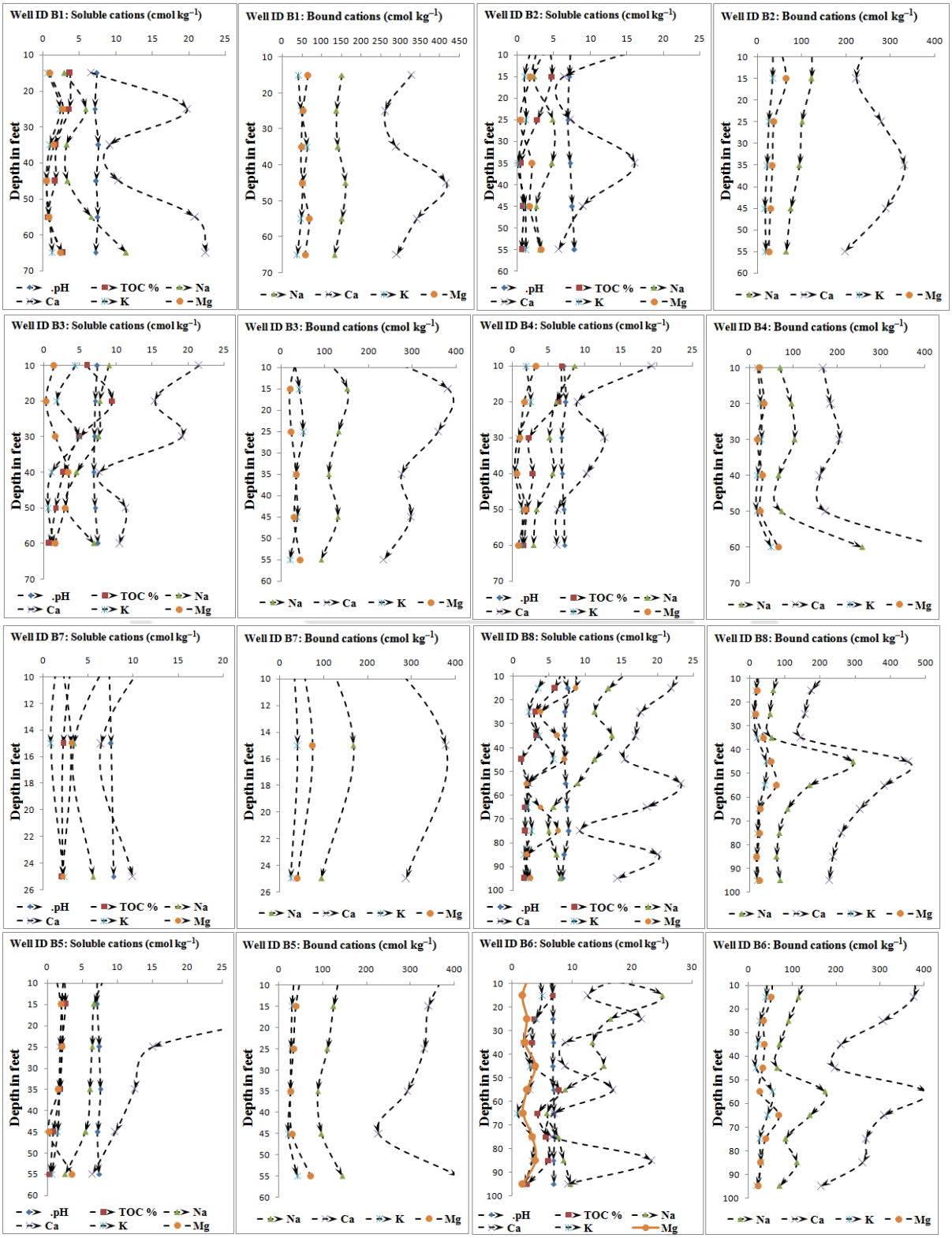

Appendix Figure B 3. 1 : Depth wise variation of bound and soluble cation exchange capacity obtained for H*As*CR sediment samples.

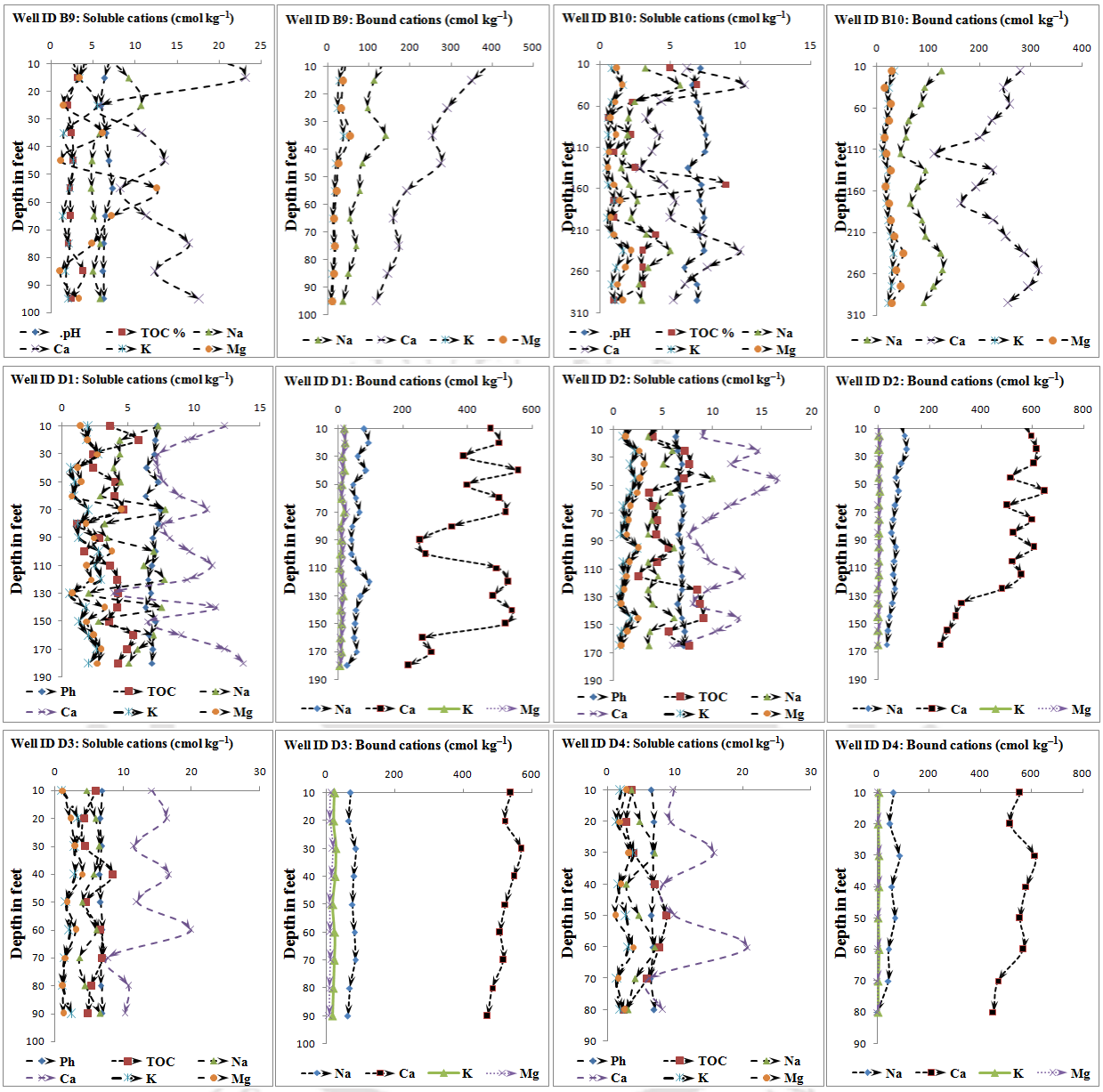

Appendix Figure B 3. 2: Depth wise variation of bound and soluble cation exchange capacity obtained for H*As*CR and L*As*CR sediment samples.

Appendix C 1

Appendix Table C 1. 1Shows total elements extraction from H*As*CR sediments

Sample ID	*As*	Fe	Mn	Mg	Cr	Cu	Zn	Pb	Ni	Al
	$\mu g g^{-1}$									
B1- 5'	6.5	534.1	624.5	217.7	53.0	63.0	130.8	248.4	178.9	9248.2
B1-10'	6.4	527.6	524.5	165.3	608.5	46.9	305.7	209.0	160.8	10464.1
B1-15'	5.8	730.8	724.9	202.5	495.0	58.5	256.9	164.7	150.5	7640.9
B1- 20'	5.7	687.4	585.0	140.5	523.4	49.2	298.6	169.2	140.7	6071.3
B1- 25'	5.4	644.9	621.6	206.6	405.1	53.1	206.5	144.6	138.7	5653.7
B1-30'	5.7	728.0	659.9	219.8	767.1	41.9	175.2	130.9	112.7	7690.1
B1-35'	5.8	764.8	706.6	261.5	627.3	48.5	248.7	166.4	99.6	7314.5
B2-5'	5.9	578.0	492.6	251.0	453.6	64.9	350.5	282.4	269.5	8043.6
B2-15'	4.4	618.4	586.1	205.4	507.9	66.3	185.4	248.8	202.0	9307.9
B2-25'	5.1	724.8	461.9	192.5	648.2	53.6	138.5	214.3	215.5	11265.9
B2-35'	5.0	672.5	619.4	214.5	527.3	71.2	191.4	206.7	224.4	8598.8
B2-45'	4.9	441.7	406.5	184.7	529.1	74.6	152.9	189.3	205.9	6662.0
B2-55'	5.3	620.2	751.8	202.5	690.6	61.3	184.9	168.4	250.5	6625.3
B2-65'	5.0	744.9	529.7	294.6	527.6	50.5	206.5	191.3	165.0	10085.2
B2-75'	5.8	864.8	738.5	237.7	404.7	56.5	240.9	226.0	187.3	10480.7
B2-85'	6.9	518.1	442.1	251.5	526.8	69.4	170.9	168.1	170.5	6186.4
B2-95'	6.6	678.0	493.8	218.5	791.9	49.9	126.9	206.1	164.3	6931.1
B3-5'	6.1	747.2	617.2	273.8	599.5	44.9	284.2	276.1	170.6	10578.7
B3-15'	4.3	624.4	530.3	175.2	527.1	57.2	207.0	214.9	137.7	9266.5
B3-25'	3.7	791.5	618.5	163.2	473.7	63.8	181.6	224.4	138.7	10449.2
B3-35'	3.5	747.6	573.0	154.5	413.7	70.6	127.6	164.5	80.7	9292.7
B3-45'	4.2	668.6	529.8	184.8	570.1	63.9	248.3	189.1	106.1	11444.9
B3-55'	1.7	794.4	498.5	143.0	510.7	46.0	167.1	130.1	99.0	7740.2
B3-65'	4.6	424.7	489.8	254.0	492.7	44.1	131.4	125.4	84.2	7500.6
B3-75'	3.8	749.7	485.5	285.5	647.8	55.9	207.7	102.0	131.4	8924.9
B3-85'	3.5	716.6	618.5	317.9	492.7	49.6	165.4	187.3	124.6	9686.5

B3-95'	3.7	656.4	665.3	257.9	701.8	52.8	248.6	127.7	144.0	12892.6
B4-5'	3.2	842.3	485.3	145.2	568.5	48.2	213.6	341.2	128.1	10536.8
B4-15'	3.0	902.8	538.7	86.6	690.3	60.9	218.7	245.5	81.7	9742.6
B4-25'	3.4	523.3	485.4	186.3	525.8	49.6	254.9	215.2	104.5	8526.5
B4-35'	1.5	699.6	649.4	240.6	403.9	58.7	221.4	139.8	128.2	10554.8
B4-45'	2.6	678.1	509.8	254.2	738.2	41.7	255.5	154.7	119.1	8125.8
B4-55'	2.3	1100.6	421.7	300.5	440.3	46.7	345.0	171.8	125.0	8548.8
B4-65'	2.4	1136.4	661.2	281.9	784.8	53.0	227.2	165.1	138.5	6539.0
B5-5'	3.4	920.5	570.2	357.6	489.9	65.7	108.5	345.2	137.0	9391.2
B5-15'	3.5	422.5	697.3	200.5	762.6	62.0	324.4	300.6	159.8	10984.8
B5-25'	3.0	798.8	529.9	187.5	571.2	64.2	288.6	319.6	148.7	8126.5
B5-35'	2.5	731.9	629.1	258.5	753.3	47.4	92.4	208.6	91.9	7945.8
B5-45'	2.9	467.7	421.7	206.5	404.6	62.1	166.5	164.3	131.5	10985.3
B5-55'	3.1	532.5	661.3	275.3	495.0	53.6	125.3	129.8	118.9	7584.9
B6-5'	3.3	840.5	753.7	333.7	473.9	70.1	286.2	258.6	124.1	8947.3
B6-15'	3.7	850.6	625.7	286.2	786.4	67.3	331.3	184.8	124.6	9404.5
B6-25'	3.0	457.1	455.4	224.5	569.6	64.9	213.4	205.6	130.6	6792.7
B6-35'	4.4	845.3	551.8	138.8	518.2	54.4	210.5	271.3	127.6	4616.9
B6-45'	3.3	1078.5	586.2	226.6	406.2	50.3	126.3	164.3	143.8	7231.7
B6-55'	3.3	887.8	541.9	170.5	882.6	51.7	164.1	185.3	88.5	6582.1
B7-5'	3.2	460.2	666.4	275.7	861.7	64.5	288.9	212.4	98.2	9206.2
B7-15'	3.2	496.8	697.3	298.5	728.2	71.1	271.3	304.3	86.7	8816.5
B7-25'	2.4	628.9	665.7	358.5	658.9	52.1	128.5	216.6	80.5	14686.5
B7-35'	2.9	531.3	591.8	265.5	549.9	74.5	185.2	255.4	139.0	8047.7
B7-45'	1.4	887.5	578.5	217.3	880.6	68.4	126.5	200.9	105.9	12068.0
B7-55'	5.0	882.1	745.8	210.6	850.6	40.6	254.3	166.9	103.8	8882.1
B8-5'	4.7	609.3	526.5	350.5	887.3	49.3	260.9	254.5	127.6	11045.7
B8-15'	4.7	451.0	395.9	267.9	682.5	50.4	288.4	286.4	136.9	12418.6
B8-25'	4.8	619.0	509.9	211.7	728.5	48.5	251.8	208.5	130.6	10033.6
B8-35'	4.9	791.3	545.2	186.1	742.6	66.2	204.6	187.2	85.4	8424.5
B8-45'	5.2	634.9	460.9	225.0	649.9	51.5	269.7	208.1	147.3	6469.6
B8-55'	5.5	460.1	586.1	255.7	866	56.7	241	204.4	86.6	9251.2

B9-5'	2.5	931.1	601.8	273.6	573.8	72.4	324.1	292.5	155.7	112539
B9-15'	4.6	1019.7	652.4	206	664.7	57.7	237.6	170.6	90.7	14676.1
B9-25'	4.6	783.2	621.7	186.9	723	75.2	167	124.0	125.1	10511.3
B9-35'	4.8	435.0	449.4	155.7	485.6	64.5	129.5	145.0	98.3	14047.4
B9-45'	5.1	486.6	429.9	167.3	649.3	52.4	205.1	172.4	127.9	10565.1
B9-55'	5.1	621.4	442.3	144.9	810.5	66.5	172.1	211.6	90.7	5029.6
B9-65'	4.5	686.5	423.2	211.9	728.4	77.9	208.5	186.6	136.4	9073.7
B9-75'	4.7	731.6	482.6	192.6	808.9	65.0	246.5	206.9	84.8	9362.5
B9-85'	4.3	492.7	391.5	206.5	824.4	59.3	295.3	235.0	120.7	8670.8
B9-95'	4.9	409.4	345.9	148.7	883.8	64.5	208.7	244.6	142.8	12855.2
B10-10'	0.3	81.3	645	261.4	738.7	48.7	144.9	245.3	156	10456.8
B10-20'	0.9	7.7	524.1	202.5	421.8	70.2	105.7	221.7	142	6186.5
B10-30'	1.2	43	501.8	227.7	500.4	56.5	168.7	167	128.2	4613
B10-40'	0.1	39.4	569.7	259.4	820.5	52.9	144.4	326	112.9	9748
B10-50'	2.7	40.4	646.3	200.5	840.6	59.6	301.7	203	121.8	10188.5
B10-60'	2.8	98.5	454	273.5	728.4	50.7	131.8	182.5	104.6	5825.5
B10-70'	0.5	74	507	239.4	656.4	52.9	244.6	205.8	121.8	8748.5
B10-80'	0.3	72.1	661.7	295.7	489.6	56.7	225.2	192.5	147.3	7390
B10-90'	3.3	69.5	500.3	210.6	521.9	49.4	245.7	171.6	164.8	5671.3
B10-100'	4.7	45.7	584.1	253.7	496.5	50.7	185.9	259.5	195.5	6839.4
B10-110'	3.1	36.8	653.7	221.1	804.5	48.6	202.5	182.5	157.2	4986.1
B10-120'	3	12	569.4	166.5	496.3	46	205.4	209.8	95.8	8656.1
B10-130'	1.1	8.5	724.1	128.6	410.1	40.5	260.4	246.2	128.1	9675.1
B10-140'	4.2	28.2	646.2	237.7	813.1	17.3	168.6	135.5	144.5	11309.2
B10-150'	2.7	35.1	821.3	201.5	492.5	13.4	208.4	170.3	101.6	6595
B10-160'	3.8	75	794.6	183.7	456.3	22.9	212.1	144.7	88.7	10004.8
B10-170'	3.7	69.8	740.7	145.7	747.1	18.1	182.5	166.5	145.2	7285.4
B10-180'	bdl	64.1	672.3	210.5	496.1	35	246.5	205	133.8	8212.6
B10-190'	0.8	33	618.6	225.4	568.4	58.6	249.1	275	108.7	10166.7
B10-200'	4.1	43.1	654.9	185.0	545.1	71.4	212.1	280.4	93.3	9256.9
B10-210'	0.4	52.6	642.2	200.8	729.4	67.0	235.3	204.5	127.3	8153.8
B10-220'	3.4	29.3	612.2	168.6	680.9	54.6	173.4	252.5	122.3	7613.3

B10-230’	0.3	28.4	693.5	148.4	651.4	41.0	130.5	233.4	127.0	6737.2
B10-240’	3.1	43.5	652.4	162.7	685.1	74.6	166.3	173.5	144.2	10095.1
B10-250’	2.3	27.2	770.5	146.3	708.9	57.8	160.9	160.8	129.4	9287.0
B10-260’	2.6	21.5	841.9	120.9	610.9	45.2	147.5	145.0	127.0	8655.4
B10-270’	2.1	47.7	855.8	101.9	586.8	71.4	125.0	153.3	124.3	7826.9
B10-280’	3.1	56.3	702.0	149.8	630.9	72.7	164.0	224.8	118.1	4544.9
B10-290’	1.4	91.4	613.1	165.2	693.2	43.2	130.5	168.5	87.8	8528.6
B10-300’	2.9	77.9	662.1	122.5	619.2	34.1	166.3	244.6	102.9	8145.1
B10-310’	2.2	82.6	739.0	86.6	669.7	35.5	204.1	201.0	88.5	8121.1

Appendix Table C 1. 2 Shows total elements extraction from L*As*CR sediments

Sample ID	*As*	Fe	Mn	Mg	Cr	Cu	Zn	Pb	Ni	Al
	μg g^{-1}									
D1-10’	13.1	538.5	484.1	851	452.1	173	330.5	145.3	92.6	7525.7
D1-20’	43.1	1008.2	492.2	938.5	536.3	94.6	225.4	120.8	62.5	5409.4
D1-50’	18.7	502.5	449.7	627.5	136.7	87.1	217	164.2	75	5851
D1-75’	10.8	391	452.1	748.7	180.6	51.1	339.3	152.5	87.7	6124.5
D1-90’	7.7	407	496.3	734.8	104.8	82	252.6	208.5	96.4	5047
D1-105’	26.3	1016.2	716.1	593	296.7	104.7	300.7	240.6	144.6	6495.8
D1-125’	18.4	634.6	656	1195	389.2	85.8	358.7	236.7	130	6109.5
D1-145’	2	420	568.3	614.7	481.3	56.6	224.2	170.8	104.8	7808.5
D1-170’	8	623.7	535.1	570.4	149.6	41.1	251.9	153	84.7	6495.1
D1-185’	8.6	632.1	590.6	606	130.4	36.5	336.7	178.4	109.8	6995.3
D2-20’	48.7	571.4	498.2	575.1	144.5	76.1	307.5	216.3	145	8550.5
D2-35’	39.5	453.7	477.2	496.9	135.1	32.2	205.9	228.4	169.7	6898.8
D2-55’	63.2	589.5	653.8	930.5	164.3	70.6	174.7	262	260.5	5645.4
D2-65’	19.2	522.3	443.3	442.6	104.7	67.3	241	208.3	173	8426.1
D2-95’	15.2	556.3	588	849.5	204.6	56.1	286.3	238.5	212.2	10444.5
D3-10’	1	624.5	511.7	498.8	449.7	76.5	344	255	214.1	8052.8
D3-30’	4.4	637	584.1	562.4	705.8	64.4	299.7	219.8	192.5	10668.9
D3-60’	62	657.6	616.8	1058.6	585	33.4	174.8	241.1	235.1	9446.1
D3-70’	10.4	637.6	964.8	675.7	655.4	52.4	258.2	228.6	208.1	11504.5
D3-85’	17	670.1	494.8	805.5	328.6	34.7	230	204.5	168.7	9853
D4-20’	0.2	566.5	497.6	931.6	695.2	63	338.5	276.5	222.5	7406.9
D4-40’	0.2	531.8	748.9	1084.1	790	65.3	364	241.4	238.8	5845.6
D4-55’	9	645.4	716.8	590.5	433.1	48.5	174.1	184.4	212.5	9891.9
D4-75’	7.8	607.7	780.6	773	609.2	38.8	96.3	160.8	201	11853.7
D4-90’	20.6	625.4	713.5	925.2	510	32.5	142.6	146.8	188.4	8212.5

Appendix C2

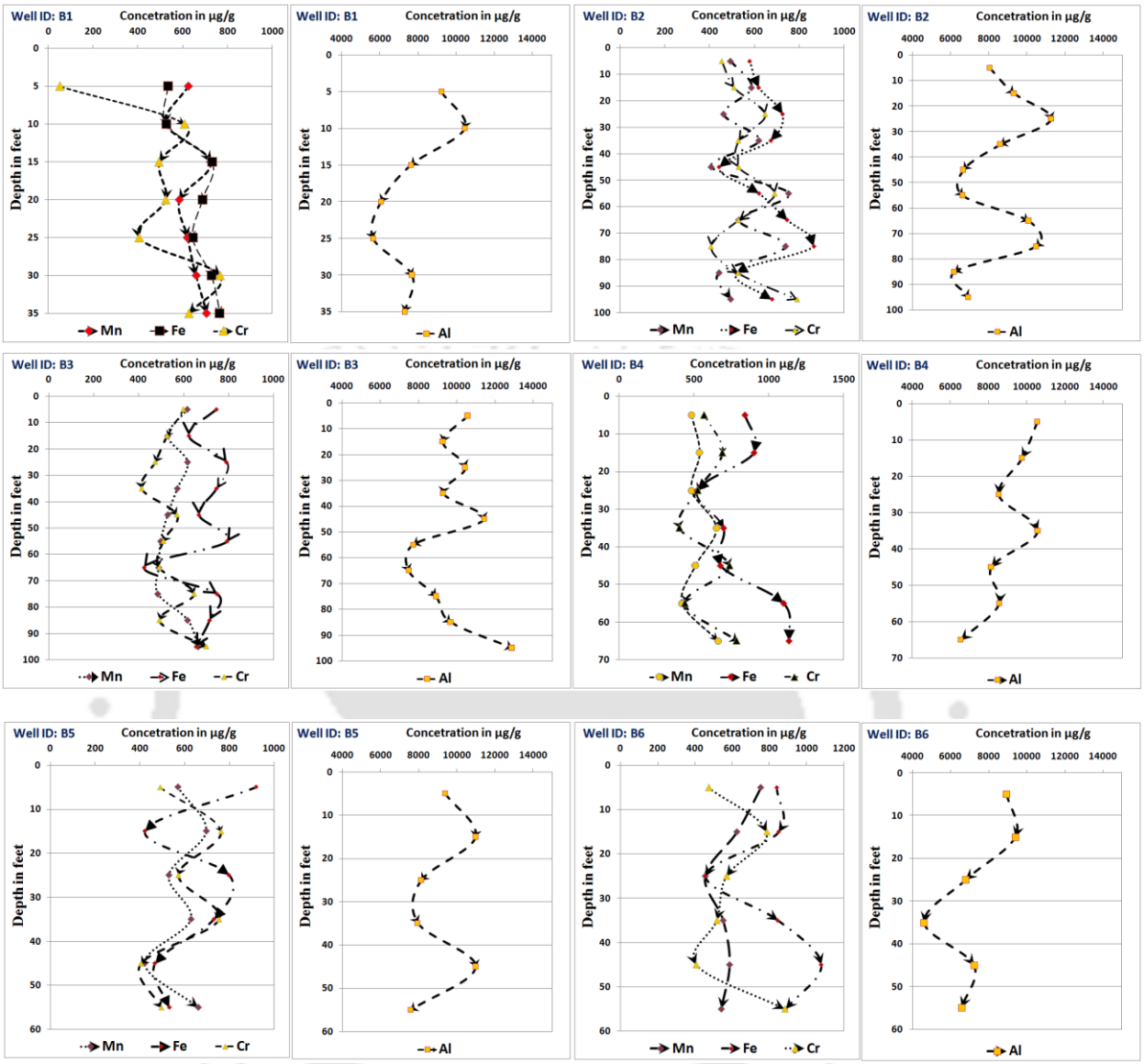

Appendix Figure C 2. 1: Total elemental concentration variation mainly for Mn, Fe, Cr, and Al has shown for H*As*CR and L*As*CR sediment samples.

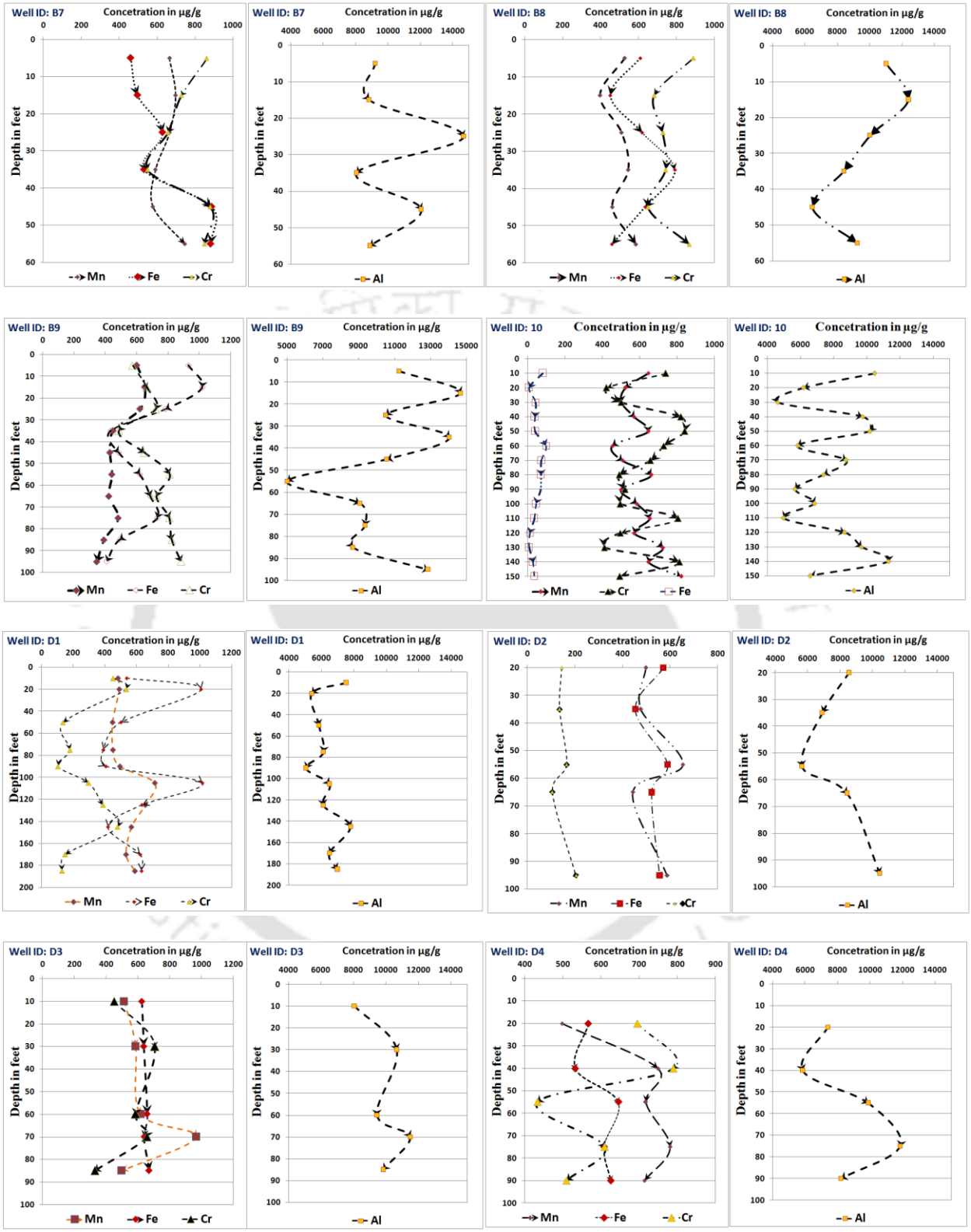

Appendix Figure C 2.2: Total elemental concentration variation mainly for Mn, Fe, Cr and Al shown for H*As*CR and L*As*CR sediment samples.

Appendix D1

Appendix Table D 1. 1: XRF results for H*As*CR sediment samples showed presence of total element composition.

Element	Sample ID / Munsell color	B1-35' Brown	B1-60' Orange	B2-25' Brown	B2-35' Yellow orange	B3-25' Yellowish	B4-45' Yellow orange	B5-20' Yellow orange	B6-50' Grey	B6-95' Grey	B7-35' Grey	B8-55' Grey	B9-60' Grey
	Sediment classification / Unit	Medium sand	Coarse & medium sand	Silt	Fine sand	Fine sand	Medium sand	Clay	Fine sand	Coarse sand	Medium sand	Medium sand	Medium sand
Mg	%	0.4	0.4	0.5	0.5	0.5	0.5	0.4	0.2	0.4	0.4	0.2	0.8
Al	%	8.1	7.4	7.8	10.4	7.8	10.4	12.7	5.6	6	8.1	5.6	8.5
Si	%	73	70.5	71.5	64.1	71.5	64.1	56.1	54.0	50.6	72.9	54	54.8
P	%	0.7	0.6	0.7	0.5	0.7	0.5	0.9	1.1	1	0.7	1.1	0.5
Cl	ppm	292.6	138	1*	283	1*	282.9	407.2	197	bdl	292.6	197	328.8
K	%	8.3	9	7.3	13	7.3	13	10.8	10.7	10.3	8.3	10.7	8.5
Ca	%	0.9	1.1	0.6	1.1	0.6	1.1	1	9.7	8.4	1	9.7	6.6
Ti	%	0.5	0.8	0.7	1.3	0.7	1.3	1.3	1.4	2.8	0.5	1.4	1.5
V	ppm	69.7	7.3	79.6	215.4	79.6	215.4	316	310.6	330.2	69.7	310.6	329.1
Cr	ppm	100.7	133.5	142.2	189.7	142.2	189.7	286.6	265.1	621.5	100.7	265.1	0.1
Mn	ppm	915.4	0.1	0.2	842.6	2*	842.6	0.2	0.4	3*	915.4	4*	4*
Fe	%	7.5	9.3	10	8.3	10.0	8.3	15.5	15.5	18.7	7.5	15.5	17.2
Ni	ppm	63.5	142	88.6	122.6	88.6	122.6	257.4	259.5	389	63.5	259.5	103.7
Cu	ppm	67	96.4	105.7	85.8	105.7	85.8	168.7	bdl	211.2	66.9	bdl	100
Zn	ppm	124.5	226	214.6	210.3	214.6	210.3	415.3	303.3	448.8	124.5	303.3	281.2
Ga	ppm	39.2	49.5	bdl	72.4	bdl	72.4	114.1	169.5	157.3	39.2	169.5	67.8
As	ppm	12.8	9.4	bdl	7	bdl	7	24.4	35.1	50.4	12.8	35.1	bdl
Rb	ppm	431	621	371.4	936.3	371.4	936.3	0.1	0.1	1*	431	1*	678.7
Sr	ppm	174	216.3	147.2	346	147.2	346	311.7	0.3	3*	174	3*	1
Y	ppm	66	72.4	75.3	102.3	75.3	102.3	132	233	279	66	233	188.1

Zr	ppm	528.7	525.7	633.5	941	633.5	941	0.1	0.2	2*	528.7	2*	2*
Ag	%	0.3	0.3	0.3	0.3	0.3	0.3	0.4	0.4	0.4	0.3	0.4	0.4
Ba	ppm	786	747.4	bdl	bdl	0.2	bdl	bdl	bdl	bdl	786	bdl	bdl
Eu	ppm	385.8	518.1	787.1	571	787.1	571	0.1	0.1	1*	385.8	1*	2*
Yb	ppm	bdl	bdl	47.5	bdl	47.5	bdl	bdl	bdl	bdl	bdl	bdl	47
Re	ppm	23.3	19.5	26	21.6	26	21.6	1	12	12.8	bdl	12	bdl
Ir	ppm	bdl	bdl	bdl	0.2	bdl	0.2	15.1	bdl	16.5	bdl	bdl	bdl
Pb	ppm	93.4	111.2	90	213.8	90	213.8	210.7	211.5	287.5	93.4	211.5	132.5
Th	ppm	bdl	bdl	bdl	bdl	bdl	bdl	bdl	bdl	bdl	bdl	bdl	99.2

Note * indicates concentration in %

Appendix Table D 1. 2: XRF results for L*As*CR sediment samples showed presence of total element composition.

Element	Sample ID / Munsell color / Sediment classification / Unit	D1-75'	D1-145'	D1-165'	D2-90'	D2-175'	D3-50'	D3-90'	D4-20'	D4-40'	D4-45'	D4-90'
	Munsell color	Brown	Greenish grey	Deep grey	Dark Grey	Deep grey	Grey fine	Grey	Pale blue	Pale blue	Pale blue	Dark grey
	Sediment classification	Medium sand	Fine sand	Medium sand	Fine sand	Coarse sand	Sand	Coarse sand	Clay	Clay	Clay	Medium sand
Mg	%	0.6	0.6	0.6	1	0.7	1.2	1	0.7	1.1	0.4	1
Al	%	11.1	10.1	9.8	14.7	11.1	10.6	10.6	15.7	14.2	8.6	9.6
Si	%	0.7	59.3	64.6	44.1	58.1	42	49.8	54.1	39.7	72.7	48
P	%	0.7	0.5	0.7	0.4	0.6	0.5	0.6	0.6	0.4	0.7	0.6
Cl	ppm	bdl	bdl	359.1	bdl	bdl	bdl	bdl	355.5	bdl	bdl	315.6
K	%	12.8	11	11.6	14.1	13.3	10.6	11.5	12.8	14.5	9.3	8.8
Ca	%	1.7	1.3	1	1.4	1.3	6.2	6.3	bdl	1.6	bdl	8.7
Ti	%	1.4	1.3	1.1	2	1.3	2.2	2	1.3	1.7	0.6	2.2
V	ppm	137.3	230.2	143.3	518.6	322.5	638	479	154.4	433.6	bdl	490
Cr	ppm	193.4	203.1	172.3	485.6	247.3	598	393.6	239.6	426.7	100.7	572.8
Mn	%	1.3	3	1	1.8	1	3.8	2.7	2.2	2.1	1.5	3.5
Fe	%	11	14.6	9.6	21	12.8	24.8	17.1	13.5	25	7	19.5
Ni	ppm	91.2	148.3	94	231.2	208.8	365.1	bdl	203.7	254.2	95.8	219.2
Cu	ppm	127.7	155.8	93.7	279	139.6	364.2	153.1	122.1	324.7	bdl	176.2
Zn	ppm	341	322.5	233.1	668.3	345.8	603.6	344.4	327	673	153.6	349.1
Ga	ppm	75.1	73.1	61.8	168.1	74.8	139.2	106.4	86	162.7	bdl	94.6
As	ppm	16.5	bdl	8.2	bdl	35	61	14.2	28	bdl	11.4	19
Rb	%	1.1	0.9	0.8	1.6	0.98	1.1	0.98	0.74	2.1	0.47	0.72
Sr	ppm	387.8	308	271.5	380.3	313.7	0.1	0.1	193.7	381	175.1	0.2
Y	ppm	138.2	146.4	115.5	193.2	107	243.1	167.4	108.8	231.7	77.4	240.2
Zr	ppm	0.1	0.2	938.6	1250	732.8	0.2	0.1	601.4	636	552.6	0.3

Nb	ppm	bdl	bdl	bdl	111.7	bdl	98.6	bdl	bdl	91.9	bdl	bdl
Ag	ppm	0.4	0.4	0.3	0.4	0.4	0.5	0.3	0.4	0.5	0.3	0.4
Ba	%	1.9	bdl	1.5	2.8	bdl	bdl	bdl	1.9	2.8	1.2	bdl
Nd	ppm	637.3	bdl	19.7	bdl	bdl	bdl	bdl	bdl	bdl	bdl	bdl
Eu	ppm	637.3	0.1	518.6	1.1*	707.6	0.2	0.1	903.8	0.1	553	0.2
Yb	ppm	23.8	bdl	86.5	bdl	bdl	bdl	bdl	bdl	bdl	bdl	bdl
Re	ppm	12.7	28.6	16.1	3.6	21.1	bdl	bdl	18	6.8	22.5	bdl
Ir	ppm	12.5	15.3	7.8	bdl	4.3	bdl	bdl	bdl	bdl	bdl	bdl
Pb	ppm	170	137	94.2	253.5	131.5	200.5	132.5	138	324.1	105.4	120.5
Th	ppm	bdl	bdl	bdl	163.1	bdl	130.1	bdl	bdl	203	bdl	156.4

Note * indicates concentration in %

Appendix E1

Appendix Table E 1. 1: results of modified sequential extraction method (SSE) for H*As*CR sediment samples

Sample ID	Mn (mg kg^{-1})						Fe (mg kg^{-1})						*As* (mg kg^{-1})						Al (mg kg^{-1})					
	F1	F 2	F 3	F 4	F5	Total	F1	F 2	F 3	F 4	F5	Total	F1	F 2	F 3	F 4	F 5	Total	F1	F 2	F 3	F 4	F 5	Total
B1-5’	33.3	1.3	81.3	56.8	157.9	330.6	209.4	121.7	1141.8	457.9	2308.7	4239.5	0.7	0.4	1.2	0.4	2.6	5.3	1882.2	961.5	6647.6	3371.4	14811.7	27674.4
B1-10’	12.2	0.9	42.4	20.4	72.9	148.8	228.6	144.3	1444	600.3	2570	4987.2	1.9	1	4.5	1	10.7	19.1	1680.2	1144.3	8193.8	3922	17468.4	32408.7
B1-15’	4.2	1.7	23.3	10.2	51.1	90.5	885	411	3158.3	1726.7	7237.3	13418.3	4	2.3	10.4	2.3	17.4	36.4	920.7	920.7	3960.7	1880.2	6619.1	14301.4
B1-20’	3.4	0.7	13	8.6	34.8	60.5	2877.9	1221.4	8384.4	4625.6	17063.1	34172.4	2.1	1.3	4.4	1.3	8.2	17.3	1106.8	340.8	3451.2	1925.4	5210.9	12035.1
B1-25’	12.2	0.5	58.2	24.6	90.8	186.3	1752.5	821.4	6225	3233.8	12732.4	24765.1	4.4	2.1	9.3	2.1	16.3	34.2	880.8	321.7	3622.7	1576.8	5997.6	12399.6
B1-30’	29.2	1.7	97	50.8	123.4	302.1	1343.4	614.1	4428.1	2435	10364.4	19185	11.3	4.8	20.7	4.8	42.8	84.4	701.2	204	4162.3	1780.4	7471.4	14319.3
B1-35’	4.4	0.7	35.4	10.6	45.4	96.5	1118.3	414.8	4152.5	2109.4	7613.7	15408.7	12.1	5.6	26.6	5.6	59.5	109.4	1187.9	503.3	4745.8	2122.1	8276.5	16835.6
B2-5’	63.5	2.6	264.2	141.3	452.8	924.4	1003.7	517.9	4553.2	2178.2	5832.1	14085.1	0.8	0.5	1.4	1	2.4	6.1	175.5	51.7	1034.8	422.3	1717.3	3401.6
B2-15’	62.8	0.8	329.2	142.8	682.8	1218.4	1738.7	892.8	6810.4	3381	15106	27928.9	2.1	1.3	3.7	3	7.8	17.9	251.3	109.5	1503.5	451.2	2596.1	4911.6
B2-25’	66.4	1.4	229.4	101.3	414.2	812.7	2417.5	1354.1	8382	4649.6	16500	33303.2	4.7	1.6	11.7	7	21	46	540.3	210.1	1902	895.1	3568.1	7115.6
B2-35’	64.8	0.7	286.4	160.7	462.8	975.4	1499.8	741.2	6642.9	2774.6	15361.2	27019.7	7.3	2	14	10	19.4	52.7	583.2	175	2541.5	1288.5	6120.2	10708.4
B2-45’	62.6	0.4	184.4	100.8	386.4	734.6	1621.6	799	6234.5	3232.4	11872.2	23759.7	15.7	6	25.5	17.5	42.1	106.8	516	243.5	2934.5	1323.9	6804	11821.9
B2-55’	64.4	0.7	207.4	120.7	427.4	820.6	1460.6	688	6847.2	3386.9	15496.6	27879.3	8.1	2.1	17.3	10.8	35.1	73.4	507.8	212.2	2294.3	1156.1	5777.3	9947.7
B2-65’	45.6	0.4	153.6	80.3	273.6	553.5	1633.8	684.3	6599.9	2974.3	12508.3	24400.6	9.4	4.2	19.7	10.2	43.2	86.7	857.6	424.3	3201.6	1635.8	7641.2	13760.5
B2-75’	42.2	1.4	152.4	80.4	228.2	504.6	1220.5	544.8	4349.6	2490.3	9578.7	18183.9	19.4	6.5	36.7	1.5	76.8	140.9	541.2	293.6	2614.8	1325.5	5057.4	9832.5
B2-85’	82.4	0.7	307.2	160.5	520.2	1071	1294.2	753.6	5032.5	2601.9	10961.5	20643.7	11.1	3.6	23.5	10.9	41.9	91	414.2	282.6	1639.9	763.1	4009.2	7109
B2-95’	42.8	1.2	225.6	100.5	432.8	802.9	1755.2	802	6639.7	3324.7	13519.6	26041.2	10.2	4.2	17.3	7	35.3	74	518.8	217.5	3244	1274	6598.7	11853
B3-5’	53.6	1.2	114.2	60.4	177.9	407.3	816.9	536.9	3411.1	1784.2	666241	672790	1.6	0.7	6.5	3.5	14.5	26.8	829.1	385.6	4567	2086.2	9668	17535.9
B3-15’	14.2	0.6	40.2	20.3	62.8	138.1	1035.1	471.2	4429.7	2188.3	9879.7	18004	1.5	0.5	6	2.9	17.2	28.1	1391.5	540.4	4128.1	2447	7589.5	16096.5
B3-25’	47.2	0.3	175.2	80.2	414.2	717.1	1525.6	772.5	5388.8	2771.1	10701.1	21159.1	1.3	0.4	4.6	2.3	10.3	18.9	1636.6	910.6	4734	2986.2	8455.3	18722.7
B3-35’	65.6	0.6	202.2	120.3	462.8	851.5	2443.1	1008.9	8623	5167.1	16619.6	33861.7	0.8	0.5	3.5	2	5.3	12.1	1368.7	701.7	6296.1	2857.1	10669.8	21893.4
B3-45’	44.2	0.5	152.8	61.1	386.4	645	1455.6	640.6	6612.2	2973.1	12498.9	24180.4	0.5	0.2	1.3	0.8	2.5	5.3	1273	478.1	5671.4	2627	949531	959581
B3-55’	71.1	1.2	273.4	140.5	547.8	1034	2636.9	1190.6	8545.3	4562.5	17185.3	34120.6	1.7	0.5	5.6	3.2	10.6	21.6	1121.5	555.5	3974.9	1904.6	8194.6	15751.1
B3-65’	42.4	0.8	204.4	100.2	432.8	780.6	2884.8	1409.5	8829	4565.2	19508.2	37196.7	2.1	0.8	8.1	3.8	19.3	34.1	782.3	418.2	3117.3	1499.4	7181	12998.2
B3-75’	46.4	0.8	149	80.4	388.2	664.8	1222	602.1	4407.8	2578.6	10790.5	19601	0.9	0.3	4.4	2.7	11.2	19.5	685.8	278.5	2864.4	1308.8	6103.1	11240.6
B3-85’	27.8	0.2	142.4	60.4	268.2	499	1258.8	536.9	6814.1	3392.6	13961.7	25964.1	2.9	1	12.1	6.4	24.4	46.8	945.8	385.2	3917.9	1635.8	8498.4	15383.1
B3-95’	44.6	0.3	172.8	100.3	366.4	684.4	1843	931.4	6554.2	3568.9	13002.7	25900.2	2.2	0.9	8.7	4.5	19	35.3	596.2	213.4	2502.8	1518.1	5996	10826.5
B4-5’	29.6	0.4	147.6	60.2	320.6	558.4	1627.3	685.5	6419.4	3317.4	13008.5	25058.1	0.1	0	0.3	0.2	0.6	1.2	1489.2	582.7	5047.2	2659.6	8313.9	18092.6
B4-15’	72.8	0.5	265.2	140.4	566.2	1045.1	2262.3	1349.9	8815.1	4571.3	18354.4	35353	0.2	0.1	1.1	0.6	2.3	4.3	513.5	210.5	2639.6	1230.2	5424.7	10018.5
B4-25’	55.6	0.8	254.8	100.3	619.6	1031.1	1655.9	649.6	6830	3249.8	15566.6	27951.9	1.7	1	6.3	3.7	12.3	25	1598.4	943.1	4126.8	2543.1	7629.8	16841.2
B4-35’	73.6	0.4	339	140.2	706.2	1259.4	2462.3	1409.5	11003.4	5174.4	19857.2	39906.8	0.8	0.5	3.8	2.1	8.2	15.4	1252.6	473.2	5401.9	2861.6	9648	19637.3
B4-45’	31.1	0.2	108.8	60.2	242.4	442.7	2725.2	1361.9	9011.4	5375.5	15851.7	34325.7	2.5	1.8	8.3	4.3	16.8	33.7	1287.7	417.8	6610.9	2937.7	11163.3	22417.4
B4-55’	49.8	0.3	149.8	80.2	360.6	640.7	1635.4	963.5	6640.6	3182.7	15036	27458.2	0.8	0.5	4.7	2.1	8.4	16.5	917.9	351.8	3714.7	1644.4	8273.2	14902
B4-65’	31.4	0.3	204.6	80.3	432.8	749.4	1052.8	605.1	4619.2	2433.6	10449.1	19159.8	1.5	0.6	6	3.3	12.5	23.9	1147.2	416.6	5400.6	2641.7	11178.8	20784.9
B5-5’	66.4	3.6	392.8	141.6	692.8	1297.2	1062.9	599.3	4821	2174.9	9574.5	18232.6	0.2	0.1	1.1	0.5	1.7	3.6	504.6	214.6	3133.2	1596.7	6773	12222.1
B5-15’	65.8	2.4	294.4	120.4	601.4	1084.4	1300.1	794.7	4641.6	2480.1	10491.2	19707.7	0.2	0.1	0.9	0.4	2	3.6	1222.5	506.2	4626.9	2240.2	10067.1	18662.9
B5-25’	66.6	3	369.4	160.5	724.4	1323.9	1458.7	724.8	478	2407.7	10324.4	15393.6	1.3	0.5	4.3	2.6	8.3	17	559.5	294.8	2613.6	1118.2	5917.8	10503.9
B5-35’	88.2	3.2	426.8	200.3	913.6	1632.1	841.1	537.9	3213.8	1848.5	7528.9	13970.2	2.2	1	6.4	2.7	12.2	24.5	1246.5	458.5	4961.7	2197.8	9086.9	17951.4
B5-45’	87.8	3.4	403.4	180.3	867.4	1542.3	1515.8	709	4819.8	2797.4	9528.9	19370.9	2.9	1.2	10.3	5.6	18.7	38.7	1065.7	417	5994	2518.3	11997.7	21992.7
B5-55’	109	5	572.8	301	930.8	1918.6	749	442.1	3410.9	1468	7761.1	13831.1	2.1	1.3	9.8	4.4	22.1	39.7	555.5	214.2	2622.1	1065.7	5509	9966.5
B6-5’	64.3	0.4	270.8	160.3	509.4	1005.2	905.9	578.1	3518.5	1591.1	5249.9	11843.5	0.3	0.2	1.3	0.7	2.1	4.6	476.1	176.3	3225.6	1253	6769.7	11900.7

B6-15’	42.4	0.2	204.4	120.1	426.4	793.5	1048.2	404.1	4598.3	2393	7235.4	15679	0.1	0.1	0.7	0.3	1.2	2.4	377.5	199.1	2241	964.7	5496.3	9278.6
B6-25’	41.2	0.9	169.2	100.1	316.2	627.6	1475.8	617	5024.7	2322	10216.5	19656	0.6	0.3	2.5	1	7	11.4	415.8	209.3	2197.4	1088.9	4127.7	8039.1
B6-35’	42.8	0.3	268.8	120.3	481.8	914	1233	780.5	4411.8	2386.3	8407.4	17219	2.1	1	8	4.3	16.3	31.7	1635.7	581.9	7102.4	3698	8089.6	21107.6
B6-45’	43.2	0.3	254.4	100	555.2	953.1	1457.5	813.2	4829.5	2806.6	10882.5	20789.3	1.5	0.6	5.7	3.3	12	23.1	1232.7	518.8	5533	2939.8	9920.9	20145.2
B6-55’	43.8	1.8	206	120.2	570.8	942.6	1672.7	819	7020.5	3413.9	13990.2	26916.3	3.3	1.5	12.8	6.5	26.1	50.2	1640.7	961.5	6798.2	3582	11205.3	24187.7
B7-5’	24.2	0.6	136.8	60.1	225.2	446.9	807.5	525.5	3718.8	1741.7	6612.4	13405.9	0.2	0.1	0.8	0.4	2.2	3.7	1106	417.8	6035.9	2640.9	12735.6	22936.2
B7-15’	24.6	0.5	164.2	80.1	586.2	855.6	2408.1	1114.4	8228.6	4392.9	16456.5	32600.5	3.4	1.3	13.3	6.6	42.1	66.7	1717.3	868.6	7291	3996.5	12014.8	25888.2
B7-25’	63.2	0.3	226.4	100.2	404.4	794.5	1665.5	546.4	7006.9	3221.6	13523.4	25963.8	2.6	1.1	12.2	6.2	46.3	68.4	1227.4	429.2	5753.3	3163.7	15848.1	26421.7
B7-35’	43.7	0.7	215.6	100.2	360.8	721	1440.8	773.6	4629.2	2805.9	10894.6	20544.1	2.2	1.3	11	5.3	30.6	50.4	1639.5	666.6	6617	3558.8	13214.9	25696.8
B7-45’	65.2	0.8	305.2	140.2	547.8	1059.2	1033.7	601.3	5376.6	2582.8	7090.7	16685.1	1.1	0.6	4.4	2.1	18.2	26.4	944.4	432.5	4356.5	2207.6	8697.6	16638.6
B7-55’	44.2	0.6	143.2	80.1	336.8	604.9	1824.9	1014.7	4409.4	3190.1	9089	19528.1	1.3	0.5	5.2	2.8	22.1	31.9	673.6	289.5	3239.5	1905.4	6636.6	12744.6
B8-5’	62.8	0.4	368.4	160.2	746.2	1338	1239.7	742	3212.4	1602.7	6971.7	13768.5	0.1	0	0.2	0.1	0.4	0.8	1564.2	670.7	5889.7	2575.3	12497.4	23197.3
B8-15’	62.2	0.4	304.8	163.2	683.6	1214.2	1554.7	911.6	4835.4	2796	11493.5	21591.2	0.1	0.1	0.4	0.2	0.7	1.5	1681.4	665.4	8298.5	4497	17158.9	32301.2
B8-25’	61.5	0.3	233.6	100.2	495.6	891.2	1734.8	819.3	7036.4	3217.8	15640	28448.3	0.3	0.1	0.9	0.5	1.4	3.2	1106	419.9	5677.2	2601.8	10885.6	20690.5
B8-35’	60.9	0.6	206.4	100.3	368.7	736.9	1457.3	650.5	4848.4	2402.7	10176	19534.9	0.6	0.3	2.5	1.5	4.8	9.7	1648	660.9	8500.9	3532.7	15236.4	29578.9
B8-45’	20.7	0.4	153.6	60.3	314.2	549.2	2059.2	1138	6908.2	3589.9	14306	28001.3	0.5	0.2	1.7	0.8	3.5	6.7	1654.2	1118.3	9169.5	4335.7	18803.3	35081
B8-55’	40.9	0.5	204.4	100.3	398.4	744.5	811.4	528.1	3207.3	1802.1	6284.5	12633.4	1.3	0.9	5.4	2.3	9.3	19.2	1348.3	701.2	6897.2	2577.3	14749.4	26273.4
B9-5’	24.3	0.5	150.8	60.4	272.8	508.8	4699.2	2027.3	19546.5	8790.7	33243.6	68307.3	0.9	0.4	3.5	1.7	7.7	14.2	1071.4	416.6	4496.6	2299.6	10837.9	19122.1
B9-15’	24.2	0.5	129.6	60.3	292.8	507.4	2321.5	1227.1	9405.5	4606.2	16227.7	33788	1.9	0.8	5.2	3.3	10.9	22.1	1025	367.3	5686.9	2594.8	11444.7	21118.7
B9-25’	69.5	6.2	246.2	140.7	413.6	876.2	3508.3	1744	13396.1	6399.6	23714.7	48762.7	3.2	1.8	14	6	24.5	49.5	1222.5	418.2	6167.9	2857.9	13282.5	23949
B9-35’	23	2.6	149.2	60.6	337.4	572.8	5273.2	2425.6	21159.7	10759.3	36062.9	75680.7	2.7	1.3	11.9	6.5	27.6	50	1227.4	421.1	6673.2	3149.5	11247.2	22718.4
B9-45’	27.9	4.6	104.2	40.4	234.2	411.3	1673.7	829.7	7024.8	3230.1	15629.2	28387.5	7.9	4.7	24	15	40.5	92.1	1273	414.2	6216.7	3242.7	13320.8	24467.4
B9-55’	25.4	2.8	142.8	60.3	305.4	536.7	2277.6	1232.3	9197.6	4214.6	16688.7	33610.8	3.5	1.4	12.5	5.4	23.4	46.2	1749.4	941.1	6077	3427.2	11734.7	23929.4
B9-65’	68.5	5.1	206.4	120.5	379.2	779.7	1488	636.1	7021.1	2840.7	14828.8	26814.7	4.6	2.1	17.3	9.1	38.4	71.5	1145.9	421.9	7265.3	3074.2	15331.3	27238.6
B9-75’	68.2	5.9	252.2	140.5	406	872.8	1043.2	423.8	4611.7	2227.6	8201.4	16507.7	2.8	1.1	8.3	4.7	19.6	36.5	901.6	392.9	4608.6	2183.6	9210.3	17297
B9-85’	67.9	5.4	205.2	100.5	394.2	773.2	1469.4	793.1	6811	2824.6	13143.2	25041.3	5.2	2.3	19.3	11.4	39.7	77.9	4732	210.1	2889.7	1253.9	5996.8	15082.5
B9-95’	48.8	4	144.8	80.4	321.2	599.2	2326	1025.7	8830	4612.1	18862.4	35656.2	6.6	2.8	27.3	12.7	50.7	100.1	1598	540.4	5765.1	2787.1	10763.4	21454
B10-10’	7.2	4.2	38.8	10.6	72.8	133.6	591.9	357.2	2189.3	992.8	5297.9	9429.1	0.2	0.1	0.5	0.3	1.7	2.8	377.1	187.7	1910.7	974.9	4248.4	7698.8
B10-20’	67.2	4.1	168.4	102.5	292.8	635	1846.1	1194.7	7016.8	3377.1	13120.2	26554.9	0.3	0.1	1.4	0.6	2.3	4.7	821.4	331.5	5035.4	2205.9	8907.7	17301.9
B10-30’	38.8	14.2	185.4	87.6	321.8	647.8	1639.1	1012.7	6631.1	3216.3	13798.8	26298	1	0.4	3.8	2.2	7.7	15.1	1271.4	458.9	7083.3	3132.8	10789.5	22735.9
B10-40’	88.3	4.8	304.8	162.8	526.6	1087.3	4092.1	1796.9	17144.2	8533.3	34855.8	66422.3	2.5	2.3	5.8	5.7	10.3	26.6	1668.4	665.4	6776.7	3070.9	12303.1	24484.5
B10-50’	67	2.8	193.4	101.9	341.6	706.7	1714.1	939.4	6633.3	3412.9	15214.2	27913.9	3.3	1.4	13	6.5	19.8	44	819.8	335.6	4865.1	2077.7	9216	17314.2
B10-60’	45.4	2.6	142.9	81.7	251.8	524.4	1394.8	605	7477.6	3176.2	14297	26950.6	3.6	1.1	13.2	6.5	22.2	46.6	1067.3	310.3	3976.2	2515	7604.6	15473.4
B10-70’	69.4	19.6	169.4	110.6	389.2	758.2	827.9	562.9	3619.8	1937.4	7226.3	14174.3	2.8	1.4	10.7	5.2	21.3	41.4	459.4	213.4	3106.7	1316.6	4734	9830.1
B10-80’	27.1	2.8	127.1	61.7	201.6	420.3	808.3	342.6	3316.1	1725.7	5632.4	11825.1	2.8	1.1	11.6	4.8	18	38.3	717.5	229.7	2537.4	1075	5980.9	10540.5
B10-90’	59.4	40.8	259.4	137.9	439.6	937.1	410.6	161.9	2111.5	914.7	4102.1	7700.8	0.4	0.1	1.1	0.6	1.6	3.8	731.4	174.7	3222.8	1232.3	6774.6	12135.8
B10-100’	21.4	13.4	101.1	68.3	243.2	447.4	1004.5	397.6	4202.8	2174.3	8428.5	16207.7	0.3	0.2	1.9	0.9	3.3	6.6	449.2	252.9	1760	1172.4	4172.9	7807.4
B10-110’	62.5	18.6	202.5	110.7	335.4	729.7	939.7	439.9	3508.3	1590.4	7260.7	13739	0.6	0.4	2.5	1.1	5.9	10.5	230.5	100.6	1654.2	603.5	3568.5	6157.3
B10-120’	8.3	3.8	28.3	21.2	70.8	132.4	409.8	180.8	2066.1	932.4	3553.7	7142.8	1.2	0.6	7.4	2.6	11.6	23.4	169.4	68.4	1169.1	401.5	2206	4014.4
B10-130’	6.3	3.1	26.3	17.2	66.2	119.1	206.8	120.4	1313.5	615.1	2582.8	4838.6	0.7	0.3	8.6	1.3	14	24.9	252.9	106.3	1681.4	702.1	2944.7	5687.4
B10-140’	9.1	4	49.1	22	94.4	178.6	626.5	259.7	2308.1	1228.5	4478.5	8901.3	0.5	0.2	2.5	1.1	6.8	11.1	351	212.2	1911.9	943.5	3343.7	6762.3
B10-150	11.3	6.1	71.3	20.3	117.8	226.8	1232.1	707.7	4429.7	2589.6	9700.3	18659.4	1.5	0.8	6.5	3.4	14.4	26.6	540	255.3	2613.6	1126.4	2831.9	7367.2
B10-160	36.6	10.8	116.6	64.2	160.8	389	2840.9	1546.9	8825.3	5550.2	18391.6	37154.9	1.2	0.6	3.7	2.1	8.6	16.2	304.6	128.7	1642.3	762.7	3677.7	6516
B10-170	37.8	6.8	117.8	63.6	186.2	412.2	1253.5	724.2	4551.7	2609.7	11316.6	20455.7	1.4	0.5	6.5	3.3	12	23.7	391.8	163.3	2531.7	1002.2	5028	9117
B10-180	32.6	5.6	92.6	40.4	145	316.2	631	399	2421.8	1407.4	6709	11568.2	0.8	0.4	3.3	1.7	4.6	10.8	458.5	169.4	3052.6	1294.2	6524.2	11498.9
B10-190	9.1	4.1	49.1	22.4	80.2	164.9	405.9	239.3	2074	932.4	4196.9	7848.5	2.1	1.2	8.4	4.3	15.7	31.7	961.5	351	4773.1	2290.2	9676.9	18052.7
B10-200	6.8	2.9	26.8	16.8	59.6	112.9	1638.6	929.9	6627.8	3175.2	13340	25711.5	0.9	0.5	3.2	1.8	4.9	11.3	1226.2	575.4	6613	2916.6	12704.7	24035.9
B10-210	7	3.9	47	21.9	67.6	147.4	623.5	343.7	3418.4	1394.2	6682.7	12462.5	0.8	0.3	2.9	1.7	4.3	10	871.1	416.6	3532.3	1833.7	8248	14901.7

B10-220	8.6	4.3	48.6	20.2	90.2	171.9	1835.1	799.6	6611.1	3562.6	12611.2	25419.6	1.1	0.5	3	1.5	5.8	11.9	580.7	228.9	2870.1	1474.6	7259.2	12413.5
B10-230	11	7.2	51	23.4	74.2	166.8	919.6	480.7	2914.3	1571.3	5335.1	11221	0.7	0.2	2.9	1.4	6.6	11.8	1088.9	421.1	4205	2354.2	10729.2	18798.4
B10-240	37.1	11.5	117.1	65.9	183.2	414.8	626.6	261.5	2384	1425.5	6934.9	11632.5	1.1	0.5	4.8	2.5	9.1	18	867	351.8	5265.9	2702.8	12059.6	21247.1
B10-250	47.3	14.8	187.3	107.8	353.8	711	1420	801	4368.1	2873.2	11109	20571.3	1.6	0.7	5.4	3.3	12.6	23.6	1260.8	417	7096.3	3092.5	13280.1	25146.7
B10-260	49.7	17	189.7	88.4	315.6	660.4	1626	960.7	5475.8	3367.6	8557.9	19988	1.2	0.5	4.3	2.7	11	19.7	1146.8	473.2	6911	2781.8	15640.4	26953.2
B10-270	50.2	21.5	170.2	91.5	394.8	728.2	660.9	242.4	2316.6	1392.6	4925.5	9538	0.8	0.5	3.8	1.7	8.2	15	984.3	540	5879.5	2778.9	14057.3	24240
B10-280	41.9	1.9	161.9	80.4	281.6	567.7	1028.4	406.5	4508	2224.1	10020.8	18187.8	0.7	0.3	2.8	1.3	7.2	12.3	1104	823.8	5671	2666.1	11693.9	21958.8
B10-290	43.4	23.4	163.4	97.2	272.6	600	1441.4	659.3	6755.1	2985.3	12322	24163.1	0.6	0.2	1.3	0.9	2.2	5.2	1636.2	630	8232.9	3716.8	10026.7	24242.6
B10-300	41.3	41.3	141.3	66.6	335.8	626.3	1391.4	756.7	4384.8	2899.5	8829.6	18262	0.7	0.3	3.7	1.7	6.3	12.7	826.3	344.5	3650.4	1904.2	7593.6	14319
B10-310	55.7	15.7	135.7	67.2	214.8	489.1	1644.1	930.1	6480.2	3191.5	12381.8	24627.7	1.2	0.5	5.5	2.5	11.7	21.4	436.1	254.1	2187.2	942.7	5011.3	8831.4

Appendix Table E 1. 2: Results of modified sequential extraction method (SSE) for L*As*CR sediment samples

Sample ID	Mn (mg kg^{-1})						Fe (mg kg^{-1})						As (mg kg^{-1})						Al (mg kg^{-1})					
	F1	F2	F3	F4	F5	Total	F1	F2	F3	F4	F5	Total	F1	F2	F3	F4	F5	Total	F1	F2	F3	F4	F5	Total
D1-10’	4.8	10.5	23.2	16.3	106.6	161.3	166.5	124.9	280.0	120.0	400.2	1091.6	0.2	0.2	bdl	bdl	5.7	6.1	111.6	298.9	1108.5	1880.2	2982.5	6381.7
D1-20’	5.2	8.3	34.8	18.7	128.4	195.4	1115.0	440.3	3602.3	623.1	5141.7	10922.4	1.3	3.1	0.3	0.1	9.3	14.0	63.5	185.7	1399.2	2466.2	4339.4	8454.0
D1-50’	3.8	8.8	28.8	14.3	160.4	216.1	4216.9	246.2	8981.7	591.8	13354.3	27390.9	2.3	1.7	4.7	1.3	10.6	20.5	54.6	176.7	369.4	909.7	1683.5	3193.9
D1-75’	4.1	8.2	33.4	16.6	127.8	190.1	416.8	205.7	10356.2	1572.8	11108.6	23660.1	3.8	0.3	1.1	0.1	17.0	22.2	102.2	509.4	1860.2	1283.2	3156.4	6911.4
D1-90’	5.0	14.1	48.4	20.8	194.8	283.1	2168.8	290.3	4631.2	1356.8	6170.5	14617.6	0.7	0.3	0.4	0.1	13.4	14.9	141.7	508.2	1346.7	2015.0	2666.5	6678.1
D1-105’	13.2	21.7	82.2	40.2	286.8	444.1	2204.4	308.6	3584.8	1294.2	2172.9	9564.9	1.1	0.3	0.9	0.2	24.4	26.9	80.6	406.4	945.2	813.6	2279.7	4525.5
D1-125’	10.3	32.4	131.6	60.9	322.2	557.4	2879.9	294.0	3917.7	1036.9	4473.4	12601.8	1.5	0.4	1.3	0.2	20.2	23.6	58.2	221.1	599.0	465.5	1157.8	2501.6
D1-145’	4.6	20.7	118.4	61.3	306.6	511.6	1768.0	300.9	6065.9	1020.8	14885.1	24040.6	1.0	0.4	1.8	0.2	2.6	6.0	96.1	332.7	829.1	2299.6	3353.9	6911.5
D1-170’	1.0	0.4	26.4	12.2	114.2	154.3	997.1	196.0	9407.1	623.7	9962.7	21186.6	1.3	0.4	2.4	bdl	8.9	12.9	144.6	495.6	1284.8	2305.7	3687.4	7918.1
D1-185’	2.6	4.6	20.4	9.4	139.4	176.4	677.3	267.9	8621.1	231.2	9176.7	18974.1	2.1	0.4	4.8	bdl	9.9	17.2	74.1	121.4	237.0	491.9	1092.2	2016.6
D2-20’	5.4	12.8	36.2	18.1	88.2	160.7	1406.6	139.9	1631.3	1013.1	2777.2	6968.0	3.7	2.4	5.0	2.1	13.0	26.2	185.7	821.4	1977.5	3710.7	6619.9	13315.1
D2-35’	6.2	15.4	51.9	23.1	141.2	237.8	1199.4	159.8	2014.3	609.1	2570.0	6552.7	2.5	1.0	4.1	1.5	6.6	15.6	152.3	812.8	1862.7	2737.0	5405.5	10970.3
D2-55’	8.5	12.4	96.7	51.2	212.4	381.2	1420.2	162.8	3909.1	1223.4	4463.1	11178.5	4.5	3.3	5.3	0.5	10.2	23.8	92.0	422.7	1191.5	2008.0	4571.5	8285.8
D2-65’	10.5	5.4	58.4	26.5	84.8	185.6	567.2	103.5	739.2	370.5	1294.8	3075.3	3.6	2.5	4.1	0.5	6.4	17.1	72.1	560.8	1520.6	3036.3	5406.8	10596.4
D2-95’	29.2	7.6	53.2	32.8	134.2	257.0	349.4	82.6	2836.8	192.0	5132.1	8592.9	4.1	2.6	4.5	1.3	7.7	20.3	159.6	748.5	1829.3	3879.7	7856.2	14473.2
D2-105’	7.4	96.8	256.4	146.7	524.4	1031.7	599.1	63.2	1925.6	304.0	2843.7	5735.6	4.6	2.6	5.6	1.1	7.2	21.0	177.1	966.8	2091.1	3364.1	7303.6	13902.7
D2-125’	66.3	134.8	460.6	204.3	888.4	1754.4	233.0	111.0	1141.4	134.6	2059.2	3679.1	4.0	3.8	6.2	2.6	16.8	33.2	147.8	821.8	1965.7	3258.2	6075.0	12268.5
D2-145’	49.5	93.0	389.2	209.5	769.2	1510.4	499.0	134.0	1825.5	282.5	2743.5	5484.5	2.6	3.5	4.1	3.0	11.2	24.3	13.4	148.2	287.9	718.3	10776.9	11944.8
D2-160’	74.8	137.6	468.8	202.9	804.2	1688.3	565.3	176.8	986.7	282.5	1904.8	3916.1	6.2	4.6	5.5	3.5	16.3	36.1	90.4	1242.4	2981.7	5482.1	11044.8	20841.5
D2-175’	85.4	163.2	582.4	282.6	1017.2	2130.8	1733.8	120.6	12091.2	270.1	13009.2	27225.0	5.7	4.4	4.8	2.4	18.4	35.8	77.0	1492.1	2642.5	4857.0	8832.3	17900.9
D2-180’	21.2	61.6	274.2	103.5	620.8	1081.3	1801.9	89.4	2125.3	700.0	3043.0	7759.5	6.6	3.9	4.7	2.7	17.7	35.5	74.9	1953.1	4310.1	7630.2	13106.2	27074.5
D3-10’	47.5	96.3	206.8	121.7	423.4	895.7	994.4	32.9	1711.0	220.4	2629.0	5587.6	12.7	2.0	4.7	2.7	50.4	72.4	78.2	293.6	1096.3	1644.0	2643.7	5755.7
D3-30’	40.0	70.5	268.2	112.1	468.4	959.1	459.2	21.2	4914.1	130.1	5832.1	11356.7	13.0	0.9	5.5	2.1	53.3	74.8	280.2	422.7	1135.3	1406.6	1705.5	4950.2
D3-60’	31.7	61.5	211.2	133.1	392.4	829.9	1528.6	43.9	24812.6	360.5	25730.6	52476.2	11.6	1.7	6.5	1.5	41.1	62.5	303.4	744.0	1850.8	2967.5	5027.2	10892.9
D3-70’	41.2	99.8	255.6	158.7	454.8	1010.2	994.4	33.5	1809.3	55.3	2727.4	5620.0	12.7	1.9	3.3	1.7	46.5	66.2	225.6	579.9	1610.2	4040.1	7067.0	13522.8
D3-85’	24.6	69.0	172.6	104.9	294.0	665.1	459.2	22.9	19589.4	113.8	20507.4	40692.8	6.8	1.3	1.1	0.6	9.8	19.6	219.5	798.6	1767.0	3126.7	6531.5	12443.2
D4-20’	31.0	58.1	113.4	67.1	184.4	454.1	1936.6	98.6	2769.7	282.3	3687.7	8774.9	0.2	0.2	bdl	0.8	1.6	2.8	261.4	1354.8	3030.6	4817.9	10686.5	20151.2
D4-40’	19.0	54.9	136.8	90.3	213.6	514.6	7518.8	34.8	24574.1	1059.9	25478.4	58666.0	0.2	0.5	bdl	0.5	0.8	1.9	153.5	924.0	2275.2	7113.8	14976.6	25443.1
D4-55’	5.7	33.7	89.4	63.4	188.2	380.5	1612.6	30.9	5497.4	1049.3	6422.2	14612.4	2.8	1.2	2.4	1.0	13.3	20.8	169.4	459.4	1472.5	2943.4	6847.9	11892.6
D4-75’	17.7	50.7	162.2	88.9	301.2	620.7	483.4	34.8	825.6	360.1	1743.6	3447.5	4.2	1.2	3.6	1.4	13.2	23.7	103.8	334.3	1366.2	3527.8	6497.3	11829.5
D4-90’	20.8	43.7	213.0	89.4	367.6	734.5	5553.3	53.3	20087.6	1045.5	20997.8	47737.5	2.1	1.5	2.0	1.7	13.8	21.1	201.6	1003.0	3540.8	7422.5	10137.9	22305.9

Appendiex F1

Appendeix Table F 1. 1: Essential input parameters used for transient state MODFLOW simulation model

Parameters	**H*As*CR**		**L*As*CR**	
Conductance [(m^2/d)/m]	Brahmaputra river	89.1	Brahmaputra river	75.3
	Manas river	2.5	Mangaldoi river	1.83
	Drain	2.4	Nanoi river	1.5
	H.B.	1E-12	General head	0.007
	Lake	0.0082		
Recharge rate (m/d)	**H*As*CR**		**L*As*CR**	
Min.	0		0	
Max.	0.00001		0.0001	
Avg.	0.000001		0.00004	
Evapotranspiration (m/d)	**H*As*CR**		**L*As*CR**	
Min.	0		0	
Max.	0.0128		0.0002	
Avg.	0.0020		0.00003	

Note: "Horizontal flow barrier" is abbreviated as H.B.

Appendiex G1

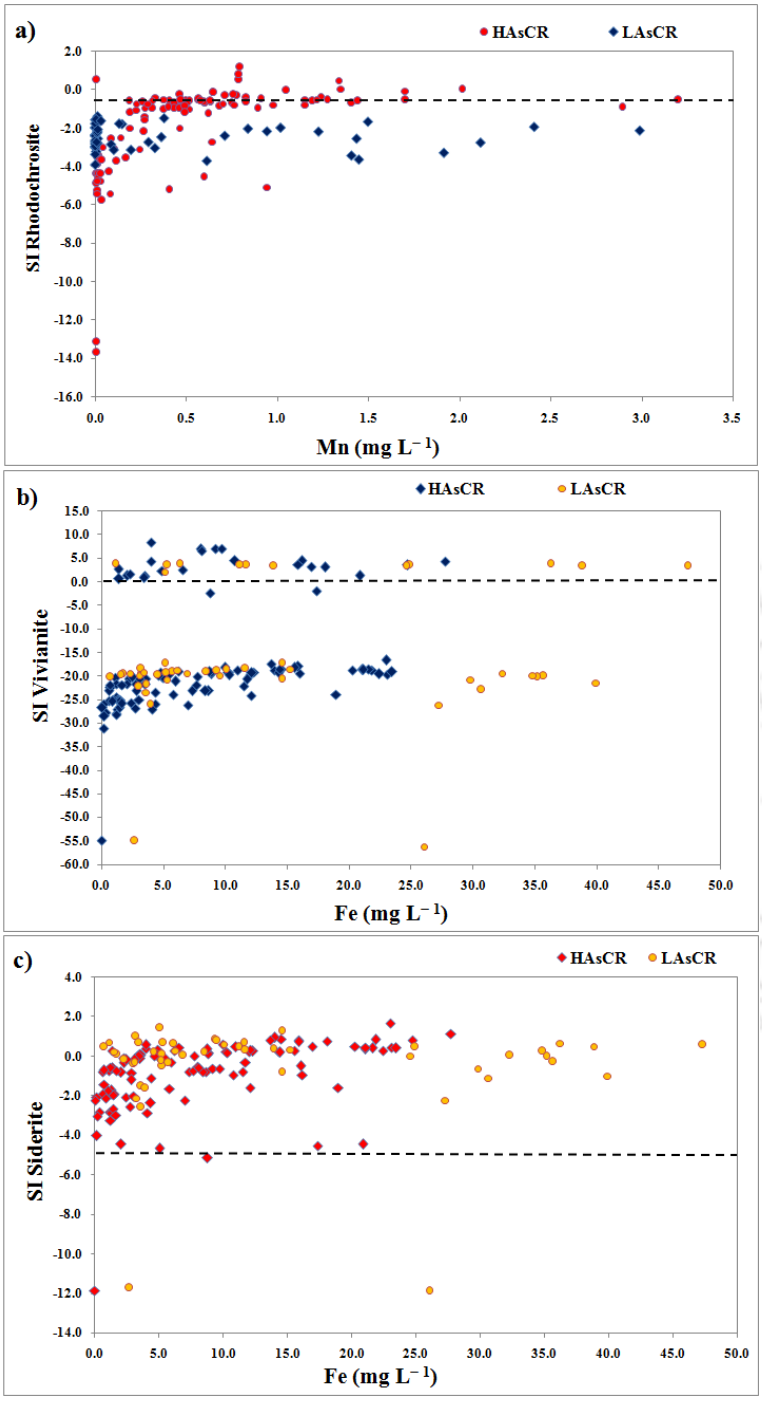

Appendix Figure G 1. 1: Bivariate plots showed the modeled SI values dependency for a) Rhodochrosite vs Mn b) Vivianite vs Fe c) Siderite vs Fe on dissolved Fe and Mn concentration measured in the 2017 year groundwater samples.

Appendix H 1

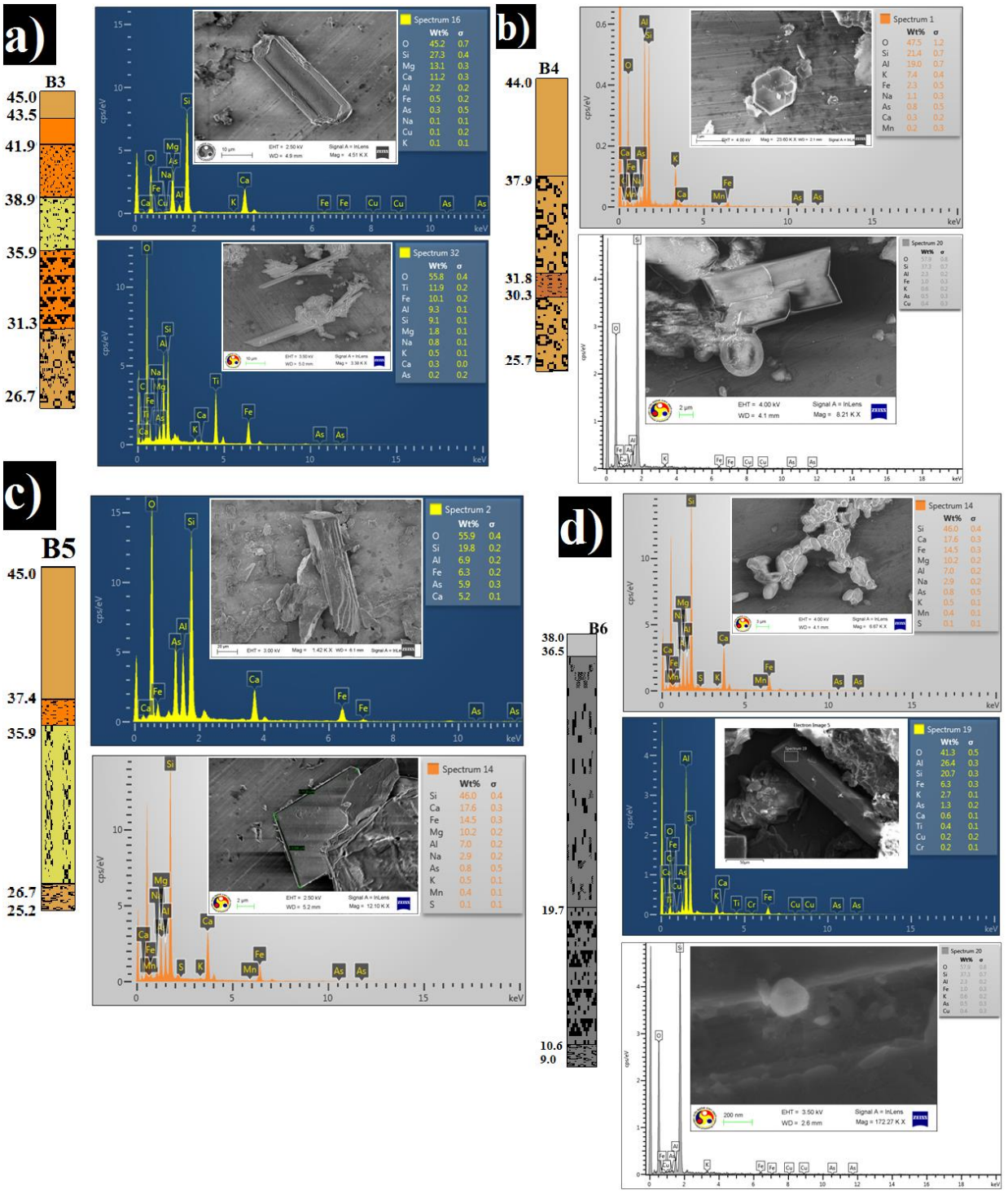

Appendix Figure H 1. 1: Morphological and elemental analysis showed the presence of a) Magnesite and Rutile minerals b) flakey Muscovite and Scorodite minerals c) Calcite and Siderite minerals d) Calcite, Arsenopyrite, and Chalcopyrite mineral.

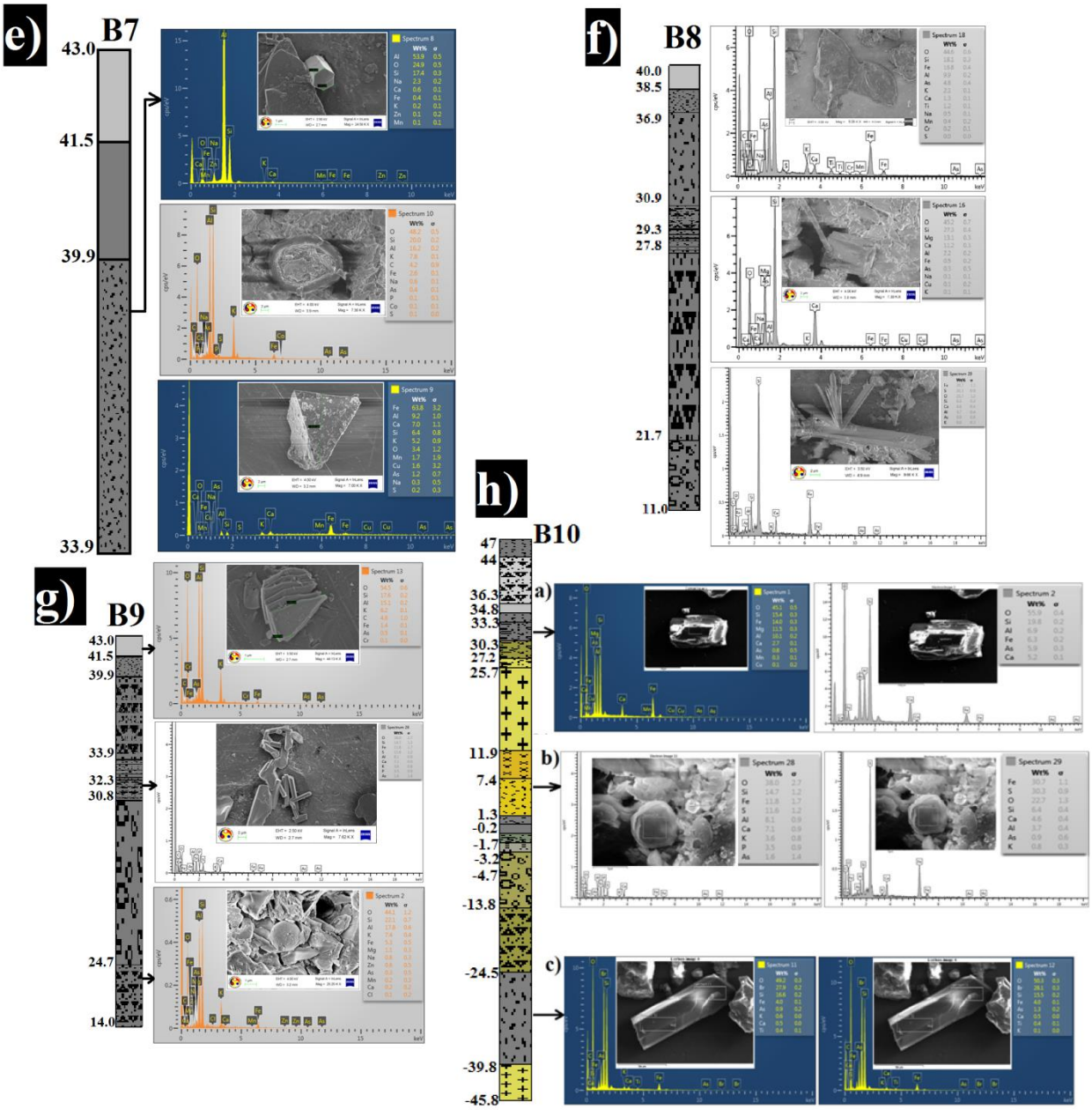

Appendix Figure H 1. 2: Morphological and elemental analysis showed presence of e) Corundum, Fly-ash and Chalcopyrite minerals, f) flakey Muscovite, Dolomite and Arsenopyrite minerals, g) layered Muscovite, Arsenopyrite and Fly-ash mineral, h) Aphro-Siderite at shallow depth, round shape Quartz, Jarosite and Scorodite at deeper depth sediment.

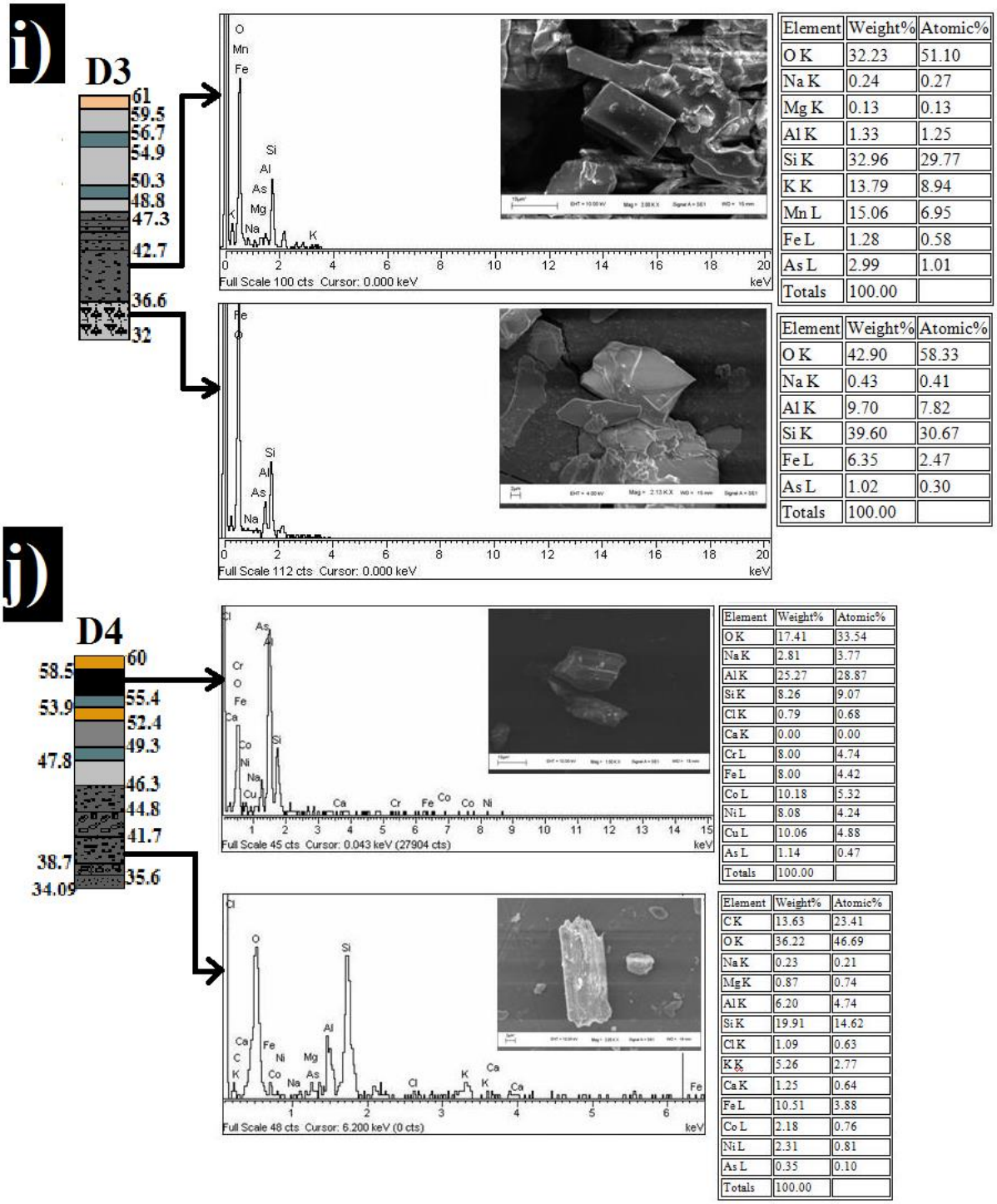

Element	Weight%	Atomic%
O K	32.23	51.10
Na K	0.24	0.27
Mg K	0.13	0.13
Al K	1.33	1.25
Si K	32.96	29.77
K K	13.79	8.94
Mn L	15.06	6.95
Fe L	1.28	0.58
As L	2.99	1.01
Totals	100.00	

Element	Weight%	Atomic%
O K	42.90	58.33
Na K	0.43	0.41
Al K	9.70	7.82
Si K	39.60	30.67
Fe L	6.35	2.47
As L	1.02	0.30
Totals	100.00	

Element	Weight%	Atomic%
O K	17.41	33.54
Na K	2.81	3.77
Al K	25.27	28.87
Si K	8.26	9.07
Cl K	0.79	0.68
Ca K	0.00	0.00
Cr L	8.00	4.74
Fe L	8.00	4.42
Co L	10.18	5.32
Ni L	8.08	4.24
Cu L	10.06	4.88
As L	1.14	0.47
Totals	100.00	

Element	Weight%	Atomic%
C K	13.63	23.41
O K	36.22	46.69
Na K	0.23	0.21
Mg K	0.87	0.74
Al K	6.20	4.74
Si K	19.91	14.62
Cl K	1.09	0.63
K K	5.26	2.77
Ca K	1.25	0.64
Fe L	10.51	3.88
Co L	2.18	0.76
Ni L	2.31	0.81
As L	0.35	0.10
Totals	100.00	

Appendix Figure H 1. 3: Morphological and elemental analysis showed the presence of i) Birnessite and Scorodite j) Enargite and Vaterite mineral.

Appendix I 1

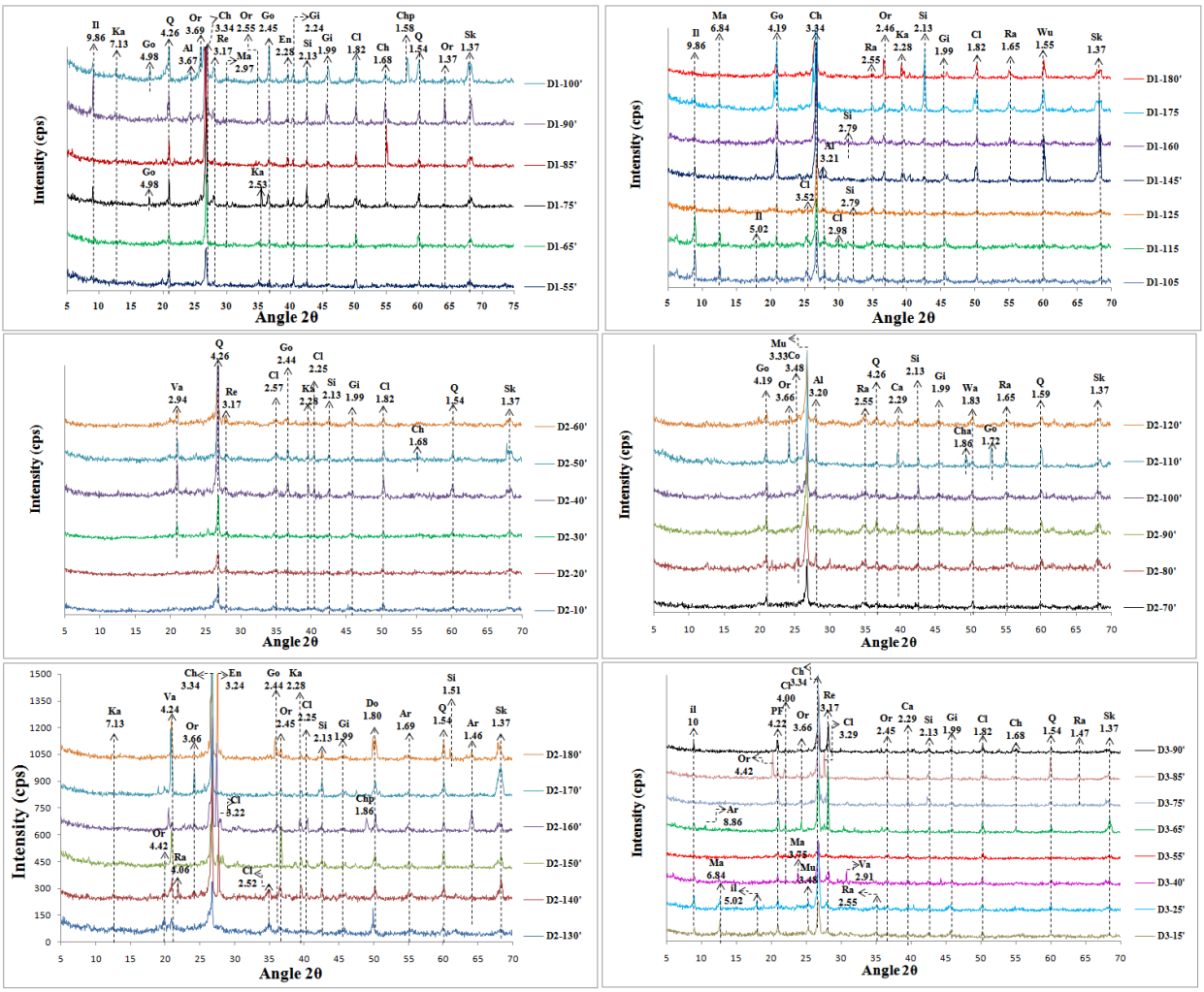

Appendix Figure I 1. 1: Mineralogy of selective depth sediments showed by d-spacing values for a respective mineral, whereas; Bi – Biotite, Gr – Graphite, Cl – Claudetite, Kya – Kyanite, Ca – Calcite, Mag – Maghemite, Gi – Gibbsite, Si – Siderite, Re – Realgar, Le – Lepidocrocite, Do – Dolomite, Q – Quartz, An – Anorthoclase, il – Illite, Chp – Chalcopyrite and Ra – Ramsdellite, abbreviation indicates mineral name, respectively.

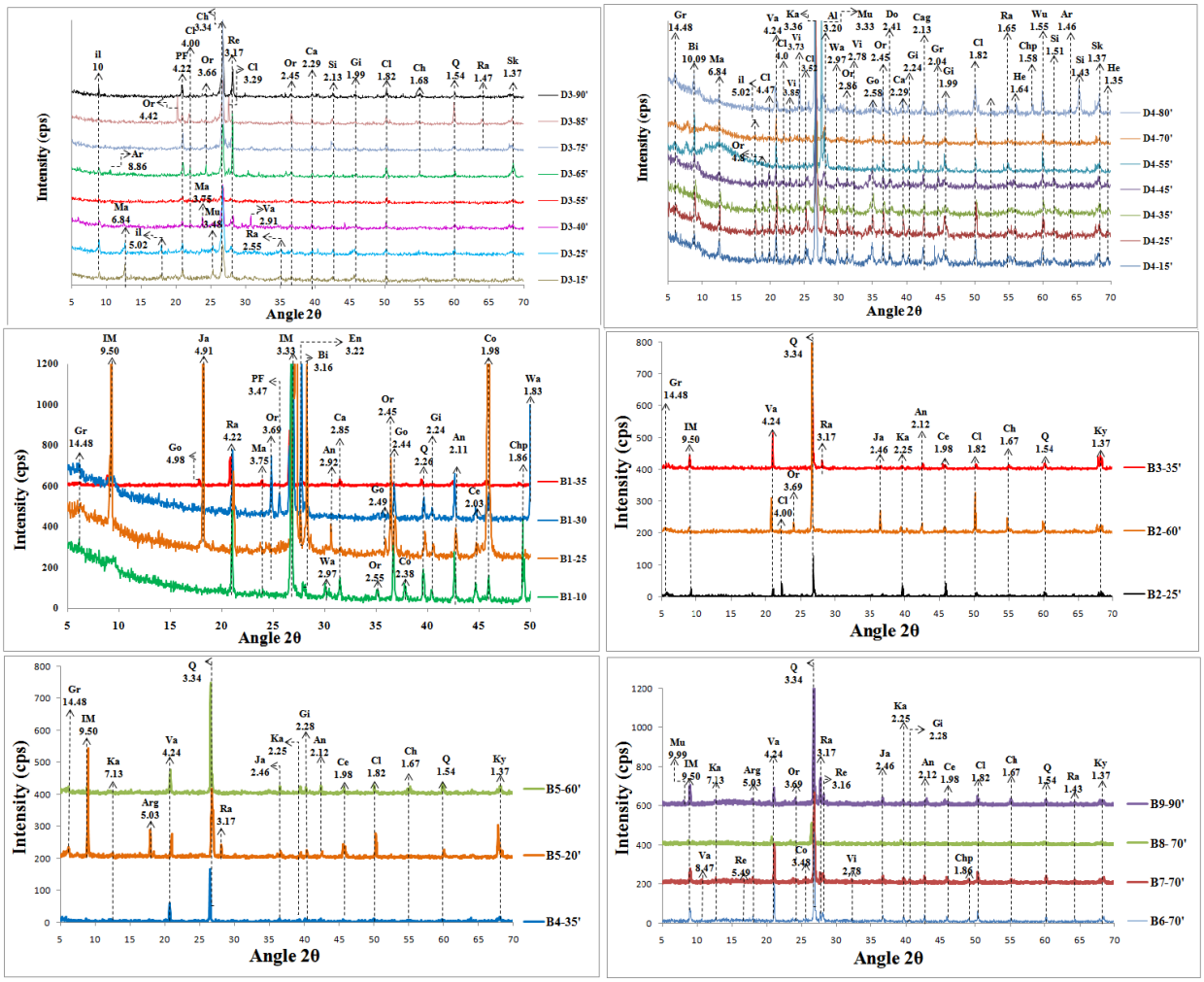

Appendix Figure I 1. 2: Mineralogy of selective depth sediments showed by d-spacing values for a respective mineral, whereas; Bi – Biotite, Gr – Graphite, Cl – Claudetite, Kya – Kyanite, Ca – Calcite, Mag – Maghemite, Gi – Gibbsite, Si – Siderite, Re – Realgar, Le – Lepidocrocite, Do – Dolomite, Q – Quartz, An – Anorthoclase, il – Illite, Chp – Chalcopyrite and Ra – Ramsdellite, abbreviation indicates mineral name, respectively.

Appendix J 1

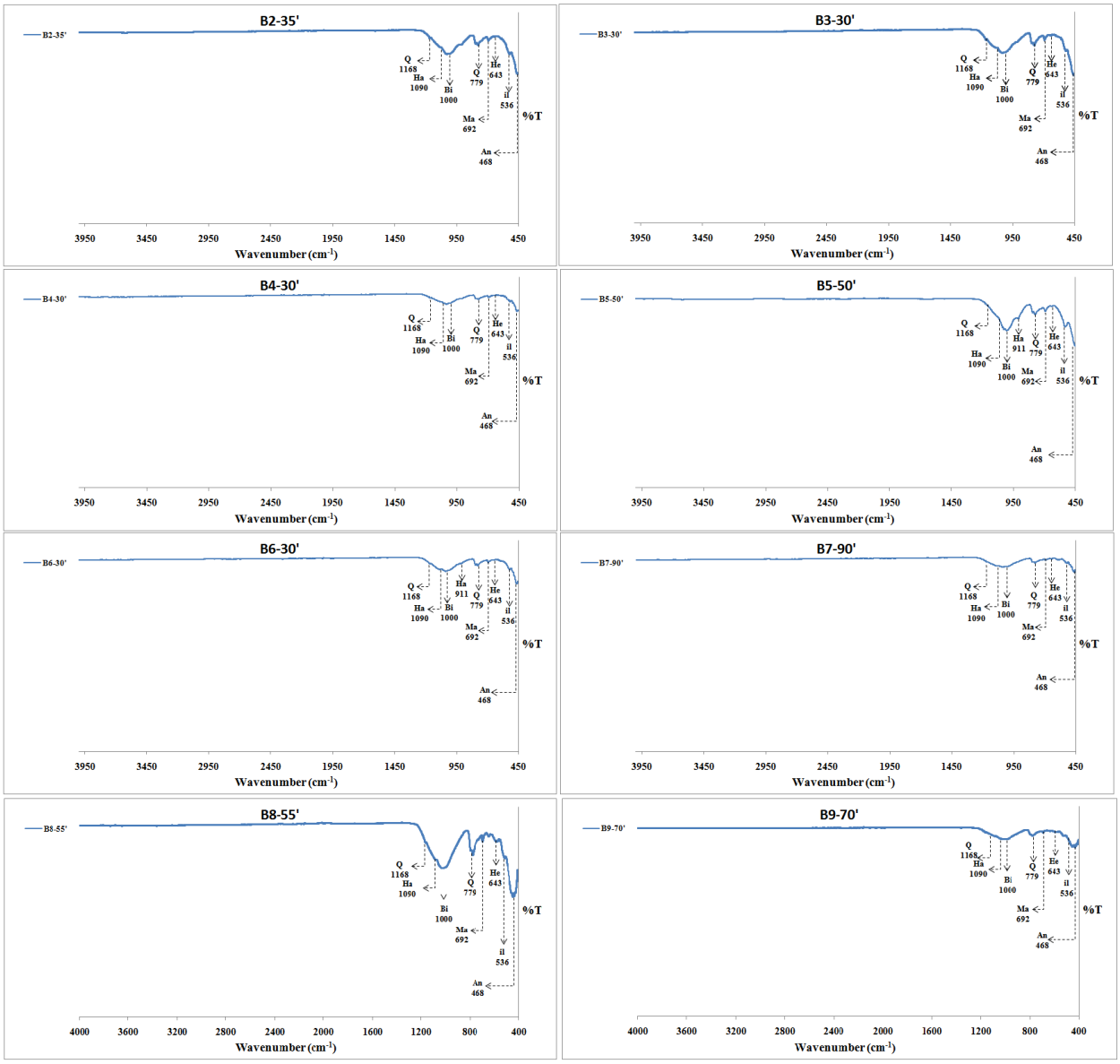

Appendix Figure J 1.1: FTIR results of shallow aquifer sediments of H*As*CR samples, % T vs. wave number portrayed strong, medium, and weak band with an associative functional group of minerals.

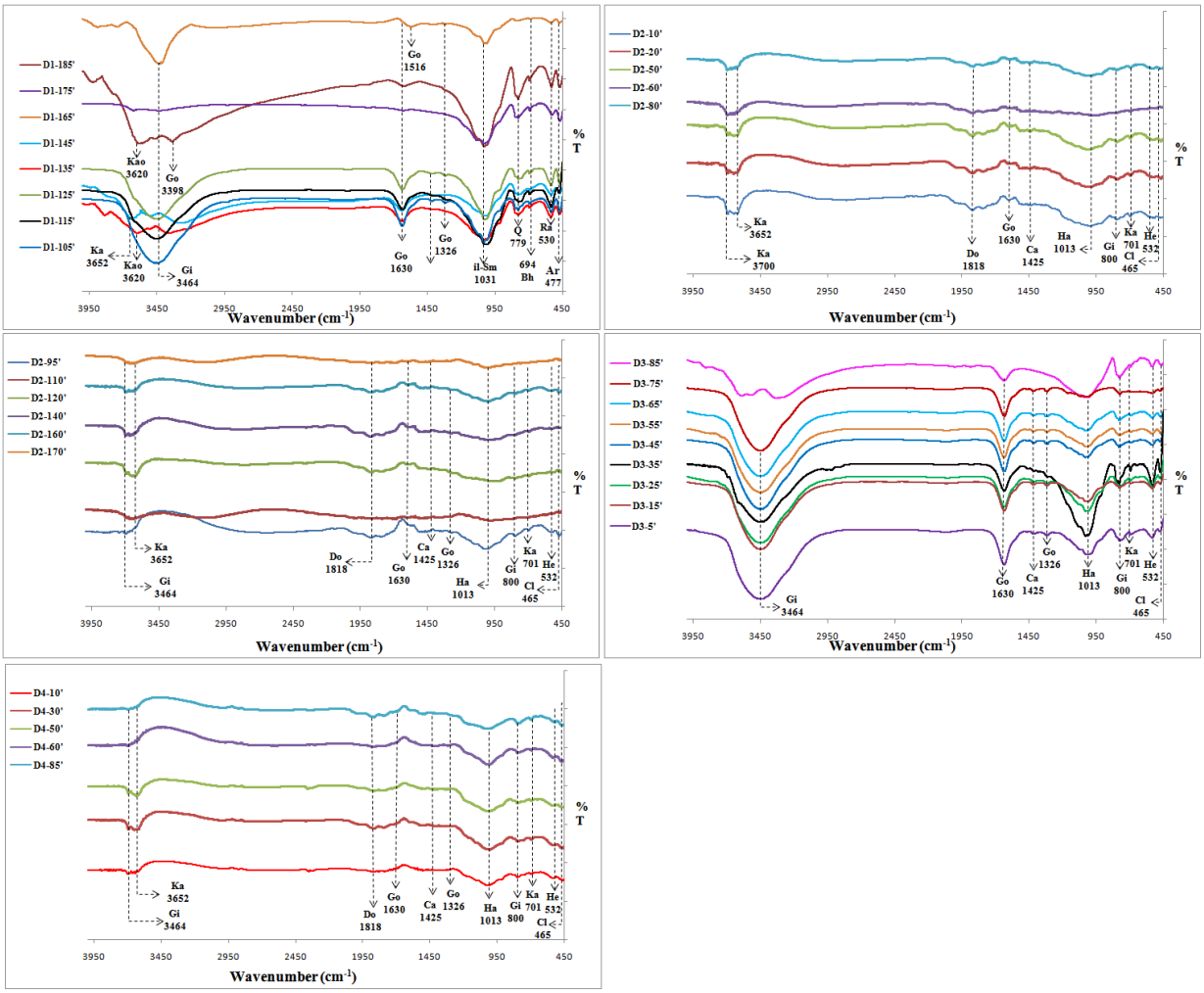

Appendix Figure J 1. 2: FTIR results of shallow aquifer sediment of L*As*CR samples, % T vs. wave number portrayed strong, medium, and weak band with an associative functional group of minerals.

Appendix K1

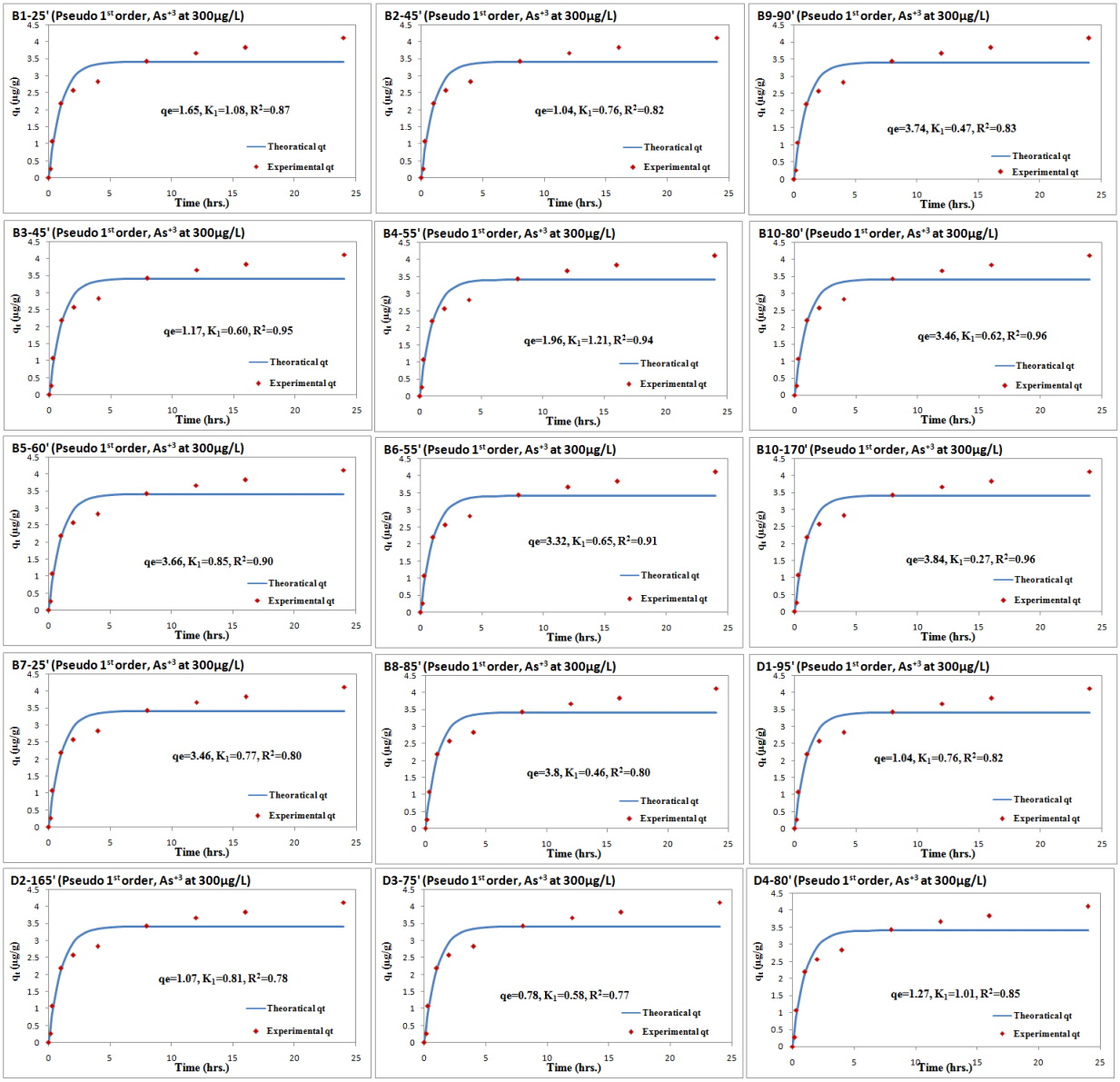

Appendix Figure K 1. 1: Pseudo 1st order kinetic reaction model results for *As*$^{+3}$ adsorption on selective sediment samples at the initial 300 µg L^{-1} concentration.

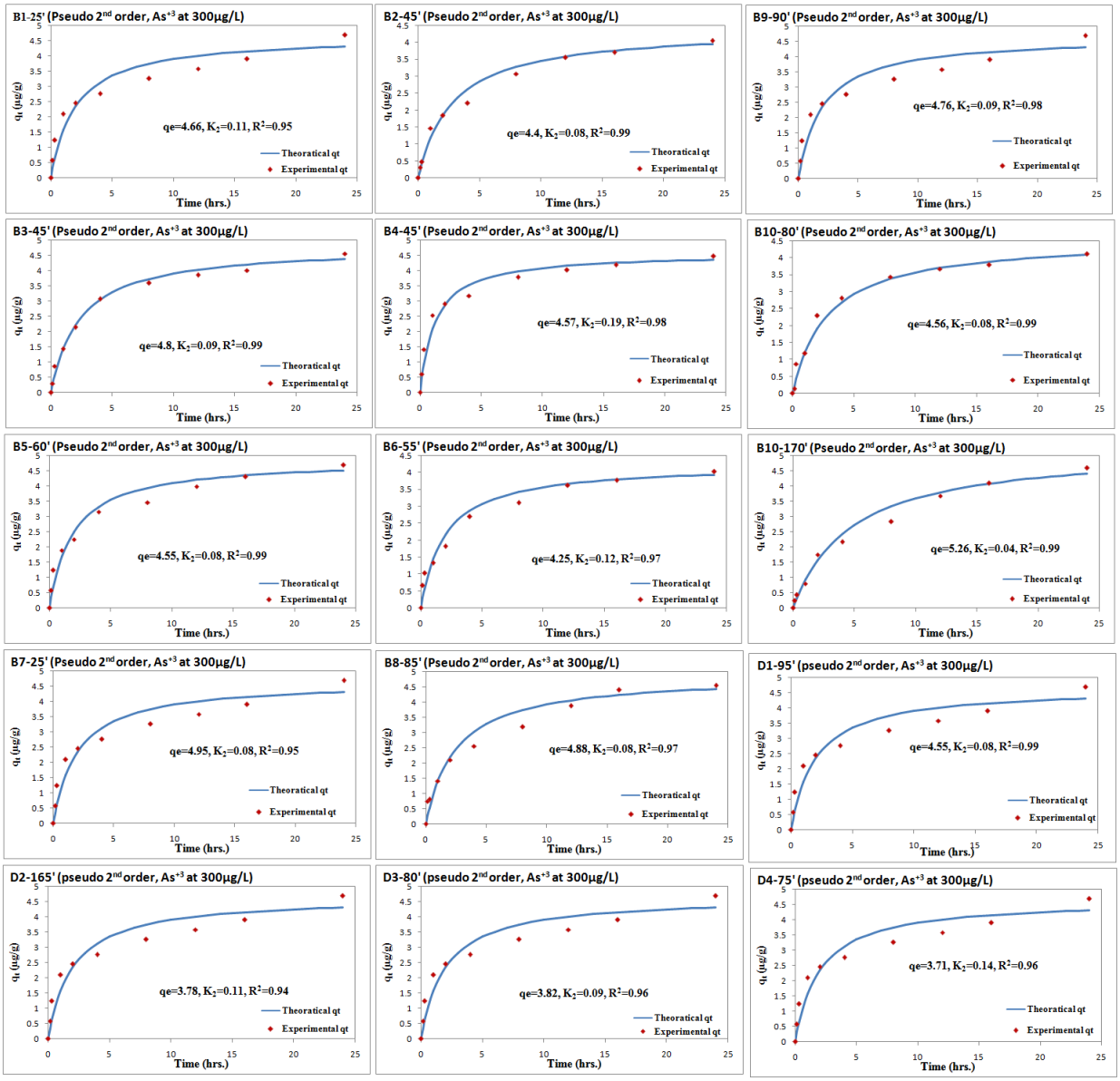

Appendix Figure K 1. 2: Pseudo 2ndorder kinetic reaction model results for *As*$^{+3}$ adsorption on selective sediment samples at the initial 300 µg L^{-1} concentration.

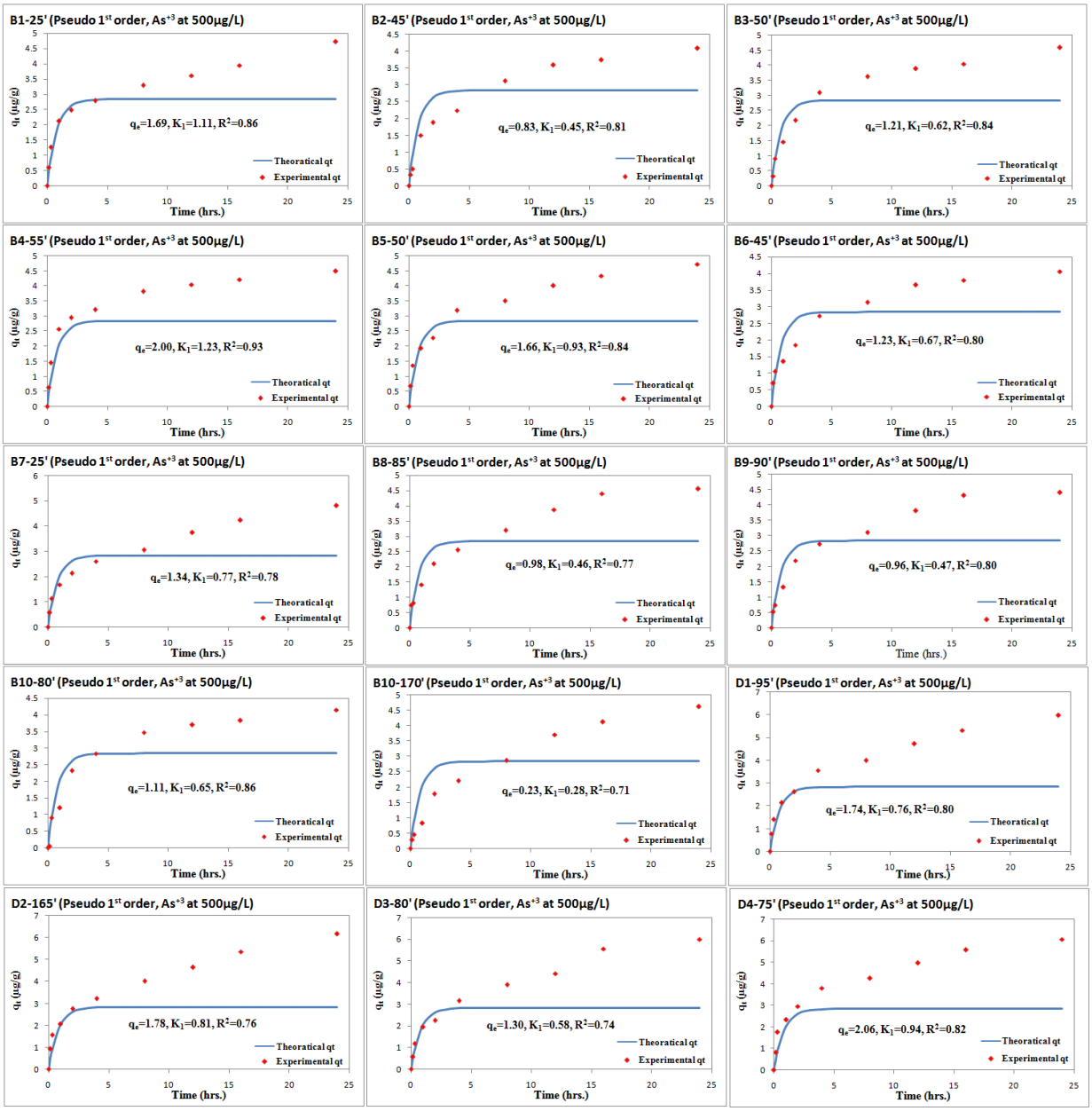

Appendix Figure K 1. 3: Pseudo 1st order kinetic reaction model results for *As*$^{+3}$ adsorption on selective sediment samples at the initial 500 µg L^{-1} concentration.

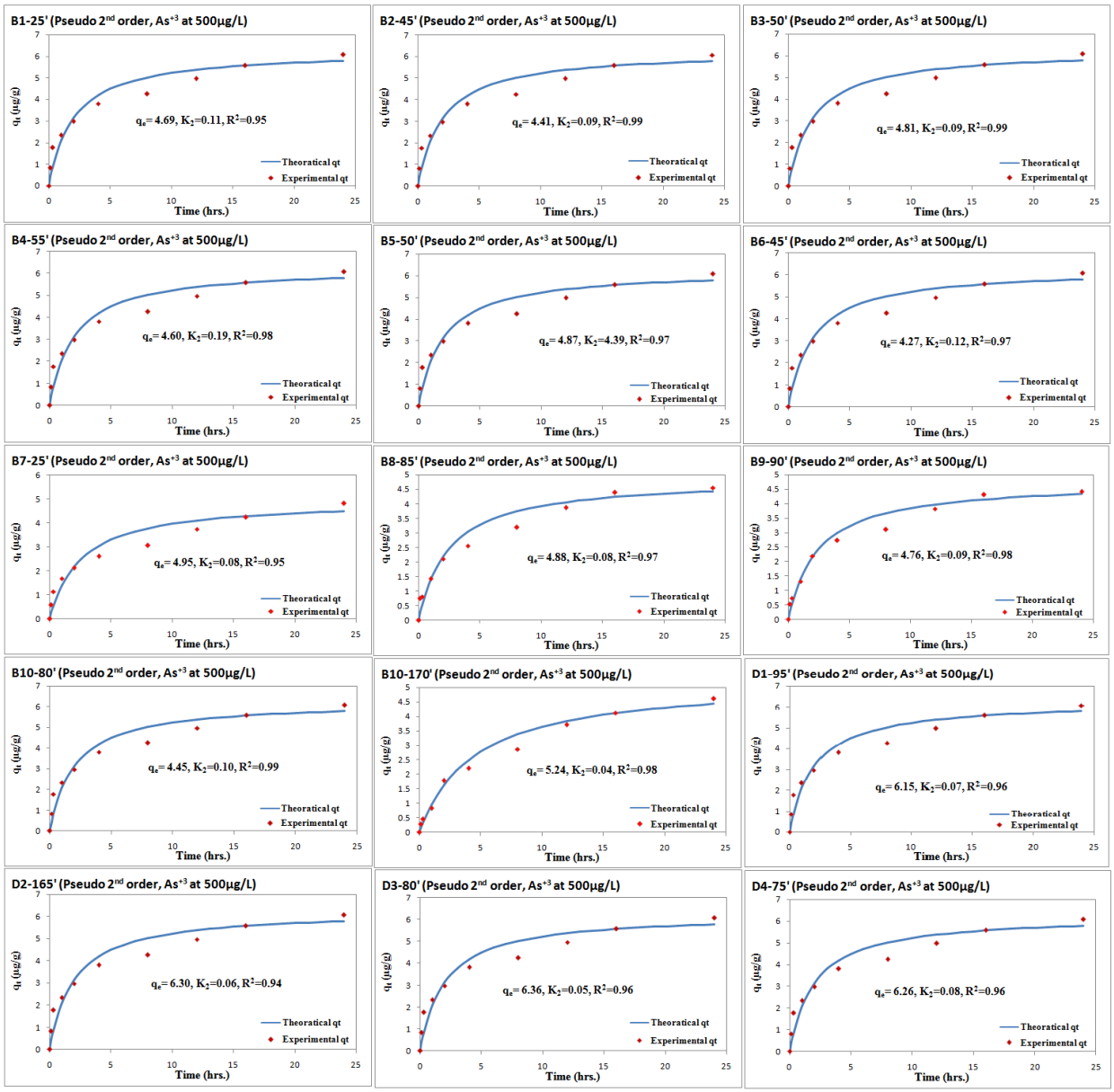

Appendix Figure K 1. 4: Pseudo 2nd order kinetic reaction model results for *As*$^{+3}$ adsorption on selective sediment samples at the initial 500 µg L^{-1} concentration.

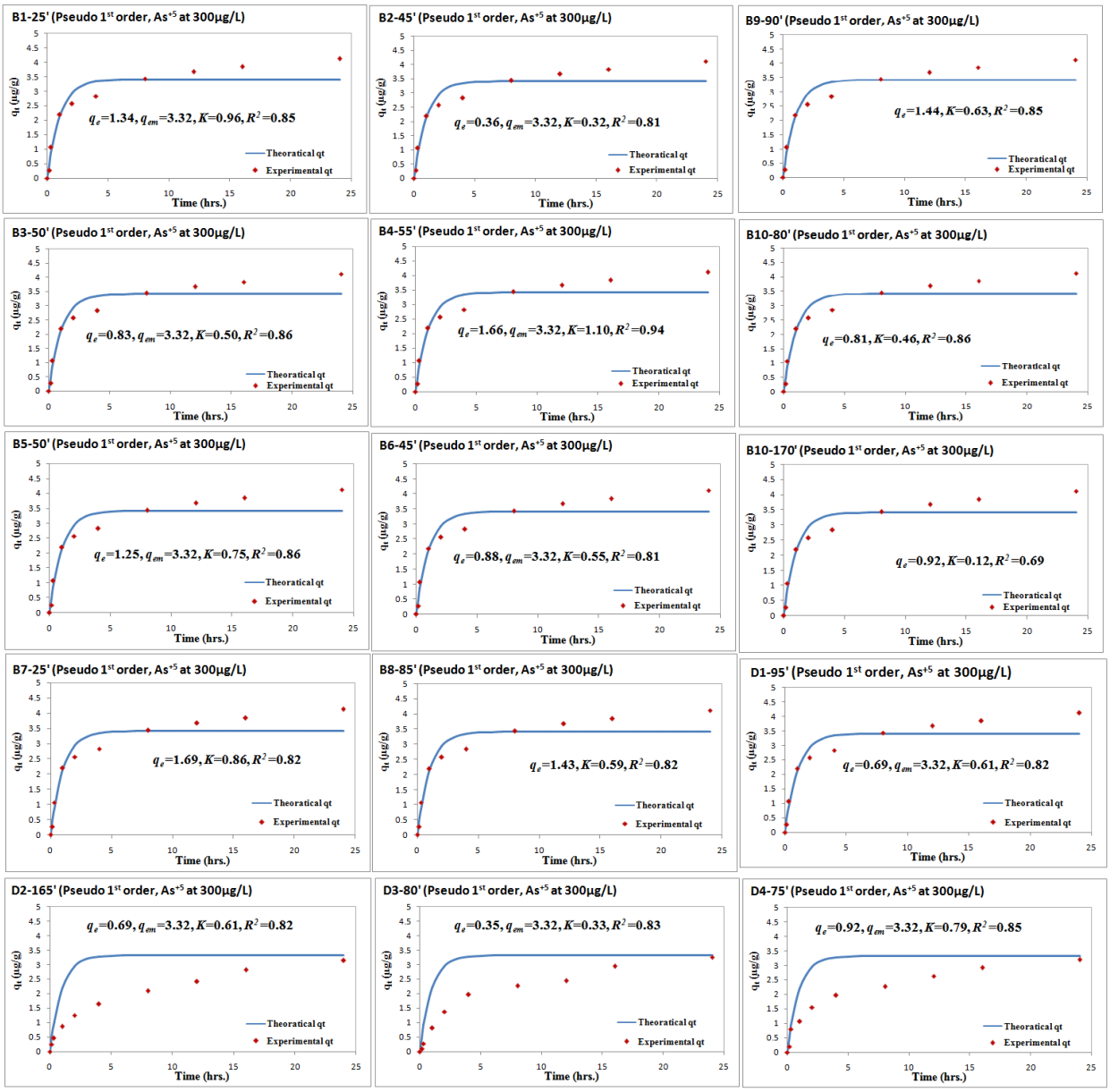

Appendix Figure K 1. 5: Pseudo 1st order kinetic reaction model results for As^{+5} adsorption on selective sediment samples at the initial 300 µg L^{-1} concentration.

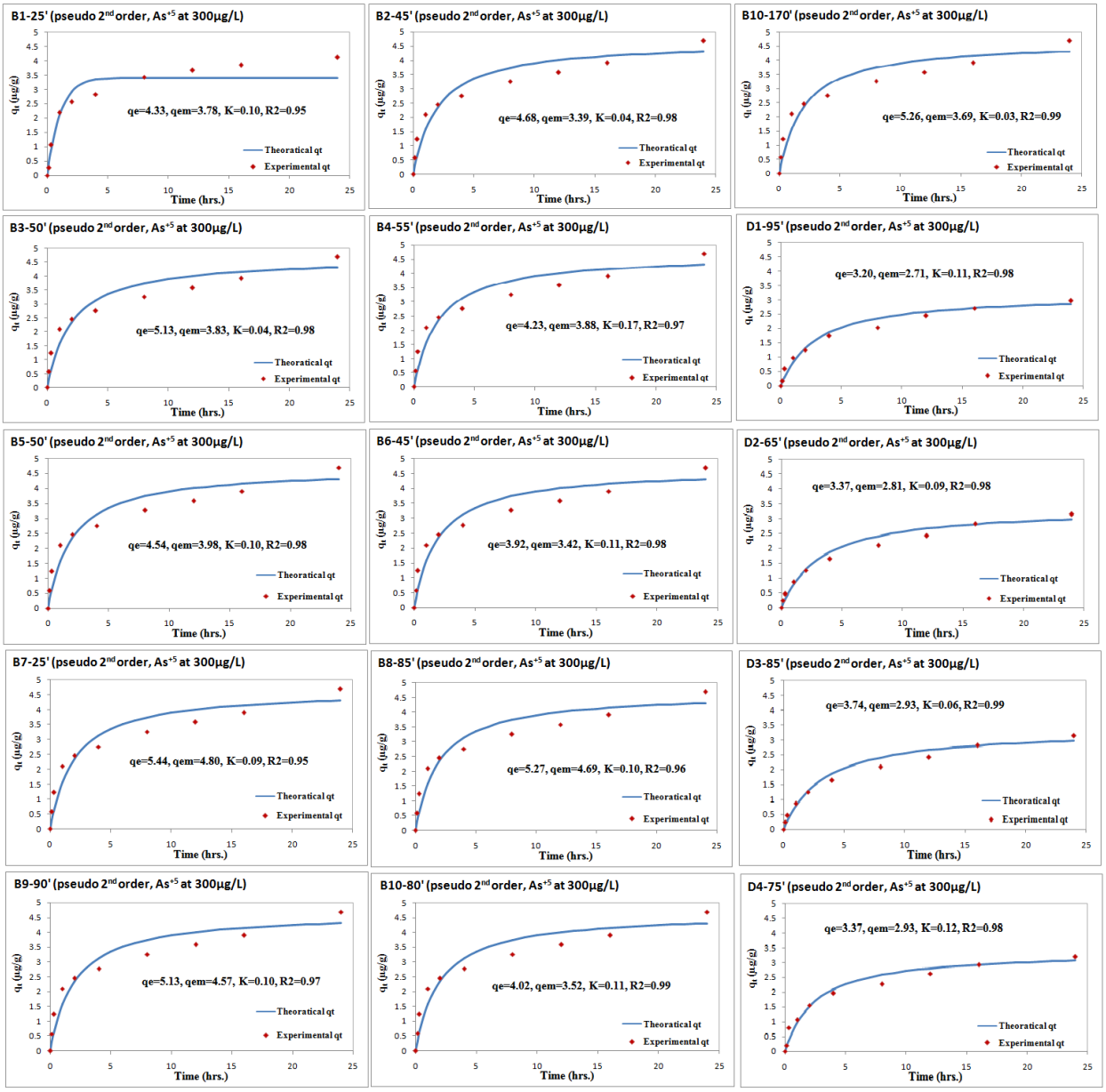

Appendix Figure K 1. 6: Pseudo 2ndorder kinetic reaction model results for *As*$^{+5}$ adsorption on selective sediment samples at the initial 300 µg L^{-1}concentration.

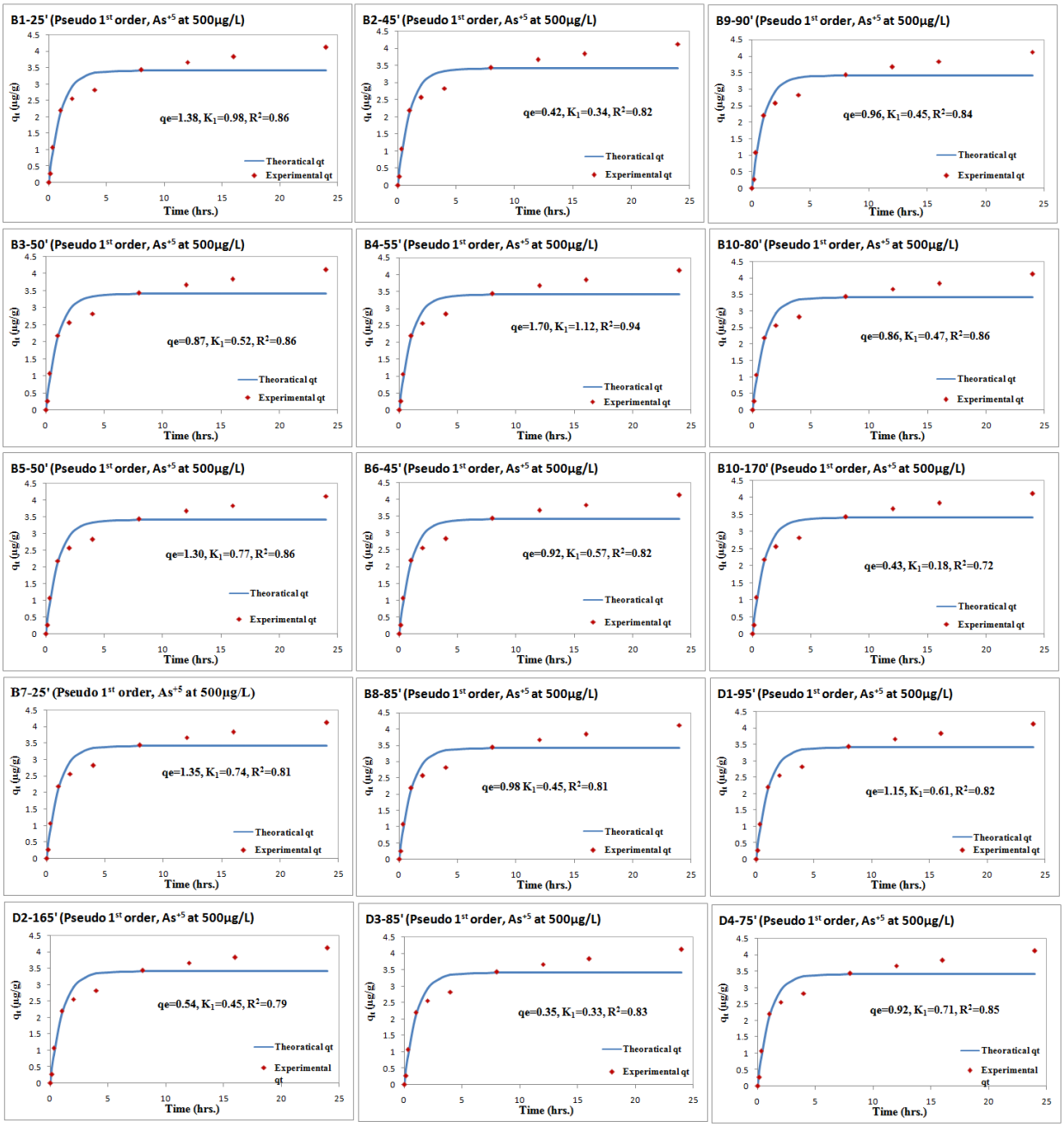

Appendix Figure K 1. 7: Pseudo 2nd order kinetic reaction model results for *As*$^{+5}$ adsorption on selective sediment samples at the initial 500 µg L^{-1} concentration.

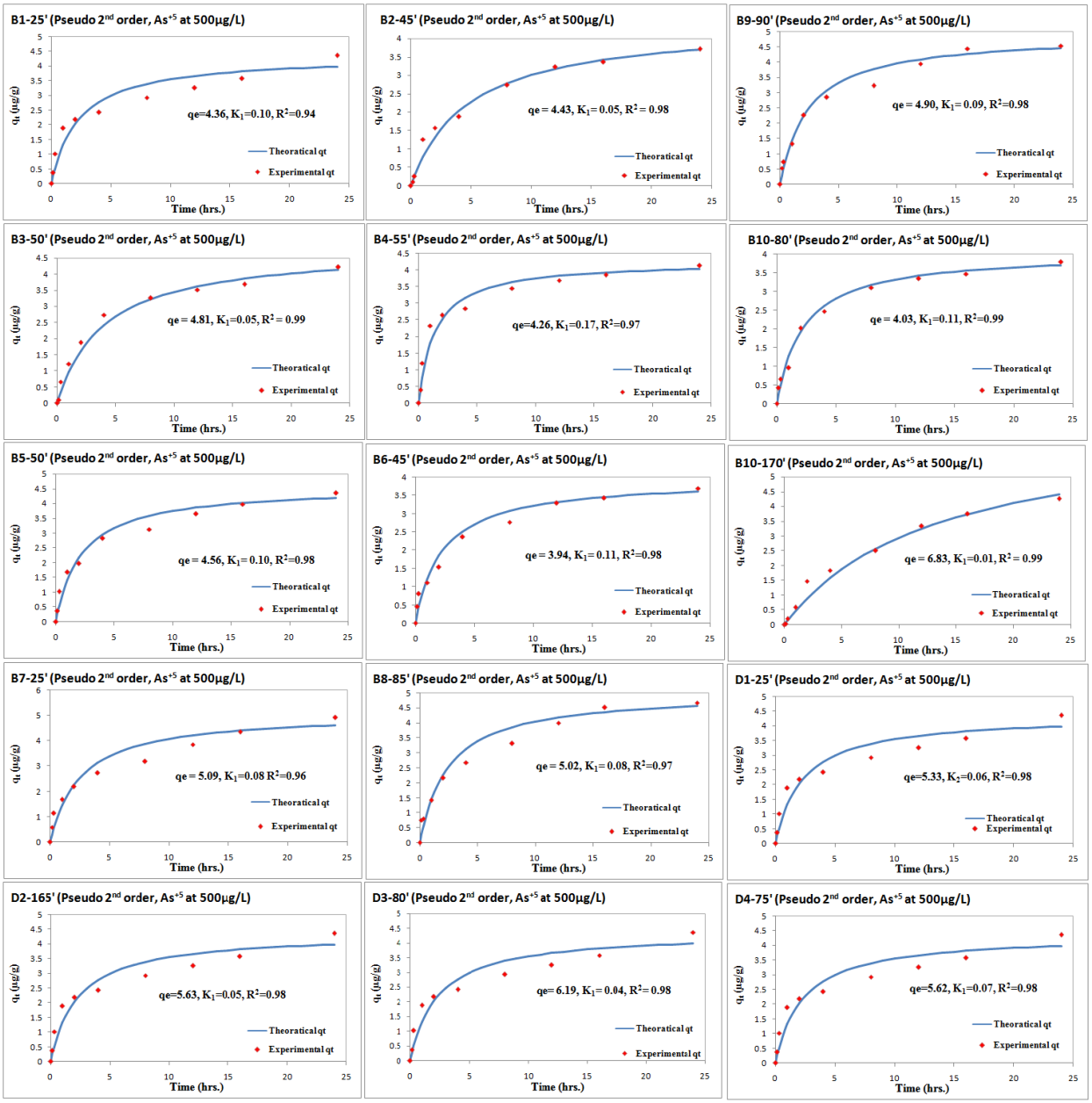

Appendix Figure K 1. 8: Pseudo 2nd order kinetic reaction model results for *As*$^{+5}$ adsorption on selective sediment samples at the initial 500 µg L^{-1} concentration.

Appendix L1

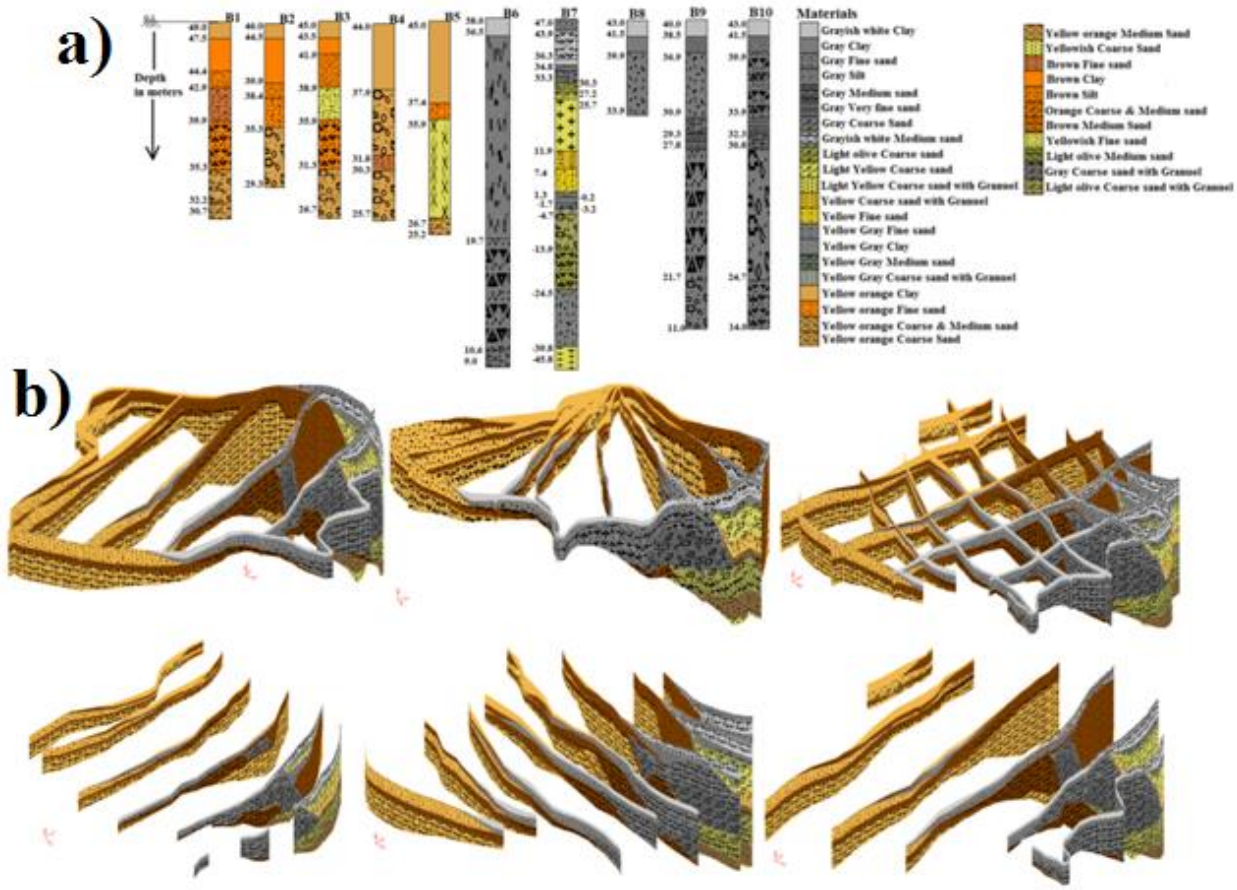

Appendix Figure L1. 1: Stratigraphy 3D view showed the distribution and extensivity of each aquifer and soil material in lateral and vertical direction, a) showed lithology of bore well H*As*CR stratigraphy whereas b) showed L*As*CR study area stratigraphy

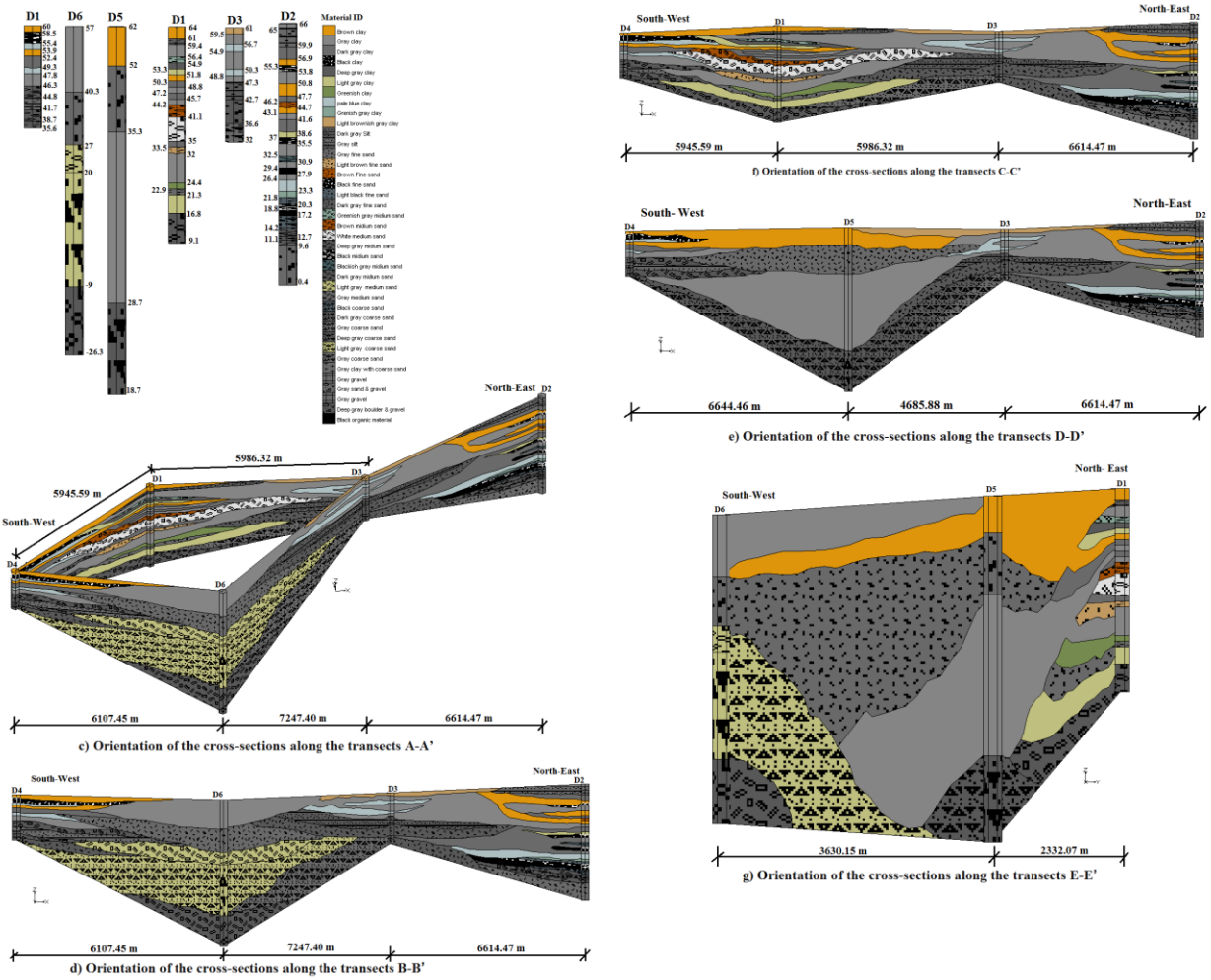

Appendix Figure L 1. 2: Five lithology cross-sections along transects (viz. A-A', B-B,' C-C,' D-D' and E-E') shown in represents aquifers connectivity and distribution in adjoining area with respect to sediment color.

Appendix M1

Appendix Figure M 1. 1: Permeability test mould showed a combination of clay (thickness = 2 cm) and Fine sand (thickness = 4 cm) setup used for the permeability test.

Appendix Figure M 1. 2: Permeability test mould showed Medium sand (thickness = 5 cm) setup used for the permeability test.

Appendix Figure M 1. 3: Permeability test mould showed Medium sand (thickness = 4 cm) and clay (thickness = 2 cm) setup used for the permeability test.

Appendix Figure M 1. 4: Permeability test mould showed medium sand (thickness = 2 cm), fine sand (thickness = 2 cm) and clay (thickness = 2 cm) setup used for permeability test.

Research output

- **Publications (accepted)**

✓ **Sathe, S.S.,** Mahanta, C., Mishra, P., 2018. Simultaneous influence of indigenous microorganism along with abiotic factors controlling arsenic mobilization in Brahmaputra floodplain, India. J. Contam. Hydrol. https://doi.org/https://doi.org/10.1016/j.jconhyd.2018.03.005

- Sathe, S. S., & Mahanta, C., 2019. Groundwater flow and arsenic contamination transport modeling for a multi aquifer terrain: Assessment and mitigation strategies. Journal of environmental management, 231, 166-181.https://doi.org/10.1016/j.jenvman.2018.08.057

- **Publications (under Review)**

- Sandip S. Sathe, Chandan Mahanta. Integrated factors controlling Arsenic release and mobilization in alluvial floodplain of Brahmaputra, India (in the journal of "Soil and Sediment Contamination an International Journal" Taylor and Francis).

- **Journal papers (under preparation)**

✓ **Sandip S. Sathe** and Chandan Mahanta, 2018. Integrated factors controlling Arsenic release and mobilization in an area interfaced near Brahmaputra alluvial floodplain of Assam, India.

✓ **Sandip S. Sathe** and Chandan Mahanta, 2018, Groundwater Arsenic contamination vis-à-vis bacteriological dynamics in an alluvial river flood plain.

✓ **Sandip S. Sathe** and Chandan Mahanta, 2018. Groundwater Arsenic Contamination: A Review of Prevalence, Mobilization, Health Risks, and Mitigation Strategies (Review Article).

- **Internal conferences/proceedings**

✓ **S. Sathe;** Chandan Mahanta; Anirudha Mahagaonkar; Leichombam Menan Devi; Girish Vyas Evidences of Arsenic release and Mobilization Mechanism for arsenic accumulation in groundwater systems caused by bacterial activity and interpretation based on sediment colorizations. *International Conference on Challenges of Anthropocene* (ICCA), 10-11 May 2017.

✓ **S. Sathe** and C. Mahanta, Morphological and Mineralogical in some Large Floodplain Aquifers. Arsenic Research and Global Sustainability: Proceedings of the Sixth *International Congress on Arsenic in the Environment* (As2016), June 19-23, 2016, Stockholm, Sweden.

✓ **S. Sathe,** C Mahanta, A Mahagaonkar, Evidence of microbiological control of arsenic release and mobilization in aquifers of Brahmaputra flood plain. Proceedings of the

Sixth *International Congress on Arsenic in the Environment* (As2016), June 19-23, 2016, Stockholm, Sweden.

- ✓ Chandan Mahanta, **S. Sathe**, Prosun Bhattacharya, (2012) Grain size, mineralogy and sediment composition as factors controlling release and mobilization of arsenic in parts of the Brahmaputra floodplains, northeastern India. *The Geological Society of America* (GSA).